Temperature-Dependent Optical Characterization of Inorganic Lead Halide Perovskites

An in-Depth Study of Fundamental Processes

MSc. Daniel Gau de León

Instituto de Física y CINQUIFIMA, Facultad de Ingeniería, Universidad de la República,
Julio Herrera y Reissig 565, C.C. 30, 11000 Montevideo, Uruguay
✉ dgau@fing.edu.uy

Tribunal: Dr. Ricardo Marotti (Orientador)
Dr. Daniel Ariosa (Presidente)
Dr. Rodolfo Jalabert
Dr. Mauricio Rodriguez
Dra. Mariana Berruet
Dr. Lorenzo Lenci (Suplente)

Declaración de autoría para las publicaciones en las que se basa una tesis doctoral por compilación de artículos:

La autoría de las <u>ideas, desarrollos, programas de computación y resultados</u> de la presente tesis doctoral pertenece exclusivamente al autor y el/<u>los</u> directores de la Tesis, salvo cuando se hace mención expresa de la autoría.

La presente tesis doctoral está compuesta por <u>3</u> artículos que han sido publicados o aceptados para publicación en revistas arbitradas. El autor deja constancia de que sus contribuciones en estos artículos no forman parte de otra tesis. Las contribuciones del autor de la tesis a cada artículo y las posibles modificaciones o actualizaciones que la información en ellos incluida haya tenido para su inclusión en la tesis son las siguientes:

Artículo <u>1</u>:

Título: Electrochemically Assisted Growth of CsPbBr$_3$-Based Solar Cells Without Selective Contacts

Autores: Daniel Ramírez, Gonzalo Riveros, Patricia Díaz, Javier Verdugo, Gerard Núñez, Susy Lizama, Pamela Lazo, Enrique A. Dalchiele, Daniel L. Gau, Ricardo E. Marotti, Juan A. Anta, Lidia Contreras-Bernal, Antonio Riquelme, Jesús Idigoras,
Correos electrónicos de los co-autores:

daniel.ramirez@uv.cl
gonzalo.riveros@uv.cl
patriciaediazg@gmail.com
javear05@hotmail.com
gerard.nunez@alumnos.uv.cl
SUSY.LIZAMA@alumnos.uv.cl
pamela.lazo@uv.cl
dalchiel@fing.edu.uy
khamul@fing.edu.uy
anta@upo.es
lidia.contreras@icmse.csic.es
jesusidigoras@hotmail.com

Estatus: publicado

Contribuciones del autor de la tesis:

1. Revisión exhaustiva de la literatura: Nuestro trabajo se inició con una rigurosa revisión de la literatura existente sobre las propiedades ópticas de las perovskitas. Esta investigación nos permitió establecer una sólida base de conocimientos y comprender el estado actual de este campo.
2. Caracterización experimental: Se llevaron a cabo mediciones de espectros de absorción y fotoluminiscencia a temperatura ambiente en un amplio conjunto de muestras preparadas en diferentes condiciones. El objetivo principal era cuantificar el impacto de estas condiciones en las propiedades ópticas de las perovskitas. Estos experimentos nos proporcionaron datos fundamentales para nuestro análisis.
3. Desarrollo de una rutina de análisis de espectros de absorción: Para analizar los resultados obtenidos, se creó una rutina de análisis de espectros de absorción, lo que permitió una evaluación precisa y sistemática de los datos. Esta herramienta se convirtió en un componente crucial de nuestros trabajos futuros.
4. Elaboración del texto del artículo: Después de un exhaustivo análisis y evaluación de los resultados, se redactó un texto detallado informando los hallazgos obtenidos. Este informe se incluyó en el artículo final, proporcionando una visión completa y consistente del impacto de las diferentes condiciones de preparación de las muestras en sus propiedades ópticas.
5. Contrastación de resultados: Para garantizar la validez y la integridad de nuestros hallazgos, los resultados de la caracterización óptica se compararon con los obtenidos mediante otros métodos. Esta comparación nos permitió obtener una comprensión más completa y robusta de la influencia del método de preparación de las muestras en sus propiedades finales.

Una vez concluido el manuscrito, se llevó a cabo una revisión y edición general del mismo para garantizar su calidad y claridad.

Modificaciones o actualizaciones para inclusión en la tesis:
Sin Modificaciones. Se adjunta el artículo publicado.

Artículo 2:
Título: Photophysical and Photoelectrochemical Properties of CsPbBr3 Films Grown by Electrochemically Assisted Deposition

Autores: Daniel L. Gau, Daniel Ramírez, Fernando Iikawa, Gonzalo Riveros, Patricia Díaz, Javier Verdugo, Gerard Núñez, Susy Lizama, Pamela Lazo, Enrique A. Dalchiele, Lidia Contreras, Jesús Idigoras, Juan A. Anta, Ricardo E. Marotti.

Correos electrónicos de los co-autores:
daniel.ramirez@uv.cl
iikawa@ifi.unicamp.br

gonzalo.riveros@uv.cl
patriciaediazg@gmail.com
javear05@hotmail.com
gerard.nunez@alumnos.uv.cl
SUSY.LIZAMA@alumnos.uv.cl
pamela.lazo@uv.cl
dalchiel@fing.edu.uy
lidia.contreras@icmse.csic.es
jesusidigoras@hotmail.com
anta@upo.es
khamul@fing.edu.uy

Estatus: publicado

Contribuciones del autor de la tesis:

1. Revisión exhaustiva de la literatura: Nuestro trabajo se inició con una amplia revisión de la literatura existente sobre las propiedades ópticas de perovskitas a bajas temperaturas. Esta investigación nos permitió establecer una sólida base de conocimientos y comprender el estado actual de este campo específico.

2. Diseño y realización de mediciones experimentales: Se llevaron a cabo mediciones de espectros de absorción y fotoluminiscencia en función de la temperatura en varias muestras seleccionadas. Dado que este tipo de mediciones no se habían realizado previamente en nuestro grupo de investigación, fue necesario diseñar un dispositivo experimental adecuado.

3. Ampliación de la rutina de análisis: Para analizar los datos obtenidos, se extendió la rutina de análisis mencionada anteriormente para incluir la dependencia de las propiedades ópticas con la temperatura. Esta ampliación permitió un análisis más completo, sistemático y detallado de los datos experimentales.

4. Complemento con medidas fotoelectroquímicas: El Dr. Ramírez aportó sus resultados de medidas fotoelectroquímicas, que sirvieron como complemento a los datos experimentales obtenidos por métodos ópticos. Una vez concluido el análisis de los datos experimentales y los resultados fotoelectroquímicos, se llevó a cabo una interpretación conjunta para obtener una visión global de los procesos fundamentales responsables de las propiedades ópticas de las perovskitas a bajas temperaturas. Este proceso de interpretación fue esencial para comprender en profundidad los fenómenos observados.

5. En este trabajo también fui el encargado de redactar el manuscrito inicial y de la edición para obtener el documento final que fue luego publicado.

Modificaciones o actualizaciones para inclusión en la tesis:
Sin Modificaciones. Se adjunta el artículo publicado.

Artículo 3:

Título: Origin of photoluminescence and experimental determination of exciton binding energy, exciton-phonon interaction, and urbach energy in γ-CsPbI₃ nanoparticles.

Autores: Daniel L. Gau, Isabel Galain, Ivana Aguiar, Ricardo E. Marotti

Correos electrónicos de los co-autores:

igalain@fq.edu.uy
iaguiar@fq.edu.uy
khamul@fing.edu.uy

Referencia bibliográfica: D. L. Gau, I. Galain, I. Aguiar, R. E. Marotti, *J. Lumin.* **2023**, *257*, 119765.

DOI: 10.1016/J.JLUMIN.2023.119765
Estatus: publicado
Contribuciones del autor de la tesis:

1. Conceptualización de la idea central del trabajo y su relevancia en el campo de las perovskitas.
2. Medición de propiedades ópticas y difracción de rayos X: Se realizaron mediciones de espectros de absorción, fotoluminiscencia en función de la temperatura y difracción de rayos X a temperatura ambiente. Estos análisis fueron realizados en varias muestras para lograr optimizar sus propiedades ópticas, composición, morfología y estabilidad.
3. Análisis de los resultados de propiedades ópticas: Se realizó un análisis exhaustivo de los resultados de las mediciones de propiedades ópticas en función de la temperatura. Utilizando las rutinas de análisis mencionadas en el trabajo anterior.
4. También se participó activamente en la interpretación de los difractogramas obtenidos por la difracción de rayos X y en el análisis de imágenes de microscopía electrónica de alta resolución (HRTEM). Esta colaboración fue esencial para comprender la estructura y morfología de las perovskitas estudiadas.
5. Redacción y preparación del manuscrito para su publicación.

Modificaciones o actualizaciones para inclusión en la tesis:
Sin Modificaciones. Se adjunta el artículo publicado.

1 Introduction

2 Fundamental Properties of Perovskites

3 Experimental Results

4 Work in Progress

5 Discussion

Work Summary

This doctoral thesis delves into the fundamental properties of perovskites, which have rapidly emerged as one of the most active fields of study in the solid-state community over the past decade. Perovskites, having the distinctive ABX_3 crystal structure, are the first solution-processed semiconductors capable of matching the properties of conventional semiconductors. Their exceptional properties have paved the way for the development of highly efficient perovskite-based devices in record time. However, many of perovskites' fundamental properties remain a mystery, inhibiting further device development and commercialization. Therefore, the aim of this work is to perform an extensive exploration of the fundamental properties of inorganic perovskite materials, including $CsPbBr_3$ thin films and γ-$CsPbI_3$ nanoparticles, using advanced temperature dependent spectroscopic techniques as continuous wave photoluminescence and transmittance. Through these techniques, we conducted a detailed study of the excitonic properties in perovskites, resulting in the extraction of key parameters like Stokes shift, exciton binding energy, exciton-phonon interaction energy and Urbach energy in both systems. The knowledge of these properties is of vital importance for the implementation of perovskite-based devices. Besides that, an in-depth study of the previously mentioned properties allowed us to develop a comprehensive, yet straightforward model to elucidate absorption and emission mechanisms, considering the strong excitonic properties of perovskites. We expect that our model serves as a crucial tool for deciphering the complex correlations between optoelectronic properties, device efficiency, and stability, as these parameters can be influenced by excitonic properties. The stability issue is of particular importance in perovskite-based devices, since the short durability is nowadays the biggest obstacle for commercialization in perovskite-based devices. As an efficient, affordable, and solution-processable material, perovskites have shown promising capabilities in transforming the solar energy sector, thus holding great potential for the decarbonization of our energy generation matrix.

To demonstrate the usefulness of the mentioned model we investigated, using temperature dependent spectroscopic techniques the effects of the amorphization process during the self-assembly of γ-$CsPbI_3$ nanoparticles into nanorods under illumination from a solar simulator. The light-induced self-assembly process in these perovskites is a phenomenon that, to the best of our knowledge, has not been previously reported in the literature. This process is also highly interesting from the fundamental point of view since it can hold the key to a better understand of surface properties of perovskites and as a new route for the synthesis of more complex nanostructures. Further, we also applied our model to explore the impact of secondary phases in non-stoichiometric $CsPbBr_3$ thin films in the optoelectronic properties of thin films.

In summary, this doctoral thesis offers valuable insights into the fundamental properties of perovskites, and it also presents a novel, comprehensive model for understanding the underlying mechanisms governing perovskite optoelectronic behavior.

Resumen del Trabajo

Esta tesis doctoral profundiza en las propiedades fundamentales de las perovskitas, que han emergido rápidamente como uno de los campos de estudio más activos en la comunidad de estado sólido durante la última década. Las perovskitas, con su distintiva estructura cristalina ABX_3, son los primeros semiconductores procesados en solución capaces de igualar las propiedades de los semiconductores convencionales. Sus propiedades excepcionales han allanado el camino para el desarrollo de dispositivos basados en perovskitas de alta eficiencia en tiempo récord. Sin embargo, muchas de las propiedades fundamentales de las perovskitas siguen siendo un misterio, inhibiendo el desarrollo y la comercialización de dispositivos adicionales. Por lo tanto, el objetivo de este trabajo es realizar una exploración extensa de las propiedades fundamentales de perovskitas inorgánicas, incluyendo películas delgadas de $CsPbBr_3$ y nanopartículas de γ-$CsPbI_3$, utilizando técnicas espectroscópicas avanzadas dependientes de la temperatura como fotoluminiscencia de onda continua y transmitancia. A través de estas técnicas, realizamos un estudio detallado de las propiedades excitónicas en perovskitas, lo que resultó en la extracción de parámetros clave como el desplazamiento de Stokes, la energía de ligación de excitón, la energía de interacción excitón-fonón y la energía de Urbach en ambos sistemas. El conocimiento de estas propiedades es de vital importancia para la implementación de dispositivos basados en perovskitas. Además, un estudio profundo de las propiedades mencionadas anteriormente nos permitió desarrollar un modelo comprensible, pero sencillo, para dilucidar los mecanismos de absorción y emisión, considerando las fuertes propiedades excitónicas de las perovskitas. Esperamos que nuestro modelo sirva como una herramienta crucial para descifrar las complejas correlaciones entre las propiedades optoelectrónicas, la eficiencia del dispositivo y la estabilidad, ya que estos parámetros pueden ser influenciados por las propiedades excitónicas. La cuestión de la estabilidad es de particular importancia en los dispositivos basados en perovskitas, ya que la corta durabilidad es en la actualidad el mayor obstáculo para la comercialización de dispositivos basados en perovskitas. Como material eficiente, asequible y procesable por solución, las perovskitas han demostrado capacidades prometedoras en la transformación del sector de la energía solar, por lo tanto, tienen un gran potencial para la descarbonización de nuestra matriz de generación de energía.

Para demostrar la utilidad del modelo mencionado, investigamos, utilizando técnicas espectroscópicas dependientes de la temperatura, los efectos del proceso de amorfización durante el autoensamblaje de las nanopartículas de γ-$CsPbI_3$ en nanovarillas bajo la iluminación de un simulador solar. El proceso de autoensamblaje inducido por la luz en estas perovskitas es un fenómeno que, hasta donde sabemos, no ha sido previamente reportado en la literatura. Este proceso es también altamente interesante desde el punto de vista fundamental ya que puede contener la clave para una mejor comprensión de las propiedades de superficie de las perovskitas y como una nueva ruta para la síntesis de nanoestructuras más complejas. Además, también aplicamos nuestro modelo para explorar el impacto de las fases secundarias en las películas delgadas no estequiométricas de $CsPbBr_3$ en las propiedades optoelectrónicas de las películas delgadas.

En resumen, esta tesis doctoral ofrece valiosas percepciones sobre las propiedades fundamentales de las perovskitas, y también presenta un modelo novedoso y completo para entender los mecanismos subyacentes que rigen el comportamiento optoelectrónico de la perovskita.

Acknowledgements

I would like to express my deep and sincere gratitude to my family and friends. Your unwavering support, understanding, and love have been my bedrock throughout this process. You've seen me at my best and my worst, and your constant belief in me has been instrumental during this long and often challenging journey. I owe a tremendous debt of gratitude to my advisor, Ricardo. His vast knowledge of solid state physics, matched by his dedication to rigorous and high-quality research, has been truly inspiring. His guidance throughout this exploration of the fascinating properties of perovskites has been invaluable, and I am fortunate to have journeyed alongside him. Special thanks are due to Daniel Ramirez and Enrique Dalchiele, along with his team, who introduced me to the captivating world of perovskite materials. Your knowledge and passion for this field sparked my curiosity and set me on the path I've followed in this research. My gratitude extends to Isabel Galain, who provided invaluable help by synthesizing samples of exceptional quality during the challenging period when COVID-19 halted our initial works. Her determination and dedication have been awe-inspiring and significantly contributed to the progress of this research. To my lab partners, Javier, Enzo, and Carina, I offer my profound appreciation for your supportive and insightful feedback on this work. I am fortunate to have worked alongside such diligent researchers, and I look forward to further collaborations in our shared future work in the field of perovskites. I hope that the results presented in these pages will serve as a foundation for a specialized group dedicated to furthering our understanding of perovskites.

Introduction
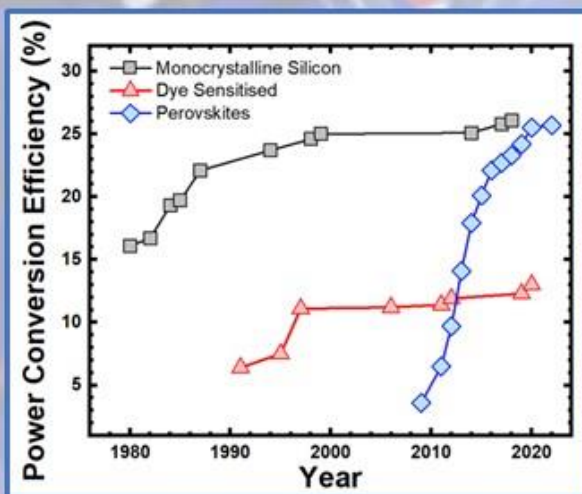
"We are like tenant farmers chopping down the fence around our house for fuel when we should be using Natures inexhaustible sources of energy – sun, wind and tide. … I'd put my money on the sun and solar energy. What a source of power! I hope we don't have to wait until oil and coal run out before we tackle that" — **Thomas Edison**

1: Introduction

1.1.   Semiconductor Physics

The development stage of a civilization is determined by the type of materials it has learned to master. Thus, the stone age man defended himself using spears, bows and arrows and other technologies that we would today call rudimentary. However, at that time these represented the cutting-edge technology. Thanks to these technologies, primitive man was able to make modifications to his environment with the aim of more easily satisfying his needs, thereby increasing his chances of survival. Later, the mastery of the use of metals began, allowing the manufacture of increasingly sophisticated and useful tools. The mastery of metals allowed the manufacture of steam machines, which were the foundation of the first industrial revolution. In the 20th century, if we look at it from the point of view of Solid State Physics (SSP), we see one of the greatest revolutions in history. This revolution was based on the previous development of semiconductor physics, which made the birth of the silicon industry possible. This industry is nowadays considered one of the most important technologically worldwide affecting technology and geopolitics, as we recently saw in the shortage of semiconductor chips. In the early stages of development of the silicon industry, in the 1960s, the first commercial transistors were implemented. Over time, the manufacturing techniques were optimized, allowing for increasingly high levels of integration in integrated circuits. This integration has been evolving sustainably, giving rise to what we now call Moore's Law (which is actually an empirical law) named after Gordon Moore, co-founder of Fairchild Semiconductor and Intel, the first to observe that the number of transistors in a dense integrated circuit doubles every two years. Integration is at the base of the computer revolution of the last century and is also what has allowed the implementation of devices with functionalities that only appeared in science fiction books 50 years ago.

The field of Semiconductor Physics has been highly active both in terms of fundamental and applied physics since its inception. Thanks to advances in this area many scientific truths have been discovered allowing us to better understand the world around us. Besides that, it is also thanks to this activity that recent innovation as LEDs (Light Emitting Devices) flat screens with high definitions and new functionalities such as touch screens. When looking at the LEDs revolution we also see another characteristic of innovation in Solid State Physics: the short time frame between a revolution in the field and its real impact on industry resulting in the emergence of new and better products. In 2014, Isamu Akasaki, Hiroshi Amano, and Shuji Nakamura received the Nobel Prize in Physics for their development of the blue LED in 1986. This sparked a revolution in lighting technologies, leading to the commercialization of LED lamps in the early 21st century, which quickly dominated the market. This resulted in a significant decrease in the amount of energy used for lighting and opened the door for new functionalities in the lighting area.

The search for increasingly better materials for the development of new technologies is far from over. On the contrary, this is one of the most active fields in science globally. Currently, some of the intensively worked topics within solid-state physics are:

• Solid-State Batteries

• Polymer Development

• Photovoltaic Solar Cells

• Devices for producing hydrogen from water

• Two-dimensional materials

• Superconductors

• Quantum Materials

• Implementation of solid-state qubits for quantum computers

• Implementation of systems for photonic, phononic, plasmonic, spintronic, and other systems

One of the main motivations guiding the evolution of devices is to mitigate the effects of climate change and meet the goals set by the IPCC (Intergovernmental Panel for Climate Change). For this reason, there is particularly intense research in the development of new materials for photovoltaic solar energy production.

1.2.   Production of Photovoltaic Solar Energy

According to the recent report by the Intergovernmental Panel on Climate Change (IPCC), there is ample evidence that unprecedented changes are currently taking place in the Earth's climate system. These changes are caused by the increasing concentration of CO_2 and other greenhouse gases in the atmosphere. In particular, it has been shown that changes in the climate system tend to increase the likelihood of extreme weather events, which in turn impact the global economy, human health, and ecosystems[1]. Fortunately, the report also demonstrates that human actions can still determine the future of the climate, and if a substantial and sustained reduction of such emissions is achieved, the impact of climate change could be significantly mitigated[2]. Based on the latest results, reducing the impacts of climate change requires a reduction of greenhouse gas emissions between 40% and 70% by 2050. One of the necessary measures to achieve the IPCC's goals is a rapid and profound transformation of the energy generation matrix. Since solar energy is an abundant resource on the Earth's surface, photovoltaic solar energy is one of the major candidates to play a crucial role in the decarbonization of energy production[3,4]. To achieve a deeper penetration of photovoltaics in the energy matrix, it is essential to develop more efficient photovoltaic solar cells that can be produced at a lower cost.

Photovoltaic Solar Cells currently play a dominant role in semiconductor physics research. These technologies are currently the ones with the highest growth rate due to their low production cost (which can still be lowered further) and low carbon footprint[1]. It has also been proven that the deployment of photovoltaic technologies has positive impacts on the economy, health, and climate. Furthermore, since solar energy is the most equitably distributed form of energy, the deployment of photovoltaic technologies will have a positive geopolitical impact by reducing the dependence on energy imports and concentration.

The current market for photovoltaic solar cells is dominated by silicon-based technologies[5]. Given the indirect character of absorption of photons in silicon the presence of defects in structure has a very

negative impact on the performance of silicon-based devices. For this reason, large amounts of high-purity silicon must be used to produce silicon cells. This increases their cost and makes their mass production difficult, thus limiting the possibility of a rapid deployment of this technology. However, thanks to intense work by the scientific community over the last few decades, production methods have been optimized to the point where it is now possible to manufacture photovoltaic solar cells with competitive production costs. In addition, the commercial panels available today have a lifespan of 25 years, and some are expected to last even up to 40 years. We can therefore say that silicon-based technologies are a reliable and mature technology. This leadership can be seen in the fact that the thanks to silicon the first Terawatt of installed photovoltaic solar energy production capacity was achieved in 2022, beating any prediction. Given the significant advancement of silicon-based technologies, it's challenging for emerging technologies to play a significant role in the photovoltaic solar energy production market. However, during the 2010s, a new technology, perovskite-based solar cells, has garnered attention from both the scientific community and the industry. This is because these cells can be manufactured with efficiencies comparable to silicon while offering lower production costs and requiring significantly less energy to produce. In fact, these cells can be synthesized through solution-based methods at low temperatures (~100°C).

1.3.   Perovskite-Based Solar Cells: The Leading Emerging Technology

Since the 90's, when commercial Si cells seemed unattainable due to their high cost, there has been intense research into new technologies for photovoltaic solar energy production. This is how dye sensitized solar cells (DSSCs) were born. This technology initially sparked great interest but their efficiency could not be increased beyond 13% (Figure 2). Nevertheless, DSSCs gave rise to what we now know as Perovskite Cells. Currently, perovskite cells made of are one of the most promising technologies to challenge silicon's dominance. In perovskite-based cells the absorbing layer has a crystalline structure with the structure ABX_3. A wide variety of materials have this structure, but in the context of this work, when the term perovskite is used, it will refer to metal halide perovskites (MHPs). In this particular type of material, A is formed by fragments such as methylammonium (MA$^+$: [CH$_3$NH$_3$]$^+$) or formamidinium (FA$^+$: [CH(NH$_2$)$_2$]$^+$) organics, inorganics like cesium (Cs$^+$), or a mixture of these, B is a divalent metal cation like lead (Pb^{++}) or tin (Sn^{++}), and X is a halide such as chloride (Cl$^-$), bromide (Br$^-$), iodide (I$^-$), or a combination of these[7,8].
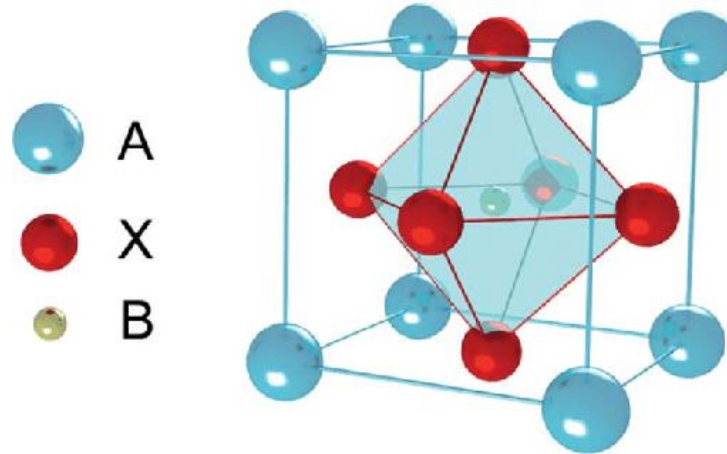
Figure 1: Perovskite cubic structure.

Considering a solid spheres model where the radius of ions A, B and X is represented by R_A, R_B and R_X respectively, the formation of a compound with perovskite structure is determined by the Goldschmidt tolerance factor defined as

$$t = \frac{R_A + R_X}{\sqrt{2}(R_B + R_X)}$$

When 0.81 < t < 1.1 the formation of a perovskite structure can be expected. Besides that, if 0.9 < t < 1.0 a cubic structure is likely and if 0.81 < t < 0.9 a it is more probable to obtain a tetragonal structure[9].

It has been shown that it is possible to produce MHPs with energy conversion efficiencies similar to silicon technologies, but at a fraction of their cost and with much lower technological requirements enabling local production of devices[6].

1.4.   History of perovskite-based solar cells

Since its invention at Bell Labs in 1954, it took Silicon solar cells almost fifty years to reach an efficiency of 25%. Perovskite-based solar cells achieved the same in just over ten years (Figure 2), thanks to a combination of advancements in cell architecture, deposition methods, and understanding of the fundamental processes responsible for their properties. Despite this unprecedented progress, the commercialization of perovskite devices is currently strongly hindered mainly due to stability issues and concerns about the toxicity of the materials used (mainly Lead-Pb).

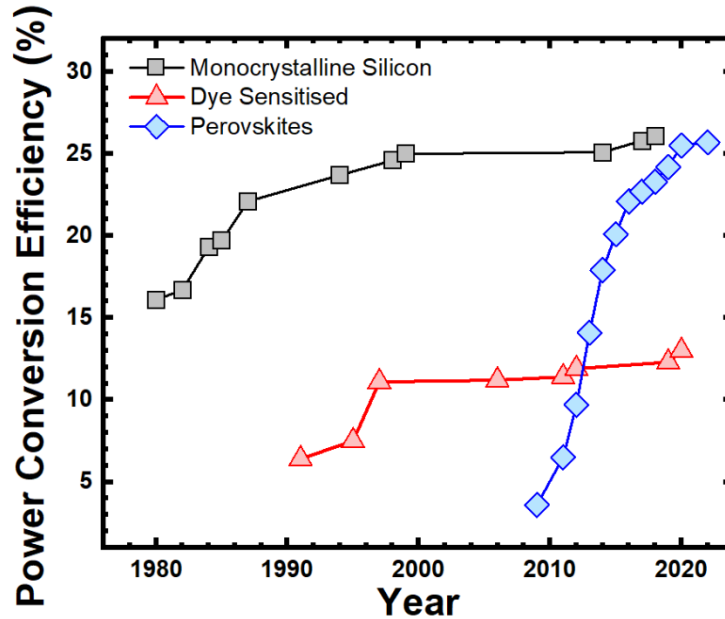*Figure 2: Evolution of efficiency in diferet Solar Cells technologies: silicon (black cubes) Dye Sensitized Solar Cells (red triangles) and Perovskties (blue rombuses). Data obtained from the National Renewable Energy Laboratory webpage https://www.nrel.gov/pv/cell-efficiency.html.*

Evolution of Architecture

Interest in lead halide perovskites started in the late 90s with the work of Mitzi and collaborators. In this initial work, the optoelectronic properties of hybrid perovskites showed strong excitonic influence[10]. Although the researchers suggested that perovskites could be used for the manufacture of LEDs or solar cells, they did not continue with the work. Later, in search of an alternative to the organic inks used in Gratzel cells, Miyasaka and collaborators implemented a solar cell with an architecture similar to that used in DSSCs that had a power conversion efficiency (PCE) of 3.8%[11]. Although this was the first report on the photovoltaic effect in perovskites, the device degraded rapidly due to the presence of a liquid electrolyte, which dissolved the perovskite layer. A major breakthrough in the development of perovskite solar cells was achieved in 2012 when a complete solid-state PSC was implemented for the first time, replacing the liquid electrolyte with Spiro-OMeTAD hole transporting layer (HTL)[12]. The elimination of the liquid electrolyte made the devices more efficient and significantly increased their durability, surpassing 500 hours for the first time. The next step was achieved by Burschka and his collaborators, who introduced the first flat architecture PSC with a PCE of 15%[13]. Another major contribution was presented in 2015 with the introduction of a $FAPbI_3$ an absorbing layer in a flat PSC[14]. This step was crucial in further increasing the stability of the devices.

Description of the Most Used Architecture in PSCs

A solar cell is a device that generates an electric current (moving electrons) by absorbing sunlight (photons) that strikes its surface. For this to be possible, several processes must occur:

1. Absorption of an incoming photon and subsequent production and separation of an electron-hole pair, which will be the charge carriers that generate the electric current.

2. The charge carriers must migrate to reach the opposite contacts that connect the cell to the external circuit. During this trip, several mechanisms such as dispersion and recombination can occur, causing the carrier not to reach the contacts, as well as other causes of energy loss.

It is also important to highlight that for a charge carrier, crossing the interface between one material and another is a process that can lead to recombination of carriers hence limiting transport of carriers, and energy loss. Therefore, in the design and implementation of a solar cell, not only the movement of the charge carriers within the materials should be considered, but also the behavior of the carriers when passing from one material to another. It is also important to note that much of the progress that is currently being made in increasing the efficiency of solar cells is in the optimization of these interfaces. To continue with this positive trend in the efficiency of perovskite-based solar cells it is important to understand the fundamental processes of charge carrier generation and dynamics within devices.

Most used perovskite solar cell Architecture

Absorption of incoming sunlight and subsequent production and separation of an electron-hole pair, which become the charge carriers that generate the electrical current. The charge carriers must travel to the opposite contacts that connect the solar cell to the external circuit. During this journey, various phenomena such as scattering and recombination can occur, causing the charge carrier to not reach the contacts and resulting in other energy losses.
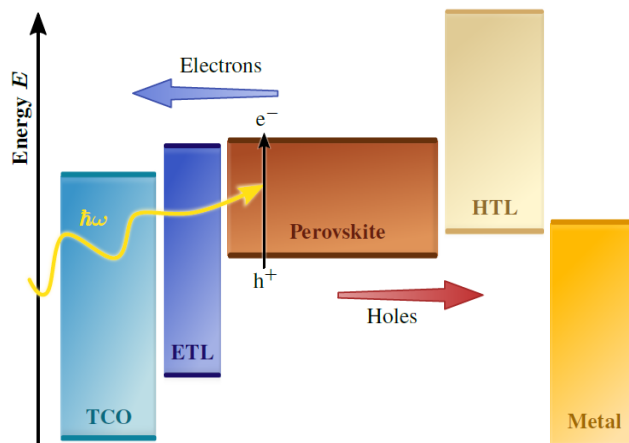

Figure 3: Basic structure of a planar perovskite solar cell. Main components from left to right are Transparent Conductive Oxide (TCO), Electron Transport Layer (ETL) Absorbing Perovskite Layer, Hole Transporting Layer (HTL) and Metallic Cathode.

Fundamental Components of Planar-architecture PSCs

As previously mentioned, perovskite-based cells have evolved their architecture over time. Currently, all cells with the highest energy conversion efficiency have a planar architecture, as shown in Figure 3, composed of 5 layers:

1. Metallic cathode

2. Hole transport layer (HTL)

3. Absorbing perovskite layer

4. Electron transport layer (ETL)

5. Transparent conductive oxide (TCO)

The function of the metallic cathode and the transparent conductive oxide is to extract the holes/electrons generated by light absorption, thus allowing a current to be established by the charge connected to the cell. Additionally, the conductive oxide also acts as a window, allowing incoming incident solar radiation to enter and be absorbed by the absorbing layer. The absorbing layer, which in LHP is formed by the perovskite, has the function of producing charge carriers from the absorption of photons with energy greater than the material's bandgap. Finally, the electron/hole transport layers act as interfaces between the absorbing layer and the electrodes, and separate the charges generated in the perovskite. Usually when the working principle of solar cells are discussed electrons and holes are considered as noninteracting. This is usually true, but they also can remain bounded forming an hydrogen-like state called an exciton. The study of the fundamental properties of excitons and the interactions with lattice vibrations (phonons) are the main topics of study of the present work.

1.5.   Colloidal Nanocrystals

Colloidal nanocrystals, defined as particles with a characteristic size smaller than 100 nm, have been an extremely active field of research since the 80s. The study of these systems has allowed the scientific comunity to understand a great number of fundamental phenomena that determine the properties of materials. In particular, the production of nanoperovskites (NPKs) has had a highly important evolution since its first report in 2015[15]. In this seminal work, it was demonstrated that the properties of NPKs can be tuned through quantum confinement and composition. Later, it was shown that the properties can also be tuned by modifying the adsorbed ligands on the surface of NPKs[16]. The abundant research in subsequent years has made it possible to obtain nanocrystals of great quality and to have great control over their size and shape. The most used methods for their production are Hot-Injection and Ligand-assisted Reprecipitation (LARP). With these methods, NPKs form an ink from which excellent quality films can be fabricated (coating and drying process) or can be used as a sensitizing material in devices, such as quantum dot solar cells (QDSCs). This has the advantage of decoupling the synthesis of the crystal and the formation of the film, thus allowing greater control over the formation of the crystals. The efficiency of QDSCs has advanced very quickly since its first report in the mid-2000s, making this technology very

promising today. Notably, today's energy conversion record in QDSC architecture, which stands at 16.6%, was achieved by a device that used NPKs ($CsPbI_3$) as a sensitizing material[16]. Although the progress in the evolution of these devices has been surprising, QDSCs still need to overcome many challenges before they can have a real impact on commercial devices. One of these problems is determined by the method of charge carrier conduction, called Hopping, in which generated charge carriers must jump from one nanocrystal to the next, resulting in low charge mobility and low carrier extraction. To solve this problem, it is necessary to continue research in the physical chemistry of the ligands, their role in stabilizing the nanostructures, and in understanding the fundamental processes that allow adsorption of these on the surface of NPKs.

1.6. Beyond solar cells

The success of perovskites in the field of photovoltaic solar cells is closely linked to the fundamental properties of these materials. The study of perovskites fundamental properties has surged in the past decade, leading to the discovery of their high absorption coefficient, large carrier diffusion lengths, high robustness to defect formation, and ease of adjusting the optical absorption edge by either varying the composition of the samples or by quantum confinement effects in nanoparticles. The discovery of these properties quickly made it evident that perovskites have the appropriate characteristics for the manufacture of other devices such as lasers, LEDs, detectors, scintillators, photocatalytic devices, and unique photon emitters, among others. Although perovskite-based devices are still in their early stages of development, the progress made to date is extremely encouraging and they are likely to reach the market in the next decade.

1.7. Challenges

While significant progress has been made in the development of perovskite-based photovoltaic solar cells over the past decade, they are still far from reaching the market. This is due to two factors that will be discussed below[17].

Degradation/Stability

Real devices are generally exposed to adverse environmental conditions such as thermal stress, humidity, and high lighting intensity. Therefore, to achieve the commercialization of perovskite-based devices, these problems must be solved. For a technology to be effectively adopted in the market, it is necessary to offer consumers a durable product. For example, commercial silicon cells guarantee a life span of about 25 years with a decrease in performance of 15%. In the case of perovskites, the maximum duration of a perovskite cell documented to date has been 100 days under standard one sun illumination at 55°C[18]. This may not seem like much, but it should also be considered that the first devices manufactured only had a life of a few minutes. It should also be noted that there are already several strategies for achieving

greater stability with encapsulation being the most successful. It should also be considered that these extra treatments/processes to which the sample must be subjected can considerably increase production costs and make the optimization process more complex because there are more materials and interfaces to design/deposit.

Toxicity

The presence of Pb in the absorbing layers presents a problem for achieving wider adoption of perovskite-based devices. This concern is well founded, as this metal is highly toxic and has been the cause of a major environmental problem during the 60s whose consequences are still palpable[19]. However, it has been demonstrated that the Pb content in perovskites is very low (0.4 g/m2), considerably lower than that used for soldering commercial Si photovoltaic panels. In addition, encapsulation techniques can be used to prevent lead from escaping from a damaged panel[20,21]. So, although the presence of Pb can be considered a non-fundamental flaw and it is possible to imagine Pb-based technologies in the market with adequate regulation, Pb-free alternatives would certainly be better. To achieve the ideal of perovskite-lead-free devices the scientific community is currently exploring different alternatives, among which we highlight:

1. The possibility of using a less toxic metal cation by completely or partially replacing the Pb cation with other metals such as Sn_2^+, Sn_4^+, Ge_2^+, Cu_2^+, Bi_3^+ and Sb_3^+. With these materials, it is currently possible to obtain solar cells with an efficiency of 14.35%. However, devices based on these materials are still far from being commercialized.

2. Use of double perovskites (elpasolite structure): these materials are characterized by the $A_2M^+M_3^+X_6$ structure, they are a great family of innovative lead-free perovskites. However, these crystals are very difficult to process.

References

[1]   J. Jean, P. R. Brown, *Emerging Photovoltaic Technologies*, **2020**.

[2]   "Español — IPCC," can be found under https://www.ipcc.ch/languages-2/spanish/, **n.d.**

[3]   P. K. Nayak, S. Mahesh, H. J. Snaith, D. Cahen, *Nat. Rev. Mater.* **2019**, *4*, 269.

[4]   M. A. Green, A. Ho-Baillie, *ACS Energy Lett.* **2017**, *2*, 822.

[5]   S. Philipps, W. Warmuth, *Fraunhofer ISE PSE Conf. Consult. GmbH* **2019**.

[6]   B. Roose, E. M. Tennyson, G. Meheretu, A. Kassaw, S. A. Tilahun, L. Allen, S. D. Stranks, *Energy Environ. Sci.* **2022**, DOI 10.1039/D2EE01343F.

[7]   Y. Jiang, X. Wang, A. Pan, *Adv. Mater.* **2019**, *31*, 1806671.

[8]   H. J. Snaith, *Nat. Mater.* **2018**, *17*, 372.

[9]   C. Li, X. Lu, W. Ding, L. Feng, Y. Gao, Z. Guo, *Acta Crystallogr. Sect. B Struct. Sci.* **2008**, *64*, 702.

[10]   D. B. Mitzi, K. Chondroudis, C. R. Kagan, *Inorg. Chem.* **1999**, *38*, DOI 10.1021/ic991048k.

[11]   A. Kojima, K. Teshima, Y. Shirai, T. Miyasaka, *J. Am. Chem. Soc.* **2009**, *131*, 6050.

[12]   H.-S. Kim, C.-R. Lee, J.-H. Im, K.-B. Lee, T. Moehl, A. Marchioro, S.-J. Moon, R. Humphry-Baker, J.-H. Yum, J. E. Moser, M. Grätzel, N.-G. Park, *Sci. Reports 2012 21* **2012**, *2*, 1.

[13]   J. Burschka, N. Pellet, S. J. Moon, R. Humphry-Baker, P. Gao, M. K. Nazeeruddin, M. Grätzel, *Nature* **2013**, *499*, DOI 10.1038/nature12340.

[14]   W. S. Yang, J. H. Noh, N. J. Jeon, Y. C. Kim, S. Ryu, J. Seo, S. Il Seok, *Science (80-.).* **2015**, *348*, DOI 10.1126/science.aaa9272.

[15]   L. Protesescu, S. Yakunin, M. I. Bodnarchuk, F. Krieg, R. Caputo, C. H. Hendon, *Nano Lett* **2015**, *15*, 3692.

[16]   X. Ling, J. Yuan, W. Ma, *Accounts Mater. Res.* **2022**, DOI 10.1021/ACCOUNTSMR.2C00081.

[17]   X. Wang, T. Zhang, Y. Lou, Y. Zhao, *Mater. Chem. Front.* **2019**, *3*, 365.

[18]   Q. Jiang, J. Tong, Y. Xian, R. A. Kerner, S. P. Dunfield, C. Xiao, R. A. Scheidt, D. Kuciauskas, X. Wang, M. P. Hautzinger, R. Tirawat, M. C. Beard, D. P. Fenning, J. J. Berry, B. W. Larson, Y. Yan, K. Zhu, *Nat. 2022 6117935* **2022**, *611*, 278.

[19]   C. C. Patterson, *Arch. Environ. Health* **1965**, *11*, DOI 10.1080/00039896.1965.10664229.

[20]   X. Li, F. Zhang, H. He, J. J. Berry, K. Zhu, T. Xu, *Nature* **2020**, *578*, 555.

[21]   R. D. Mendez L, B. N. Breen, D. Cahen, *ACS Appl. Mater. Interfaces* **2022**, *14*, 29766.

[22]   A. Binek, M. L. Petrus, N. Huber, H. Bristow, Y. Hu, T. Bein, P. Docampo, *ACS Appl. Mater. Interfaces* **2016**, *8*, 12881.

[23]   L. Xie, Q. Zeng, Q. Li, S. Wang, L. Li, Z. Li, F. Liu, X. Hao, F. Hao, *J. Phys. Chem. Lett.* **2021**, *12*, 9595.

FUNDAMENTAL PROPERTIES OF PEROVSKITES
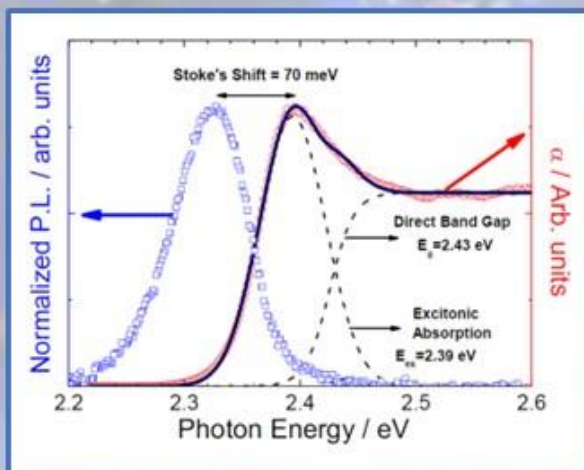
'One shuldn't work on semiconductors, that is a filthy mess; Who knows whether any semiconductor exist…" — **Wolfgang Pauli**

2. Fundamental Properties of Perovskites

2.1. Background

The outstanding success of lead halide perovskites in the development of the new generation of solar cells has put this family of materials in the forefront of optoelectronic materials research. This intense research activity has allowed not only to reach a 26.6 PCE in perovskite based solar cells in 2022, but also to unveil many outstanding properties in perovskites that make them ideal candidates to build a new generation of optoelectronic devices as LEDs[1–3], lasers[4–7], radiation detectors[8–11] and CO_2 reduction devices [12,13],[14] among others. The great success achieved by perovskites in the last decade is attributed to several outstanding properties as a direct bandgap (tunable in the visible spectrum varying their composition)[15], long charge carriers diffusion length[16,17], low Urbach energies[18] and high absorption coefficient[19,20]. Besides that, defects states are shallow (close to the band edge) which is produced by the electronic nature of conduction and valence bands. Valence band maximum and conduction band minimum are formed from the Pb-6s and I-5p atomic orbitals and the Pb-6p and I-5p orbitals respectively, which are both antibonding[21,22], in contrast to what happens in semiconductors as CdSe and GaAs. Defect tolerance in perovskites makes it possible to reach low levels of nonradiative recombination despite high densities of traps states (that can be several orders of magnitude higher than the ones present in traditional semiconductors as Si or GaAs). Despite that, defects do play a crucial role in charge-carrier transport and as nonradiative recombination centers responsible for devices efficiencies and stability. In fact, the most recent advances in the race to increase the efficiency of perovskite-based solar cells were only possible thanks to the development of new passivation techniques. In similar fashion, defects produced by the removal of ligands and surface halides strongly influence the quantum yield (QY) in colloidal perovskite nanoparticles.

Remarkably, the outstanding properties that make perovskite-based devices possible are obtained in solution-processed absorber/emitter layers, in stark contrast to classical semiconductors such as GaAs, CdS, InP that are usually prepared using complex processes as epitaxial growth. The simplicity of preparation also makes perovskite-based devices potentially cheaper and able to be manufactured locally in medium sized facilities[23].

To date the most studied lead halide perovskites are the ones with A cation formed by an organic molecule, typically Methylammonium (MA=CH_3NH_3) and that are normally named hybrid. The organic component introduces instabilities in devices given by external factors as high temperature [24], electric fields [25,26], moisture [27,28], UV radiation [29–31] and photo-oxidation [32,33] which are common in real life device operation conditions. This is seen as an obstacle to obtaining commercial perovskite-based devices. Inorganic perovskites, that change the organic cation by Cs, have been proposed as an alternative. Experimental results consistently show that inorganic perovskites retain the desirable properties of hybrid perovskites while allowing a higher stability[34–39].

The most studied inorganic perovskites are $CsPbBr_3$ and $CsPbI_3$. Since the first report of the synthesis of these materials in the form of nanoparticles a great effort from the scientific community has allowed to vary the morphology of the nanostructures obtaining nanocubes, nanorods, nanoplatelets, nanosheets between others[40]. It has also been possible to lower reaction temperatures and to engineer surface properties by changing ligands and precursors. Previously mentioned studies also allowed us to conclude that the optical and electronic properties of these materials are strongly dependent on their dimensionality. This feature is highly desirable for the design of optoelectronic devices. It has been experimentally proven that reducing the dimensionality in perovskites allows to obtain high photoluminescence quantum yield (PLQY) without the need of core-shell structures as in the case of classical semiconductors. For all these reasons, and many others, inorganic $CsPbX_3$ perovskites are nowadays at the forefront of materials for the development of a new generation of optoelectronic devices.

Despite the great progress made in the last decade a lot is still unknown about perovskites. This is particularly notable in the identification of the fundamental processes behind the properties that make perovskites such good candidates for the implementation of devices. More precisely in the case of optoelectronic properties it is of great importance to have a deep understanding of the photogenerated species, their lifetimes and interaction between charge carriers and with the semiconductor lattice. The interaction of charge carriers with phonons is particularly important since this deeply influences charge transport, which is a fundamental parameter in the design of optoelectronic devices. To study the fundamental properties of perovskites optical spectroscopy techniques as transmittance and photoluminescence are a great tool[41–43]. Moreover, the dependence in these spectra with temperature is a great tool for studying the nature of charge carriers and the fundamental process of interaction with lattice vibrations. It is through knowledge of these processes that it is possible to understand how to optimize devices performance and feed back into the material preparation process to find out the optimal synthesis conditions.

2.2.   Dielectric Function

All the optical properties of a material are condensed in the dielectric function $\epsilon(\omega) = \epsilon_r(\omega) + i\epsilon_i(\omega)$. The real and imaginary parts of this function are related by the Kramers-Kronig relations [43,44]. This relation implies that only one of these expressions is necessary to describe the optical properties of a particular material.

$$\epsilon_r(\omega) - 1 = \frac{2}{\pi} VP \int_0^\infty \frac{\omega' \epsilon_i(\omega')}{\omega'^2 - \omega^2} d\omega'$$

$$\epsilon_i(\omega) = \frac{2\omega}{\pi} VP \int_0^\infty \frac{\epsilon_r(\omega')}{\omega'^2 - \omega^2} d\omega'$$

Where VP represents the Cauchy's principal value of the integral.

It has been extensively reported that MHP's present high dielectric function values in a broad frequency range[45–47]. High values of ε allow an effective screening of defects and charge carriers which can negatively affect the performance of optoelectronic devices. Besides that, as will be discussed later, it also influences the binding energies in excitons. In hybrid MHP's the origin of the high values in $\varepsilon(\omega)$ is attributed to the particular perovskite structure with flexible organic cations in the A-site[48].

The temperature dependence of the dielectric function remains a complex topic within the field, with conflicting data often reported in the literature. Nevertheless, it is usually accepted that three primary effects contribute to the temperature dependency of the dielectric constant[49]. The first is the decrease in the number of polarizable particles per unit volume as the temperature increases, as these particles provide the medium for the electromagnetic interaction and their reduction invariably impacts the permittivity of the material. Secondly, the increase of macroscopic polarizability due to volume expansion plays a significant role. As temperature rises, materials tend to expand, thus altering the interactions between the particles, which in turn affects the polarizability. Lastly, the temperature dependence of the macroscopic polarizability at constant volume is also a contributing factor. Even in a scenario where the volume is held constant, changes in temperature can affect the ability of the material to polarize in response to an electric field.

It is important to note, however, that these three factors do not consider the influence of collective phenomena. For instance, the formation of polarons, which are quasiparticles resulting from the interaction between charge carriers and phonons in a crystal lattice, can induce a screening effect, thereby reducing the dielectric constant.

Despite the importance of understanding the dielectric function in perovskites, a comprehensive and systematic study evaluating the effect of temperature on this property remains to be undertaken. This underlines the need for further research to unravel the complex interplay of factors influencing the temperature-dependent dielectric function in perovskites.

2.3.   Excitons

In a semiconductor the ground, or vacuum, state of electrons consists of a completely filled valence band and a completely empty conduction band. This state is characterized by a total momentum $\vec{K} = 0$, angular momentum $\vec{L} = 0$ and spin $\vec{S} = 0$. The absorption of a photon with energy greater than the bandgap excites an electron from the valence band to the conduction band, simultaneously creating a hole (an electron vacancy) in the valence band. When this happens, we say the system is excited. The electron and the hole are created in the same region in space and, since they have opposite charge, they can remain bounded forming a quasiparticle called an exciton [50,51]. There are two types of excitons:

- Frenkel or tightly bound excitons
- Wannier-Mott excitons

Frenkel excitons have very small radius (smaller than a lattice cell or molecule), and the electron-hole systems remain strongly bound. They are usually observed in insulators and molecular materials. Unlike Frenkel excitons Wannier excitons are delocalized and have a large radius extending over many lattice sites in the crystal (Figure 1a). Given the electron-hole separation is large, it is possible to consider that the system is embedded in a uniform dielectric material with its properties determined by the average of the real structure[51]. In this effective mass approximation when an electron and a hole are formed after the absorption of a photon the Coulomb interaction between them is given by the expression

$$V(r) = -\frac{e^2}{4\pi\epsilon_0\epsilon r} \qquad r = |\vec{r}_e - \vec{r}_h|$$
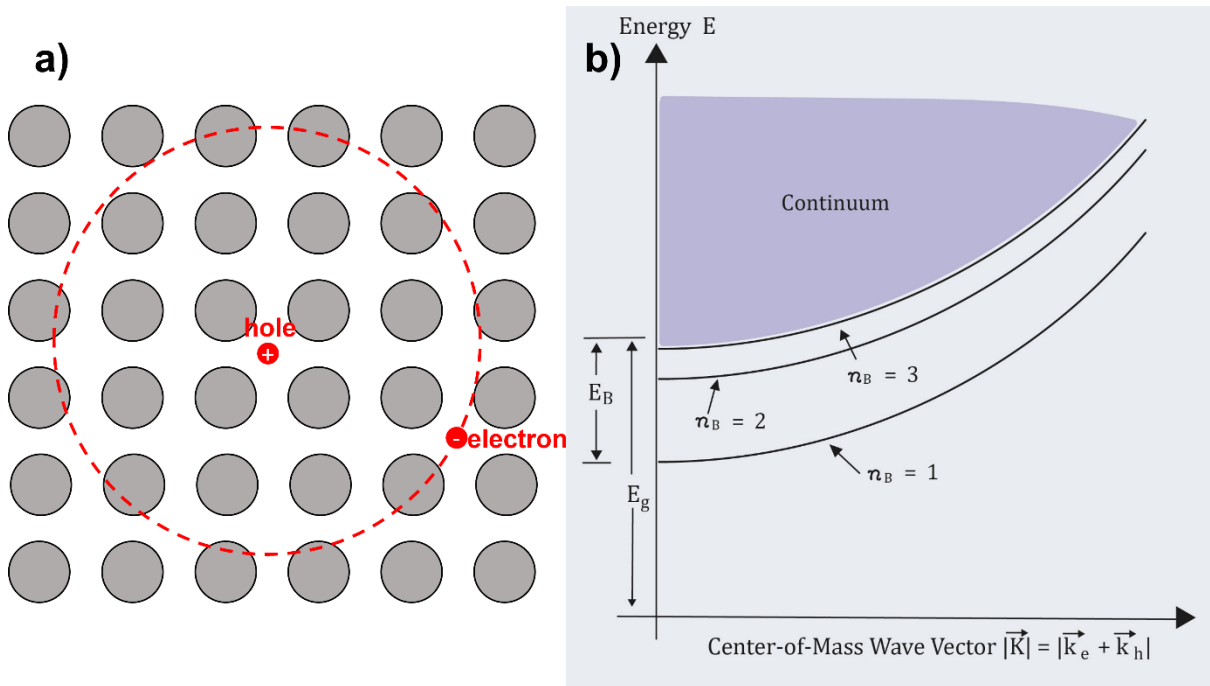

Figure 1: a) Representation of a Wannier exciton b) dispersion relation for excitons.

where r_e and r_h represent the positions of electron and hole respectively. In the parabolic band approximation, the wavefunction of the exciton can be expressed as a linear combination of electron $\psi_{k_e}(\vec{r}_e)$ and hole wavefunctions $\psi_{k_h}(\vec{r}_h)$ as[52]

$$\Psi(\vec{r}_e, \vec{r}_h) = \sum_{\vec{k}_e, \vec{k}_h} C\,(\vec{k}_e, \vec{k}_h)\psi_{k_e}(\vec{r}_e)\psi_{k_h}(\vec{r}_h)$$

Considering the Wannier function representation for electron $\left(a_{\vec{R}_e}(\vec{r}_e)\right)$ and hole $\left(a_{\vec{R}_h}(\vec{r}_h)\right)$ the previous expression can be written as

$$\Psi(\vec{r}_e, \vec{r}_h) = \sum_{\vec{R}_e, \vec{R}_h} \Phi(\vec{R}_e, \vec{R}_h) a_{\vec{R}_e}(\vec{r}_e)\, a_{\vec{R}_h}(\vec{r}_h)$$

with $\Phi(\vec{R}_e, \vec{R}_h)$ representing the exciton envelope wavefunction. This last equation follows a wave equation given by[52]

$$\left[-\left(\frac{\hbar^2}{2m_e}\right)\nabla^2_{\vec{R}_e} - \left(\frac{\hbar^2}{2m_h}\right)\nabla^2_{\vec{R}_h} - \frac{e^2}{4\pi\epsilon_0\epsilon}\right]\Phi(\vec{R}_e, \vec{R}_h) = E\,\Phi(\vec{R}_e, \vec{R}_h)$$

where m_e and m_h represent the effective masses of electron and hole respectively. Defining now a coordinate for the center of mass of the system $\vec{R}$ and a relative coordinate $\vec{r}$ as

$$\vec{R} = \frac{m_e\vec{R}_e + m_h\vec{R}_h}{m_e + m_h} \qquad and \qquad \vec{r} = \vec{R}_e - \vec{R}_h$$

Considering that the Coulomb interaction do not depend on $\vec{R}$ two equations, one for the center of mass and other for the relative motion are obtained given by equations (1) and (2).

$$\left(-\frac{\hbar^2}{2M}\right)\nabla^2_{\vec{R}}\psi(\vec{R}) = E_R\psi(\vec{R}) \tag{1}$$

$$\left(-\frac{\hbar^2}{2\mu}\nabla^2_{\vec{r}} - \frac{e^2}{4\pi\epsilon_0\epsilon r}\right)\phi(\vec{r}) = E_r\phi(\vec{r}) \tag{2}$$

with $\mu = \frac{m_e\,m_h}{m_e + m_h}$ representing the reduced mass of the exciton.

The total energy of the exciton E is obtained adding E_R and E_r. The solution to equation (1) describes a free particle, whose center of mass has a kinetic energy $E_R = \frac{\hbar K^2}{2M}$, as represented by

$$\psi_{\vec{K}}(\vec{R}) = N^{1/2}\exp i\,\vec{K}\cdot\vec{R} \tag{3}$$

On the other hand, the solution to (2) can be expressed as a function of three quantum numbers n, l and m representing the principal quantum number, the angular momentum and the magnetic quantum number respectively.

$$\phi_{nlm}(\vec{r}) = R_{nl}(r)Y_{lm}(\theta, \phi)$$

Where $R_{nl}(r)$ is expressed in terms of the Laguerre polynomials and $Y_{lm}(\theta, \phi)$ are spherical harmonics[52]. In the case of isotropic masses E_r can be expressed as a function of n only by the expression

$$E_r(n) = E_g - \frac{E_B}{n^2} \quad n = 1,2,3,\dots$$

with $E_B = 13.6 \, eV \, \frac{\mu}{m_0 \epsilon^2}$ (where m_0 is the electron rest mass) is the energy needed to ionize the exciton which is usually called the Exciton Binding Energy.

The total envelope function for the exciton can now be obtained combining the previously mentioned solutions giving as a result equation (4)

$$\Phi_{nlm}(\vec{R}, \vec{r}) = N^{-\frac{1}{2}} \exp(i\vec{K} \cdot \vec{R}) \, R_{nl}(r) \, Y_{lm}(\theta, \phi) \tag{4}$$

And the energy spectrum for the system is, as represented in Figure 1-b:

$$E_{nlm} = E_g - \frac{E_B}{n^2} + \frac{\hbar^2 \vec{K}^2}{2M} \quad n = 1,2,3,\dots \tag{5}$$

From these results the size of the exciton in its ground level (S_1) can be expressed relative to the Bohr radius of the hydrogen atom a_B^H and the electron mass m_0 as

$$a_B^{ex} = \frac{a_B^H \epsilon m_0}{\mu}$$

The radii of the excited states with $n_B > 1$ can be considered with different levels of complexity[50]. As previously mentioned in semiconductors a_B^{ex} is usually much larger than the lattice constant, what justifies the use of the effective mass approximation.

Broadening effects in excitonic lines

Ideally excitonic resonances are represented by a $\delta - function$ due to momentum conservation. However, real systems present a finite width in excitonic states that can be divided in homogeneous and inhomogeneous broadenings[53]. Homogeneous broadenings are mainly originated in phonon (optical and acoustic) scattering and any other mechanisms affecting the excitonic lifetime as tunneling and recombination. On the other hand, the main inhomogeneous broadening sources are interface roughness, alloy potential fluctuations, background impurity broadening and well to well fluctuations in multi-quantum well systems[53].

Excitons in Metal Halide Perovskites:

Understanding of the excitonic properties present in perovskites is of fundamental importance for the implementation of devices. In particular, a correct determination of E_B is crucial since for light-emitting devices a high value of E_B is desirable given that the working principle of LEDs is based

on the radiative recombination of excitons. So, excitons should be the dominant photoexcited specie what can be achieved increasing E_B, what also reduces the probability of thermal dissociation. To achieve this, nanostructured emitting layers can be important, since it has been proven that they can increase E_B and the quantum efficiency of LEDs[48]. On the other hand, perovskites with low exciton binding energies are desirable for photovoltaic applications because dissociation of excitons is less energetically costly. A value of E_B smaller than the thermal energy at room temperature (26 meV) is desirable, since this can ensure a high value of free carriers in solar cells. Given that a correct determination of E_B is so important several methods as magnetoabsorption, temperature dependence of photoluminescence intensity, optical absorption (Elliot analysis) as well as theoretical calculations are usually employed to determine this parameter[48]. It must be noted that the measured value for E_B is usually highly dependent of the experimental method used. Besides, it has also been proven experimentally that E_B is highly dependent on morphology[54] and quality of samples[55]. This feature of perovskites makes them suitable for different applications since this can be used as a design parameter. In the case of perovskites the precise mechanisms determining the measured values of E_B are under debate[56]. However, it is evident that they are determined by the specific lattice properties.

2.4.   Phonons

Similarly, to what happens with the electromagnetic waves inside a cavity, the energy in the mechanical waves produced in the crystal lattice is quantized. This is experimentally proved by the thermal and conduction properties of the crystalline solids which can only be understood correctly considering phonons: the quantum of energy in the elastic waves[44].

Although phonons do not really have momentum, for all practical reasons it can be considered that their momentum is $\hbar\vec{q}$, where $\vec{q}$ is the wavevector of the wave/phonon. This quantity is usually called crystal momentum, and it is of particular importance when selection and conservation rules are considered. In solids with more than two atoms in the unit cell two different kinds of phonons can be present. The movement of the atoms can be parallel to the direction of the wavevector, as in soundwaves, or perpendicular, as in the waves of a string, and we name them longitudinal acoustical (LA) or transversal acoustic (TA) phonons respectively. On the other hand, when the movement of neighboring atoms in the lattice is out-of-phase, as when the lattice is excited by infrared radiation, we speak about optical phonons. Optical phonons can also be longitudinal (LO) or transversal (OT). The study of phonons in a solid is of particular importance in the context of excitons, since the formation of these quasi-particle from free electrons and holes is only possible with the presence of phonons that are fundamental for the energy and momentum conservation[57].

The presence of phonons in semiconductors leads to several effects among which we highlight:

  i.   Carrier-phonon interactions fundamentally influences carrier dynamics hence limiting charge carrier mobility produced by scattering events.

ii. A change in the effective masses produced by a change in the band structure of semiconductors. Even though this effect is small it can be relevant in transport processes.
iii. Introduction of phonon sidebands in the absorption/emission spectra.
iv. Homogeneous (Lorentzian) broadening of spectral lines, manifested as finite width in the absorption emission spectra.
v. The presence of phonons is the fundamental cause of relaxation of hot carriers after photon absorption.

The temperature dependence of excitonic linewidths with temperature was theoretically analyzed using perturbative methods by Segall and collaborators[58–61]. The authors analyzed the temperature-dependent influence of LO and acoustic phonons in the linewidths of excitons and obtained a simple model that has been extensively used to quantify exciton-phonon interaction in semiconductors[58,60–63]. Segall's model considers three different contributions for exciton-phonon interactions

i) **Piezoelectric effect: (Exciton-Acoustic phonons)** In non-centrosymmetric crystals local strain can induce a local electrical polarization field thus affecting electrons.
ii) **Deformation potential: (Exciton-Acoustic phonons, is dominant)** phonons produce displacements of atoms form its lattice equilibrium sites which produces modifications in the band structure of the material, thus affecting carriers. For small deformations the change in energy is described by the deformation potentials.
iii) **Fröhlich interaction: (exciton-LO)** the presence of charge carriers in polar semiconductors locally distorts the lattice due to Coulombic interaction. These distortions can be transverse or longitudinal with the direction of propagation of the carrier. These distortions produce TO or LO phonons. The interaction produces an increase in the effective mass of carriers known as Fröhlich coupling.

With these considerations it is possible to show that the temperature dependence of the FWHM (Γ) in the $1S$ excitonic state is given by equation (6)

$$\Gamma(T) = \Gamma_{inh} + \Gamma_{Ac} + \Gamma_{LO} = \Gamma_{inh} + \varphi_{Ac}T + \frac{\varphi_{LO}}{e^{\frac{E_{LO}}{k_B T}} - 1} \tag{6}$$

Here, Γ_{inh} quantifies the inhomogeneous broadening present in the sample having its origin in scattering due to crystal disorder and impurities. The second and third terms represent interactions of excitons with acoustic and optical (LO) phonons respectively. The probability of interaction of excitons with phonons is proportional to phonon population that is determined by a Bose-Einstein distribution characterized by an energy E_{LO}. In the case of acoustic phonons E_{LO} is very low producing a lineal dependence with temperature. Finally, φ_{Ac} and φ_{LO} are constants. The formal derivation of this expression is laborious and is beyond the scope of this work[58].

It must be highlighted that the previously described excitonic states are obtained considering the Born-Oppenheimer approximation, i.e., assuming that the atoms are frozen, thus vibrations of the lattice are not considered. Similarly, when the phononic states are considered the electronic degrees of freedom are ignored. The consideration of excitons and phonons as independent entities is then an approximation since they interact. A more complete analysis of the problem requires the analysis of a new quasi-particle called polaron, formed by the coupling of exciton and phonon. It has been

stated that polaronic-protected charge carriers may be the cause of the large diffusion lengths despite the moderate mobilities in MAPI perovskites. An exact calculation of the polaron spectrum is hard to obtain since finite-order perturbation theory cannot be used in this case[64]. So, polaronic effects are beyond the scope of the present work.

2.5.   Elliot Formula: Excitonic Effects in the Absorption Spectra

As previously stated, the optical properties of materials are determined by the dielectric function $\epsilon(\omega)$. A particular expression of $\epsilon(\omega)$ is obtained when a particular kind of excitations are considered. In the simplest case, when only transitions from the valence band to the conduction band are considered and the one-electron approximation is assumed, Fermi's Golden Rule gives the expression for the imaginary part of the dielectric function[22,43]:

$$\epsilon_i(\omega) \propto \frac{1}{\omega^2} \int_{BZ} |P_{cv}(\vec{k})|^2 \delta(E_c(\vec{k}) - E_v(\vec{k}) - \hbar\omega)\, d^3\vec{k}$$

In this expression $\hbar\omega$ is the energy of the incident radiation, $E_c(k)$ and $E_v(k)$ are the energies of conduction and valence band respectively, and $|P_{cv}|$ is the momentum transition matrix element for transitions from valence to conduction band in the dipole approximation. The integral is performed in the first Brillouin zone. Considering that the transition matrix element can be considered approximately constant close to the band edge this result can be simplified using the oscillator strength $f_{cv} \propto |P_{cv}|/\omega$ a simplified version is obtained integrating in $\vec{k}$

$$\epsilon_i(\omega) \propto \frac{1}{\omega} f_{cv} \cdot D_j(\hbar\omega)$$

Where $D_j(E_{cv})$ is the joint density of states (JDOS). This function describes the density of optical transitions for a given energy difference $E_{cv} = E_{cv}(k) = E_c(k) - E_v(k)$ and takes the form:

$$D_j(E_{cv}) = \frac{1}{4\pi^3} \int_{S_k} \frac{dS_k}{|\nabla_k(E_{cv})|}$$

So, when only transitions from the valence band to the conduction band are considered around the band edge the dielectric function $\epsilon_i(\omega)$ is mainly determined by the shape of the JDOS. The singularities in $D_j(Ecv)$, obtained when $|\nabla_k(E_{cv})| = 0$, are called critical points or Van-Hove singularities. The energy of these critical points can be experimentally determined by modulation spectroscopy.

For a direct semiconductor the critical point is an M_0 kind i.e., $D_j = 0$ for $E < E_g$ and $D_j = (E - E_g)^{1/2}$ for $E > E_g$. Therefore, close to the band edge the imaginary part of ϵ_i is given by the function:

$$\epsilon_i(\omega) = \begin{cases} \dfrac{constant}{\omega^2} \sqrt{\hbar\omega - E_g} & for\ \hbar\omega \geq E_g \\ 0 & for\ \hbar\omega \leq E_g \end{cases}$$

From this expression the absorption coefficient of the semiconductor can be calculated as[43]

$$\alpha(\omega) = \frac{\omega}{c_0 \cdot n(\omega)} \cdot \epsilon_i(\omega)$$

So

$$\alpha(\hbar\omega) = \frac{constant}{nc_0} f_{cv} D_j(\hbar\omega) = \begin{cases} \frac{constant}{\hbar\omega n} \sqrt{\hbar\omega - E_g} & for \quad \hbar\omega \geq E_g \\ 0 & for \quad \hbar\omega \leq E_g \end{cases} \qquad (7)$$

From this last expression we can see that $\alpha(\hbar\omega)$ is also mainly determined by the square-root of the JDOS. This expression is suitable for the determination of the bandgap energy of direct semiconductors with no excitonic effects.

Absorption of Excitonic Semiconductors and Elliot Formula

In materials with a strong excitonic behavior, in addition to band-to-band transitions previously mentioned, the probability of conversion of photons into excitons must be considered. The fingerprint of the presence of excitons in a material is a (usually strong) absorption peak for energies just below the bandgap[50,51]. As in the previous section using the Fermi's golden rule, it is possible to calculate the probability of formation of an exciton from its wavefunction (deduced in section 2.3.) giving the expression:

$$W_{Of} \propto \sum_f \left| P_{Of} \right|^2 \delta(E_f(\vec{K}) - E_0 - \hbar\omega)$$

In this expression $\left| P_{0f} \right|^2$ is the matrix element describing the transition from ground state (0) with an associated energy E_0 to the final excited state where an exciton with energy E_f and wave vector $\vec{K}$ is formed. Moreover, since the momentum of photons is negligible, we can consider $\vec{K} \cong 0$. In his original work [65] Elliot calculated an expression for the transition matrix, and also proved that the oscillator strength f_{n_B} of the $n_B - th$ excitonic transition is proportional to $\Phi_{nlm}(r = 0)$ i.e., the envelope function

$$f_{n_B} \propto \left| P_{0f} \right|^2 \propto \left| \phi_{n_B, l, m}^{env}(r = 0) \right|^2$$

The condition $r = 0$ is identical to $r_e = r_h$ and hence f_{n_B} can be interpreted as the probability of finding a conduction-band electron and a valence-band hole in the same unit cell. This is equivalent to consider the overlap of the electron and hole wavefunctions[22].

Now the dielectric function of the system and its associated absorption coefficient $\alpha(\hbar\omega)$ consists of two contributions: discrete lines produced by excitons (bound electron-hole pairs) and continuum above-bandgap excitonic states.

As previously discussed, excitonic states are determined by a series of states below the bandgap with energies determined by equation (5). In absorption spectra a strong peak is expected for excitonic

energies. Besides that, given the analogy between excitons and the hydrogen atom, we can expect that the oscillator strength f_{n_B} are nonzero only for states with quantum number $l = 0$. So, the absorption of a photon can only produce excitons with s-like wavefunction. Moreover, it can be proven that $f_{n_B} \propto 1/n^3$ [52]. So, the excitonic part of the absorption in a semiconductor consists of the sum of discrete peaks (ideally δ functions) that decrease in amplitude with the third power of n_B^3. This is

$$\epsilon_i(\omega) \propto \frac{1}{\omega^2} \sum_{n_B=1}^{\infty} \frac{1}{n_B^3} \, \delta\left(\hbar\omega - E_g + \frac{E_B}{n_B^2}\right)$$

For energies above the bandgap of the semiconductor excitons are ionized, so electrons and holes are not bound. However, Coulomb attraction is not zero, producing a residual effect that leads to a correlation of their position in space. This leads to an overlap of the wavefunctions, and an envelope function given by the expression

$$\left|\Phi_{n,l,b}\right|^2 = \frac{\tau e^\tau}{NV \sinh(\tau)}$$

Where N represents the number of unit cells, V the volume of one unit cell and $\tau = \pi \sqrt{\frac{E_B}{\hbar\omega - E_g}}$. Besides, the density of states for excitons, considering the dispersion relation given by expression (5), is

$$D(\hbar\omega) \propto \sqrt{\hbar\omega - E_g}$$

From these results the imaginary part of the dielectric functions can be calculated to be

$$\epsilon_i(\omega) \propto \frac{\sqrt{\hbar\omega - E_g}}{\omega^2} \cdot \frac{\tau e^\tau}{\sinh(\tau)}$$
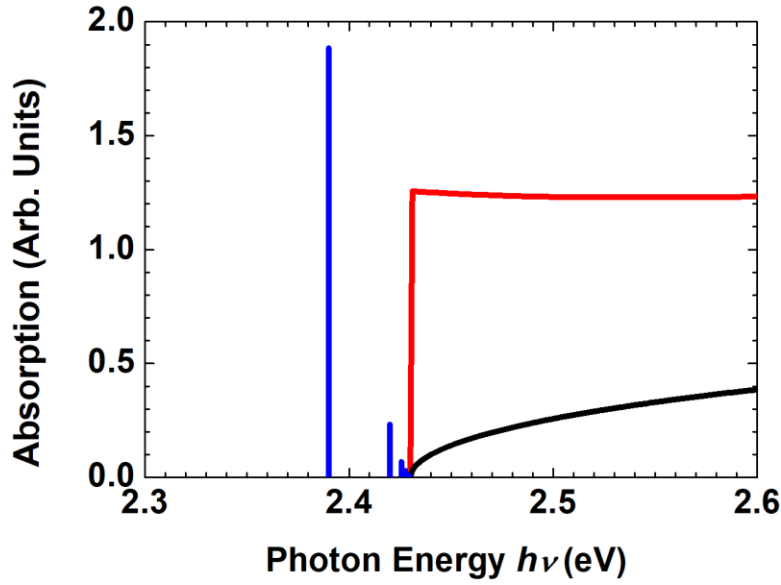
Figure 2: Absorption predicted by Elliot formula consisting of discrete excitonic absorptions (blue) and continuous band to band transitions (red). Solid black curve represents the predicted absorption when electron-hole Coulombic interaction is not considered.

The complete expression for the absorption of an excitonic semiconductor, known as Elliot formula, is obtained considering both continuous (band to band) and discrete (excitonic) states as represented in Figure 2. This formula has the expression:

$$\alpha(\hbar\omega) \propto \frac{\mu_{cv}^2}{\hbar\omega}\left[\sum_j \frac{2\pi(E_B^3)^{1/2}}{j^3}\delta\left(\hbar\omega - E_g + \frac{E_B}{n_B^2}\right) + \theta(\hbar\omega - E_g)\frac{\pi\sqrt{E_B}\exp\tau}{\sinh\tau}\right] \tag{8}$$

where θ represents a Heaviside function. It should be noted that Coulomb interaction between electrons and holes also affects the continuum band-to-band absorption. This can be quantified with the Sommerfeld enhancement factor S obtained from the ratio between the absorption when no coupling between electron and hole are considered (equation (7)) and the band-to-band contribution in equation (8)

$$S = \frac{\alpha_{band-to-band}}{\alpha_{no\_excitons}} = \frac{2\pi\sqrt{\frac{E_B}{\hbar\omega - E_g}}}{1 - \exp\left(-2\pi\sqrt{\frac{E_B}{\hbar\omega - E_g}}\right)}$$

The formation of excitons in perovskites has significant advantages, particularly enhancing the absorption coefficient of these materials. The presence of excitons contributes to an increased correlation in the positions of electrons and holes, which in turn leads to a greater overlap of wavefunctions due to the Coulomb interaction between these charge carriers[22]. Consequently, this electron-hole interaction is a primary driver behind the remarkably high absorption coefficients observed in perovskites. This attribute is especially advantageous when employing perovskites as absorbing layers in photovoltaic devices, as it allows the utilization of exceedingly thin layers,

thereby maximizing charge-carrier extraction and improving overall device efficiency. Therefore, contrary to initial assumptions, the formation of excitons can indeed be beneficial, provided that the exciton binding energy is not excessively high, allowing for effective charge carrier separation.

The expression given for the Elliot function is not suitable to fit experimental data since in practice both excitonic lines and bandgap have a finite width. So, to implement a suitable expression to fit the data only one excitonic peak is considered and its absorption is modeled using a Gaussian function and the Heaviside function is implemented with a Sigmoidal curve. This allows to obtain excellent fittings, and experimental values for bandgap energy and excitonic energy and peak width. Besides, the deconvolution of excitonic and band-to-band transitions, as shown in Figure 3.
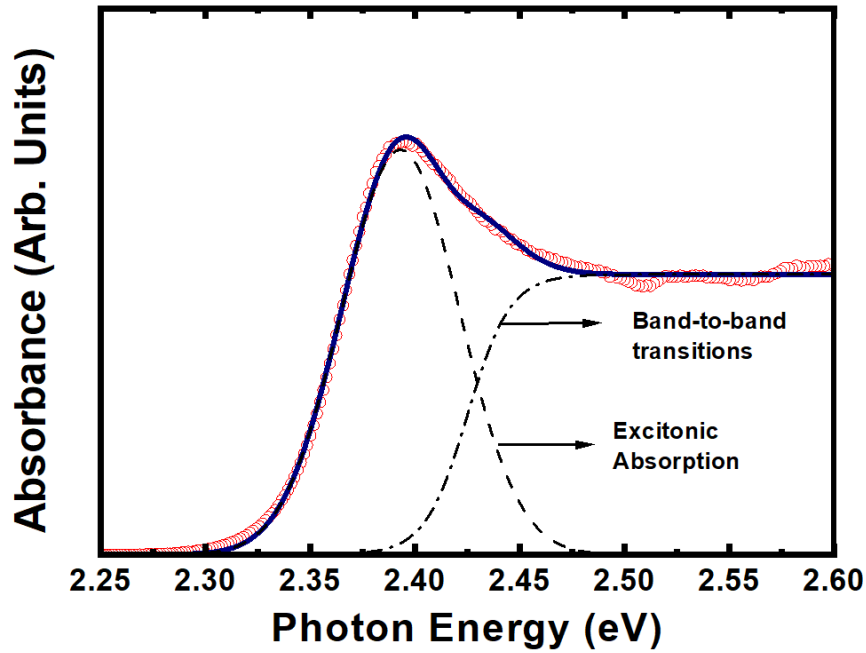

Figure 3: Absorbance spectra of a CsPbBr₃ thin film. Using the Elliot formula to fit the experimental data it is possible to deconvolute the absorbance into excitonic and band-to-band absorption.

2.6.   Temperature dependence of bandgap energy in Lead-Halide Perovskites

In all cases the optical bandgap of lead halide perovskites increases with temperature. This is an atypical behavior when compared with classic tetragonal semiconductors such as GaAs or Si. The atomic origin of this unusual behavior is still unclear[66] and there are still many unanswered questions. The understanding of this behavior is nowadays of great interest to complete the picture in the intriguing optoelectronic properties of this family of materials. Besides, the knowledge of these fundamental properties can be one of the lacking ingredients for a large-scale deployment of perovskite-based devices on the market.

It is usually accepted that in the quasi-harmonic approximation, and when no crystalline phase transitions are present, the dependence of E_g with T is produced by two competing phenomena lattice thermal expansion and electron-phonon interaction[67–70] as expressed by equation (9).

$$\frac{dE_g}{dT} = \left[\frac{\partial E_g}{\partial T}\right]_{Expansion} + \left[\frac{\partial E_g}{\partial T}\right]_{e-ph} \tag{9}$$

In traditional tetragonal semiconductors the contribution of the first term is usually negligible. Lattice thermal expansion/contraction can be related to the distortion in the electronic band structure when a hydrostatic pressure is applied as shown by equation (10)[67,68,71] where $\alpha_V = \frac{1}{V}\frac{dV}{dT}\big|_P$ represents the volumetric expansion coefficient, $B_0 = -V\frac{dP}{dV}\big|_T$ the bulk modulus and $\frac{dE_g}{dP}$ the pressure coefficient of the bandgap. This last term can be either positive or negative and can be considered temperature independent[71].

$$\left[\frac{\partial E_g}{\partial T}\right]_{Expansion} = \frac{dV}{dT}\bigg|_P \frac{dP}{dV}\bigg|_T \frac{dE_g}{dP} = -\alpha_V B_0 \frac{dE_g}{dP} \tag{10}$$

To estimate the contribution of lattice expansion experiments (low temperature to minimize electron-phonon coupling) and calculations have been performed with different results. On the one hand Francisco-López[71] and collaborators concluded from experimental results that thermal expansion and electron-phonon coupling have similar contributions to $\frac{dE_g}{dT}$. On the other hand, DFT calculations performed for MAPbI₃ single crystals, show that the dominant contribution to bandgap change is lattice expansion and this term can be an order of magnitude greater than the electron-phonon interaction of corner sharing $[PbX_6]^{4-}$ octahedra[66]. This last result is the usually accepted by the community. However, these results are highly debated since there are a lot of unanswered questions. This is especially notable in nanostructured perovskites where the effect of defects distributions, surface electronic states phonon modes and quantum and dielectric confinements are in its infancy.

For a correct determination of the electron-phonon interaction detailed, and hence complicated, calculations are necessary. Several theoretical frameworks have been considered[66]: First, Fan considered the self-energy of an electron to calculate the temperature dependence of the band structure[72]. Later Antončík introduced a Deby-Waller term correction in the lattice potential. Nowadays it is widely recognized that self-energy and Debye-Waller corrections are both relevant and are in fact related[73]. This was condensed in a general second-order adiabatic theory (1976) proposed by Allen and collaborators[74].

This approach rigorously introduced the correct self-energy (third term) and Debye-Waller (second term) corrections thar correspond with the Feynman diagrams represented in Figure 4.
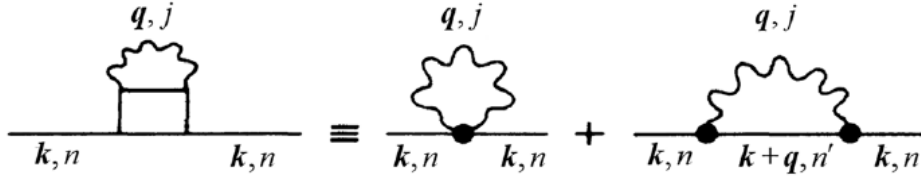
Figure 4: Feynman diagrams used in the calculation of the Debye-Waller self-energy terms.

To use equation (9) it is fundamental to know (i) the electronics states and (ii) the phonon spectrum of the lattice.

i) Electronic states corresponding with eigenvectors Ψ_{nk} (corresponding with the $n-th$ band and wave vector k) can be obtained, within the empirical pseudopotential approximation, from the secular equation

$$\sum_{G'}\left[\left[\frac{\hbar^2}{2m}(k+G)^2 - \varepsilon_{nk}\right]\delta_{GG'} + \sum_{\kappa}V_{\kappa}(G-G')S_{\kappa}(G-G')\right]C_{n\kappa}(G') = 0$$

Where G and G' represent reciprocal-lattice vectors, Ω_C represents the volume of the unit cell and V_{κ} and S_{κ} the pseudopotential form factor and the structure factor of $\kappa - nth$ atom in the unit cell. Solving these equations, it is found that the eigenvectors take the form

$$\Psi_{nk} = \frac{1}{\Omega_C^{1/2}}\sum_{G}C_{nk}(G)\exp i(k+G)\cdot r$$

Besides, Fourier coefficients C_{nk} in this last expression must meet the normalization condition

$$\sum_{G}|C_{nk}(G)|^2 = 1$$

ii) Cardona et al[69] gave an expression for the phonon spectrum of semiconductors calculated using the rigid ion model. In these model phonon modes of branch j with wave vector q and frequency ω_{jk} contribute to the renormalization of band energies. So, the total contribution is given by the expression

$$\Delta E_{nk}(T) = \sum_{jq}\frac{\partial E_{nk}}{\partial n_{jq}}\left(n_{jq}(T)+\frac{1}{2}\right) = \sum_{jq\kappa}\frac{A(n,k,j,q,\kappa)}{\omega_{jq}M_{\kappa}}\left(n_{jq}(T)+\frac{1}{2}\right)$$

Where n_{jq} represents the occupation factor of phonons i.e., $n_{jq} = \left(\exp(\beta\hbar\omega_{jq})-1\right)^{-1}$ and $\beta = 1/k_BT$.

Given the complexity in this model Cardona and collaborators proposed a semi-empirical simplified expression based on a Bose-Einstein two-oscillator model where the $\frac{\partial E_{nk}}{\partial n_{jq}}$ coefficient is

approximated, for phonons with average frequency ω_i, by an effective electron-phonon interaction parameter A_i. In practice, to analyze experimental data only two terms, corresponding to acoustical and optical phonons, are used [60,66], i.e.

$$E_g(T,M) = E_0 + \frac{A_{ac}}{M_{ac}E_{ac}}\left(\frac{1}{\exp\frac{E_{ac}}{k_BT} - 1} + \frac{1}{2}\right) + \frac{A_{op}}{M_{op}E_{op}}\left(\frac{1}{\exp\frac{E_{op}}{k_BT} - 1} + \frac{1}{2}\right) \tag{11}$$

In equation (11) E_0 represents the unrenormalized bandgap energy value, A_{ac} and A_{op} are the relative weight of the acoustic/optical phonons in the coupling, E_{ac} and E_{op} are the effective energies of acoustic and optical phonons respectively, and M_{ac} and M_{op} represent the atomic masses of the oscillators. It has also been experimentally shown that the contributions of acoustic and optical phonons have opposite influence in the bandgap energy[60,70]. More precisely, acoustic phonons produce a blue-shift while optical phonons produce a red-shift when temperature is increased. The use of the two oscillators model is justified by the following three characteristics in perovskites[60,66]:

1. Acoustic phonons oscillations are produced by heavy Pb atoms while optical phonons are produced by the oscillation of light halogen atoms.
2. The bands of $CsPbX_3$ perovskites are formed by the p-band and s-band of Pb, and the p-band of halide ions in the $[PbX_6]^{4-}$ octahedra.
3. Electron-phonon interactions are dominated by phonon modes of corner-sharing $[PbX_6]^{4-}$ octahedra.

2.7.   Photoluminescence

Fundamentals

In general luminescence can be defined as a nonequilibrium radiation over thermal radiation background arising in the presence of intermediate processes of energy transformation between absorption and emission. Emission process has a characteristic time and the possibility of quenching determined by the particular intermediate processes[75]. When a material absorbs photons of a certain energy, usually ultraviolet light, and then emits photons of a lower energy the process is denominated Photoluminescence (PL). This emission of light is caused by the recombination of excited electrons with holes in the material's energy band structure. Photoluminescence is divided into two major categories: intrinsic and extrinsic[75].

Intrinsic photoluminescence can be further divided into three categories:

- Band-to-band is produced by the recombination of an electron in the conduction band with a hole in the valence band.
- Excitonic: Aa previously discussed an exciton is a quasiparticle formed by an electron and a hole bounded by Coulomb interaction. When the bounded electron-hole system recombines, a photon is emitted producing a photoluminescence signal.
- Cross-luminescence is produced by the recombination of an electron in the valence band with a hole in the outermost core band.

Extrinsic luminescence is caused by intentionally incorporating impurities or defects into the lattice of other materials with no intrinsic luminescence. Extrinsic luminescence is also subdivided into two categories:

- Unlocalized: electrons and holes of the host lattice participate in the luminescence process.
- Localized: luminescence excitation and emission process are confined in a localized luminescence center.

In perovskites the origin of the observed photoluminescence is still under debate. To set this discussion is also one of the most important fundamental problems, since this can provide very important knowledge about fundamental processes involved in the working principles of devices. In the present work strong evidence supporting the excitonic nature of photoluminescence in inorganic perovskites will be given. The presented conclusion will be withdrawn from a detailed analysis of the temperature dependence of the photoluminescence spectra of $CsPbBr_3$ thin films and $CsPbI_3$ nanoparticles.

Excitons and Photoluminescence: Arrhenius Plot

In perovskites PL spectra it is usually observed experimentally that the integrated photoluminescence I (area under the curve) decreases with temperature T following a pattern that

can be described by an Arrhenius diagram. This trend can be understood considering the excitonic nature of PL. To explain this, consider a model in which electrons can be free in the conduction band, with energy E_0, or forming an exciton. In this last case the electron has an energy $E_1 (< E_0)$ with the difference between these two energies being the exciton binding energy E_B. The average number of electrons in the levels, N_0 and N_1 respectively, is governed by the Boltzmann law (equation (12) and the total number remains constant, i.e.:

$$N_0(T) + N_1(T) = N_G(T) \quad with \quad N_{0,1}(T) = \alpha_{0,1} \exp\left(-\frac{E_{0,1}}{k_B T}\right) \tag{12}$$

Thus, the dependence of the PL with temperature is determined by the previously mentioned Arrhenius equation (13)

$$I(T) = \frac{I_0}{1 + a \exp(-E_B/K_B T)} \tag{13}$$

with $a := \frac{\alpha_1}{\alpha_0}$. In this scenario the activation energy calculated from the fitting of the Arrhenius diagram corresponds to the exciton binding energy E_B. In some cases, for example in CsPbBr3 results[61,76–78], a second activation energy must be considered to obtain a good fitting. This indicates the presence of a second quenching channel for PL. The nature of this second channel cannot be determined by this method.

2.8.   Stokes Shift:

The Stoke shift is defined as the difference between the maximum of excitonic absorption and the maximum of excitonic (PL) emission (Figure 5). In light emitting devices the presence of a Stokes shift is desirable since this reduces the self-absorption problem produced by the overlapping between the emission and absorption spectra. On the other hand, in solar cells small Stokes shift are desirable to allow re absorption of emitted photons. So, understanding and controlling the Stokes shift is important in optimizing the design and performance of optoelectronic devices. To understand how this parameter can be engineered it is of great importance to understand the fundamental processes producing the Stokes Shift. In general Stokes shift can have different origins as[79]:

1. **Vibrational Relaxation (thermalization)**: After a molecule/atom absorbs a photon, it usually finds itself in an excited vibrational state. The molecule can then undergo a process called vibrational relaxation, where it loses vibrational energy and drops down to the lowest vibrational state of the excited electronic state.

2. **Structural Reorganization**: When a molecule/atom absorbs a photon and is excited to a higher energy state, it may undergo a change in its structure or conformation. This could cause the molecule/atom to emit light of a different energy when it returns to the ground state.

3. **Non-radiative Decay Processes**: Non-radiative decay processes such as internal conversion or intersystem crossing can also lead to a Stokes shift. These processes involve transitions to different electronic states and can result in the loss of energy before the photon is emitted.

Several paths have been proposed to optimize Stokes Shift value among which we highlight: optimization of particle size, reaction temperature, core shell, doping with rare earth metals and addition of organic ligands [80].

According to our results in the case of perovskites thermalization of charge carriers is the dominant process producing stokes shift. This can be very clearly identified from the dependence of the Stokes shift with temperature as explained in the following section.

Exciton Thermalization:

As shown in Figure 5 the PL spectra is redshifted from the excitonic absorption. This behavior is usual in perovskites. Nowadays the origin of this difference, called Stokes Shift, is highly debated. As we will show in the next lines these behavior can be understood from temperature dependence of the Stokes Shift and the FWHM of the PL linewidth[81].
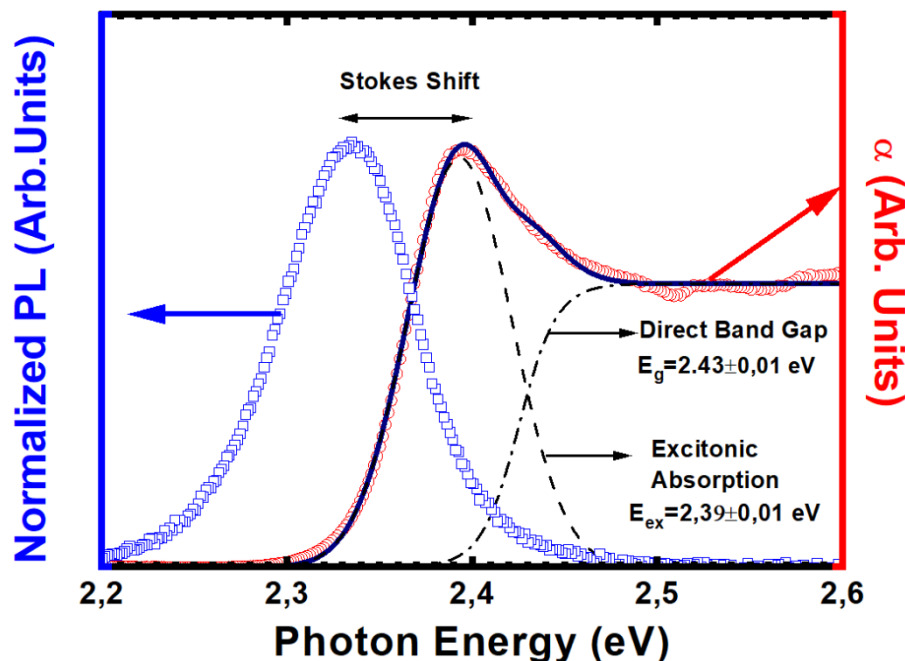

Figure 5: Photoluminescnce (blue squares) and absorbance (red circles) deconvoluted fitting with the Elliot function (black solid) and contributions from excitonic and band to band absorption (black dashed).

Under continuous wave excitation the absorption of photons produces, after energy and momentum relaxation, excitons in a quasi-equilibrium state characterized by a thermal distribution

with an effective temperature T_C. In general, T_C is larger than the temperature of the lattice. Besides that, it is experimentally found that both can be approximated by the temperature of the sample for temperatures above 50 K[81]. If excitonic linewidth exceeds thermal energy the low energy side of the inhomogeneous excitonic bands is enhanced by thermal population producing the Stokes Shift. At thermal equilibrium PL spectrum can be expressed as the product of the excitonic absorptance $\alpha(E)$ and a thermal distribution (Boltzman factor) characterized by a temperature T_C and an energy E_0, i.e.[82]:

$$I_{PL}(E) \approx \alpha(E) \exp\left(-\frac{E - E_0}{K_B T_C}\right)$$

In turn, the absorbance can be expressed as the sum of the fundamental excitonic absorption α_0 and higher excited states $\tilde{\alpha}$. If excitonic absorption is considered as a Gaussian characterized by a center E_0 and a deviation σ the photoluminescence spectra can be expressed as

$$I_{PL}(E) \approx \alpha_0 \exp\left(-\frac{(E - E_0)^2}{2\sigma^2}\right) \exp\left(-\frac{E - E_0}{K_B T_C}\right) + \tilde{\alpha} \exp\left(-\frac{E - E_0}{K_B T_C}\right)$$

$$I_{PL}(E) \approx \alpha_0 \exp\left(-\frac{\left(E - E_0 + \sigma^2/K_B T_C\right)^2}{2\sigma^2} + \frac{\sigma^2}{2(K_B T_C)^2}\right) + \tilde{\alpha} \exp\left(-\frac{E - E_0}{K_B T_C}\right) \tag{14}$$

From this last expression, if the absorption of the exciton is dominate by its fundamental state, we can conclude that the PL spectrum can be essentially described by a Gaussian profile with the same linewidth than the excitonic absorption but redshifted by a factor $\sigma^2/K_B T_C$. This parameter is the Stokes Shift that can be expressed from the FWHM ($\Gamma = 2\sqrt{2\ln(2)}\,\sigma$) as

$$SS \cong 0.180 \frac{\Gamma^2}{K_B T_C} \tag{15}$$

This last expression can be tested using temperature dependence optical characterization. To test this result is one of the main purposes of the present work[18]. As discussed later, the excellent agreement between the model and experimental results shows that Stokes Shift originates in a thermalization process in the broadened exciton band.

2.9.   Excitation-power dependence of Photoluminescence

In lead halide perovskites, both hybrid and inorganic, PL is usually characterized by a single well defined peak a few meV below the bandgap as shown in Figure 5 [61,83]. Near band edge power dependence of photoluminescence in direct semiconductors have several characteristic features among which we highlight:

- The power dependence of PL spectra intensity (I) is described by a $I \sim L^k$, where L is the power of the exciting laser radiation.

- When the radiation used for optical pumping has an energy greater than the bandgap of the semiconductor $1 < k < 2$ for free and bound exciton emission and $k < 1$ for free-to-bound and donor-acceptor pair recombination.

Therefore, the origin of PL can be identified experimentally studying the power dependence of the PL intensity[84]. Previously mentioned features for photoluminescence can be explained from rate equations describing the different transitions producing photoluminescence which are, as represented in Figure 6:

- free exciton recombination (A)
- radiative recombination of donor (B) and acceptor (C) bound excitons
- donor-acceptor pair recombination (D)
- radiative recombination of free electrons and a neutral acceptor (E)
- radiative recombination of a free hole and a neutral donor (F)
- nonradiative transitions of free electrons and holes to ionized donors (G) and acceptors (H)

Photoexcitation processes as the excitation of an electron-hole pair by above-bandgap (I) or resonant formation of excitons (J) are also represented in Figure 6.
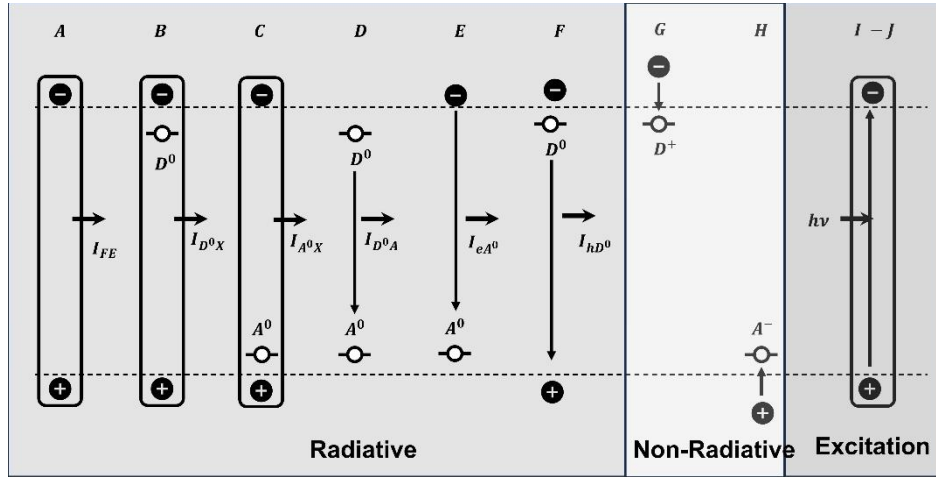

Figure 6: Radiative, non-radiative transitions producing near-band-edge photoluminescence and absorption (excitation) processes.

These processes can be described by a set of six coupled differential equations (eq. 16 to eq 21) under the assumption that the electron concentration in the conduction band n equals the concentration in the valence band p $(n = p)$ and neglecting thermal dissociation of excitons.

$$\frac{dn}{dt} = iL - an^2 - gn(N_D - N_{D^0}) - enN_{A^0} \tag{16}$$

$$\frac{dn_{FE}}{dt} = an^2 + jL - \left[\frac{1}{\tau_{FE}} + \frac{1}{\tau_{FE}^{nr}}\right]n_{FE} - bn_{FE}N_{D^0} - cn_{FE}N_{A^0} \tag{17}$$

$$\frac{dn_{DX}}{dt} = bn_{FE}N_{D^0} - \left[\frac{1}{\tau_{DX}} + \frac{1}{\tau_{DX}^{nr}}\right]n_{DX} \tag{18}$$

$$\frac{dn_{AX}}{dt} = cn_{FE}N_{A^0} - \left[\frac{1}{\tau_{AX}} + \frac{1}{\tau_{AX}^{nr}}\right]n_{AX} \tag{19}$$

$$\frac{dN_{A^0}}{dt} = h(N_A - N_{A^0})n - cn_{FE}N_{A^0} + \left[\frac{1}{\tau_{AX}} + \frac{1}{\tau_{AX}^{nr}}\right]n_{AX} + dN_{D^0}N_{A^0} \tag{20}$$

$$\frac{dN_{D^0}}{dt} = g(N_D - N_{D^0})n - bn_{FE}N_{D^0} + \left[\frac{1}{\tau_{DX}} + \frac{1}{\tau_{DX}^{nr}}\right]n_{DX} - dN_{D^0}N_{A^0} - fN_{D^0}n \tag{21}$$

In these expressions L represents the laser intensity, n_{FE}, n_{DX} and n_{AX} represent the concentrations of free, donor (D) and acceptor (A) bound excitons respectively, N_D and N_A represent the concentrations of donor and acceptors, N_{D^0} and N_{A^0} the concentration of neutral donors and acceptors. On the other hand, τ_{FE} and τ_{FE}^{nr} represent the radiative and nonradiative (nr) lifetimes of donor/acceptor free excitons and τ_{DX}, τ_{DX}^{nr}, τ_{AX}, τ_{AX}^{nr} the radiative and nonradiative lifetimes of donor and acceptor bound excitons. Finally, the coefficients $a, b, ..., l$ represent the transition rates in the processes $A, B, ..., L$ represented in Figure 6. In these expressions is also assumed that bound excitons recombine leaving neutral donors and acceptors.

When *steady state excitation* is considered the luminescence intensities I of free (FE) and donor (D^0X) acceptor (A^0X) bound excitons are determined from eq 17 to 19 to be[84].

$$I_{FE} = \frac{n_{FE}}{\tau_{FE}} = \frac{\beta}{\tau_{FE}}n^2 \tag{22}$$

$$I_{D^0X} = \frac{n_{DX}}{\tau_{DX}} = \frac{bN_{D^0}\beta}{1 + \tau_{DX}/\tau_{DX}^{nr}}n^2 \tag{23}$$

$$I_{A^0X} = \frac{n_{AX}}{\tau_{AX}} = \frac{cN_{A^0}\beta}{1 + \tau_{AX}/\tau_{AX}^{nr}}n^2 \tag{24}$$

where

$$\beta = \frac{a}{\left[\frac{1}{\tau_{FE}} + \frac{1}{\tau_{FE}^{nr}}\right] + bN_{D^0} + cN_{A^0}} \tag{25}$$

Besides, if the intensity of free-to-bound transitions is considered proportional to the respective transition rates the expressions for intensities takes the form

$$I_{hD^0} \sim nN_{D^0} \tag{26}$$

$$I_{eA^0} \sim nN_{A^0} \tag{27}$$

When the concentration of neutral donors and acceptors remains constant under excitation only equations 16 to 19 are relevant, and three different regimes must be considered:

i.   Only a small portion of the free electron-hole pairs form excitons and most photoexcited carriers recombine via defect states of donors and acceptors. This case allows to neglect the term an^2 in equation 16. Therefore, the electron concentration in the conduction band is determined by the expression

$$n = \frac{i}{eN_{A^0} + g(N_D - N_{D^0})} L \tag{28}$$

Using this expression in equations 22 to 24 gives[84]

$$I_{FE} = \frac{\beta}{\tau_{FE}} \frac{i^2}{[eN_{A^0} + g(N_D - N_{D^0})]^2} L^2 \tag{29}$$

$$I_{D^0X} = \frac{bN_{D^0}\beta}{1 + \tau_{DX}/\tau_{DX}^{nr}} \frac{i^2}{[eN_{A^0} + g(N_D - N_{D^0})]^2} L^2 \tag{30}$$

$$I_{A^0X} = \frac{cN_{A^0}\beta}{1 + \tau_{AX}/\tau_{AX}^{nr}} \frac{i^2}{[eN_{A^0} + g(N_D - N_{D^0})]^2} L^2 \tag{31}$$

So, a quadratic power dependence in PL intensity is expected if this process originates in free and bound exciton recombination lines. On the other hand, from eq 26 to 28 we find that PL intensity originated in free-to-bound transitions must have a linear power dependence.

ii. When exciton recombination is the dominant process linear terms in equation 16 can be neglected and we obtain $n \sim L^{1/2}$ for steady state excitation. From eq 22 to 24 we obtain that $I \sim L$ for PL of excitonic nature and from eq 26 and 27 $I \sim L^{1/2}$ for free-to-bound transitions.

iii. When neither excitonic nor donor-acceptor recombination is the dominant process the linear and quadratic terms in 16 are of similar magnitude. This produces a curved $\log(I) - \log(L)$ plots.

When the power of excitation is low case (i) should apply. When the excitation level increases a larger number of excitons should be expected, hence the behavior of the system should approximate to case (ii). For this reason, when PL is originated in excitonic recombination $1 < k < 2$.

In conclusion, as previously mentioned the fundamental recombination processes originating the PL spectra can be identified from the power dependence of photoluminescence intensity I. In particular, in this work it will be proved that the power dependence of PL intensity has $k = 1.3$ for CsPbI₃ nanoparticles. This will be one of the arguments to support the excitonic nature of photoluminescence in this kind of perovskites.

2.10.   Urbach Tail

The Urbach tail refers to the exponential edge seen at energies below the bandgap energy in the absorption spectra semiconductors as observed in Figure 3 and 5. In an ideal, perfectly ordered semiconductor crystal, there would be no states in the bandgap, and the absorption coefficient would sharply rise from zero to a high value. However, in real semiconductors, there are always imperfections like thermal vibrations of the lattice (phonons), impurities, defects, or local variations in the material composition or structure, which lead to the existence of localized states in the bandgap. These states give rise to a smooth increase in the absorption edge below the band edge, as electrons can be thermally excited into these localized states, and then absorb a photon to reach the conduction band.

The mentioned edge has an energy dependence that can be modeled by an empirical expression given by equation (32)[85–88]

$$\alpha(E,T) = \alpha_0 \exp\left[\frac{(E - E_0)}{E_U}\right] \tag{32}$$

where E_U is called Urbach Energy and is a measurement of the width of the absorption edge and is also usually associated with a measurement of lattice disorder[86]. E_0 is the Urbach Focus that generally in traditional semiconductors has a value larger than the bandgap[50]. However, lead halide perovskites, due to its particular dependence on temperature. E_0 is smaller than the bandgap, and is usually considered as the lowest possible value for the bandgap that could be obtained in a sample with perfect crystallinity[85] at 0K.

The work by Cody[89] and Yang shows that the disorder present in the lattice has two components. First, the excitation of phonon modes produces thermal disorder that can be characterized by the mean square displacement of atoms from its equilibrium position in the lattice $\langle U^2 \rangle_T$. Second, the contribution of structural disorder is represented by the mean square deviation of the atomic position from a perfectly ordered crystal $\langle U^2 \rangle_X$. So, the Urbach energy can be expressed as the sum of these two contributions as

$$E_U(T,X) = K\{\langle U^2 \rangle_T + \langle U^2 \rangle_X\} \tag{33}$$

Thermal disorder can be described using the Einstein oscillator model characterized by an Einstein temperature Θ_E and structural disorder can be normalized to the zero-point uncertainty in the atomic positions $\langle U^2 \rangle_0$ hence $X = \langle U^2 \rangle_X / \langle U^2 \rangle_0$ is a measure of the structural disorder[89]. With these considerations an explicit expression for the temperature dependence of the Urbach energy (equation (34)) can be obtained.

$$E_U(T,X) = K\frac{\Theta_E}{\sigma_0}\left[\frac{1 + X}{2} + \frac{1}{\exp\left(\frac{\Theta_E}{T}\right) - 1}\right] \tag{34}$$

From the Cody model, it can also be proved that a linear relation between E_g and E_U, as expressed by 35, can be obtained.

$$E_g(T,X) = E_g(0,0) - \langle U^2 \rangle_0 D \left(\frac{E_U(T,X)}{E_U(0,0)} - 1 \right) \tag{35}$$

In this expression $E_g(0,0)$ and $E_U(0,0)$ correspond to the values of the bandgap energy and Urbach energy at $T = 0 \, K$ in a material with no structural disorder ($X = 0$), and D is a second-order deformation potential.

In practice, fitting experimental data with the previous expressions is challenging. So usually the dependence of $\boldsymbol{E_U}$ with temperature is modeled using equation 36[90]:

$$E_U(T) = E_{U_0} \coth\left(\frac{E_p}{2K_B T} \right) \tag{36}$$

Where E_p is the phonon energy ($h\nu_P$) interacting with the excitons and E_{U_0} is a constant value determined by the static lattice disorder.

2.11.   Charge Carrier Dynamics

When a photon with an energy greater than the bandgap of a semiconductor is absorbed an electron-hole pair is generated. This process is usually called photoexcitation. The behavior of charge carriers immediately after excitation is usually of crucial importance for devices design since they are responsible for establishing the electrical currents. For this reason, a deep understanding of charge carrier dynamics is essential for designing high-performance, energy-efficient, and reliable electronic devices.

In general, there are two kinds of excitations near the band edge in direct bandgap semiconductors: free carriers and excitons. The ratio of free carriers/excitons in a semiconductor is determined (at a fixed temperature) by the exciton binding energy. In organic semiconductors excitons are dominant (E_B hundreds of meV). On the other hand, in inorganic semiconductors free charges are more common. The prevailing view for metal halide perovskites is that, since they are characterized by exciton binding energies lower than 50 meV, their properties are determined by a mix of excitonic and free charge behavior. This is to some extent responsible for their unique properties as[48]

- When excitons are formed after photoexcitation they are short lived. They dissociate in free carriers after a very short time.
- The presence of excitons strongly determines the absorption properties and transient absorption spectra. (See Elliot formula).
- After photoexcitation the excited charge carriers come back to a ground state by means of radiative or nonradiative recombination.

Early-time relaxation dynamics of photogenerated charge carriers

Immediately after absorption the system is out of equilibrium, so the excess energy must be released through some of the allowed processes of the system. Charge carriers have finite life before recombination as evidenced by the fast time decay in photoluminescence spectra[61,91,92].To examine the decay rate of free-charge-carriers density $n(t)$ the presence of three mechanisms must be considered[91,93]:

i) monomolecular recombination: usually attributed to Shockley-Reed-Hall recombination that is considered as a nonradiative process.
ii) bimolecular recombination: resulting from band-to-band recombination.
iii) Auger (or three body) recombination: is a many-body process involving an electron-hole recombination, accompanied by energy and momentum transfer to a third particle (electron or hole). Auger recombination is in general a non-radiative process.

Previously mentioned processes, schematically represented in Figure 7, are characterized by rate constants k_1, k_2 and k_3 respectively. Hence, the decay rate of a free-charge-carrier density $n(t)$ is expressed by the rate equation:

$$\frac{dn}{dt} = -k_1 n - k_2 n^2 - k_3 n^3$$

These three mechanisms contribute to the total recombination rate $r(n,t) = k_1 + k_2 n + k_3 n^2$. Different fluences can make one or other process dominant.

This parameter determines the charge-carrier diffusion rate L_D according to[93]

$$L_D(n) = \sqrt{\frac{\mu k_B T}{r(n)e}}$$

where μ, T, k_B and e represents the charge-carrier mobility, temperature, Boltzmann constant and elementary charge respectively.

When a particular device or material is designed the relative importance of these mechanisms has to be tailored to perform adequately. For example, in solar cells the monomolecular process (trap related) must be minimized, which is mostly achieved by optimizing synthesis conditions. The reduction of k_1 will increase the diffusin length L_D which can increase the efficiency of the device. On the other hand, for light-emitting applications the radiative recombination mechanism must be incentivized.
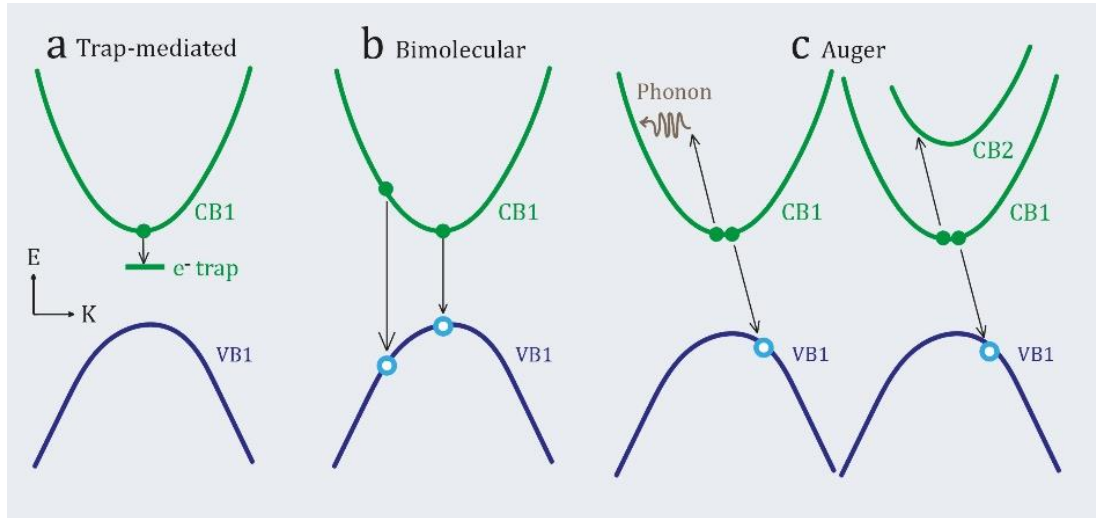

Figure 7: Schematic representation of recombination processes: a) Trap- mediated recombination b) Bimolecular recombination c) Auger recombination.

So, a detailed understanding of the processes dictating the transient behavior of photoluminescence is not only desirable, but a valuable asset to optimize the performance of perovskite-based devices. However, despite significant strides made in this field, a comprehensive model that encapsulates the full scope of photoluminescence behavior reported in the literature remains elusive. This is recognized as one of the most significant open problems in the study of perovskites fundamental properties. Such a model must not only reconcile the diverse and often contradictory behavior of photoluminescence with respect to power and temperature. Besides that, perovskites offer an extensive range of compositional and morphological diversity, thus significantly complicating the

pursuit of a comprehensive model. Despite substantial research efforts, the literature still lacks a systematic study exploring the dependencies of transient photoluminescence properties on these parameters. Such a study would not only enhance our understanding of perovskites optoelectronic properties but would also act as a foundational stone towards the development of the much sought-after comprehensive model.

Additionally, accurate determination of charge-carrier lifetime stands as a crucial factor for the design and realization of efficient electronic components. As we continue our exploration of perovskites and their exciting potential, it is essential to press forward in these fundamental areas of study, increasing the available experimental results in order to bridge the gaps in our knowledge, and striving for a comprehensive understanding of this unique class of materials.

References:

[1]   X. Di, Z. Hu, J. Jiang, M. He, L. Zhou, W. Xiang, X. Liang, *Chem. Commun.* **2017**, *53*, 11068.

[2]   X. Zhang, W. Wang, B. Xu, S. Liu, H. Dai, D. Bian, S. Chen, K. Wang, X. W. Sun, *Nano Energy* **2017**, *37*, 40.

[3]   Z. Xiao, R. A. Kerner, L. Zhao, N. L. Tran, K. M. Lee, T.-W. Koh, G. D. Scholes, B. P. Rand, *Nat. Photonics* **2017**, *11*, 108.

[4]   C.-Y. Huang, C. Zou, C. Mao, K. L. Corp, Y.-C. Yao, Y.-J. Lee, C. W. Schlenker, A. K. Y. Jen, L. Y. Lin, *ACS Photonics* **2017**, *4*, 2281.

[5]   Y. Xu, Q. Chen, C. Zhang, R. Wang, H. Wu, X. Zhang, G. Xing, W. W. Yu, X. Wang, Y. Zhang, M. Xiao, *J. Am. Chem. Soc.* **2016**, *138*, 3761.

[6]   H. Zhu, Y. Fu, F. Meng, X. Wu, Z. Gong, Q. Ding, M. V Gustafsson, M. T. Trinh, S. Jin, X. Y. Zhu, *Nat. Mater.* **2015**, *14*, 636.

[7]   A. S. Polushkin, E. Y. Tiguntseva, A. P. Pushkarev, S. V Makarov, *Nanophotonics* **2020**, *9*, 599.

[8]   X. Hu, X. Zhang, L. Liang, J. Bao, S. Li, W. Yang, Y. Xie, *Adv. Funct. Mater.* **2014**, *24*, 7373.

[9]   V. Adinolfi, O. Ouellette, M. I. Saidaminov, G. Walters, A. L. Abdelhady, O. M. Bakr, E. H. Sargent, *Adv. Mater.* **2016**, *28*, 7264.

[10]   J. Yu, X. Chen, Y. Wang, H. Zhou, M. Xue, Y. Xu, Z. Li, C. Ye, J. Zhang, P. A. Van Aken, *J. Mater. Chem. C* **2016**, *4*, 7302.

[11]   C. C. Stoumpos, C. D. Malliakas, J. A. Peters, Z. Liu, M. Sebastian, J. Im, T. C. Chasapis, A. C. Wibowo, D. Y. Chung, A. J. Freeman, B. W. Wessels, M. G. Kanatzidis, *Cryst. Growth Des.* **2013**, *13*, 2722.

[12]   Y.-F. Xu, M.-Z. Yang, B.-X. Chen, X.-D. Wang, H.-Y. Chen, D.-B. Kuang, C.-Y. Su, *J. Am. Chem. Soc.* **2017**, *139*, 5660.

[13]   J. Hou, S. Cao, Y. Wu, Z. Gao, F. Liang, Y. Sun, Z. Lin, L. Sun, *Chem. Eur. J.* **2017**, *23*, 9481.

[14]   S. Shyamal, S. K. Dutta, N. Pradhan, *J. Phys. Chem. Lett.* **2019**, *10*, 7965.

[15]   L. Protesescu, S. Yakunin, M. I. Bodnarchuk, F. Krieg, R. Caputo, C. H. Hendon, *Nano Lett* **2015**, *15*, 3692.

[16]   S. D. Stranks, G. E. Eperon, G. Grancini, C. Menelaou, M. J. P. Alcocer, T. Leijtens, L. M. Herz, A. Petrozza, H. J. Snaith, *Science (80-.).* **2013**, *342*, 341.

[17]   P. Becker, J. A. Márquez, J. Just, A. Al-Ashouri, C. Hages, H. Hempel, M. Jošt, S. Albrecht, R. Frahm, T. Unold, *Adv. Energy Mater.* **2019**, *9*, 1900555.

[18]   D. L. Gau, I. Galain, I. Aguiar, R. E. Marotti, *J. Lumin.* **2023**, *257*, 119765.

[19]   A. Filippetti, A. Mattoni, *Phys. Rev. B - Condens. Matter Mater. Phys.* **2014**, *89*, 125203.

[20]   W. J. Yin, J. H. Yang, J. Kang, Y. Yan, S. H. Wei, *J. Mater. Chem. A* **2015**, *3*, 8926.

[21]   T. Umebayashi, K. Asai, T. Umebayashi, K. Asai, T. Kondo, T. Kondo, A. Nakao, *Phys. Rev. B* **2003**, *67*, 155405.

[22]   F. Ruf, *Excitonic Effects and Bandgap Instabilities in Perovskite Solar Cells*, KIT Scientific Publishing, **2020**.

[23]   B. Roose, E. M. Tennyson, G. Meheretu, A. Kassaw, S. A. Tilahun, L. Allen, S. D. Stranks, *Energy Environ. Sci.* **2022**, DOI 10.1039/D2EE01343F.

[24]   B. Conings, J. Drijkoningen, N. Gauquelin, A. Babayigit, J. D'Haen, L. D'Olieslaeger, A. Ethirajan, J. Verbeeck, J. Manca, E. Mosconi, F. De Angelis, H. G. Boyen, *Adv. Energy Mater.* **2015**, *5*, 1500477.

[25]   T. Leijtens, E. T. Hoke, G. Grancini, D. J. Slotcavage, G. E. Eperon, J. M. Ball, M. De Bastiani, A. R. Bowring, N. Martino, K. Wojciechowski, M. D. McGehee, H. J. Snaith, A. Petrozza, *Adv. Energy Mater.* **2015**, *5*, 1500962.

[26]   S. Bae, S. Kim, S. W. Lee, K. J. Cho, S. Park, S. Lee, Y. Kang, H. S. Lee, D. Kim, *J. Phys. Chem. Lett.* **2016**, *7*, 3091.

[27]   J. Jiang, Q. Wang, Z. Jin, X. Zhang, J. Lei, H. Bin, Z. G. Zhang, Y. Li, S. F. Liu, *Adv. Energy Mater.* **2018**, *8*, 1701757.

[28]   T. Wu, Y. Wang, Z. Dai, D. Cui, T. Wang, X. Meng, E. Bi, X. Yang, L. Han, *Adv. Mater.* **2019**, *31*, 1900605.

[29]   G. Abdelmageed, L. Jewell, K. Hellier, L. Seymour, B. Luo, F. Bridges, J. Z. Zhang, S. Carter, *Appl. Phys. Lett.* **2016**, *109*, 233905.

[30]   B. Chen, J. Song, X. Dai, Y. Liu, P. N. Rudd, X. Hong, J. Huang, *Adv. Mater.* **2019**, *31*, DOI 10.1002/ADMA.201902413.

[31]   A. F. Akbulatov, L. A. Frolova, M. P. Griffin, I. R. Gearba, A. Dolocan, D. A. Vanden Bout, S. Tsarev, E. A. Katz, A. F. Shestakov, K. J. Stevenson, P. A. Troshin, *Adv. Energy Mater.* **2017**, *7*, 1700476.

[32]   H. Huang, H. Yuan, K. P. F. Janssen, G. Solís-Fernández, Y. Wang, C. Y. X. Tan, D. Jonckheere, E. Debroye, J. Long, J. Hendrix, J. Hofkens, J. A. Steele, M. B. J. Roeffaers, *ACS Energy Lett.* **2018**, *3*, 755.

[33]   M. C. Brennan, S. Draguta, P. V. Kamat, M. Kuno, *ACS Energy Lett.* **2018**, *3*, 204.

[34] M. Kulbak, D. Cahen, G. Hodes, *J. Phys. Chem. Lett.* **2015**, *6*, 2452.

[35] M. Kulbak, S. Gupta, N. Kedem, I. Levine, T. Bendikov, G. Hodes, D. Cahen, *J. Phys. Chem. Lett.* **2016**, *7*, 167.

[36] J. Duan, Y. Zhao, B. He, Q. Tang, *Angew. chemie Int. Ed.* **2018**, *57*, 3787.

[37] J. Liang, C. Wang, Y. Wang, Z. Xu, Z. Lu, Y. Ma, H. Zhu, Y. Hu, C. Xiao, X. Yi, *J. Am. Chem. Soc.* **2016**, *138*, 15829.

[38] X. Chang, W. Li, L. Zhu, H. Liu, H. Geng, S. Xiang, J. Liu, H. Chen, *ACS Appl. Mater. Interfaces* **2016**, *8*, 33649.

[39] R. E. Beal, D. J. Slotcavage, T. Leijtens, A. R. Bowring, R. A. Belisle, W. H. Nguyen, G. F. Burkhard, E. T. Hoke, M. D. McGehee, *J. Phys. Chem. Lett.* **2016**, *7*, 746.

[40] Y. Fu, H. Zhu, J. Chen, M. P. Hautzinger, X. Y. Zhu, S. Jin, *Nat. Rev. Mater.* **2019**, *4*, DOI 10.1038/s41578-019-0080-9.

[41] J. I. Pankove, **1975**, 422.

[42] B. Sapoval, C. Hermann, *Physics of Semiconductors*, Springer Science & Business Media, **2003**.

[43] O. Stenzel, *Phys. Thin Film Opt. Spectra An Introd. Second Ed.* **2015**, 1.

[44] Von N. W. Ashcroft; N. D. Mermin, *Solid State Physics. , New York 1976, XXII, 826 Seiten*, **1976**.

[45] J. G. Labram, D. H. Fabini, E. E. Perry, A. J. Lehner, H. Wang, A. M. Glaudell, G. Wu, H. Evans, D. Buck, R. Cotta, L. Echegoyen, F. Wudl, R. Seshadri, M. L. Chabinyc, *J. Phys. Chem. Lett.* **2015**, *6*, 3565.

[46] J. M. Frost, A. Walsh, *Acc. Chem. Res.* **2016**, *49*, 528.

[47] I. Anusca, S. Balčiūnas, P. Gemeiner, Š. Svirskas, M. Sanlialp, G. Lackner, C. Fettkenhauer, J. Belovickis, V. Samulionis, M. Ivanov, B. Dkhil, J. Banys, V. V Shvartsman, D. C. Lupascu, *Adv. Energy Mater.* **2017**, *7*, 1700600.

[48] Y. Jiang, X. Wang, A. Pan, *Adv. Mater.* **2019**, *31*, 1806671.

[49] A. J. Bosman, E. E. Havinga, *Phys. Rev.* **1963**, *129*, DOI 10.1103/PhysRev.129.1593.

[50] C. F. Klingshirn, **2012**, DOI 10.1007/978-3-642-28362-8.

[51] M. Fox, *Optical Properties of Solids*, AAPT, **2002**.

[52] P. Y. Yu, M. Cardona, *Fundamentals of Semiconductors*, Springer Berlin, Heidelberg, Heidelberg, **2010**.

[53] J. Singh, *Electronic and Optoelectronic Properties of Semiconductor Structures*, Cambridge University Press, Cambridge, **2003**.

[54] M. Yu, S. Yuan, H. Y. Wang, J. S. Zhao, Y. Qin, L. M. Fu, J. P. Zhang, X. C. Ai, *Phys. Chem. Chem. Phys.* **2018**, *20*, 6575.

[55] G. Grancini, A. R. Srimath Kandada, J. M. Frost, A. J. Barker, M. De Bastiani, M. Gandini, S. Marras, G. Lanzani, A. Walsh, A. Petrozza, *Nat. Photonics 2015 910* **2015**, *9*, 695.

[56] L. M. Herz, *J. Phys. Chem. Lett.* **2018**, *9*, 6853.

[57] J. Singh, *Excit. Energy Transf. Process. Condens. Matter* **1994**, DOI 10.1007/978-1-4899-0996-1.

[58] S. Rudin, T. L. Reinecke, B. Segall, *Phys. Rev. B* **1990**, *42*, 11218.

[59] A. D. Wright, C. Verdi, R. L. Milot, G. E. Eperon, M. A. Pérez-Osorio, H. J. Snaith, F. Giustino, M. B. Johnston, L. M. Herz, *Nat. Commun.* **2016**, *7*, 1.

[60] R. Saran, A. Heuer-Jungemann, A. G. Kanaras, R. J. Curry, *Adv. Opt. Mater.* **2017**, *5*, 1700231.

[61] D. L. Gau, D. Ramírez, F. Iikawa, G. Riveros, P. Díaz, J. Verdugo, G. Núñez, S. Lizama, P. Lazo, E. A. Dalchiele, L. Contreras, J. Idigoras, J. Anta, R. E. Marotti, *ChemPhysChem* **2022**, *23*, e202200286.

[62] X. B. Zhang, T. Taliercio, S. Kolliakos, P. Lefebvre, *J. Phys. Condens. Matter* **2001**, *13*, 7053.

[63] R. L. Z. Hoye, J. Hidalgo, R. A. Jagt, J. P. Correa-Baena, T. Fix, J. L. MacManus-Driscoll, *Adv. Energy Mater.* **2022**, *12*, 2100499.

[64] M. I. Vasilevskiy, *Semicond. Nanocrystal Quantum Dots Synth. Assem. Spectrosc. Appl.* **2008**, 217.

[65] R. J. Elliott, *Phys. Rev.* **1957**, *108*, 1384.

[66] J. Xu, S. Yu, X. Shang, X. Chen, *Adv. Photonics Res.* **2022**, 2200193.

[67] P. Lautenschlager, P. B. Allen, M. Cardona, *Phys. Rev. B* **1985**, *31*, 2163.

[68] S. Gopalan, P. Lautenschlager, M. Cardona, *Phys. Rev. B* **1987**, *35*, 5577.

[69] M. Cardona, *Solid State Commun.* **2005**, *133*, 3.

[70] C. Yu, Z. Chen, J. Wang, W. Pfenninger, N. Vockic, J. T. Kenney, K. Shum, *J. Appl. Phys.* **2011**, *110*, 063526.

[71] A. Francisco-López, B. Charles, O. J. Weber, M. I. Alonso, M. Garriga, M. Campoy-Quiles, M. T. Weller, A. R. Goñi, *J. Phys. Chem. Lett.* **2019**, *10*, 2971.

[72] H. Y. Fan, *Phys. Rev.* **1951**, *82*, 900.

[73] E. Antončík, *Czechoslov. J. Phys.* **1955**, *5*, 449.

[74] P B Allen, V Heine, *J. Phys. C Solid State Phys.* **1976**, *9*, 2305.

[75] S. Shionoya, *Lumin. Solids* **1998**, 95.

[76] A. Dey, P. Rathod, D. Kabra, *Adv. Opt. Mater.* **2018**, *6*, 1800109.

[77] F. Gabelloni, F. Biccari, G. Andreotti, D. Balestri, S. Checcucci, A. Milanesi, N. Calisi, S. Caporali, A. Vinattieri, *Opt. Mater. Express* **2017**, *7*, 4367.

[78] B. A. Koscher, J. K. Swabeck, N. D. Bronstein, A. P. Alivisatos, *J. Am. Chem. Soc.* **2017**, *139*, 6566.

[79] A. Kitai, *Luminescent Materials and Applications*, **2008**.

[80] S. Gull, M. H. Jamil, X. Zhang, H. sing Kwok, G. Li, *ChemistryOpen* **2022**, *11*, e202100285.

[81] M. Gurioli, A. Vinattieri, J. Martinez-Pastor, M. Colocci, *Phys. Rev. B* **1994**, *50*, 11817.

[82] J. Humlíček, E. Schmidt, L. Bočánek, R. Svehla, K. Ploog, *Phys. Rev. B* **1993**, *48*, 5241.

[83] D. Ramírez, G. Riveros, P. Díaz, J. Verdugo, G. Núñez, S. Lizama, P. Lazo, E. A. Dalchiele, D. L. Gau, R. E. Marotti, J. A. Anta, L. Contreras-Bernal, A. Riquelme, J. Idigoras, *ChemElectroChem* **2020**, *7*, 3961.

[84] T. Schmidt, K. Lischka, W. Zulehner, *Phys. Rev. B* **1992**, *45*, 8989.

[85] S. Singh, C. Li, F. Panzer, K. L. Narasimhan, A. Graeser, T. P. Gujar, A. Köhler, M. Thelakkat, S. Huettner, D. Kabra, *J. Phys. Chem. Lett.* **2016**, *7*, 3014.

[86] S. Zeiske, O. J. Sandberg, N. Zarrabi, C. M. Wolff, M. Raoufi, F. Peña-Camargo, E. Gutierrez-Partida, P. Meredith, M. Stolterfoht, A. Armin, *J. Phys. Chem. Lett.* **2022**, *13*, 7280.

[87] T. H. Keil, *Phys. Rev.* **1966**, *144*, 582.

[88] M. Ledinsky, T. Schönfeldová, J. Holovský, E. Aydin, Z. Hájková, L. Landová, N. Neyková, A. Fejfar, S. De Wolf, *J. Phys. Chem. Lett.* **2019**, *10*, DOI 10.1021/acs.jpclett.9b00138.

[89] G. D. Cody, T. Tiedje, B. Abeles, B. Brooks, Y. Goldstein, *Phys. Rev. Lett.* **1981**, *47*, 1480.

[90] B. Pejova, B. Abay, I. Bineva, *J. Phys. Chem. C* **2010**, *114*, 15280.

[91] M. J. Trimpl, A. D. Wright, K. Schutt, L. R. V. Buizza, Z. Wang, M. B. Johnston, H. J. Snaith, P. Müller-Buschbaum, L. M. Herz, *Adv. Funct. Mater.* **2020**, *30*, 2004312.

[92] B. Tang, L. J. Ruan, C. Qin, A. Shu, H. He, Y. Ma, *Adv. Opt. Mater.* **2020**, *8*, 2000498.

[93] L. M. Herz, *http://dx.doi.org/10.1146/annurev-physchem-040215-112222* **2016**, *67*, 65.

[94] M. Sardela, *Pract. Mater. Charact.* **2014**, 1.

Results
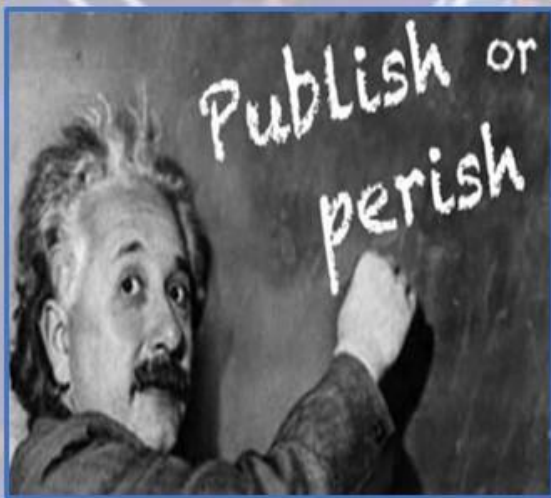
3. Experimental Results

3.1. Work description

This text describes a research project in the field of inorganic perovskites of $CsPbBr_3$ and γ-$CsPbI_3$, two materials that are currently being widely studied due to their excellent optoelectronic properties, with which high-performance optoelectronic devices have been implemented in a short time. In the initial work (Electrochemically Assisted Growth of $CsPbBr_3$-Based Solar Cells Without Selective Contacts), $CsPbBr_3$ films were characterized at room temperature. The characterizations were carried out on a large number of samples prepared under different conditions, since one of the initial objectives of the work was to determine the synthesis conditions that allowed obtaining films with optimal stoichiometry in an original synthesis method proposed by Dr. Daniel Ramirez. It was discovered that in all cases, the samples present a strong influence of excitons. This was especially marked in the optical properties that present an absorption spectrum that can be modeled using the Elliott Equation. It was also observed that the photoluminescence is characterized by a well-defined single peak with a characteristic energy lower than the peak that characterizes excitonic absorption. It was also observed that the difference between the energy associated with absorption and excitonic emission, called the Stokes Shift, depends on the preparation conditions.

Subsequently, to confirm and deepen the study of excitons, measurements of optical properties were carried out by lowering the temperature from room temperature to 30 K using a cryostat. Thanks to these characterizations, the anomalous behavior of perovskites was discovered that produces an increase in the bandgap with temperature, which is also observed in photoluminescence. Variation of excitonic peaks was also observed as well as a decrease in their amplitude with increasing temperature. Analyzing these results, techniques such as the Segall equation were learned for the analysis of the broadening of the photoluminescence peak and the obtaining of activation energies from the Arrhenius diagram. Information on the fundamental processes that determine the optoelectronic properties of perovskites could also be obtained. The results obtained (for the sample with the optimized stoichiometry) were published in a second manuscript entitled 'Photophysical and Photoelectrochemical Properties of $CsPbBr_3$ Films Grown by Electrochemically Assisted Deposition'.

In 2020, due to the health situation, work with $CsPbBr_3$ samples was interrupted due to Dr. Ramirez's inability to continue preparing samples in his laboratory. For this reason, in 2021, work began with inorganic perovsktias samples of γ-$CsPbI_3$, where high-quality nanoparticles were obtained with the help of MSc Isabel Galain (Area of Radiochemistry of the Faculty of Chemistry - UdelaR) who has extensive experience in synthesizing nanostructures using the Hot-Injection method. Thanks to the excellent quality of the samples prepared by MSc Galain and the previous experience we had gained in our work with $CsPbBr_3$, we were able to publish a third paper ('Origin of photoluminescence and experimental determination of exciton binding energy, exciton-phonon interaction, and urbach energy in γ-$CsPbI_3$ nanoparticles'). In this work, in addition to determining important parameters from an applied point of view for this type of systems, we managed to give a

complete vision of the fundamental processes that determine the optoelectronic properties of γ-CsPbI₃ perovskites. The results generally seen in the literature allow us to believe that our description can be extended to other metal halide perovskites, both organic and inorganic.

During the aforementioned work, I was particularly struck by the behavior of the nanoparticles shown in Figure 2b of the manuscript. In this figure, a surprising alignment between the crystal planes of neighboring nanoparticles is observed, and to my surprise, some of these crystal planes continue from one nanoparticle to the next. Since I had never observed this before, I embarked on a search for similar results in the literature but could not find any. However, I came across another effect that is probably related to the aforementioned result, which is light-induced self-assembly. This effect is obtained by illuminating colloidal nanoparticles with a solar simulator, causing them to spontaneously assemble into 1D nanorods or other nanostructures. This effect has been mainly studied in CsPbBr₃ perovskites. Trying to reproduce the results obtained for this material, I attempted to irradiate γ-CsPbI₃ nanoparticles and found that this phenomenon also occurs. In addition, building on what we learned during our previous work, we conducted a detailed study of the optical properties of the samples before and after irradiation. This allowed us to analyze the evolution of the fundamental processes, particularly the quality of the crystal structure, in the nanoparticles and nanorods. This work is now part of a new manuscript entitled "Light-Induced Self-assembly and Effect of Amorphization in Photoluminescence Spectra of γ-CsPbI₃ Nanocrystals," which we recently submitted for publication and in which we report the phenomenon of light-induced self-assembly for the first time in γ-CsPbI₃ nanoparticles.

3.2.   Experimental Setup

Optical characterization was performed by continuous-wave photoluminescence (PL) spectroscopy and transmittance from 10 to 290 K. Samples were cooled in a CTI Cryogenics CRYODYNE cryostat. For PL measurements the excitation source was a Thorlabs M365FP1 LED (365 nm, 9.8 mW), filtered with a 400 nm low-pass filter, and the emitted light was collected with an Ocean Optics Flame S-UV-VIS-ES spectrometer as depicted in Figure 8. The result is a well-defined peak, corresponding to the light emitted from excitonic recombination as previously discussed, from which energy, width and area can be directly obtained.

Changing the excitation source to a halogen lamp (Ocean-Optics HL 2000) and the spectrometer by an Ocean-Optics S2000, transmittance T was measured. Transmittance is obtained[1] as the ratio between light intensity of the transmitted light through the sample $I_T(\lambda)$ and the intensity of the light source $I_S(\lambda)$, i.e

$$T(\lambda) = \frac{I_T(\lambda)}{I(\lambda)}$$

To evaluate the absorption of the sample the absorbance A is defined (for weakly reflective samples) as

$$A = -\ln(T)$$

Absorbance is related to absorption coefficient α by the expression[94] $A = \frac{d}{\ln 10}\,\alpha$, where d represents the width of the sample.
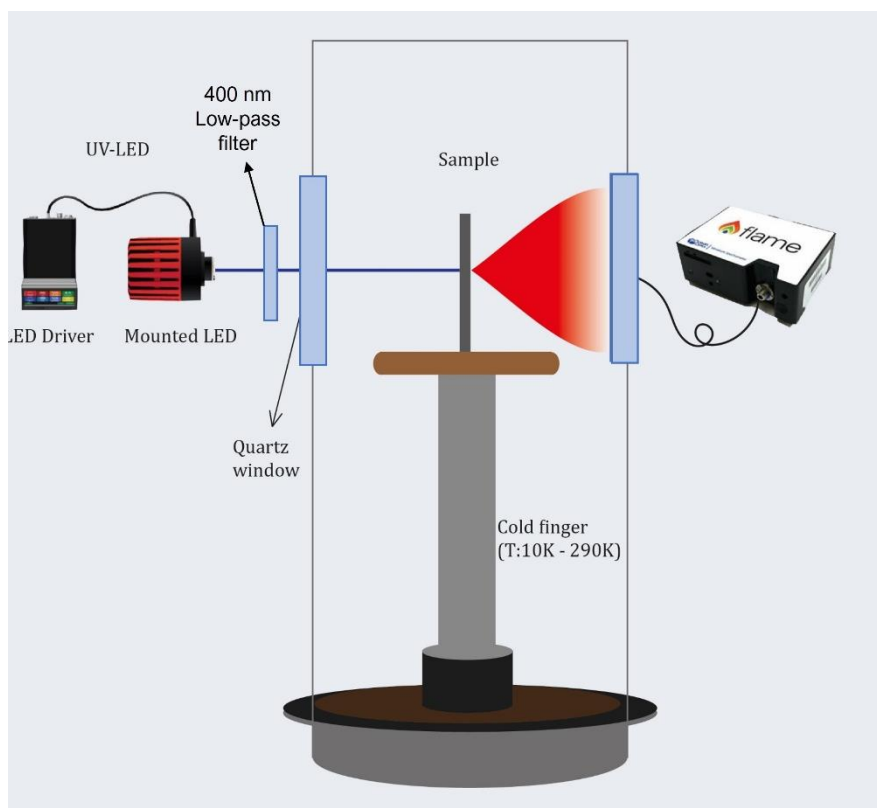

Figure 8: Experimental Setup used to perform temperature dependent measurements of photoluminescence and transmittance.

Using the previously described device measurements with an interval of 10 K were performed. This gives an important amount of data to fit. To perform these fittings in an efficient and systematic way MATLAB routines were implemented to analyze the photoluminescence and the transmittance/absorbance spectra. It is expected that these routines can be used to extend the analysis performed in these works to other perovskite samples. This can be of particular interest to study how important parameters for the implementation of devices as bandgap energy, exciton-phonon interaction, exciton binding energy and Stokes Shift depend on size, morphology, composition, and synthesis method of nanoparticles. Also, it is my intention soon to improve the usability and extend the capabilities of the mentioned routine so that they can be uploaded in a public repository thus making it possible for other colleges to perform a similar analysis. I consider that giving this possibility can be a great tool to standardize the analysis of optical properties of perovskites which can make results obtained from different samples comparable. This is nowadays very hard to do since different researchers perform analysis using different methods and criteria. In my opinion this is delaying the so needed understanding of the fundamental properties of perovskites and so delaying the development of perovskite-based devices.

References

[1]   M. Sardela, *Pract. Mater. Charact.* **2014**, 1.

ChemElectroChem

Articles
doi.org/10.1002/celc.202000782

Chemistry Europe
European Chemical
Societies Publishing

Electrochemically Assisted Growth of CsPbBr₃-Based Solar Cells Without Selective Contacts

Daniel Ramírez,*[a] Gonzalo Riveros,[a] Patricia Díaz,[a] Javier Verdugo,[a] Gerard Núñez,[a] Susy Lizama,[a] Pamela Lazo,[a] Enrique A. Dalchiele,[b] Daniel L. Gau,[b] Ricardo E. Marotti,[b] Juan A. Anta,[c] Lidia Contreras-Bernal,[c] Antonio Riquelme,[c] and Jesús Idigoras[c]

In this work we report a simple and cost-effective CsPbBr₃-based solar cell without ordinary selective contacts. To do so we follow an electrochemical approach consisting of three successive steps: (1) electrodeposition of PbO₂ directly on top of FTO substrates, (2) heterogeneous phase reaction with gaseous HBr and (3) spin-coating of methanolic CsBr solutions followed by annealing. This method is more adequate for large-scale environmentally friendly production as it reduces chemical waste, particularly toxic lead. The resulting films were structurally and optically characterized showing good coverage of the FTO substrates, absence of defects such as pinholes and orthorhombic structure. Photovoltaic and impedance character-ization was carried out by pressing a carbon coated metal spring onto the CsPbBr₃ film until obtaining maximized open-circuit potential (V_{oc}) and short-circuit photocurrent density (j_{sc}) under simulated sunlight. The stabilized current at fixed voltage (SCFV) technique gave a maximum PCE value of 2.70% close to devices with similar configuration. Impedance measurements demonstrated analogous behavior to that of state-of-art CsPbBr₃ based solar cells, comprising a recombination arc at mid-high frequencies, geometrical capacitance and ideality factors closed to 2, typical of SRH recombination in the perovskite bulk.

Introduction

New photovoltaic systems based on perovskite solar cells (PSC), have reached impressive efficiencies compared with commercial technologies such as silicon.[1–2] The most studied material of this group is CH₃NH₃PbI₃, known as MAPI, which has proven high efficiencies in single junction solar cells.[3–4] However, the lack of stability of these cells under ambient conditions is a continuous drawback that has braked the success of this technology at commercial level. Other PSCs based on fully inorganic perovskites such as CsPbBr₃ are more stable but they are less efficient compared with those based on MAPI.[5–19,20–27] This is mainly due to the high band gap of CsPbBr₃, close to 2.31 eV, which is far from the optimal value for single junction solar cells. On the other hand, the good optoelectronic properties of CsPbBr₃ have found other applications such as light-emitting diodes (LEDs), photodetectors, photo-electrochemical sensing and water splitting, photocatalysis for pollutants

degradation, CO₂ reduction and organic synthesis, among others.[28–37] CsPbBr₃ based PSCs remains an interesting material for photovoltaics and other optoelectronic applications due to its high stability under ambient conditions. The absence of organic cations in this perovskite means that no glovebox is strictly required and freshly made CsPbBr₃ films are usually quite robust. At a laboratory scale, the synthesis of photovoltaic perovskites involves toxic precursors such as lead salts that are usually spin-coated on substrates to prepare PSCs. The main drawback of this method is that more than 90% of this lead-containing solutions are wasted out the sample holder, thus discarding this method in terms of industrial efficiency and environmental impact.[38] Several electrolytes containing toxic metals as electroactive specie can be reused during several deposition cycles before its depletion together with an easy disposal of a liquid waste. In fact, endeavors toward the fabrication of PSCs modules using mainly slot die and doctor blade techniques have resulted in acceptable efficiencies.[38] In the particular case of CsPbBr₃, a two-step approach is commonly preferred in the laboratory. In the first step, a hot PbBr₂ solution is spin-coated onto either flat[10,15,19] or mesoporous substrates.[5–6,8–9,11–12,14–15,18,19] The second step involves conversion of PbBr₂ to CsPbBr₃ by dipping the film into methanolic CsBr solutions. The actual way this second step proceeds depends on the substrate. Fluorine doped Tin Oxide (FTO) substrates are the most adequate choice for this because freshly CsPbBr₃ films are better adhered to FTO substrates. In fact, the spin coating conversion is currently preferred independently of the nature of the substrate.[11] In all cases, the as-formed CsPbBr₃ film must be submitted to a mild annealing process at a temperature ranging from 250 to 400 °C to stabilize the orthorhombic phase of CsPbBr₃.[19] Only in a few cases, a

[a] Dr. D. Ramírez, Dr. G. Riveros, P. Díaz, J. Verdugo, G. Núñez, S. Lizama, P. Lazo
Instituto de Química y Bioquímica, Facultad de Ciencias
Universidad de Valparaíso
Avenida Gran Bretaña 1111, Playa Ancha, Valparaíso, Chile
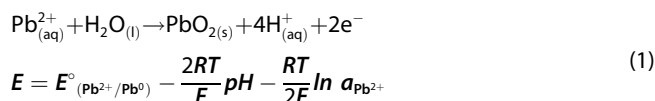E-mail: daniel.ramirez@uv.cl
[b] Prof. E. A. Dalchiele, D. L. Gau, Prof. R. E. Marotti
Instituto de Física, Facultad de Ingeniería
Universidad de la República
Julio Herrera y Reissig 565, C.C. 30, 11000 Montevideo, Uruguay
[c] Dr. J. A. Anta, Dr. L. Contreras-Bernal, A. Riquelme, Dr. J. Idigoras
Departamento de Sistemas Físicos, Químicos y Naturales Universidad Pablo de Olavide
41013, Sevilla, Spain

ChemElectroChem

Articles
doi.org/10.1002/celc.202000782

Chemistry Europe
European Chemical
Societies Publishing

one-step approach is employed where the perovskite precursors are jointly dissolved and spin-coated once over substrates.[7,13] Other novel protocols to build PSCs are based in the use of CsPbBr$_3$ quantum dots as raw materials to form CsPbBr$_3$ films through either chemical conversion or thermal assisted resumption.[16,17] More recently, alternative methods of deposition such as vacuum and pulsed laser deposition have been proposed, among others.[20,23]

The electrochemical deposition is another approach to implement scalable procedures for solar cell preparation but its use to build PSCs has been restricted to a laboratory scale.[39,40] This less explored method includes the electrochemical deposition of a lead precursor such as PbI$_2$,[41] PbO[42–45] or PbO$_2$.[46–48] MAPI-based PSCs have exhibited best power conversion efficiencies (PCE) of 14.59% and 10.19% for PbO and PbO$_2$ precursors, respectively.[43] Particularly, PbO$_2$ has a widely accepted electrochemical formation mechanism via anodic reaction of Pb(II) either in acidic or alkaline conditions.[49,50] In acid media this occurs according to Eq. (1):

$$Pb^{2+}_{(aq)} + H_2O_{(l)} \rightarrow PbO_{2(s)} + 4H^+_{(aq)} + 2e^-$$
$$E = E^\circ_{(Pb^{2+}/Pb^0)} - \frac{2RT}{F}pH - \frac{RT}{2F}ln\ a_{Pb^{2+}} \tag{1}$$

PbO$_2$ films can be converted into MAPI through a two-step conversion. First, the thermodynamically favorable reaction of PbO$_2$ with either vapor[48] or ethanolic[47] HI to form PbI$_2$ as intermediate [Eq. (2)]:

$$PbO_{2(s)} + 4HI_{(g)} \rightarrow PbI_{2(s)} + 2H_2O_{(g)} + I_{2(g)} \tag{2}$$
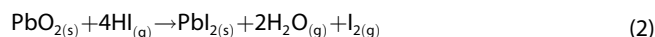
PbI$_2$ is further converted into the final MAPI film by reaction with CH$_3$NH$_3$I dissolved in isopropanol.[47,48]

In this work, we make use of the electrochemical deposition technique as an alternative to spin-coating to control the lead transfer from precursors towards a substrate for further CsPbBr$_3$ deposition. As a novel strategy we have used very little amounts of hot HBr in a closed rounded glass flask which reacted with an electrodeposited PbO$_2$ film to obtain an intermediate PbBr$_2$ film. This film was further converted into CsPbBr$_3$ by spin-coating a methanolic CsBr solution followed by annealing. The resulting films yield comparable photovoltaic performance with other less cost-effective procedures for preparation of fully inorganic perovskites.

Results and Discussion

Electrochemical Deposition of PbO$_2$ on FTO and its Conversion into CsPbBr$_3$

As described in the Introduction [Eq. (1)], galvanostatic electrodeposition of PbO$_2$ over FTO has proven useful to prepare MAPI. After PbO$_2$ films were formed and characterized, their conversion to PbBr$_2$ was designed in a similar way as reported by Kemel et al.[48] They reported for the first time the chemical reduction of PbO$_2$ films to PbI$_2$ under exposure to HI vapors.

The overall reaction included the oxidation of iodide to iodine. According to the electrochemical series of standard reduction potentials, built for aqueous media at pH 0 and 25 °C, it can be predicted that iodide is thermodynamically a good reductor for lead(IV) in PbO$_2$. The as formed lead (II) is simultaneously stabilized as PbI$_2$ thanks to its low Ksp value (Ksp PbI$_2$ = 9.8 × 10^{-9}).[51] Following the same reasoning, bromide is a weaker reductor compared to iodide, but still is capable to reduce Pb (IV) to Pb(II).[51] Although our conversion conditions are not standard, it is reasonable to assume the thermodynamic feasibility of the conversion. On the other hand, PbI$_2$ is less water soluble than PbBr$_2$ according to their K_{sp} values (K_{sp} PbI$_2$ = 9.8 × 10^{-9}, Ksp PbBr$_2$ = 6.6 × 10^{-6})[51] which makes PbBr$_2$ solid films more sensible to the presence of water than PbI$_2$. Further, Kemmel et al. performed the conversion to PbI$_2$ at 90 °C using silica particles in a reactor, so that water molecules coming mainly from the HI solution can be absorbed. Other desiccants including silica and molecular sieves led to low quality PbBr$_2$ films, with clear signals of water-driven deterioration such as condensation or "dew" prints. Surprisingly, after raising the temperature to 250 °C without any kind of desiccant, the quality of films was much better. This could be attributed to the smaller amount of concentrated HBr used (1.5 μL vs. 20 μL in previous work) together with the effect of the high temperature (250 °C). Minimizing the amount of concentrated HBr, the presence of water was also minimized while ensuring the minimum stoichiometric amount necessary to complete conversion into PbBr$_2$. Following these ideas, we propose that the conversion of PbO$_2$ into PbBr$_2$ occurs according to Eq. (3):

$$PbO_{2(s)} + 4HBr_{(g)} \rightarrow PbBr_{2(s)} + 2H_2O_{(g)} + Br_{2(g)} \tag{3}$$
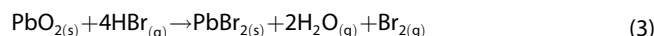
Structural Properties

The efficacy of the procedure described above has been followed by X-ray diffraction experiments performed on the successive layers. We found that the precursor films (Supporting information, Scheme SI-1a) can be indexed to the orthorhombic structure of α-PbO$_2$, in agreement with reported structural characterization of electrodeposited lead oxide films.[52] Scheme SI-1b confirms the successful conversion to the rhombic PbBr$_2$ structure and the absence of impure phases. Figure 1 shows typical diffraction patterns of different thin film samples grown by different spin-coating cycle numbers (#4, #10 and #13) that can be indexed to the orthorhombic structure of CsPbBr$_3$. The XRD pattern corresponding to the thin film grown by #10 spin-coating cycles (see pattern (b) in Figure 1), exhibited only diffraction peaks which are consistent with the CsPbBr$_3$ phase. No obvious impurity phases are found in these samples, then, this result cross-check a good crystallization and high purity of CsPbBr$_3$. Furthermore, diffraction peaks are observed at 24.1°, 25.3° and 28.5°, which are unique crystallographic features of the orthorhombic phase that are missing from the cubic crystal structure of the CsPbBr$_3$.[53] The last is in agreement with other reported results indicating a room-temperature stable ortho-

ChemElectroChem

Articles
doi.org/10.1002/celc.202000782

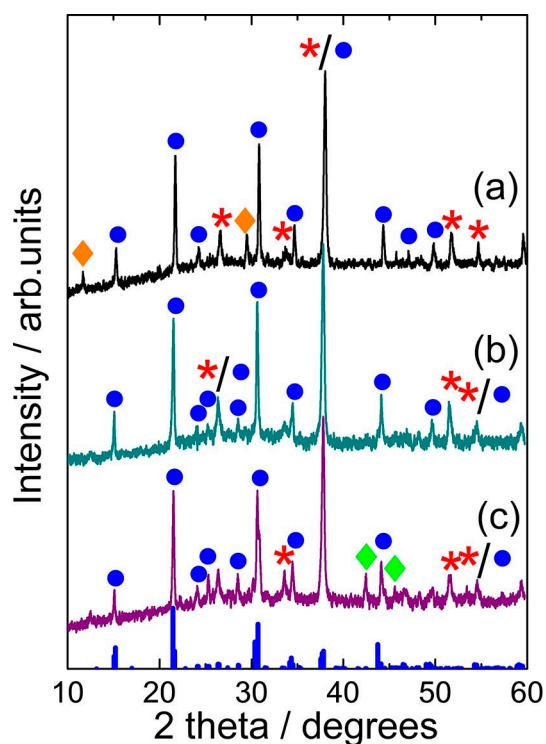**Chemistry Europe**
European Chemical
Societies Publishing

Figure 1. X-ray diffraction patterns of perovskite CsPbBr$_3$ thin films grown by different spin-coating cycle numbers: (a) #4, (b) #10 and (c) #13 cycles. The JCPDS pattern of orthorhombic CsPbBr$_3$ is also shown for comparison at the bottom of this diffractogram (thick blue bars). The characteristic peaks of: CsPbBr3 are marked with blue symbols (●), those corresponding to tetragonal CsPb2Br5 phase are marked with orange diamond markers (♦), and those corresponding to the rhombohedral Cs4PbBr6 phase indicated by green diamond symbols (♦). The signals marked with (*) are associated to the FTO/glass substrate.

Figure 2. SEM images of substrates during the different stages of CsPbBr$_3$ preparation, including spin-coating (s-c) cycles. Scale bars equals 500 nm in both frontal and lateral views.

rhombic CsPbBr$_3$ phase.[54–56] In contrast, films grown through #4 and #13 spin-coating cycles show the presence of additional diffraction peaks that do not correspond to CsPbBr$_3$. In the case of diffraction pattern of a sample grown by 4# spin-coating cycle numbers, diffraction peaks marked with orange diamond markers indicate the presence of residual tetragonal CsPb$_2$Br$_5$ phase. This is a clear indication of a PbBr$_2$-rich phase.[19,57] On the other hand, the XRD pattern of the sample grown by 13# spin-coating cycles, suggests the presence of small amounts of secondary rhombohedral Cs$_4$PbBr$_6$ phase (CsBr-rich phase).

Morphological Analysis

Figure 2 shows the different stages in CsPbBr$_3$ formation from bare FTO. In contrast to a previous study,[48] where well-covered films were obtained only after 500 s, we accomplished a very homogeneous and well-covering PbO$_2$ film after 280 s of reaction with the same current density. This is probably due to the positive effect of the activation protocol with HNO$_3$ on the FTO pieces before electrodeposition. After conversion into PbBr$_2$, full coverage of the FTO and a granular morphology can be observed. In Figure 2 it can also be seen a different number and grain size distribution depending of the number of spin-
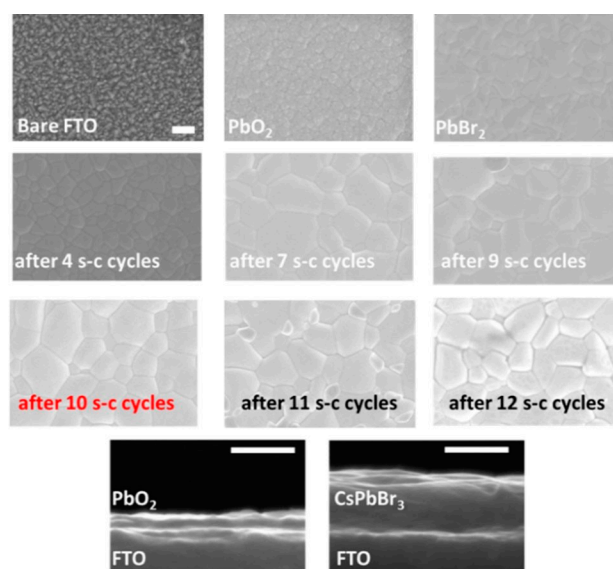
coating cycles which were compared each other (*vide infra*). Faraday's law predicts at a current density of 70 mC cm^{-2} thicknesses of 94 nm and 440 nm for PbO$_2$ and CsPbBr$_3$, respectively. These calculated values compared very well with the experimental thickness of the final CsPbBr$_3$ films according to the SEM images: 89 and 428 nm respectively.

EDS analysis was employed on the samples to obtain the Pb/Cs ratio. Results as a function of the number of spin-coating cycles with methanolic CsBr solution are depicted in Figure 3a. 9# spin-coating cycles appear to be ideal to reach the desired composition. The inset with photographs in Figure 3 shows clearly that the yellow color characteristic of CsPbBr$_3$ becomes fully evident after the 6th cycle. In contrast, less spin-coating cycles can only stabilize the white colored CsPb$_2$Br$_5$ compound.[58] This is also in agreement with the interpretation given by Duan et col.[15] and with the XRD results from Figure 1a. When the number of spin-coating cycles was higher than 10, the composition of films changed substantially (Figure 3) which could indicate the formation of a new compound, namely the pale yellow colored Cs$_4$PbBr$_6$.[59] This result is also confirmed by Figure1c from our XRD analysis. The grain size (Figure 3b) estimated from SEM analysis also evolved with the number of spin-coating cycles and approached to its highest value when the number of spin-coating cycles was 10. Starting from PbBr$_2$ (included in an inset in Figure 3b), after 5 cycles the grain size exhibited a great increase from 550 nm to over 1 μm which matches with the stoichiometry of the CsPb$_2$Br$_5$ phase (Figure 3a). Subsequent spin-coating cycles increased and decreases slightly the grain size. At 9 cycles the grain size was particularly lowered but after the 10th cycle recovered its value until reach a maximum. Evolution of grain size between 11 at 12 cycles demonstrated the predominance of the Cs$_4$PbBr$_6$ phase under formation. In spite of the slight deviation of the CsPbBr$_3$ samples prepared with 10# spin-coating cycles from
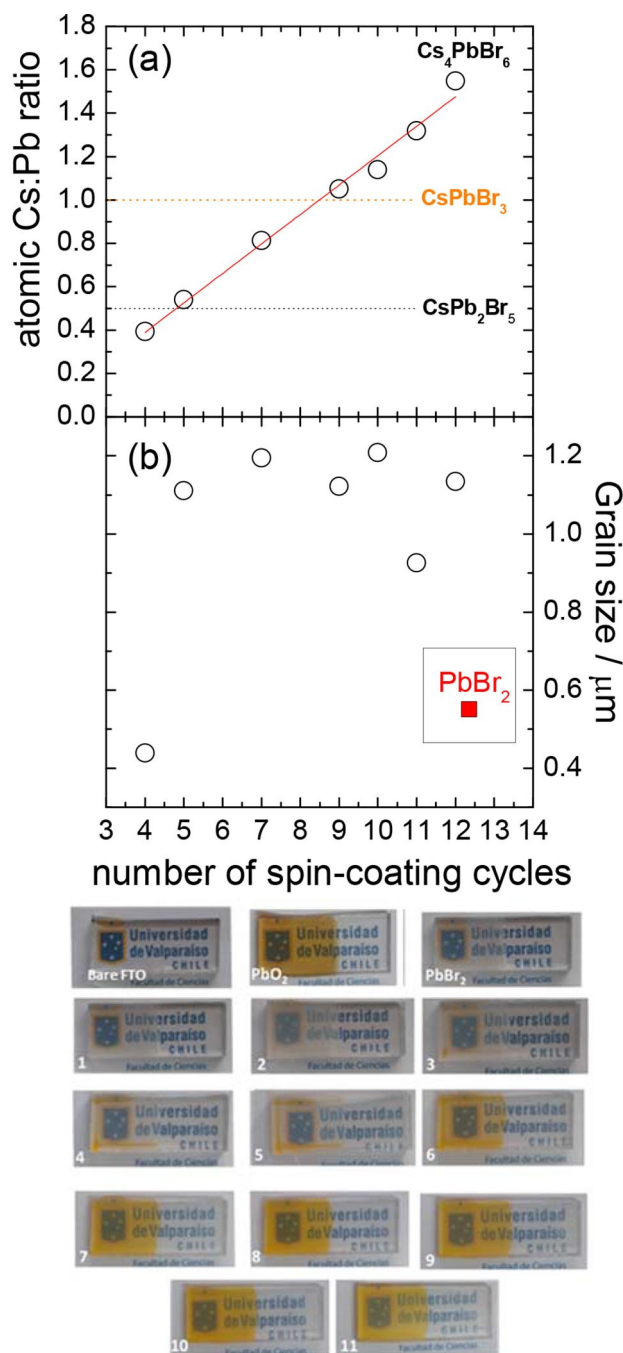
Figure 3. a) Atomic Cs:Pb ratio and b) grain size versus the number of spin-coating cycles with CsBr over $PbBr_2$. The inset in (b) shows the mean grain size of $PbBr_2$ before starting the spin-coating cycles. The photographs showed below the main graph evidence the changes in aspect when $PbBr_2$ was progressively converted into $CsPbBr_3$. The numbers in each photograph correspond to the number of spin-coating cycles.

the theoretical stoichiometric composition, these samples presented the best photovoltaic behavior (*vide infra*) as demonstrated by its j-V characteristic (Scheme SI-2) and compared with the response of samples after 9 cycles. We then confirm and conclude that under these conditions an optimal spin-coating cycle number equal to 10# should be performed

and thus this condition was selected to continue further analyses.

Optical Properties

Figure 4 collects optical absorption data (transmittance and absorption coefficient) of the resulting $CsPbBr_3$ films. The spectrum shows a clear peak close to 2.4 eV, and a continuous interband absorption for energies above this value. This behavior indicates that the optical properties of the material around the absorption edge are dominated by the presence of excitons. Using Elliot's expression (Supporting information) to fit the experimental data between 2.2 eV and 2.6 eV, the absorption spectrum was deconvoluted into two components: one corresponding to an excitonic absorption and the other to a direct absorption edge as shown in Figure 5 (dashed line). The results of these fittings, performed on all samples, show average
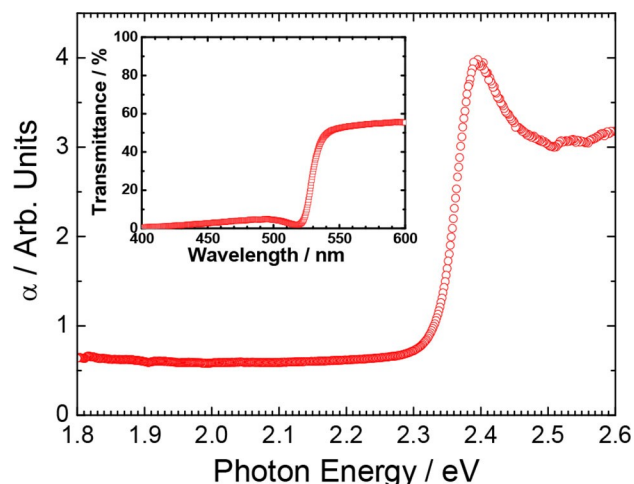

Figure 4. Absorption coefficient α showing the characteristic shape of an excitonic behavior. Inset: Typical transmittance spectra of the $CsPbBr_3$ samples (10# spin-coating cycles).
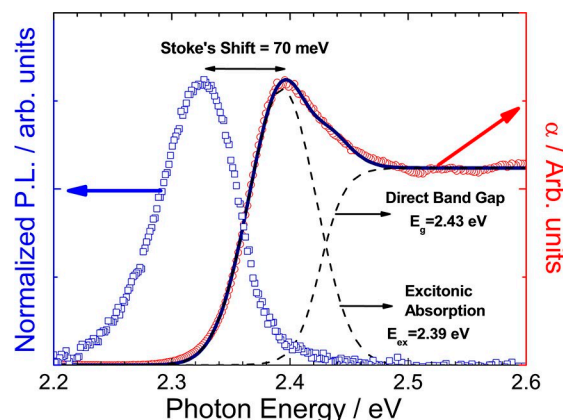

Figure 5. Experimental Absorption coefficient α (red circles) fit results using the Elliot formula (black continuous), deconvolution in excitonic absorption and direct band gap (black dashed), photoluminescence spectra (blue squares). $CsPbBr_3$ samples with 10# spin-coating cycles.

ChemElectroChem

Articles
doi.org/10.1002/celc.202000782

**Chemistry
Europe**

European Chemical
Societies Publishing

values among 4 and 11 spin-coating cycles for the energy of the band gap and exciton of 2.43 ± 0.01 eV and 2.39 ± 0.01 eV respectively. Thus, the exciton binding energy can be estimated to be around 40 meV, relatively close to thermal energy of 26 meV. Similar behavior have already been observed in the optical properties of other types of perovskites with the ABX_3 structure in both thin films and nanoparticles.[60–63]

Photoluminescence measurements (blue squares in Figure 5) carried out for samples from 4 to 11 spin-coating cycles, resulted in an emission that varies slightly between 2.30 and 2.34 (± 0.01) eV giving a mean value for the difference with the excitonic peak of 62 ± 5 meV and particularly 70 meV for 10 spin-coating cycles. In a second manuscript under preparation these optical properties are further analyzed and interpreted.

Photovoltaic Properties and Impedance Characterization

The j-V response of our system was presented in Figure SI-2 from which it becomes clear that sample with 9 and 11 spin-coating cycles were less efficient compared with the sample prepared with 10 cycles. The biggest grain size from this conditions also supported this interpretation (Figure 3b). The high hysteresis, particularly close to V_{oc} did not allow the objective estimation of the fill factor (FF) and the efficiency using this technique. The origin of such a large hysteresis, especially at open-circuit appears to be related to the particular experimental set-up we are using and it is probably due to slow ion migration toward the carbon contact. However, a precise description of this phenomenon is out of the scope of this paper. Thus we followed the recommendations stablished in which recommend in this case the use of stabilized current at fixed voltage (SCFV) technique to assess the PCE.[64] Our best cell obtained through this methodology gave a PCE value as high as 2.70%, measured at +0.8557 V with the steady state condition achieved after 1 h (Figure 6a). This PCE value is quite close to a similar configuration reported in the literature: 2.35%.[15] This demonstrates the potentiality of the electrochemical approach to build photovoltaic devices with simple configurations based on cost-effective materials. From Figure 6b, the external quantum efficiency (EQE) response is quite similar to that from a previous study where $CsPbBr_3$ was prepared by spin-coating. As expected, the spectrum exhibited a sharp decrease from *ca* 530 nm,[18] in line with the optical analysis of Figure 4. Thus, the previous work described in Ref.[18] can be regarded as a good reference for comparison between these two different methods.

In Figure 7a and b a typical impedance spectrum at open circuit of a $CsPbBr_3$ based device is presented. The spectrum is recorded once the sample contacted with the carbon-coated tip and after V_{oc} stabilization is reached. The IS response shows one main arc in the Nyquist plot, associated to the peak appearing at $\sim 5 \times 10^4$ Hz. This signal reflects mainly the recombination process of the device.[18] A second signal can be also detected in most devices below 1 Hz. This is attributed to the slow ionic motion in the perovskite film. We have used a simple Rs(RC)-equivalent circuit to fit the high frequency part of
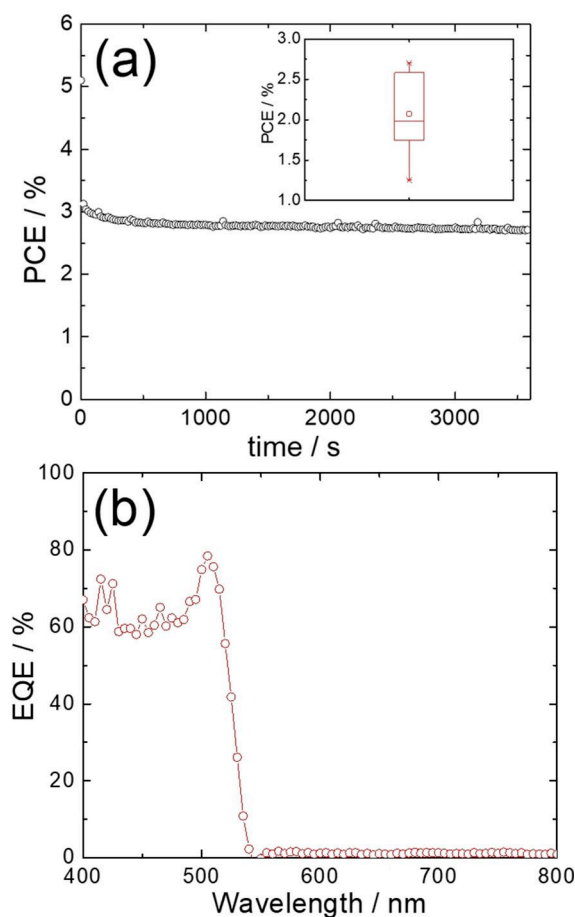

Figure 6. a) % PCE from the maximum power point as function of time for the champion solar cell. Inset: statistical analysis of % PCE from SCFV measurements after 1 h; b) External quantum efficiency (EQE) versus monochromatic wavelength.
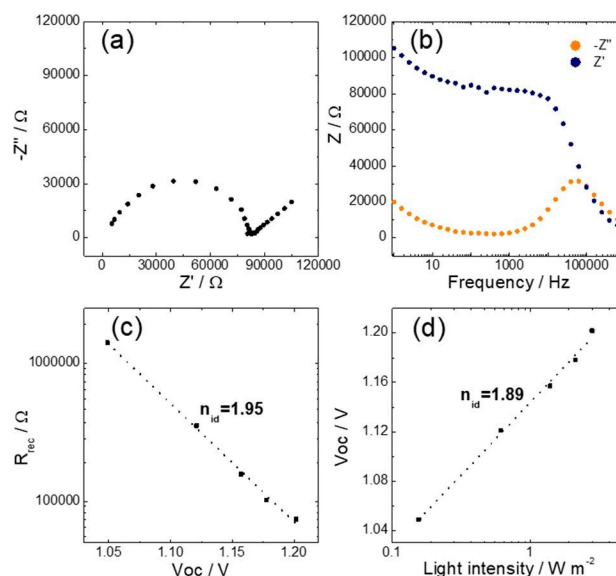

Figure 7. a, b) IS data at open-circuit condition ($V_{oc} = 1.195$ V) of a $CsPbBr_3$ PSC fabricated in this work. c) Recombination resistance versus V_{oc}. d) Semilogarithmic plot of the V_{oc} as a function of the light intensity

ChemElectroChem

Articles
doi.org/10.1002/celc.202000782

Chemistry Europe
European Chemical
Societies Publishing

the spectrum and to extract the resistance and the capacitance associated with the recombination signal. This analysis is done at various illumination intensities, resulting in varying V_{oc} values. Typical results for the recombination resistance are plotted in Figure 7c. A plot of the V_{oc} versus light intensity is shown in Figure 7d.

The recombination resistance shows a clear exponential behavior with respect to the open circuit potential, in accordance with the following theoretical expression [Eq. (4), Ref. [18] and references therein]:

$$R_{rec} = R_{00} \exp\left(-\frac{\beta q V_{OC}}{k_B T}\right) \tag{4}$$

where β is the recombination parameter. This is related to the ideality factor of the device via $m = 1/\beta$ and

$$V_{OC} \sim \frac{m k_B T}{q} \ln(I) \tag{5}$$

Figure 7d plots the open-circuit potential as function of logarithmic values of the light intensity. A linear fit of the data yields typically m values in 1.8–2.2 range. Furthermore, for a given device, the ideality factor extracted from the $V_{oc}-\ln(I)$ plot is fully consistent with that obtained from the recombination resistance. After scaling by the smaller nominal area of the carbon-coated tip, both the numerical values of the recombination resistance and the capacitance are in line with previous literature values for $CsPbBr_3$ based perovskite solar cells. Thus, the capacitance is voltage independent (results not shown) with values of $1-2\ 10^{-7}\ F\,cm^{-2}$, very close to those reported for $CsPbBr_3$-based perovskite solar cells with a more elaborated architecture including a hole transport layer and a gold contact. This result further confirms that the electrochemical method used here produces high quality films with recombination features of the same nature and magnitude of the best samples reported.[5,6,8,18] This shows that the experimental setup used here probes correctly the impedance response of the perovskite film, producing a true recombination resistance and a true geometrical capacitance.

Conclusions

A novel method to manufacture $CsPbBr_3$ perovskite solar cells have been developed through an electrochemically assisted method. Features such as homogeneity and well-covering thickness of as deposited PbO_2 precursor were well transferred to the $PbBr_2$ intermediate by means of a heterogeneous reaction with hydrogen bromide with a high control of lead waste. $PbBr_2$ intermediate was subsequently converted into $CsPbBr_3$ by a multiple-step spin coated method. Structural and optical analyses revealed these $CsPbBr_3$ films are well crystalized as orthorhombic phase with good optical absorption. PCE, EQE and ideality factor values obtained without neither electron nor hole transporting layers are quite concordant with state-of-art $CsPbBr_3$ solar cells thus demonstrating the feasibility and

potentiality of this cost-effective device. This strategy opens the possibility to integrate the electrochemical methods to a scalable technology for PSCs.

Experimental Section

All the chemical reagents were of analytical grade and used without previous treatment. For aqueous solutions, deionized water (Milli-Q water, $18.2\ \Omega\,cm$) was used. Fluorine doped tin oxide coated glasses (FTOs, TEC 15, Xop Glass, $12-14\ \Omega/sq$) were used as substrates. These substrates were cleaned with an Hellmanex solution (1%) in an ultrasonic bath. After rinsing with a copious amount of water, the FTOs were again sonicated in acetone and ethanol. Then, the substrates were rinsed with water, dried using a N_2 stream and activated in concentrated HNO_3 (65%) for 3 minutes under ultrasonic conditions. Finally, the FTOs were rinsed again with water and dried with a N_2 stream.

A classic glass electrochemical cell was employed for the electrochemical deposition of PbO_2. A lead-based electrolyte was prepared following the methodology reported.[48] $Na(C_2H_3O_2)_2 \times 3H_2O$ was dissolved in 40 mL of water, and then the pH value was adjusted to 5.5 with glacial acetic acid. Separately, $PbC_2H_3O_2 \times 3H_2O$ was also dissolved in 40 mL of deionized water and added slowly to the sodium acetate solution. The final pH value was adjusted to 5.5 before use, resulting in 0.1 M Pb(II) as final concentration. The electrochemical setup was formed by the freshly prepared FTO substrate as working electrode. An $Ag/AgCl_{sat.}$ (0.196 V vs SHE) and a Pt mesh served as reference and auxiliary electrode respectively. The FTO substrate was located in front and parallel to the Pt mesh keeping a distance near to 0.8 cm each other in order to favor the homogeneous growth of PbO_2 film over the immersed portion of FTO. A current density of $0.25\ mA\,cm^{-2}$ was imposed until a fixed charge density of $70\ mC\,cm^{-2}$ was consumed during the electrolysis.

Prior to the conversion, fresh PbO_2 samples were thoroughly rinsed with water, dried with a nitrogen stream and heated at 250°C for 5 minutes. After that, the hot substrates were placed inside a rounded glass flask, which contained 1.5 µL of HBr (47%).The PbO_2 face was placed in opposition to the position of the HBr aliquot. A wide tubular furnace was used to hold the system at 250°C for 10 minutes. Then, the $PbBr_2$ film was slowly cooled down until 120°C.

On the other hand, a methanolic 0.07 M CsBr solution was prepared by heating at 40°C and stirring. 50 µL of CsBr solution was deposited on the $PbBr_2$ film and then spin coated in a one-step setup at 3000 rmp for 30 s. Afterward the substrate was annealed at 250°C for 5 min. This last step was repeated until 13 times in order to obtain the optimized conditions to form stable $CsPbBr_3$ orthorhombic phase.

Scanning electron microscopy (SEM, Zeiss Gemini SEM-300) was used for frontal imaging of samples. The system was coupled with a Silicon Drift detector (Oxford Instruments) for EDS analysis. A field-emission scanning electron microscopy (FE-SEM, Quanta 250 FEG) was used for lateral imaging of samples. The crystalline character of the films was determined by X-ray diffraction (XRD) measurements, carried out in a standard theta-2 theta scans on a Philips PW180 diffractometer (30 kV, 40 mA, $CuK\alpha$ radiation with $\lambda = 1.5406$ Å). The optical characterization was performed measuring the transmittance T and photoluminescence of the samples at room temperature. To measure the transmittance, the samples were excited with a halogen source (Ocean-Optics HL 2000), and the transmitted light was collected with an integrating sphere (Ocean-Optics FOIS-1) connected to an Ocean Optics Flame-S-UV-

ChemElectroChem

Articles
doi.org/10.1002/celc.202000782

**Chemistry
Europe**
European Chemical
Societies Publishing

VIS-ES spectrometer. With the same spectrometer, photoluminescence measurements were performed but exciting with a Thorlabs M365FP1 LED (365 nm, 9.8 mW).

The electric contact for photovoltaic and impedance measurements were performed using a carbon coated string tip. The empirical criterion that we have implemented to probe the photovoltaic response of the CsPbBr$_3$ film is to increase the pressure with which this carbon coated string tip is pressed to the perovskite film until both V_{oc} and j_{sc} were maximized in the device. After measurement, the contacting area between the carbon coated string tip and the perovskite surface can be estimated by optical microscopy. The value obtained by this method is 2.09×10^{-4} cm^2 which we have subsequently used for the estimation of the nominal current density and efficiency of the device.

Following this procedure, j-V curves were traced using a solar simulator LOT (model LS0500) and an Autolab potentiostat (model PGSTAT 302N), at a calibrated light intensity of AM1.5G 100 mW cm^{-2}, using a Si-based reference solar cell. Strong hysteresis is systematically observed from the forward and reverse scans carried out at a scan rate of 10 mV s^{-1}, using this procedure. For this reason, maximum power potential (MPP) values and power to current efficiencies (PCE) were obtained using the stabilized current at fixed voltage (SCFV) technique.[64] At each imposed-bias, photocurrent density values were recorded once the steady-state had been reached under continuous light soaking until power is optimized. External quantum efficiency (EQE) was measured with a photovoltaic device characterization system Bentham (PV300) using monochromatic light under DC mode.

Impedance spectroscopy (IS) measurements were carried out using the same experimental set-up used in the PCE and EQE measurements and with the carbon-coated tip positioned at the same point that maximized the V_{oc}. The same Autolab potentiostat equipped with a FRA2 module was used in the IS studies. The measurements were conducted at open-circuit conditions under varying white-light illumination intensities in the 1–10^6 Hz frequency range and a voltage perturbation of 20 mV. Linearity of the measurement was verified by Lissajous analysis.

Conflict of Interest

The authors declare no conflict of interest.

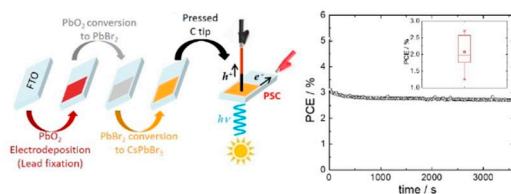**Keywords:** Electrodeposition · heterogeneous phase conversion · perovskite solar cell · optoelectronic properties

[1] S. Colella, M. Mazzeo, A. Rizzo, G. Gigli, A. Listorti, *J. Phys. Chem. Lett.* **2016**, *7*, 4322–4334.
[2] Best Research-Cell Efficiency Chart. https://www.nrel.gov/pv/cell-efficiency.html.
[3] M. Grätzel, *Nat. Mater.* **2014**, *13*, 838–842.
[4] B. Saparov, D. B. Mitzi, *Chem. Rev.* **2016**, *116*, 4558–4596.
[5] J. Liang, C. Wang, Y. Wang, Z. Xu, Z. Lu, Y. Ma, H. Zhu, Y. Hu, C. Xiao, X. Yi, G. Zhu, H. Lv, L. Ma, T. Chen, Z. Tie, Z. Jin, J. Liu, *J. Am. Chem. Soc.* **2016**, *138*, 15829–15832.
[6] X. Chang, W. Li, L. Zhu, H. Liu, H. Geng, S. Xiang, J. Liu, H. Chen, *ACS Appl. Mater. Interfaces* **2016**, *8*, 33649–33655.
[7] R. E. Beal, D. J. Slotcavage, T. Leijtens, A. R. Bowring, R. A. Belisle, W. H. Nguyen, G. F. Burkhard, E. T. Hoke, M. D. McGehee, *J. Phys. Chem. Lett.* **2016**, *7*, 746–751.
[8] M. Kulbak, D. Cahen, G. Hodes, *J. Phys. Chem. Lett.* **2015**, *6*, 2452–2456.
[9] M. Kulbak, S. Gupta, N. Kedem, I. Levine, T. Bendikov, G. Hodes, D. Cahen, *J. Phys. Chem. Lett.* **2016**, *7*, 167–172.
[10] C.-X. Qian, Z.-Y. Deng, K. Yang, J. Feng, M.-Z. Wang, Z. Yang, S. Liu, H.-J. Feng, *Appl. Phys. Lett.* **2018**, *112*, 93901.
[11] J. Duan, Y. Zhao, B. He, Q. Tang, *Angew. Chem.* **2018**, *130*, 3849.
[12] Z. Liu, B. Sun, X. Liu, J. Han, H. Ye, T. Shi, Z. Tang, G. Liao, *Nano-Micro Lett.* **2018**, *10*, 34.
[13] P. Luo, Y. Zhou, S. Zhou, Y. Lu, C. Xu, W. Xia, L. Sun, *Chem. Eng. J.* **2018**, *343*, 146–154.
[14] Y. Li, J. Duan, Y. Zhao, Q. Tang, *Chem. Commun.* **2018**, *54*, 8237–8240.
[15] J. Duan, Y. Zhao, B. He, Q. Tang, *Small* **2018**, *14*, 1704443.
[16] X. Zhang, Z. Jin, J. Zhang, D. Bai, H. Bian, K. Wang, J. Sun, Q. Wang, S. F. Liu, *ACS Appl. Mater. Interfaces* **2018**, *10*, 7145–7154.
[17] J. B. Hoffman, G. Zaiats, I. Wappes, P. V. Kamat, *Chem. Mater.* **2017**, *29*, 9767–9774.
[18] L. Contreras-Bernal, S. Ramos-Terrón, A. Riquelme, P. Boix, J. Idígoras, I. Mora-Seró, J. A. Anta, *J. Mater. Chem. A* **2019**, *7*, 12191–12200.
[19] I. Poli, J. Baker, J. McGettrick, F. De Rossi, S. Eslava, T. Watson, P. J. Cameron, *J. Mater. Chem. A* **2018**, *6*, 18677–18686.
[20] C. Chen, Y. Wu, L. Liu, Y. Gao, X. Chen, W. Bi, X. Chen, D. Liu, Q. Dai, H. Song, *Adv. Sci.* **2019**, *6*, 1802046.
[21] J. Lei, F. Gao, H. Wang, J. Li, J. Jiang, X. Wu, R. Gao, Z. Yang, S. Liu, *Sol. Energy Mater. Sol. Cells* **2018**, *187*, 1–8.
[22] Y. Zhang, L. Luo, J. Hua, C. Wang, F. Huang, J. Zhong, Y. Peng, Z. Ku, Y. Cheng, *Mater. Sci. Semicond. Process.* **2019**, *98*, 39–43.
[23] H. Wang, Y. Wu, M. Ma, S. Dong, Q. Li, J. Du, H. Zhang, Q. Xu, *ACS Appl. Energy Mater.* **2019**, *2*, 2305–2312.
[24] G. Liao, Y. Zhao, J. Duan, H. Yuan, Y. Wang, X. Yang, B. He, Q. Tang, *Dalton Trans.* **2018**, *47*, 15283–15287.
[25] J. Duan, Y. Zhao, X. Yang, Y. Wang, B. He, Q. Tang, *Adv. Energy Mater.* **2018**, *8*, 1802346.
[26] Y. Zhao, J. Duan, H. Yuan, Y. Wang, X. Yang, B. He, Q. Tang, *Sol. RRL* **2019**, *3*, 1800284.
[27] Y. Liu, B. He, J. Duan, Y. Zhao, Y. Ding, M. Tang, H. Chen, Q. Tang, *J. Mater. Chem. A* **2019**, *7*, 12635–12644.
[28] Y. Iso, T. Isobe, *ECS J. Solid State Sci. Tech.* **2018**, *7*, R3040–R3045.
[29] L. Zhang, X. Yang, Q. Jiang, P. Wang, Z. Yin, Z. Zhang, H. Tan, Y. Yang, M. Wei, B. R. Sutherland, E. H. Sargent, J. You, *Nat. Commun.* **2017**, *8*, 15640.
[30] C. C. Stoumpos, C. D. Malliakas, J. A. Peters, Z. Liu, M. Sebastian, J. Im, T. C. Chasapis, A. C. Wibowo, D. Young Chung, A. J. Freeman, B. W. Wessels, M. G. Kanatzidis, *Cryst. Growth Des.* **2013**, *13*, 2722–2727.
[31] Y. Xu, M. Yang, B. Chen, X. Wang, H. Chen, D. Kuang, C. Su, *J. Am. Chem. Soc.* **2017**, *139*, 5660–5663.
[32] H. Wu, X. Li, C. Tung, L. Wu, *Adv. Mater.* **2019**, *31*, 1900709.
[33] X. Zhu, Y. Lin, J. San Martin, Y. Sun, D. Zhu, Y. Yan, *Nat. Commun.* **2019**, *10*, 2843.
[34] L. Gao, W. Luo, Y. Yao, Z. Zou, *Chem. Commun.* **2018**, *54*, 11459–11462.
[35] Y. Li, Z. Shi, S. Li, L. Lei, H. Ji, D. Wu, T. Xu, Y. Tian, X. Li, *J. Mater. Chem. C* **2017**, *5*, 8355–8360.
[36] Y. Zhu, X. Tong, H. Song, Y. Wang, Z. Qiao, D. Qiu, J. Huang, Z. Lu, *Dalton Trans.* **2018**, *47*, 10057–10062.
[37] S. Schünemann, M. Van Gastel, H. Tüysüz, *ChemSusChem* **2018**, *11*, 2057–2061.
[38] Y. Galagan, *J. Phys. Chem. Lett.* **2018**, *9*, 4326–4335.
[39] H. Deligianni, S. Ahmed, L. T. Romankiw, *Electrochem. Soc. Interface* **2011**, *20*, 47–53.
[40] F. Tsin, A. Venerosy, J. Vidal, S. Collin, J. Clatot, L. Lombez, M. Paire, S. Borensztajn, C. Broussillou, P. P. Grand, S. Jaime, D. Lincot, J. Rousset, *Sci. Rep.* **2015**, *5*, 8961.

ChemElectroChem

Articles
doi.org/10.1002/celc.202000782

Chemistry
Europe
European Chemical
Societies Publishing

[41] J. C. Hill, J. A. Koza, J. A. Switzer, *ACS Appl. Mater. Interfaces* **2015**, *7*, 26012–26016.

[42] X.-P. Cui, K.-J. Jiang, J.-H. Huang, X.-Q. Zhou, M.-J. Su, S.-G. Li, Q.-Q. Zhang, L.-M. Yang, Y.-L. Song, *Chem. Commun.* **2015**, *51*, 1457–1460.

[43] J.-H. Huang, K.-J. Jiang, X.-P. Cui, Q.-Q. Zhang, M. Gao, M.-J. Su, L.-M. Yang, Y. Song, *Sci. Rep.* **2015**, *5*, 15889.

[44] I. Zhitomirsky, L. Gal-Or, A. Kohn, H. W. Hennicke, *J. Mater. Sci. Lett.* **1995**, *14*, 807–810.

[45] S. Sawatani, S. Ogawa, T. Yoshida, H. Minoura, *Adv. Funct. Mater.* **2005**, *15*, 297–302.

[46] J. A. Koza, J. C. Hill, A. C. Demster, J. A. Switzer, *Chem. Mater.* **2016**, *28*, 399–405.

[47] H. Chen, Z. Wei, X. Zheng, S. Yang, *Nano Energy* **2015**, *15*, 216–226.

[48] G. Popov, M. Mattinen, M. L. Kemell, M. Ritala, M. Leskelä, *ACS Omega* **2016**, *1*, 1296–1306.

[49] X. Li, D. Pletcher, F. C. Walsh, *Chem. Soc. Rev.* **2011**, *40*, 3879–3894.

[50] A. A. Vertegel, E. W. Bohannan, M. G. Shumsky, J. A. Switzer, *J. Electrochem. Soc.* **2001**, *148*, C253–C256.

[51] D. R. Lide, ed., *CRC Handbook of Chemistry and Physics, Internet Version 2007*, (87th Edition), http:/www.hbcpnetbase.com, Taylor and Francis, Boca Raton, FL, **2007**.

[52] X. Zhao, C. Li, Y. Wang, W. Xu, *Int. J. Electrochem. Sci.* **2018**, *13*, 3745–3756.

[53] A. Kostopoulou, M. Sygletou, K. Brintakis, A. Lappas, E. Stratakis, *Nanoscale* **2017**, *9*, 18202–18207.

[54] K. Chen, S. Shünemann, S. Song, H. Tüysüz, *Chem. Soc. Rev.* **2018**, *47*, 7045–7077.

[55] C. Tenailleau, S. Aharon, B. Cohen, L. Etgar, *Nanoscale Adv.* **2019**, *1*, 147–153.

[56] G. Murugadoss, R. Thangamuthu, *Sol. Energy* **2019**, *179*, 151–163.

[57] J. Yin, H. Yang, K. Song, A. M. El-Zohry, Y. Han, O. M. Bakr, J. L. Bredas, O. F. Mohammed, *J. Phys. Chem. Lett.* **2018**, *9*, 5490–5495.

[58] I. Dursun, M. De Bastiani, B. Turedi, B. Alamer, A. Shkurenko, J. Yin, A. M. El-Zohry, I. Gereige, A. AlSaggaf, O. F. Mohammed, M. Eddaoudi, O. M. Bakr, *ChemSusChem* **2017**, *10*, 3746–3749.

[59] M. I. Saidaminov, J. Almutlaq, S. Sarmah, I. Dursun, A. A. Zhumekenov, R. Begum, J. Pan, N. Cho, O. F. Mohammed, O. M. Bakr, *ACS Energy Lett.* **2016**, *1*, 840–845.

[60] X. Chen, H. Lu, Y. Yang, M. C. Beard, *J. Phys. Chem. Lett.* **2018**, *9*, 2595–2603.

[61] M. C. Brennan, J. E. Herr, T. S. Nguyen-Beck, J. Zinna, S. Draguta, S. Rouvimov, J. Parkhill, M. Kuno, *J. Am. Chem. Soc.* **2017**, *139*, 12201–12208.

[62] W. Wu, W. Liu, Q. Wang, Q. Han, Q. Yang, *J. Alloys Compd.* **2019**, *787*, 165–172.

[63] J. Li, X. Yuan, P. Jing, J. Li, M. Wei, J. Hua, J. Zhao, L. Tian, *RSC Adv.* **2016**, *6*, 78311–78316.

[64] R. B. Dunbar, B. C. Duck, T. Moriarty, K. F. Anderson, N. W. Duffy, C. J. Fell, J. Kim, A. Ho-Baillie, D. Vak, T. Duong, Y. Wu, K. Weber, A. Pascoe, Y. Cheng, Q. Lin, P. L. Burn, R. Bhattacharjee, H. Wang, G. J. Wilson, *J. Mater. Chem. A* **2017**, *5*, 22542–22558.

ARTICLES

Dr. D. Ramírez*, Dr. G. Riveros, P. Díaz, J. Verdugo, G. Núñez, S. Lizama, P. Lazo, Prof. E. A. Dalchiele, D. L. Gau, Prof. R. E. Marotti, Dr. J. A. Anta, Dr. L. Contreras-Bernal, A. Riquelme, Dr. J. Idigoras

1 – 9

Electrochemically Assisted Growth of CsPbBr$_3$-Based Solar Cells Without Selective Contacts

Minimizing the lead: A simple and cost-effective CsPbBr$_3$-based solar cell without ordinary selective contacts is reported. An electrochemical approach consisting of three successive steps: (1) electrodeposition of PbO$_2$ directly on top of FTO substrates, (2) heterogeneous phase reaction with gaseous HBr and (3) spin-coating of methanolic CsBr solutions followed by annealing was used. This method is more adequate for large-scale environmentally friendly production as it reduces chemical waste, particularly toxic lead.

ChemElectroChem

Supporting Information

Electrochemically Assisted Growth of CsPbBr$_3$-Based Solar Cells Without Selective Contacts

Daniel Ramírez,* Gonzalo Riveros, Patricia Díaz, Javier Verdugo, Gerard Núñez, Susy Lizama, Pamela Lazo, Enrique A. Dalchiele, Daniel L. Gau, Ricardo E. Marotti, Juan A. Anta, Lidia Contreras-Bernal, Antonio Riquelme, and Jesús Idigoras
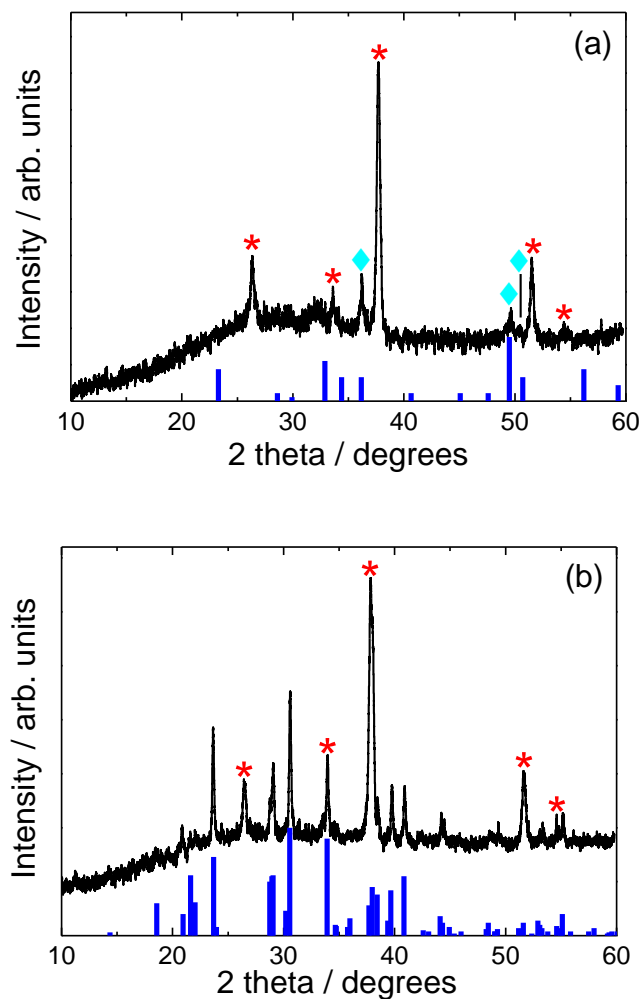
Figure SI-1. (a) X-ray diffraction pattern of a lead oxide thin film electrodeposited onto an FTO/glass substrate. The signals marked with blue light diamond symbols (♦), correspond to α-PbO$_2$ phase. The JCPDS pattern of orthorhombic ☐-PbO$_2$ is placed at the bottom of this diffractogram (thick blue bars). (b) X-ray diffraction pattern of a chemically synthesized lead bromide thin film. The JCPDS pattern of rhombic PbBr$_2$ is also shown for comparison at the bottom of this diffractogram (thick blue bars). In both Figures, the signals marked with (*) are associated to the FTO/glass substrate.

Average crystallite size was calculated from a full width at half maximum (FWHM) of X-ray diffraction peaks by using Scherrer formula [1]:

$$D = \frac{k\lambda}{\beta\cos\theta} \tag{SI-1}$$

Where D is the crystallite diameter, λ is the wavelength of the incident radiation, k = 0.94 is the shape factor, θ is the Bragg angle, and β is the full width at half maximum (FHWM) in radians. The average crystallite size evaluated from $CsPbBr_3$ diffraction peak at 21.5° was ca. 39 nm for a typical sample grown by 10# spin-coating cycles, hinting their nanocrystalline character.

Elliot function

Excitons are defined as quasiparticles formed by the Coulombian interaction between an electron (in the conduction band) and a hole (in the valence band) produced by absorbing a photon with energy lower, but close, to that of the band gap [2]. The energy states allowed for the excitons can be obtained by solving the quantum problem of two bodies, separating the movement of the carriers in a movement corresponding to the center of mass of the system (M) and another corresponding to the relative movement of the particles. The first of these contributions provides a continuous term proportional to the momentum of an electron in the conduction band $(\hbar k)^2$ in total energy (E_R), while the second, being analogous to the problem of the hydrogen atom, provides discrete levels of energy (E_r). So the allowed energetic states for the exciton are [3]:

$$E_{ex} = E_g + E_R + E_r \approx E_g + \frac{(\hbar k_c)^2}{2M} - R_{ex}\left(\frac{1}{n^2}\right) \tag{SI-2}$$

In this expression R_{ex} is the exciton binding energy, defined as the difference between the minimum energy excitonic state and the lowest energy state of the conduction band, E_g is the band gap energy and *n* is an integer labeling the different energy levels. Given these allowed energy states and also considering that only transitions with null angular momentum ($l = 0$) are allowed in this kind of materials [4] it is obtained that the absorption edge can be modeled by the Elliot function [5]:

$$\alpha(\hbar\omega) = P_{cv}\left[\theta(\hbar\omega - E_g)\cdot\left(\frac{\pi e^x}{\sinh{(\pi x)}}\right) + R_{ex}\sum_{n=1}^{\infty}\frac{4\pi}{n^3}\cdot\delta(\hbar\omega - E_g + R_{ex}/n^2)\right] \quad \text{(SI-3)}$$

In this expression $\hbar\omega$ is the photon energy, the term P_{cv}, which is determined by the matrix elements of the allowed transitions, is considered constant, θ and δ are the Heaviside and Dirac delta functions, respectively, and the parameter $x = \sqrt{\frac{R_{ex}}{(\hbar\omega - E_g)}}$ is defined.
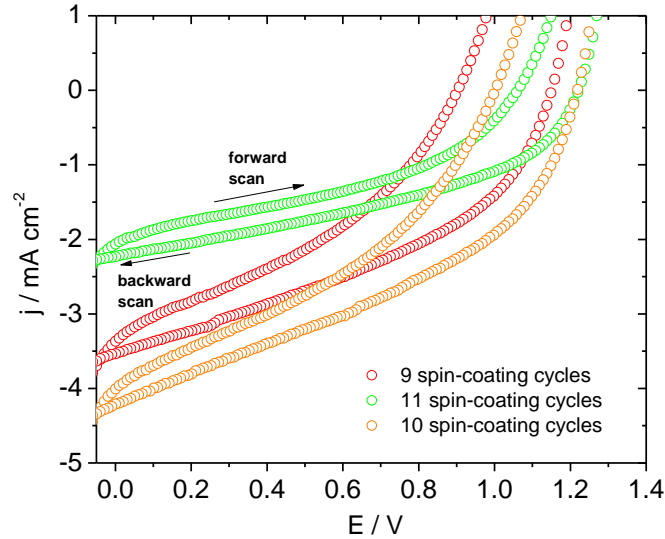
j-V curves

Figure SI-2. j-V characteristics taken for samples with 9, 10 and 11 spin coating cycles.

References

[1] Cullity, B. D. Elements of X-ray diffraction, Addison-Wesley Pub. Co.: Reading, Massachusetts, 1978.

[2] Fox, M.; Optical Properties of Solids, Oxford University Press: New York, 2010.

[3] Chen, X.; Lu, H., Yang, Y.; Beard, M. C. Excitonic Effects in Methylammonium Lead Halide Perovskites, *J. Phys. Chem. Lett.* **2018**, 9, 2595−2603.

[4] Peyghambarian, N.; Koch, S. W.; Mysyrowicz, A. Introduction to semiconductor optics, Prentice-Hall series in solid state physical electronics: London, 1993.

[5] Elliot, R. J. Intensity of Optical Absorption by Excitons. *Phys. Rev.* **1957**, 108, 1384-1389.

ChemPhysChem

Research Article
doi.org/10.1002/cphc.202200286

Chemistry
Europe
European Chemical
Societies Publishing

www.chemphyschem.org

Photophysical and Photoelectrochemical Properties of CsPbBr₃ Films Grown by Electrochemically Assisted Deposition

Daniel L. Gau+,*[a] Daniel Ramírez+,*[b] Fernando Iikawa,[c] Gonzalo Riveros,[b] Patricia Díaz,[b] Javier Verdugo,[b] Gerard Núñez,[b] Susy Lizama,[b] Pamela Lazo,[b] Enrique A. Dalchiele,[a] Lidia Contreras,[d] Jesús Idigoras,[d] Juan Anta,[d] and Ricardo E. Marotti[a]

Perovskite have had a great impact on the solid-state physics world in the last decade not only achieving great success in photovoltaics but, more recently, also in the implementation of other optoelectronic devices. One of the main obstacles for the adoption of Pb-based perovskite technologies are the high amounts of Pb needed in the conventional preparation methods. Here we present for the first time a detailed analysis of the photophysical and photoelectrochemical properties of CsPbBr₃ films directly grown on fluorine-doped tin oxide (FTO) coated glass through a novel technique based in the electro-deposition of PbO₂ as CsPbBr₃ precursor. This technique allows to save up to 90% of the Pb used compared to traditional methods and can be scalable compared with the commonly used spin-coating process. The low temperature analysis of their photoluminescence spectra, performed in both steady state and time dependence, revealed a strong interaction between electrons and longitudinal optical (LO) phonons dominant at high temperatures. On the other hand, the electrochemical and photoelectrochemical analysis proves that CsPbBr₃ prepared using this new method has state-of-the-art features, showing a p-type behavior under depletion regime. This is also confirmed by photoelectrochemical measurements using p-benzoquinone as target molecule. These results prove that the proposed method can be used to produce excellent CsPbBr₃ films, saving much of the lead waste.

Introduction

The research activity of the scientific community in the field of perovskites has increased dramatically in the last decade, mostly driven by the outstanding results obtained in photo-voltaic devices. This activity has allowed the perovskite solar cells (PSC) to increase their efficiencies from 3.8%[1] in the year 2009 to 25.5% in single junction architectures and 28% in multiple junction architecture, as reported in 2020.[2] From this intense research many of the outstanding optoelectronic properties of these materials have been unveiled, allowing many new applications of perovskites besides solar cell as LEDs,[3–5] lasers,[6–9] radiation detectors[10–13] and CO₂

reduction[14–16] devices among others. Electrochemical proper-ties of perovskites have also been exploited for electrodeposi-tion purposes as in the case of electropolymerized PEDOT on CH₃NH₃PbI₃ (MAPI).[17] Further, the constant search for new and better photoelectrochemical devices has also led perovskites to find applications in water splitting devices,[18–22] quantification on analytes[23] and degradation of organic compounds.[24] Although the technologies based on perovskites have not yet fully matured, they show very promising results allowing to spot a future with perovskite-based devices in the market.

In recent years, all-inorganic perovskite solar cells have attracted the attention in the scientific community, mainly because they provide excellent stability under ambient con-ditions compared to their organic counterparts.[25–30] One of the most studied inorganic perovskites has been CsPbBr₃. This perovskite shows very interesting physicochemical properties such as a wide direct bandgap of 2.43 eV, an exciton binding energy of around 40 meV,[31–33] a diffusion length for electrons (holes) of 5.5 μm (2.5 μm)[34] as well as high resistance to photothermal exposure.[35] Furthermore, the material properties can be improved by doping with Cl(-I),[36] Fe(II),[16] SnBr₂[37] and Sb(III)[38] among others, giving the possibility of tuning the bandgap over the visible spectra.

To achieve a full development of the PSC, and an extended implementation of this technology in the energy grid, several obstacles have to be overcome. One of them is to reduce the lead use in manufacturing methods, since its negative impact on the environment and human health.[39,40] For this purpose, a number of interesting efforts to recycle lead containing wastes

[a] D. L. Gau,+ Dr. E. A. Dalchiele, Dr. R. E. Marotti
Facultad de Ingeniería, Instituto de Física, Universidad de la República, Herrera y Reissig 565, C.C. 30, 11000 Montevideo, Uruguay
E-mail: dgau@fing.edu.uy

[b] Dr. D. Ramírez,+ Dr. G. Riveros, P. Díaz, J. Verdugo, G. Núñez, S. Lizama, P. Lazo
Instituto de Química y Bioquímica, Facultad de Ciencias, Universidad de Valparaíso – Avenida Gran Bretaña 1111, Playa Ancha, 2360102 Valparaíso, Chile
E-mail: daniel.ramirez@uv.cl

[c] Dr. F. Iikawa
Institute of Physics "Gleb Wataghin", University of Campinas, 13083-859 Campinas, São Paulo, Brazil

[d] Dr. L. Contreras, Dr. J. Idigoras, Dr. J. Anta
Área de Química Física, Departamento de Sistemas Físicos, Químicos y Naturales, Universidad Pablo de Olavide, 41013, Sevilla, Spain

[+] These authors contributed equally.

ChemPhysChem

Research Article
doi.org/10.1002/cphc.202200286

**Chemistry
Europe**

European Chemical
Societies Publishing

have been regarded, mainly from car batteries and from perovskite solar cells.[41,42] An interesting perspective is also given by G. Hodes who compared the mass consumption of lead per power unit from a car and a perovskite solar cell thus demonstrating a transition to a less lead-based energy generation similarly to the diminishing of carbon footprint.[43] Taking into account this issue, recently, our group has reported a new method to produce selective contact free $CsPbBr_3$ based solar cells, using an electrochemically assisted method that is both simple, lead waste saving and potentially scalable to fix lead on electrodes compared with other techniques such as spin-coating.[33] Besides, it was also shown that the power conversion efficiencies of the obtained samples are close to the state-of-the-art values, even without the need of using neither electron nor hole transporting layers. Efforts have been made[44–48] to prepare solar cells assisted by electrochemical deposition using different materials. However, scalability experiments to prove this hypothesis for perovskite based solar cells are still lacking.[33] Thus, our results open a field for the study of such fully inorganic perovskites.

Although $CsPbBr_3$ photoelectrodes can work without transporting layers, better performance can be obtained by covering the active film with a bi-functional material that serves as both a protective layer, that prevents the contact with liquid water, and as a charge transporter.[18,49–52] The basic electrochemical properties directly assessed on $FTO/CsPbBr_3$ electrodes immersed in dry liquid electrolytes have been achieved in a few cases including low polarity organic solvents,[53] but its photoelectrochemical features as well as its semiconducting behavior has been scarcely informed compared with its MAPI counterpart.[54]

Thus, this work has two main purposes. First, to show the good optical properties of the $CsPbBr_3$ films obtained by the electrochemically assisted method reported previously, while also analyzing the fundamental properties behind them. Second, and in connection with their optical characterization, to study the semiconducting properties as well as the photoelectrochemical properties of these $CsPbBr_3$ electrodes grown on FTO.[33] Consequently, we will show that there are many potential applications of photoelectrochemical devices in non-aqueous media to carry out either organic synthesis or degradation of organic pollutants taking advantage of the solubility of many organic compounds in low polarity solvents.

Experimental

$CsPbBr_3$ films were grown on FTO substrates according to a novel procedure recently reported by our group.[33] Briefly, PbO_2 was galvanostatically electrodeposited on clean FTO pieces using a fix charge density of $70 \, mC \, cm^{-2}$. Films were converted into $PbBr_2$ through a heterogeneous phase reaction between solid PbO_2 and gaseous HBr in a glass reactor at $250\,°C$ for 10 minutes. After completion, samples were finally converted into orthorhombic $CsPbBr_3$ by spin-coating 0.07 M CsBr in methanol at 3000 rpm followed by annealing at $250\,°C$ for 5 minutes (Figure S1). 10 spin-coating cycles were enough to achieve the full conversion, obtaining a uniform film with optimized stoichiometry as can be

seen in Figures S2 and S3. This film was used for further characterizations presented in this work.

The optical characterization was performed by continuous-wave (CW) and time-resolved (TR) photoluminescence (PL) spectroscopy at different temperatures. For the CW measurements, the samples were cooled from 285 to 30 K in a CTI Cryogenics CRYODYNE cryostat, exciting the sample using a Thorlabs M365FP1 LED (365 nm, 9.8 mW) and collecting the emitted light with an Ocean Optics Flame S-UV-VIS-ES spectrometer. Then, changing the excitation source for a halogen lamp (Ocean-Optics HL 2000) the transmittance T was measured, and from this we calculated the absorptance $\alpha = -\ln T$. Time-resolved PL was carried out using a cold-finger He cryostat, a 371 nm pulsed diode-laser (Hamamatsu, 0.1 ns nominal pulse width) with an average power of $170 \, \mu W$ at 10–20 MHz, and a Streak-Camera (Hamamatsu C4334) coupled with 0.5 m spectrometer (Acton, SpectraPro 2500i).

Electrochemical and photoelectrochemical characterizations were carried out in deaerated 0.1 M Tetrabutylammonium hexafluorophosphate ($TBAPF_6$) in anhydrous dichloromethane (DCM) as background electrolyte at room temperature. Electrochemical (linear sweep voltammetry, cyclic voltammety and capacitance) and photoelectrochemical measurements were carried out with a Gamry Potentiostat/Galvanostat (model G300) and an Autolab potentiostat (model PGSTAT 302 N), respectively. A Pt coil was used as auxiliary electrode and a silver wire immersed in $0.01 \, M \, AgNO_3$ solution prepared in CH_3CN as reference electrode. The latter was daily calibrated using a solution of 5 mM ferrocene and 0.1 M $TBAPF_6$ in DCM and freshly polished glassy carbon as working electrode giving 0.205 ± 0.007 V vs our $Ag/AgNO_3$ electrode. To obtain the electrochemical window where $CsPbBr_3$ was stable with no Faradaic reactions involved, linear sweep voltammetry measurements were carried out using a glass electrochemical cell in the dark. Each potential scan ($50 \, mV \, s^{-1}$) was made with a freshly prepared $CsPbBr_3$ electrode having a single use. Electrochemical impedance measurements were carried out in the potential range where only capacitive current densities were present and at different frequencies using a perturbation amplitude of ± 5 mV from each DC potential value. The electrochemical cell was mounted into a Faraday cage in the dark.

During photoelectrochemical measurements a quartz cell was employed as electrochemical cell and 10 mM p-benzoquinone was chosen as redox target being added to the aforementioned supporting electrolyte. In order to attenuate the optical absorption of the p-benzoquinone solution, each $CsPbBr_3$ electrode was mounted in front of a flat quartz window using a glass cover slip n°1 as spacer, thus giving a nominal distance between the quartz window surface and the electrode surface close to 0.15 mm. A solar simulator LOT (model LS0500) at a calibrated light intensity of AM1.5G $100 \, mW \, cm^{-2}$ (using a Si-based reference solar cell) was utilized as light excitation source. Potentiodynamic (scan rate: $10 \, mV \, s^{-1}$) and potentiostatic experiments were made under chopped light. The potential value chosen for photo-chronoamperometry experiments was selected according to the potentiodynamic profiles.

Results and Discussion

Optical Properties

In Figure 1a and 1b the absorptance and PL spectra of the analyzed sample at 30 K and 285 K are presented. The absorptance spectra show a pronounced excitonic absorption
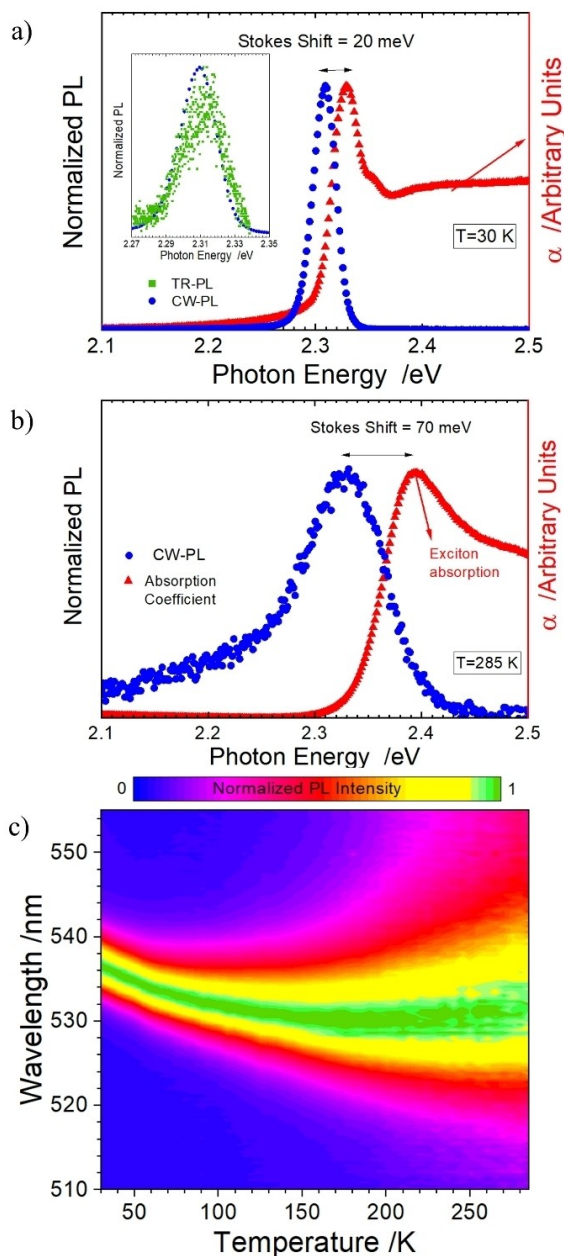
ChemPhysChem

Research Article
doi.org/10.1002/cphc.202200286

**Chemistry
Europe**
European Chemical
Societies Publishing

Figure 1. Absorptance (red triangles) and Normalized PL spectra (CW blue circles and TR green squares) obtained at 30 K a) and at room temperature b). Heat map of temperature dependent normalized PL spectra of a CsPbBr$_3$ film obtained between 285 and 30 K c).

approximately 200 K, and when the temperature was further lowered it red-shifted. This effect can be appreciated in more detail in the inset of Figure 2 (see below), where the position of the maximum in the PL spectra (obtained using a Gaussian fitting) as a function of the temperature is depicted. Two aspects must be considered to explain this behavior. First, the dependence of bandgap energy with temperature in the quasi-harmonic approximation is determined by two competing phenomena with antagonist effects that can be described by equation 1.[55,56]

$$\frac{\partial E_g}{\partial T} = \left(\frac{\partial E_g}{\partial V}\right)\left(\frac{\partial V}{\partial T}\right) + \frac{\partial}{\partial T}\sum_{j,\vec{q}}^{N}\left(\frac{\partial E_g}{\partial n_{j,\vec{q}}}\right)\left(n_{j,\vec{q}} + \frac{1}{2}\right) \tag{1}$$

The first term in this expression describes the effect of lattice expansion on bandgap energy and is determined by the hydrostatics deformation potential $\frac{\partial V}{\partial T}$ and the expansion coefficient $\frac{\partial E_g}{\partial V}$. Lattice expansion tends to increase the bandgap energy when the temperature is increased,[57–61] as observed at low temperatures. On the other hand, the second term -where $n_{j,\vec{q}}$ represents the phonon occupation number in the phonon branch j with wave vector $\vec{q}$- quantifies the interaction of electrons with LO phonons. This interaction is produced by the deformation potential, and results in a decrease on the bandgap energy[56,62] when temperature is increased (although some authors claim the opposite[61]) as observed at high temperature range. Second, the dependence of the Stokes-shift with temperature. In our case this parameter increased from 20 meV at 30 K to 70 meV at room temperature. This effect has already been reported in perovskite samples, and has been attributed to carrier thermalization in the broadened density of states.[59,63,64] Similar dependence of PL spectra with temperature have been reported in other types of materials with the perovskite structure, both in the form of thin films and nanostructures.[65,66] In some of these compounds, discontinuities have also been observed in the results, which are
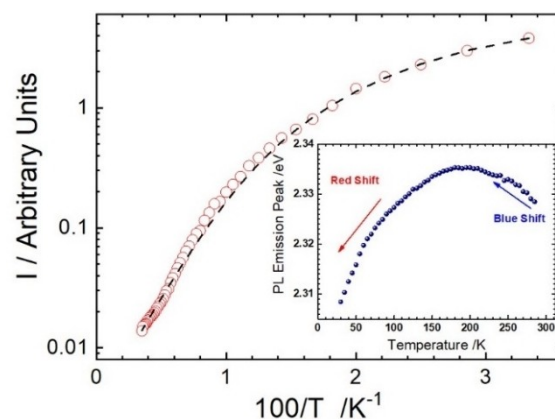
for low energies that red shifts and increases its amplitude when the temperature is lowered. A similar behavior is observed in the PL spectra, that besides moving its maximum to lower energies also becomes more symmetrical and narrower. The PL spectra versus temperature heat map shown in Figure 1c, illustrates the normalized amplitude of the PL spectrum as a function of temperature between 285 and 30 K. All PL spectra present a broad emission band in the visible range and show different behaviour in two temperature ranges. An initial blue-shift of the PL peak from room temperature to

Figure 2. Integral of the PL spectra (*I*) as a function of the temperature: experimental data (red circles) fitting using two activation energies (dashed black). Inset: photon energy of the PL maximum as a function of temperature showing a blue-shift for temperatures above 195 K, and a red shift for temperatures below this value, as the temperature is diminished.

ChemPhysChem

Research Article
doi.org/10.1002/cphc.202200286

**Chemistry
Europe**

European Chemical
Societies Publishing

attributed to phase changes in the crystalline structure. These phase transitions are absent in our CsPbBr$_3$ sample for the temperature range analysed, which is of crucial importance for the manufacture of electronic devices with stable performance.

Each of the CW-PL spectra was fitted using a Gaussian curve, characterized by three parameters, the full width at half maximum (FWHM), the centre of the emission peak, and the integral (area) of the intensity spectra I.

Figure 2 shows the Arrhenius plot of I vs temperature. From this plot the thermal activation energies E_a were obtained using an Arrhenius-like expression (dashed black line in Figure 2) with two activation energies.[63]

$$I(T) = \frac{I_0}{1 + A_1 e^{\frac{-E_{a1}}{k_B T}} + A_2 e^{\frac{-E_{a2}}{k_B T}}} \quad (2)$$

In equation 2 I_0 is the PL intensity at 0 K, k_b is the Boltzmann constant, E_{a1} and E_{a2} are the activation energies, and A_1 and A_2 are constants. In order to obtain a good fit of the model with the data, we had to consider two thermal dissociation channels.[67] This indicates that there are two quenching channels for photoluminescence with activation energies $E_{a1} = 13 \pm 2\ meV$ and $E_{a2} = 39 \pm 5\ meV$. It has been argued that these energies correspond to excitonic states below the free exciton energies.[63] The origin of these states is still under debate, but there is evidence showing that they can be originated in surface states, which strongly influence the photoluminescence properties.[68,69]

Concerning to the temperature dependent FWHM (Γ), the interaction of electrons and phonons can be analysed. These interactions can have three different origins: i) the deformation potential that accounts for the interaction of electrons with optical and acoustic phonons, ii) the piezoelectric effect that can produce the interaction of acoustic phonons with electrons in crystals without a centre of symmetry iii) the Fröhlich interaction which describes the effect of the electric field created by longitudinal optical phonons (LO) in electrons.[56,70,71] The contribution of the different interactions in the PL spectra is highly dependent on temperature since the phonon population is also thermally determined. Thus, the observed broadening of the PL spectra can be fitted using the independent Boson model,[70] also known as Segall's expression (equation 3), which considers three contributions to the broadening.

$$\Gamma(T) = \Gamma_{inh} + \Gamma_{Ac} + \Gamma_{LO} = \Gamma_{inh} + \varphi_{Ac} T + \frac{\varphi_{LO}}{e^{\frac{E_{LO}}{k_B T}} - 1} \quad (3)$$

The first term, Γ_{inh}, is a constant inhomogeneous broadening, which has its origin in crystal disorder. Γ_{Ac} represents the coupling of the electrons with the low energy acoustic phonons, which has a linear behavior. Finally, Γ_{LO} represents the interaction of electrons and longitudinal optical phonons. The bosonic nature of phonons governs the population of the energy states of the system, so the Bose-Einstein distribution must be considered in this last term. Besides that, $E_{LO} = \hbar\omega_{LO}$ is the characteristic phonon energy. After fitting the experimental

data with this model, the obtained values for the parameters were $\Gamma_{inh} = 23 \pm 2\ meV$, $\varphi_{Ac} = 86 \pm 28\ \mu eV/K$ and $E_{LO} = 30 \pm 4\ meV$. Figure 3 shows the result of the fitting and the contribution from the different terms of the Segall's expression. This result indicates that the process is dominated by optical phonons, especially at high temperatures, which is the main cause for the photoluminescence quenching. These results are very similar to those reported by Wolf et al. also working with CsPbBr$_3$ thin films processed at low temperatures.[72]

Finally, the time dependence of the PL spectra from 6 K to 45 K was analyzed. These results were fitted using two exponential decays as shown in equation 4.

$$I(t) = A_1 e^{-\frac{t}{\tau_1}} + A_2 e^{-\frac{t}{\tau_2}} \quad (4)$$

In this expression τ_1 and τ_2 are the characteristic decay times and A_1 and A_2 are constants. These times were calculated using two measurements with time windows of 50 (see Figure S4) and 100 ns. Using the 50 ns (100 ns) a better estimation of the short (long) times can be obtained. The results are shown in the inset of Figure 4 where it can be observed that both times monotonically increase with temperature. It must be addressed that the short times are close to the decay time from the laser pulse width (estimated in 200 ps and shown on the left side of Figure 4) therefore they may be shorter than the reported values. Although the increase of these times with the increase of temperature may seems not to be compatible with the quenching of the luminescence and the increase of FWHM with the increase of temperature, the results are in good agreement with some previous reports on CsPbBr$_3$.[73,74] These results were interpreted as due to exciton fission[73] and the thermal motion of free excitons.[74] However, other reports show mono-exponential decays[75] and also non-monotonic dependence on temperature.[63] Besides that, different functions have
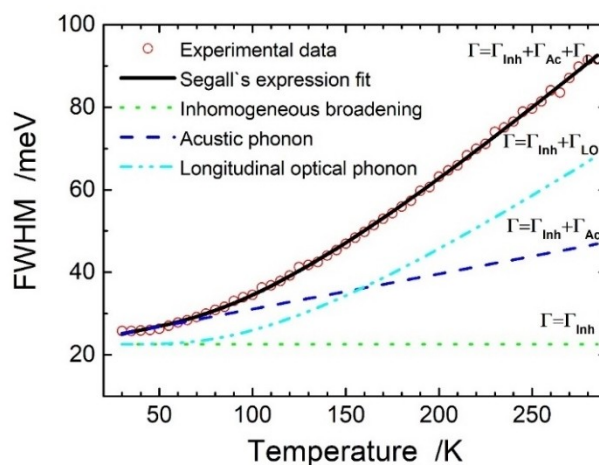

Figure 3. Temperature dependence of the photoluminescence FWHM: experimental data (red circles), Segall's expression fit (solid black) which can be deconvoluted into three contributions: Inhomogeneous broadening (green dots), acoustic phonons (blue dashed) and longitudinal optical phonons (cyan dash-dot dot).
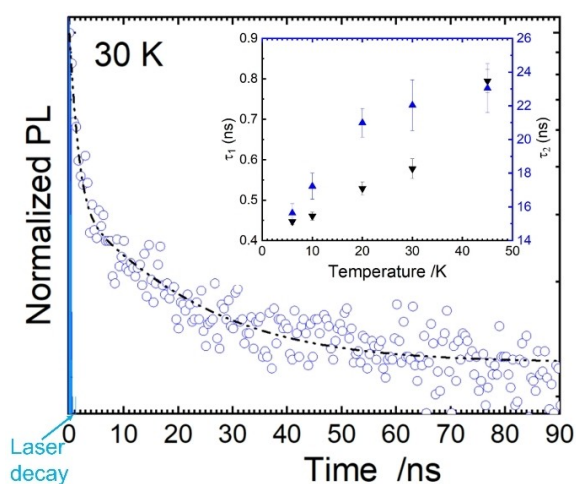
ChemPhysChem

Research Article
doi.org/10.1002/cphc.202200286

Chemistry Europe
European Chemical
Societies Publishing

Figure 4. Temporal dependence of photoluminescence spectra obtained at 30 K (blue circles) fitted with two exponential decays (dash-dot curve). Inset: Temperature dependence of decay times τ_1 (black down triangles) and τ_2 (blue up triangles).

Figure 5. Linear sweep voltammetry of CsPbBr$_3$ samples in 0.1 M TBAPF$_6$ dissolved in CH$_2$Cl$_2$ under Ar ambient. Scan rate: 50 mV s^{-1}. Inset: electrodes photographs taken after polarization was completed. The aspect of the immersed sections after completion of the potential scans are shown within dotted line squares.

been used to fit the data making a direct comparison between the reported decay times very difficult. According to M.J. Trimpl et al[76] the fast initial decay can be explained considering an initial charge-carrier trapping characterized by a short time τ_1. Then, trapping and detrapping processes balance producing a quasi-equilibrium system where PL transients are originated in the recombination of trapped electrons with valence-band holes characterized by time τ_2.

Electrochemical and Photoelectrochemical Properties

The electrochemical window with no Faradaic processes was estimated by assessing the limit for the first oxidation and reduction processes from linear potentiodynamic scans depicted in Figure 5. At positive scans, starting from the open circuit potential value (pointed by the red arrow), the CsPbBr$_3$ electrodes exhibited a current density wave near to +0.7 V with a peak centred at *ca* +1.1 V. At more positive potentials a second wave is also developed. When stopping the polarization at the anodic potential limit and withdrawing the electrode from the cell, it looked bleached as seen in the right-side photograph included in Figure 5. This can be attributed to an irreversible oxidation of one constituent from the CsPbBr$_3$, thus limiting its use to potentials below the onset of the first positive current density wave.

During the negative scan of a new CsPbBr$_3$ electrode, again starting from the open circuit potential, a negative current density wave is developed at a potential near to −1.3 V. Similarly to the anodic scan, when stopping the polarization at the cathodic potential limit and withdrawing the electrode from the electrolyte, a grayish aspect of the CsPbBr$_3$ film is seen as shown in the left-side photograph included in Figure 5. This is also explained by an irreversible process, in this case a reduction involving the perovskite film.
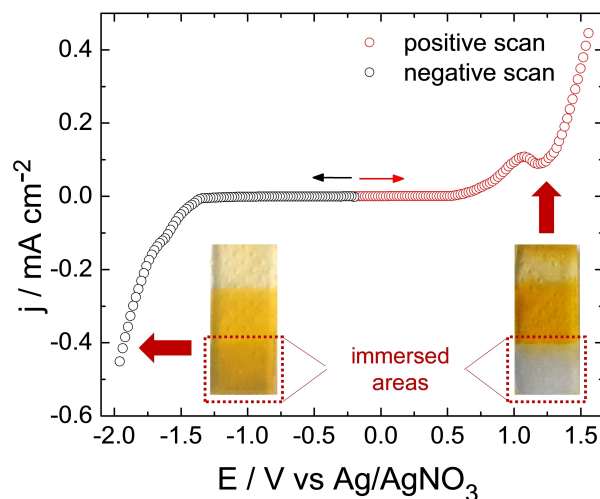
According to these results, a wide electrochemical window close to 2.0 V and with no Faradaic processes is available for EIS measurements. In this window capacitive current densities as high as 1 µA cm^{-2} were measured, in agreement with a criterion of low current densities for capacitive currents.[80,81] Under this condition, it was assumed a simple equivalent electric circuit formed by the electrolyte resistance in series with the semiconductor space charge capacitance for EIS measurements following the recommendations given in reference.[82]

Capacitance measurements of CsPbBr$_3$ electrodes are depicted in Figure 6a as Mott-Schottky plots. The use of frequencies higher than 500 Hz was not possible since Lissajous plots revealed departure from linearity between AC perturbation thus response beyond that frequency was not registered. Measurements carried out in quite similar conditions have been possible in MAPI recognizing its semiconducting behaviour from frequencies as low as 500 Hz to values as high as 5–10 kHz.[79,83,84] This wide frequency domain towards low values for capacitance measurements has also been found in other orthorhombic and defect tolerant photovoltaic materials.[85] From these references it can be noted that the use of different deposition methods on top of different substrates (i.e. spin-coating, drop casting, and spray-coating) leads to different crystallization conditions. It is known that the way of crystallization strongly affects the electrical behavior of photovoltaic perovskites.[86,87] Thus, the physical meaning of this particular response in our samples could be addressed in that direction. Further research focused on different deposition techniques could enlighten the way for understanding this behavior what is out of the scope of this work. To face the impossibility of measuring the capacitance at frequencies higher than 500 Hz, we have measured at frequencies as low as 100 Hz and then analyzed the acceptor density (N_A) and flat band potential (E_{FB}) obtained from these experiments. The slopes of each Mott-
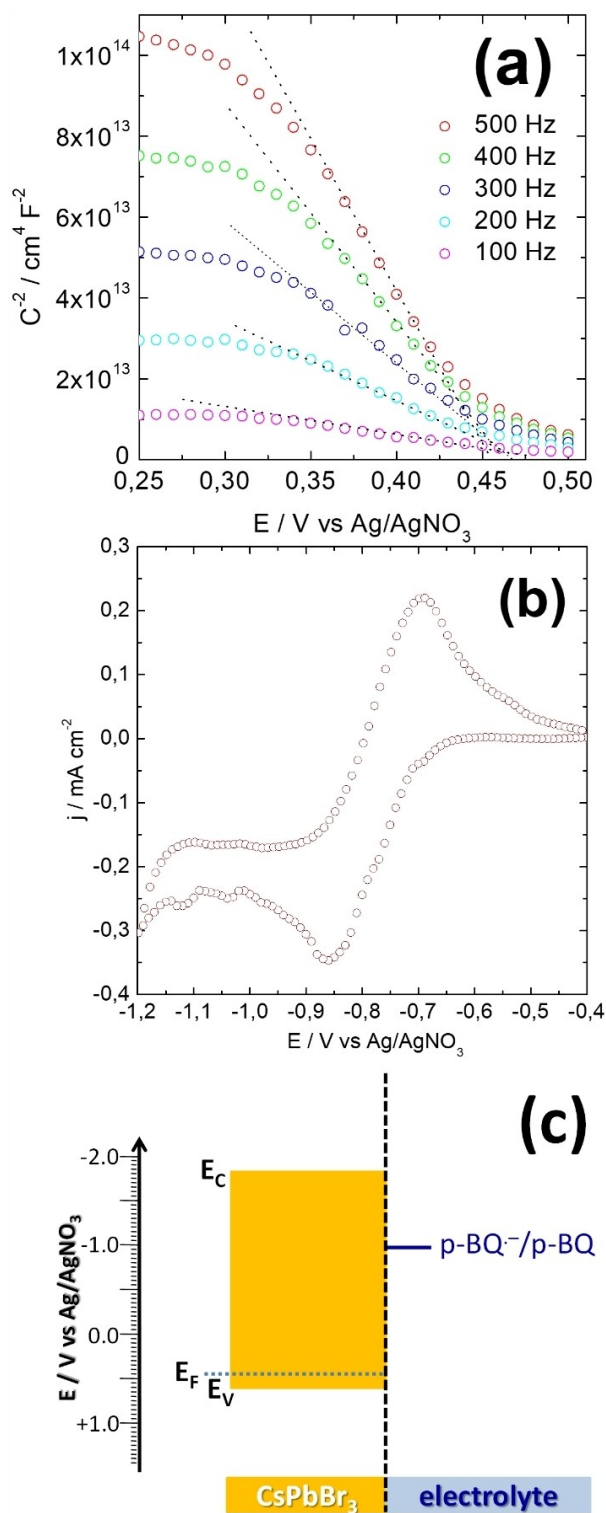
ChemPhysChem

Research Article
doi.org/10.1002/cphc.202200286

Chemistry
Europe
European Chemical
Societies Publishing

Figure 6. Mott-Schottky plots of CsPbBr$_3$ samples measured at different frequencies in 0.1 M TBAPF$_6$ dissolved in DCM (a), cyclic voltamperogram of 10 mM p-BQ + 0.1 M TBAPF$_6$ + Ar in polished glassy carbon. Scan rate: 50 mV s^{-1} (b) and energy level diagram, expressed as potential relative to the Ag/AgNO$_3$ electrode, sketching the CsPbBr$_3$ electrode compared with the redox couple p-BQ·$^-$/p-BQ (c).

Schottky plot were consistent with the p-type behavior of the orthorhombic CsPbBr$_3$ films on FTO substrates. All tested samples presented frequency dispersion as evidenced in previous studies for spin-coated MAPI films.[83] The apparent N_A values were calculated from the Mott-Schottky treatment assuming a relative permittivity for orthorhombic CsPbBr$_3$ of 22,[88] which were found between 1.06×10^{17} and 8.53×10^{15} cm^{-3} spanning from 100 to 500 Hz, respectively. The dispersion in frequency of the as-measured capacitances can be attributed either to a complex electrical response from the semiconductor surface or to a non-constant relative permittivity of the material.[89,90] Further, higher capacitance values obtained at too low frequencies can be influenced not only by the space charge distribution but by other effects such as ion migration. The N_A value obtained at the highest frequency limit employed here is of the same order with the previous results obtained from MAPI electrodes ($\sim 10^{15}$ cm^{-3}).[83,91] The mean E_{FB} obtained from the intercept at zero in the y-axis from the Mott-Schottky plot was 0.47 ± 0.02 V. This small discrepancy of E_{FB} as a function of frequency can be acceptable as reported in MAPI samples and common oxide semiconductors as TiO$_2$ electrodes.[83,89]

Prior to photoelectrochemical measurements of CsPbBr$_3$ electrodes, cyclic voltammetry was carried out of glassy carbon electrodes in 10 mM p-BQ electrolyte (Figure 6b). These experiments make it possible to verify the half-wave potential value, $E_{1/2}$, for the one-electron reduction of p-BQ to its radical anion, being the latter initially absent. The as-obtained value of $E_{1/2}$ equals to -0.767 V and it was used with the E_{FB} value from CsPbBr$_3$ electrodes to build the energy level diagram in the dark depicted in Figure 6c. To obtain the position of the valence band edge, E_V, the approximation given by Domen et col[92] was used. The effective mass of CsPbBr$_3$ considered to our estimations was $0.143\,m_0$, where m_0 is the electron rest mass, according to a previous study.[93] The total density of acceptors, p_0, was approximated to the $N_A = 8.53 \times 10^{15}$ cm^{-3} (obtained at 500 Hz), while the E_g value used was 2.43 eV as reported in our previous work.[33] From this energy band diagram (Figure 6c) it can be clearly predicted the photoelectrochemical reduction of p-BQ using the CsPbBr$_3$ electrodes under solar light illumination and negative potential biased.

The potentiodynamic response of CsPbBr$_3$ electrodes under chopped light using 10 mM p-BQ as redox target also confirmed the p-type behavior of CsPbBr$_3$ (Figure 7a). Photocurrent densities obtained under these conditions are comparable with those obtained from CsPbBr$_3$ nanoparticles using the same target molecule and solvent thus demonstrating the feasibility of polycrystalline CsPbBr$_3$ films to be used in solar-driven processes such as organic reactions.[46] From the linear sweep voltammetry experiment it can be clearly seen that the photoelectrochemical process includes recombination on the whole potential range studied. The photochronoamperogram presented in the inset of Figure 7a was obtained by polarizing the samples at -0.7 V. The shape of these j-t transients matches well with the classical behavior exhibited by p-type semiconductors with hole-electron pair generation, charge transfer and recombination. The data was normalized by using the
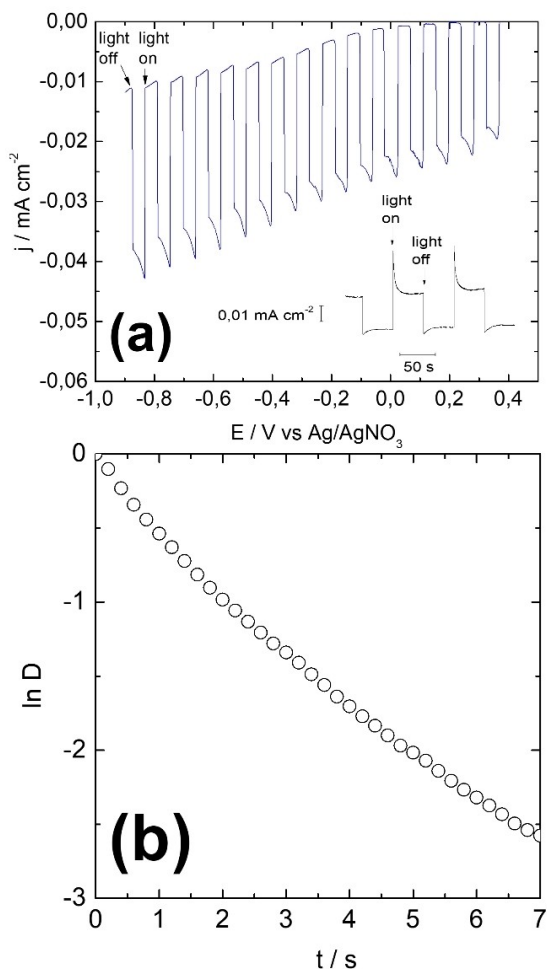
ChemPhysChem

Research Article
doi.org/10.1002/cphc.202200286

**Chemistry
Europe**
European Chemical
Societies Publishing

Figure 7. Potentiodynamic profiles taken at 10 mV s^{-1} (scanned in the negative direction of potential) under chopped light (100 mW cm^{-2}) for orthorhombic CsPbBr$_3$ samples immersed in 10 mM p-BQ + 0.1 M TBAPF$_6$ (a). The inset with scale bars shows a photochronoamperometric response (for simplicity photocurrent densities are presented in an inverted scale) after fixing a potential difference of −0.7 V under chopped light. Normalized plot of the photocurrent-time dependence for data shown in the inset (b).

model proposed by Peter[94] through the ratio (D) given by equation 8.

$$D = \frac{j(t) - j(\infty)}{j(0) - j(\infty)} = e^{-t/\tau} \qquad (8)$$

Where $j(t)$, $j(\infty)$ and $j(0)$ are the current densities at a time t, at the steady-state and instantaneous respectively. The time constant τ equals to $(k_{ct} + k_{rec})^{-1}$ where k_{ct} and k_{rec} are the charge transfer and recombination rate constants respectively. If the only way of recombination considered is that surface mediated, the plot of ln D versus t from the experimental data should be a straight line with a slope equal to $-1/\tau$.[74] The lack of such trend under the experimental conditions is evident from Figure 7b. So, it can be concluded that other mechanism

can dominate the recombination process or even a band edge unpinning can be involved, as recently discussed by Peter and colleagues, thus warrantying further investigation.[96,97] From a qualitative point of view, the ratio between $j(0)$ and $j(\infty)$ (figure 7a), close to 0.45, is indicative of a low efficiency electron transfer from CsPbBr$_3$ to p-BQ. This result is not surprising and proves that recombination in CsPbBr$_3$ is high under different conditions, either on FTO or coupled with more interphases in fully solid-state solar cells.[33,98]

The PL and photoelectrochemical results can be jointly analyzed in function of the fluences calculated from their corresponding excitation sources. The calculated fluence of the PL excitation source was 1.8×10^{16} photons s^{-1} cm^{-2}. This value is in the same order of that calculated from the solar simulator (AM 1.5 spectrum) used in the photoelectrochemical measurements (4.5×10^{16} photons s^{-1} cm^{-2}). Here, only photons with sufficient energy to create mobile electron-hole pairs were considered, that is those with energy higher than that corresponding to the previously determined bandgap (511 nm).[33] On the other hand, very recently Herz and colleagues have proven the short lifetimes of photogenerated carriers (~ns) and the prevalence of monomolecular recombination for polycrystalline CsPbBr$_3$ films grown on quartz at illumination fluences several orders of magnitude higher than those calculated in our experiments.[99] Previous studies have proven that PL quenching in MAPI films grown on transparent conductive oxides (FTO/ITO) is weak and resemble more to films grown on glass/quartz than to those grown on classic electron transporting layers such as TiO$_2$.[100,101] The pronounced quenching obtained on TiO$_2$ confirms the poor charge extraction in the FTO/perovskite interphase. Recombination studies also revealed the prevalence of Schockley-Read-Hall mechanism in this FTO/MAPI interphase as in the case of our recently reported FTO/CsPbBr$_3$/C solar cell.[33,100] Regarding the aforementioned analysis, if it is assumed that CsPbBr$_3$ films grown either on quartz or FTO have similar short carrier lifetimes at room temperature, this feature would not contribute to compensate the usual poor charge collection in FTO/perovskite interphases.[100,102] In fact, carrier lifetimes in the order of microseconds would be necessary to suppress recombination in such interphase thus improving charge collection in FTO.[100] From these evidences, it can also be concluded that the whole recombination process from CW-PL and photochronoamperograms measurements, has a minor contribution of band to band process at room temperature.

Conclusions

The photophysical and photoelectrochemical properties of CsPbBr$_3$ films prepared by a novel electrochemically assisted method on FTO were analyzed. From the temperature dependence of the steady state photoluminescence spectra, it can be concluded that a strong interaction between electrons and LO phonons takes place, especially at high temperatures. This is the main reason for the photoluminescence quenching. The time dependent photoluminescence measurements showed

that photoluminescence transients are characterized by two decay times originated in a fast initial charge carrier trapping followed by recombination of trapped electrons with valence band holes. These decay times increase with temperature. Besides that, electrochemical stability was found to be closer to state-of-the-art $CsPbBr_3$ showing a p-type behavior under depletion regime. Further, photoelectrochemical activity revealed the potential of polycrystalline films for organic charge transfer reactions. The analysis of photocurrent transients revealed that recombination process is more complex than a one only surface mediated with low band to band recombination in agreement with PL emission at room temperature. This novel method of deposition can be suitable to explore scalable production of $CsPbBr_3$ films, thus avoiding the excess of toxic lead waste without loss of quality.

Author Contributions

Daniel L. Gau: Performed the absorption and photoluminescence experiments and the related data analysis and results interpretations. Daniel Ramírez: Performed the electrochemical impedance measurements and the related data analysis and results interpretations. Fernando Iikawa: Gave guidance for the time resolved PL experiments and helped in the interpretation of the results. Gonzalo Riveros: Tune-up of electrochemical and optical setup for electrochemical and photoelectrochemical measurements together with discussion of results for the manuscript. Patricia Díaz: Tune-up the protocol to prepare samples during each step. Javier Verdugo: Tune-up the protocol to prepare samples during each step. Gerard Núñez: Tune-up the protocol to prepare PbO_2 samples. Susy Lizama: Tune-up the protocol to prepare PbO_2 samples. Pamela Lazo: Tune-up of optical setup for electrochemical and photoelectrochemical measurements together with discussion of results for the manuscript. Enrique, A. Dalchiele: Gave valuable guidance for tuning-up the preparation of samples during each step and in the interpretation of the PL results to give overall consistency to the manuscript. Lidia Contreras: Gave guidance in the interpretation of the photoelectrochemical and PL results as in the overall consistency of the manuscript. Jesús Idígoras: Gave guidance to tune-up the conversion of $PbBr_2$ films into $CsPbBr_3$. Juan Anta: Gave valuable guidance in the interpretation of the photoelectrochemical and PL results as in the overall consistency of the manuscript. Ricardo E. Marotti: Gave guidance for the steady state PL experiments and helped in the interpretation of the results. DLG and DR wrote the first version of the manuscript.

Acknowledgements

Conflict of Interest

The authors declare no conflict of interest.

Data Availability Statement

The data that support the findings of this study are available from the corresponding author upon reasonable request.

[1] A. Kojima, K. Teshima, Y. Shirai, T. Miyasaka, *J. Am. Chem. Soc.* **2009**, *131*, 6050.
[2] M. A. Green, E. D. Dunlop, J. Hohl-Ebinger, M. Yoshita, N. Kopidakis, A. W. Y. Ho-Baillie, *Prog. Photovoltaics* **2019**, *28*.
[3] X. Di, Z. Hu, J. Jiang, M. He, L. Zhou, W. Xiang, X. Liang, *Chem. Commun.* **2017**, *53*, 11068.
[4] X. Zhang, W. Wang, B. Xu, S. Liu, H. Dai, D. Bian, S. Chen, K. Wang, X. W. Sun, *Nano Energy* **2017**, *37*, 40.
[5] Z. Xiao, R. A. Kerner, L. Zhao, N. L. Tran, K. M. Lee, T.-W. Koh, G. D. Scholes, B. P. Rand, *Nat. Photonics* **2017**, *11*, 108.
[6] C.-Y. Huang, C. Zou, C. Mao, K. L. Corp, Y.-C. Yao, Y.-J. Lee, C. W. Schlenker, A. K. Y. Jen, L. Y. Lin, *ACS Photonics* **2017**, *4*, 2281.
[7] Y. Xu, Q. Chen, C. Zhang, R. Wang, H. Wu, X. Zhang, G. Xing, W. W. Yu, X. Wang, Y. Zhang, M. Xiao, *J. Am. Chem. Soc.* **2016**, *138*, 3761.
[8] H. Zhu, Y. Fu, F. Meng, X. Wu, Z. Gong, Q. Ding, M. V. Gustafsson, M. T. Trinh, S. Jin, X. Y. Zhu, *Nat. Mater.* **2015**, *14*, 636.
[9] A. S. Polushkin, E. Y. Tiguntseva, A. P. Pushkarev, S. V. Makarov, *Nat. Photonics* **2020**, *9*, 599.
[10] X. Hu, X. Zhang, L. Liang, J. Bao, S. Li, W. Yang, Y. Xie, *Adv. Funct. Mater.* **2014**, *24*, 7373.
[11] V. Adinolfi, O. Ouellette, M. I. Saidaminov, G. Walters, A. L. Abdelhady, O. M. Bakr, E. H. Sargent, *Adv. Mater.* **2016**, *28*, 7264.
[12] J. Yu, X. Chen, Y. Wang, H. Zhou, M. Xue, Y. Xu, Z. Li, C. Ye, J. Zhang, P. A. Van Aken, *J. Mater. Chem. C* **2016**, *4*, 7302.
[13] C. C. Stoumpos, C. D. Malliakas, J. A. Peters, Z. Liu, M. Sebastian, J. Im, T. C. Chasapis, A. C. Wibowo, D. Y. Chung, A. J. Freeman, B. W. Wessels, M. G. Kanatzidis, *Cryst. Growth Des.* **2013**, *13*, 2722.
[14] Y.-F. Xu, M.-Z. Yang, B.-X. Chen, X.-D. Wang, H.-Y. Chen, D.-B. Kuang, C.-Y. Su, *J. Am. Chem. Soc.* **2017**, *139*, 5660.
[15] J. Hou, S. Cao, Y. Wu, Z. Gao, F. Liang, Y. Sun, Z. Lin, L. Sun, *Chem. Eur. J.* **2017**, *23*, 9481.
[16] S. Shyamal, S. K. Dutta, N. Pradhan, *J. Phys. Chem. Lett.* **2019**, *10*, 7965.
[17] G. F. Samu, R. A. Scheidt, G. Zaiats, P. V. Kamat, C. Janáky, *Chem. Mater.* **2018**, *30*, 4202.
[18] L.-F. Gao, W.-J. Luo, Y.-F. Yao, Z.-G. Zou, *Chem. Commun.* **2018**, *54*, 11459.
[19] P. Da, M. Cha, L. Sun, Y. Wu, Z.-S. Wang, G. Zheng, *Nano Lett.* **2015**, *15*, 3452.
[20] M. T. Hoang, N. D. Pham, J. H. Han, J. M. Gardner, I. Oh, *ACS Appl. Mater. Interfaces* **2016**, *8*, 11904.
[21] M. Crespo-Quesada, L. M. Pazos-Outón, J. Warnan, M. F. Kuehnel, R. H. Friend, E. Reisner, *Nat. Commun.* **2016**, *7*, 12555.
[22] S. Nam, C. T. K. Mai, I. Oh, *ACS Appl. Mater. Interfaces* **2018**, *10*, 14659.

ChemPhysChem

Research Article
doi.org/10.1002/cphc.202200286

Chemistry
Europe
European Chemical
Societies Publishing

[23] Y. Zhu, X. Tong, H. Song, Y. Wang, Z. Qiao, D. Qiu, J. Huang, Z. Lu, *Dalton Trans.* **2018**, *47*, 10057.

[24] D. Cardenas-Morcoso, A. F. Gualdrón-Reyes, A. B. Ferreira Vitoreti, M. García-Tecedor, S. J. Yoon, M. Solis de la Fuente, I. Mora-Seró, S. Gimenez, *J. Phys. Chem. Lett.* **2019**, *10*, 630.

[25] M. Kulbak, D. Cahen, G. Hodes, *J. Phys. Chem. Lett.* **2015**, *6*, 2452.

[26] M. Kulbak, S. Gupta, N. Kedem, I. Levine, T. Bendikov, G. Hodes, D. Cahen, *J. Phys. Chem. Lett.* **2016**, *7*, 167.

[27] J. Duan, Y. Zhao, B. He, Q. Tang, *Angew. Chem. Int. Ed.* **2018**, *57*, 3787.

[28] J. Liang, C. Wang, Y. Wang, Z. Xu, Z. Lu, Y. Ma, H. Zhu, Y. Hu, C. Xiao, X. Yi, *J. Am. Chem. Soc.* **2016**, *138*, 15829.

[29] X. Chang, W. Li, L. Zhu, H. Liu, H. Geng, S. Xiang, J. Liu, H. Chen, *ACS Appl. Mater. Interfaces* **2016**, *8*, 33649.

[30] R. E. Beal, D. J. Slotcavage, T. Leijtens, A. R. Bowring, R. A. Belisle, W. H. Nguyen, G. F. Burkhard, E. T. Hoke, M. D. McGehee, *J. Phys. Chem. Lett.* **2016**, *7*, 746.

[31] L. Protesescu, S. Yakunin, M. I. Bodnarchuk, F. Krieg, R. Caputo, C. H. Hendon, *Nano Lett.* **2015**, *15*, 3692.

[32] D. Fröhlich, K. Heidrich, H. Künzel, G. Trendel, J. Treusch, *J. Lumin.* **1979**, *18*, 385.

[33] D. Ramírez, G. Riveros, P. Díaz, J. Verdugo, G. Núñez, S. Lizama, P. Lazo, E. A. Dalchiele, D. L. Gau, R. E. Marotti, J. A. Anta, L. Contreras-Bernal, A. Riquelme, J. Idigoras, *ChemElectroChem* **2020**, *7*, 3961.

[34] M. I. Saidaminov, M. A. Haque, J. Almutlaq, S. Sarmah, X. Miao, R. Begum, A. A. Zhumekenov, I. Dursun, N. Cho, B. Murali, *Adv. Opt. Mater.* **2017**, *5*, 1600704.

[35] A. F. Akbulatov, L. A. Frolova, N. N. Dremova, I. Zhidkov, V. M. Martynenko, S. A. Tsarev, S. Y. Luchkin, E. Z. Kurmaev, S. M. Aldoshin, K. J. Stevenson, P. A. Troshin, *J. Phys. Chem. Lett.* **2020**, *11*, 333.

[36] B. Li, Y. Zhang, L. Zhang, L. Yin, *J. Power Sources* **2017**, *360*, 11.

[37] H. Guo, Y. Pei, J. Zhang, C. Cai, K. Zhou, Y. Zhu, *J. Mater. Chem. C* **2019**, *7*, 11234.

[38] X. Zhang, H. Wang, Y. Hu, Y. Pei, S. Wang, Z. Shi, V. L. Colvin, S. Wang, Y. Zhang, W. W. Yu, *J. Phys. Chem. Lett.* **2019**, *10*, 1750.

[39] A. Babayigit, A. Ethirajan, M. Muller, B. Conings, *Nat. Mater.* **2016**, *15*, 247.

[40] N. K. Noel, S. D. Stranks, A. Abate, C. Wehrenfennig, S. Guarnera, A.-A. Haghighirad, A. Sadhanala, G. E. Eperon, S. K. Pathak, M. B. Johnston, *Energy Environ. Sci.* **2014**, *7*, 3061.

[41] A. Binek, M. L. Petrus, N. Huber, H. Bristow, Y. Hu, T. Bein, P. Docampo, *ACS Appl. Mater. Interfaces* **2016**, *8*, 12881.

[42] L. Xie, Q. Zeng, Q. Li, S. Wang, L. Li, Z. Li, F. Liu, X. Hao, F. Hao, *J. Phys. Chem. Lett.* **2021**, *12*, 9595.

[43] G. Hodes, *Science* **2013**, *342*, 317.

[44] L. Deligianni, S. Ahmed, L. T. Romankiw, *Electrochem. Soc. Interface* **2011**, *20*, 47.

[45] S. Taunier, J. Sicx-Kurdi, P. P. Grand, A. Chomont, O. Ramdani, L. Parissi, P. Panheleux, N. Naghavi, C. Hubert, M. Ben-Farah, J. P. Fauvarque, J. Connolly, O. Roussel, P. Mogensen, E. Mahé, J. F. Guillemoles, D. Lincot, O. Kerrec, *Thin Solid Films* **2005**, *480–481*, 526.

[46] F. De Rossi, T. M. Brown, A. Reale, A. Di Carlo, *IEEE J. Photovolt.* **2014**, *4*, 1552.

[47] M. Gurulakshmi, A. Meenakshamma, G. Siddeswaramma, K. Susmitha, Y. P. Venkata Subbaiah, T. Narayana, M. Raghavender, *Sol. Energy* **2020**, *199*, 447.

[48] F. Bittner, T. Oekermann, M. Wark, *Mater.* **2018**, *11*, 232.

[49] J. Liang, D. Chen, X. Yao, K. Zhang, F. Qu, L. Qin, Y. Huang, J. Li, *Small* **2020**, *16*, 1903398.

[50] R. Tang, S. Zhou, H. Li, R. Chen, L. Zhang, L. Yin, *Appl. Catal. B* **2020**, *265*, 118583.

[51] J.-F. Liao, Y.-F. Xu, X.-D. Wang, H.-Y. Chen, D.-B. Kuang, *ACS Appl. Mater. Interfaces* **2018**, *10*, 42301.

[52] I. Poli, U. Hintermair, M. Regue, S. Kumar, E. V. Sackville, J. Baker, T. M. Watson, S. Eslava, P. J. Cameron, *Nat. Commun.* **2019**, *10*, 2097.

[53] R. A. Scheidt, G. F. Samu, C. Janáky, P. V. Kamat, *J. Am. Chem. Soc.* **2018**, *140*, 86.

[54] M.-Z. Yang, Y.-F. Xu, J.-F. Liao, X.-D. Wang, H.-Y. Chen, D.-B. Kuang, *J. Mater. Chem. A* **2019**, *7*, 5409.

[55] M. Cardona, *Solid State Commun.* **2005**, *133*, 3.

[56] R. Saran, A. Heuer-Jungemann, A. G. Kanaras, R. J. Curry, *Adv. Opt. Mater.* **2017**, *5*, 1700231.

[57] B. J. Foley, D. L. Marlowe, K. Sun, W2 A. Saidi, L. Scudiero, M. C. Gupta, J. J. Choi, in *Appl. Phys. Lett.*, AIChE, **2015**, pp. 581–586.

[58] J. M. Frost, K. T. Butler, F. Brivio, C. H. Hendon, M. Van Schilfgaarde, A. Walsh, *Nano Lett.* **2014**, *14*, 2584.

[59] S. Singh, C. Li, F. Panzer, K. L. Narasimhan, A. Graeser, T. P. Gujar, A. Köhler, M. Thelakkat, S. Huettner, D. Kabra, *J. Phys. Chem. Lett.* **2016**, *7*, 3014.

[60] C. Yu, Z. Chen, J. Wang, W. Pfenninger, N. Vockic, J. T. Kenney, K. Shum, *J. Appl. Phys.* **2011**, *110*, 063526.

[61] A. Francisco-López, B. Charles, O. J. Weber, M. I. Alonso, M. Garriga, M. Campoy-Quiles, M. T. Weller, A. R. Goñi, *J. Phys. Chem. Lett.* **2019**, *10*, 2971.

[62] W. Wu, W. Liu, Q. Wang, Q. Han, Q. Yang, *J. Alloys Compd.* **2019**, *787*, 165.

[63] A. Dey, P. Rathod, D. Kabra, *Adv. Opt. Mater.* **2018**, *6*, 1800109.

[64] A. Patanè, A. Levin, A. Polimeni, L. Eaves, P. C. Main, M. Henini, G. Hill, *Phys. Status Solidi* **2001**, *224*, 41.

[65] F. Ruf, M. F. Aygüler, N. Giesbrecht, B. Rendenbach, A. Magin, P. Docampo, H. Kalt, M. Hetterich, *APL Mater.* **2019**, *7*, 31113.

[66] F. Ruf, A. Magin, M. Schultes, E. Ahlswede, H. Kalt, M. Hetterich, *Appl. Phys. Lett.* **2018**, *112*, 83902.

[67] D. Bimberg, M. Sondergeld, E. Grobe, *Phys. Rev. B* **1971**, *4*, 3451.

[68] F. Gabelloni, F. Biccari, G. Andreotti, D. Balestri, S. Checcucci, A. Milanesi, N. Calisi, S. Caporali, A. Vinattieri, *Opt. Mater. Express* **2017**, *7*, 4367.

[69] B. A. Koscher, J. K. Swabeck, N. D. Bronstein, A. P. Alivisatos, *J. Am. Chem. Soc.* **2017**, *139*, 6566.

[70] S. Rudin, T. L. Reinecke, B. Segall, *Phys. Rev. B* **1990**, *42*, 11218.

[71] X. B. Zhang, T. Taliercio, S. Kolliakos, P. Lefebvre, *J. Phys. Condens. Matter* **2001**, *13*, 7053.

[72] C. Wolf, T.-W. Lee, *Mater. Today* **2018**, *7*, 199.

[73] B. T. Diroll, H. Zhou, R. D. Schaller, *Adv. Funct. Mater.* **2018**, *28*, 1800945.

[74] X. Lao, Z. Yang, Z. Su, Z. Wang, H. Ye, M. Wang, X. Yao, S. Xu, *Nanoscale* **2018**, *10*, 9949.

[75] K. Wei, Z. Xu, R. Chen, X. Zheng, X. Cheng, T. Jiang, *Opt. Lett.* **2016**, *41*, 3821.

[76] M. J. Trimpl, A. D. Wright, K. Schutt, L. R. V. Buizza, Z. Wang, M. B. Johnston, H. J. Snaith, P. Müller-Buschbaum, L. M. Herz, *Adv. Funct. Mater.* **2020**, *30*, 2004312.

[77] J. T. Mulder, I. Du Fossé, M. Alimoradi Jazi, L. Manna, A. J. Houtepen, *ACS Energy Lett.* **2021**, *6*, 2519.

[78] P. W. Atkins, *Physical chemistry*, Oxford Univ. Press. Oxford **1998**, p. 806.

[79] G. F. Samu, R. A. Scheidt, P. V. Kamat, C. Janáky, *Chem. Mater.* **2018**, *30*, 561.

[80] D. Ramírez, G. Riveros, K. Álvarez, B. González, C. J. Pereyra, E. A. Dalchiele, R. E. Marotti, D. Ariosa, F. Martín, J. R. Ramos-barrado, *Mater. Sci. Semicond. Process.* **2017**, *68*, 226.

[81] J. Rousset, E. Saucedo, D. Lincot, *Chem. Mater.* **2009**, *21*, 534.

[82] A. Hankin, F. E. Bedoya-Lora, J. C. Alexander, A. Regoutz, G. H. Kelsall, *J. Mater. Chem. A* **2019**, *7*, 26162.

[83] H.-Y. Hsu, L. Ji, H. S. Ahn, J. Zhao, E. T. Yu, A. J. Bard, *J. Am. Chem. Soc.* **2015**, *137*, 14758.

[84] A. Guerrero, E. J. Juarez-Perez, J. Bisquert, I. Mora-Sero, G. Garcia-Belmonte, *Appl. Phys. Lett.* **2014**, *105*, 133902.

[85] D. Tiwari, F. Cardoso-Delgado, D. Alibhai, M. Mombrú, D. J. Fermín, *ACS Appl. Energ. Mater.* **2019**, *2*, 3878.

[86] I. Mora-Seró, *Joule* **2018**, *2*, 585.

[87] S. Ravishankar, S. Gharibzadeh, C. Roldán-Carmona, G. Grancini, Y. Lee, M. Ralaiarisoa, A. M. Asiri, N. Koch, J. Bisquert, M. K. Nazeeruddin, *Joule* **2018**, *2*, 788.

[88] S. Govinda, B. P. Kore, M. Bokdam, P. Mahale, A. Kumar, S. Pal, B. Bhattacharyya, J. Lahnsteiner, G. Kresse, C. Franchini, A. Pandey, D. D. Sarma, *J. Phys. Chem. Lett.* **2017**, *8*, 4113.

[89] S. P. Harrington, T. M. Devine, *J. Electrochem. Soc.* **2008**, *155*, C381.

[90] A. Hankin, F. E. Bedoya-Lora, J. C. Alexander, A. Regoutz, G. H. Kelsall, *J. Mater. Chem. A* **2019**, *7*, 26162.

[91] Z. Li, C. C. Mercado, M. Yang, E. Palay, K. Zhu, *Chem. Commun.* **2017**, *53*, 2467.

[92] A. Ishikawa, T. Takata, J. N. Kondo, M. Hara, H. Kobayashi, K. Domen, *J. Am. Chem. Soc.* **2002**, *124*, 13547.

[93] Y. Kang, S. Han, *Phys. Rev. Appl.* **2018**, *10*, 044013.

[94] L. M. Peter, in *Dynamic Aspects of Semiconductor Photoelectrochemistry* (Ed.: M. Schiavello), Springer Netherlands, Dordrecht, **1988**, pp. 243–273.

[95] L. M. Abrantes, L. M. Peter, *J. Electroanal. Chem.* **1983**, *150*, 593.

[96] L. M. Peter, A. B. Walker, T. Bein, A. G. Hufnagel, I. Kondofersky, *J. Electroanal. Chem.* **2020**, *872*, 114234.

[97]   Gurudayal, L. M. Peter, L. H. Wong, F. F. Abdi, *ACS Appl. Mater. Interfaces* **2017**, *9*, 41265.

[98] L. Contreras-Bernal, S. Ramos-Terrón, A. Riquelme, P. P. Boix, J. Idígoras, I. Mora-Seró, J. A. Anta, *J. Mater. Chem. A* **2019**, *7*, 12191.

[99] S. G. Motti, F. Krieg, A. J. Ramadan, J. B. Patel, H. J. Snaith, M. V. Kovalenko, M. B. Johnston, L. M. Herz, *Adv. Funct. Mater.* **2020**, *30*, 1909904.

[100] Y. Wang, Z. Hu, C. Gao, C. Yang, H. Zhang, J. Zhang, X. Zhou, Y. Zhu, *ACS Appl. Electron. Mater.* **2019**, *1*, 2334.

[101] Q. Han, J. Ding, Y. Bai, T. Li, J. Y. Ma, Y. X. Chen, Y. Zhou, J. Liu, Q. Q. Ge, J. Chen, J. T. Glass, M. J. Therien, J. Liu, D. B. Mitzi, J. S. Hu, *Chem* **2018**, *4*, 2405.

[102] W. Ke, G. Fang, J. Wan, H. Tao, Q. Liu, L. Xiong, P. Qin, J. Wang, H. Lei, G. Yang, M. Qin, X. Zhao, Y. Yan, *Nat. Commun.* **2015**, *6*, 1.

A detailed analysis of the photo-physical and photoelectrochemical properties of CsPbBr$_3$ films electro-chemically grown through a novel technique on fluorine-doped tin oxide is presented. An analysis of the low-temperature photoluminescence spectra reveals a strong interaction between electrons and longitudinal optical phonons.
(Photo)electrochemical analysis proves that CsPbBr$_3$ shows a p-type and recombinative behavior close to that of state-of-the-art methods to prepare CsPbBr$_3$.
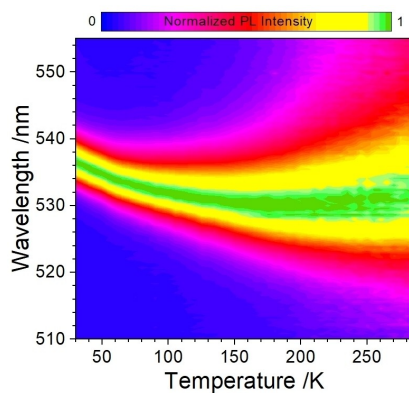
D. L. Gau*, Dr. D. Ramírez*, Dr. F. Iikawa, Dr. G. Riveros, P. Díaz, J. Verdugo, G. Núñez, S. Lizama, P. Lazo, Dr. E. A. Dalchiele, Dr. L. Contreras, Dr. J. Idigoras, Dr. J. Anta, Dr. R. E. Marotti

1 – 11

Photophysical and Photoelectro-chemical Properties of CsPbBr$_3$ Films Grown by Electrochemically Assisted Deposition

ChemPhysChem

Supporting Information

Photophysical and Photoelectrochemical Properties of CsPbBr$_3$ Films Grown by Electrochemically Assisted Deposition

Daniel L. Gau[+],* Daniel Ramírez[+],* Fernando Iikawa, Gonzalo Riveros, Patricia Díaz, Javier Verdugo, Gerard Núñez, Susy Lizama, Pamela Lazo, Enrique A. Dalchiele, Lidia Contreras, Jesús Idigoras, Juan Anta, and Ricardo E. Marotti

$$PbO_{2(s)}+4HBr_{(g)} \rightarrow PbBr_{2(s)}+2H_2O_{(g)}+Br_{2(g)}$$

$250°C - 5$ min.

**PbO$_2$ conversion
to PbBr$_2$**

FTO

**PbO$_2$
Electrodeposition
(Lead fixation)**

**PbBr$_2$ conversion
to CsPbBr$_3$**

$$Pb^{2+}_{(aq)}+H_2O_{(l)} \rightarrow PbO_{2(s)}+4H^+_{(aq)}+2e^-$$
$$Q = 70 \text{ mC cm}^{-2}$$

$$PbBr_2+CsBr \rightarrow CsPbBr_3$$
(10 spin-coating cycles)
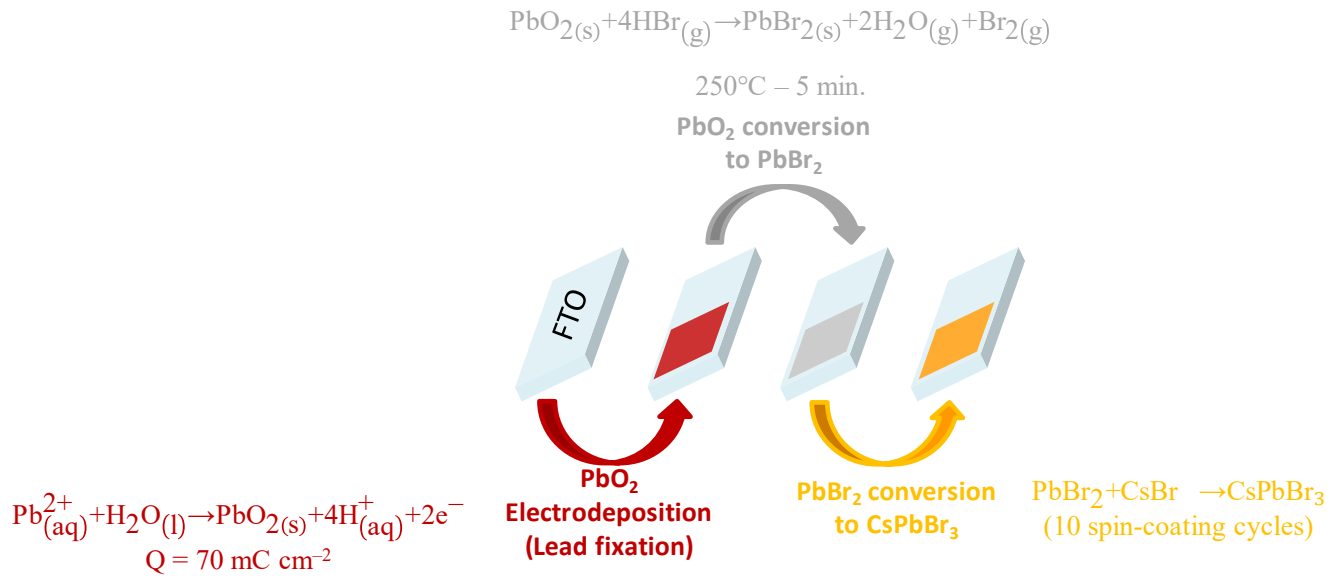
Fig. S1. Sketching for the CsPbBr$_3$ reaction including the fundamental reactions involved during the whole process.

1 µm	EHT = 2.00 kV	Signal A = InLens	ESB Grid = 2 V	29 May 2019
	WD = 3.8 mm	Mag = 12.91 K X	D_01.tif	1.48e-006 Torr STEM Seg. Mode = ODF + BF
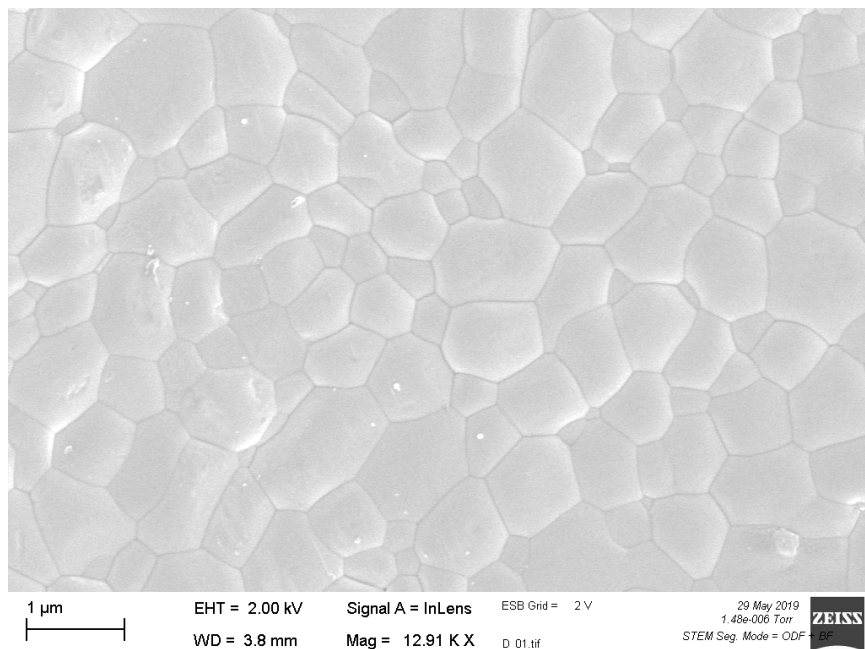
Fig. S2. FE-SEM image for CsPbBr$_3$ prepared after 10 cycles of spin-coating with CsBr dissolved in methanol. The image was taken using a Zeiss Gemini SEM-300 microscope.
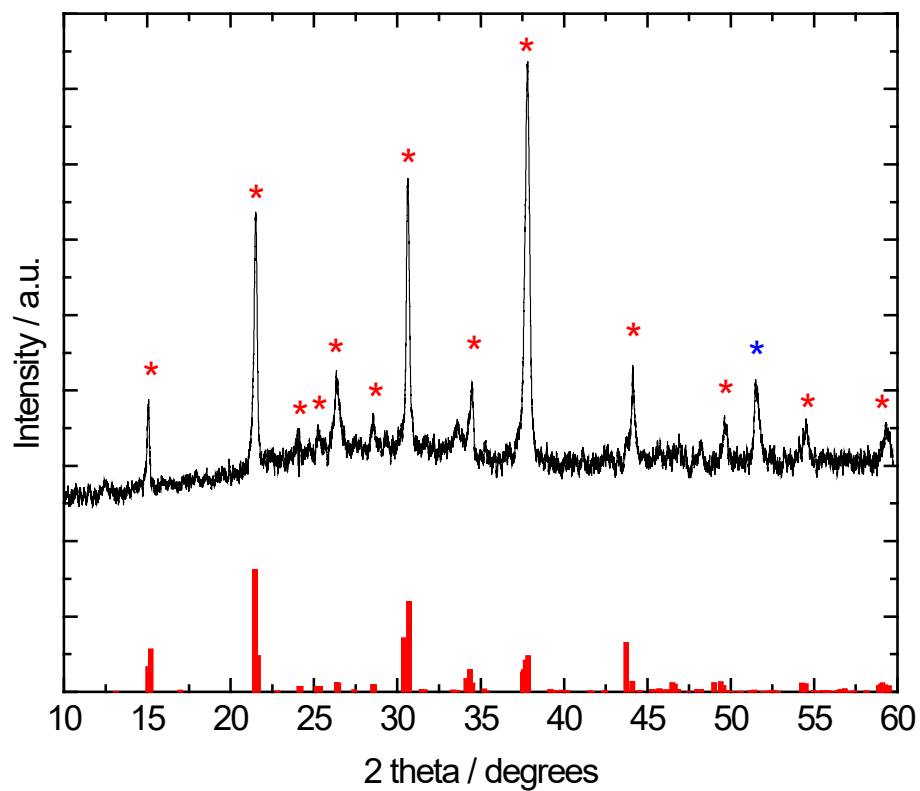
Fig. S3. XRD data for a CsPbBr$_3$ film prepared after 10 cycles of spin-coating with CsBr dissolved in methanol followed by annealing at 250°C. Orthorhombic CsPbBr$_3$ pattern is also shown. CsPbBr$_3$ and FTO substrate phases are indicated by red and blue asterisks respectively. The measurement was performed in a Philips PW180 diffractometer (30 kV, 40 mA, CuKα radiation with λ = 1.5406 Å).
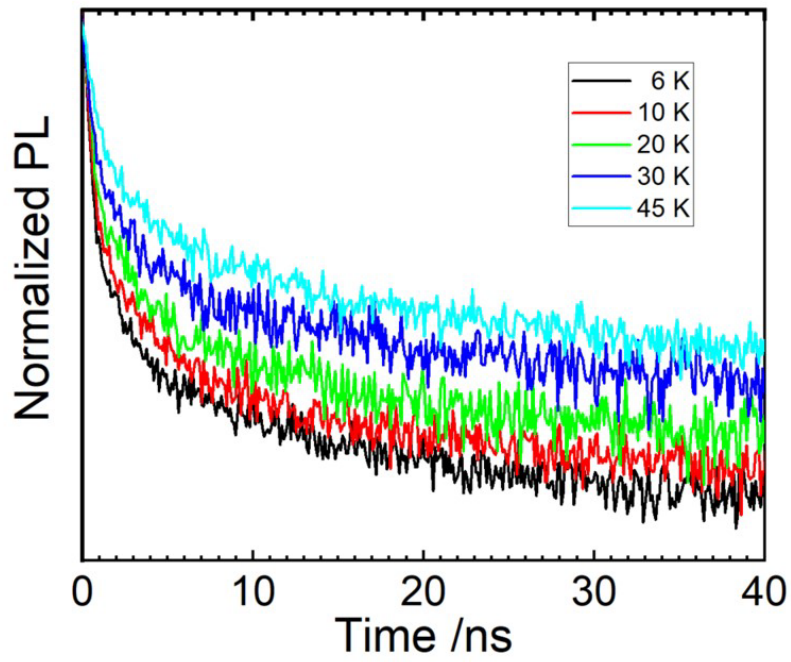
Fig. S4: Temperature dependence of PL decay for the 50 ns time window.

Full Length Article

Origin of photoluminescence and experimental determination of exciton binding energy, exciton-phonon interaction, and urbach energy in γ-CsPbI₃ nanoparticles

Daniel L. Gau [a],[*], Isabel Galain [b], Ivana Aguiar [b], Ricardo E. Marotti [a]

[a] *Facultad de Ingeniería, Instituto de Física, Universidad de la República, Herrera y Reissig 565, C.C. 30, 11000 Montevideo, Uruguay*
[b] *Área de Radioquímica, Facultad de Química, Universidad de la República, Av. General Flores 2124, Montevideo, Uruguay*

ABSTRACT

Recently inorganic perovskites have had a deep impact in perovskites-based devices allowing the fabrication of high efficiency and high stability devices. To continue with the development of these technologies a detailed study of the optoelectronic properties of these materials is necessary since this is a fundamental tool for the design of new and more efficient devices. In the present work, the optical properties of γ-CsPbI₃ nanoparticles are studied using temperature dependent spectroscopic techniques of transmittance and photoluminescence. The absorption spectrum shows a marked excitonic behavior especially at low temperatures. Analyzing this spectrum with the Elliot function the evolution with temperature of the bandgap energy and the exciton binding energy is studied. From the evolution of the shape of the excitonic peak, both in the absorption and photoluminescence, we determined the excitonic recombination nature of photoluminescence and exciton-phonon interaction energy. Once proven the excitonic nature of photoluminescence we prove that the Stokes Shift has its origin in excitonic thermalization. Finally, analyzing the low energy region of the absorption spectrum the Urbach energy was determined. The obtained values, which are very low for solution processed nanoparticles, indicates that the nanoparticles present excellent crystallinity.

1. Introduction

In the last decade, what seems to be the next step in the evolution of solar cells has emerged with the advent of perovskite based solar cells. These devices have had an outstanding increase in their energy conversion efficiency, which jumped from 3.8% [1] to over 25% [2] in a bit more than a decade. The devices responsible for this unprecedented improvement are generally based in hybrid organic-inorganic absorbing layers. The presence of organic components, usually CH_3NH_3, introduce instabilities [3] given by external factors as high temperature [4], electric fields [5,6], moisture [7,8], UV radiation [9–11] and photo-oxidation [12,13]. These instabilities, common in real life operation of solar cells, are nowadays seen as a major bottleneck in the implementation of commercial perovskite-based technologies [4, 14–18]. Despite a huge improvement in stability has been achieved [19] devices available today are far from the objective of a marketable device.

The previously mentioned limiting factors have drawn the attention to inorganic perovskites since it is expected that the inorganic absorbers can increase the stability of photovoltaic devices [20–22]. Up to now the most explored alternative has been α-CsPbI₃, due to its high thermal stability and moisture resistance [22,23], ~1.7 eV direct bandgap at room temperature [22,24,25] (the most suitable of the inorganic lead halide perovskites (LHPs) for photovoltaic applications), high carrier mobility [26] and shallow defects enabling defect tolerance [27–29]. Since its first use as absorbing layer in a planar configuration perovskite solar cells (PSC) achieving 2.9% energy conversion [25]. CsPbI₃ has been successfully used in PSC with several reports reaching a conversion efficiency exceeding 10% [30–35] and a certified record efficiency of 17.06% [36]. Even though the great success of cubic α-CsPbI₃ this phase is thermodynamically unstable and spontaneously transforms into the yellow orthorhombic δ phase, with no photovoltaic or optoelectronic properties at room temperature [22,25]. It has been proven, both theoretically and experimentally, that the γ phase of CsPbI₃ has superior structural stability properties when compared with other polymorphs [37]. In fact, several reports on high efficiency and stability cells,

---

including a device with (uncertified) power conversion efficiency of 17.4% and a lifetime (estimated using high temperature accelerated degradation) of five years operating continuously at 35 °C, have been recently reported [35,38,39].

To further improve efficiency and lifetime of CsPbI$_3$ based solar cells and other optoelectronic devices a deep understanding of the fundamental properties of this material is essential. It is of particular importance the study of photoexcited states near the bandgap. These states affect light absorption and emission processes and charge transport, which is of the outmost importance for the implementation of optoelectronic devices [40]. The nature of the photoexcited states is nowadays one of the most important debated subjects upon the perovskite's community. If photoexcitation produces unbound electron-hole pairs a conductive plasma of free charges is formed [41–44]. On the other hand, if excitons (Coulombically bound electron–hole states) population dominates, they produce an insulating gas of neutral particles. This can hinder the collection of the photogenerated charges as they must be separated first using a heterojunction [45]. In this case, the exciton binding energy E_B must be overcome for electrons and holes to contribute to the photocurrent [46]. For $E_B < k_B T$, where $k_B T = 26\ meV$ is the thermal energy at room temperature, this energy may suffice to dissociate the exciton making this condition highly desirable. Metal halide perovskites (MHPs) constitute a particular class of semiconductor materials. Their exciton binding energies, ranging from 5 to 50 meV, place them between traditional inorganic semiconductors, mostly dominated by free carriers, and organic semiconductors, which are materials with strong excitonic behavior [40]. The current view is that if excitons are formed, they rapidly dissociate intro free carriers with a characteristic dissociation time in the ps range. On the other hand, excitons undeniably play a fundamental role in the band edge absorption and emission processes.

In this study, we present an in-depth analysis of the optoelectronic properties of room temperature stable γ-CsPbI$_3$ nanoparticles. This was carried out performing temperature dependent (10 K–290 K) continuous wave photoluminescence (PL) and absorbance spectroscopy. A complete and consistent theoretical framework that allows to analyze the results obtained in these samples, in order to compare them and thus gain a better understanding of the fundamental processes, is presented. The absorbance spectra are studied fitting the Elliott function. From the results important parameters for the use of γ-CsPbI$_3$ in optoelectronic devices as bandgap energy, exciton binding energy, exciton-phonon interaction and Urbach energy were obtained. Besides, from the evolution of the shape of PL and absorption spectra with temperature the excitonic nature of the PL spectra was proved. This is one of the most discussed topics within the community dedicated to the study of perovskite properties. The exciton binding energy is also obtained form the Arrhenius plot of the integrated PL intensity, which corroborates the result obtained form the Elliott function. Considering the excitonic nature of the PL spectra the existence and temperature dependence of the Stokes shift can be clearly understood as an excitonic thermalization process. The effect of using the Tauc plot to calculate the bandgap energy and why this does not give a good result is also introduced. The values obtained for the Urbach energy are very low for solution processed nanoparticles indicating the nanoparticles present excellent crystallinity. The results are compared to the ones obtained in other LHP, which are currently the most widely used perovskites for the manufacture of optoelectronic devices. With these comparisons the possible application of γ-CsPbI$_3$ nanoparticles is highly supported.

2. Results and discussion

XRD diffraction results show peaks at $2\theta = 14.3°$, and the splitting at 28.6° and 29.0°, which suggest an orthorhombic γ structure, as recently reported [37,39,47]. The assignment of these peaks is done in Fig. 1. The presence of these dominating peaks is originated in the slow evaporation of toluene which gives nanoparticles time to arrange in a preferential
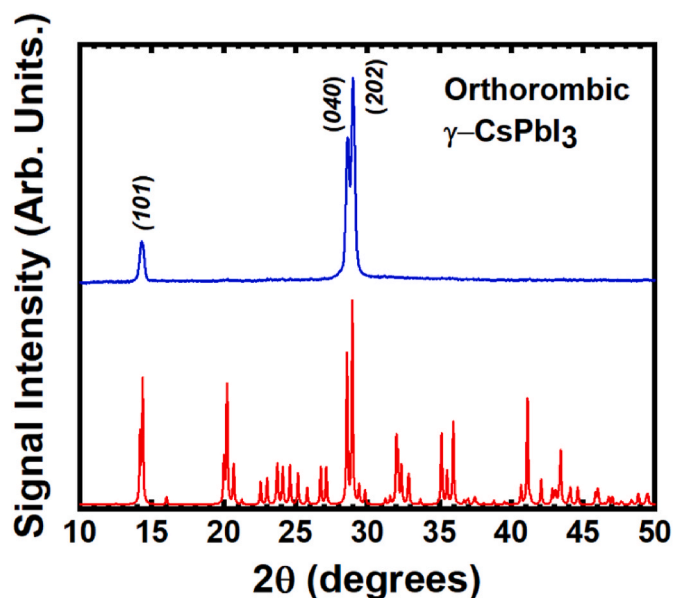

Fig. 1. γ-CsPbI$_3$ XRD patterns: ICSD 4127359 (red) and experimentally obtained (blue).

direction after being dropped on the substrate. Similar results were reported by Tang et al. [47]. Using the Scherrer equation the size of the quantum dots was estimated as 38 nm from the $2\theta = 14.3°$ peak. The mean size of the nanoparticles was further confirmed by Transmission Electron Microscopy (TEM) images. Fitting the results of the particle size histogram (Fig. S1) an average particle size of 32 ± 5 nm was obtained. Besides that, nanoparticles are very uniform in shape and size, and show a level of self-assembly into ordered arrays (Fig. 2 a), as is usual in MHPS of different compositions [48]. Self-assembled systems are nowadays of great interest both in fundamental and applied physics since superlattices can present new interesting collective properties not present in the individual nanoparticles as superfluorescence [49]. In the applications these systems are good candidates for the implementation of a new generation of QD enhanced LCDs and LEDs [50].

A remarkable alignment between atomic planes of two adjoining nanoparticles can be observed in Fig. 2 b. The alignment can be parallel (Fig. 2 c) or perpendicular (Fig. 2 d). In the first case it is even possible to see planes that continue from one nanoparticle to the other. We believe this effect indicates that the studied nanoparticles present a huge potential for the realization of self-assembled superlattices (SLs) into other larger structures, as has been reported for CsPbBr$_3$ [51].

In Fig. 3 the absorption spectra along with the normalized PL obtained at 10 K and 290 K are presented. The results obtained at 10 K show a sharp absorption peak followed by a softer increase of intensity, as is usually observed in LHP, both hybrid and inorganic. This behavior is characteristic of a strong excitonic absorption followed by interband transitions [52–54]. It can also be observed that the PL spectra consist of a well-defined peak located below the excitonic absorption. The origin of this difference, denominated Stokes Shift, is discussed below.

2.1. Absorption

Given the strong excitonic nature of the absorption spectra previously discussed, to obtain the relevant optical parameters from the absorption spectra the Elliott function must be used. The expression derived by Elliott (equation (*1*)) considers the absorption of semiconductors with strong excitonic effects as the sum of two terms. The first term consists of a series of discrete excitonic absorption peaks below the bandgap while the second one describes the continuous states present when the Coulomb attraction of electrons and holes is considered
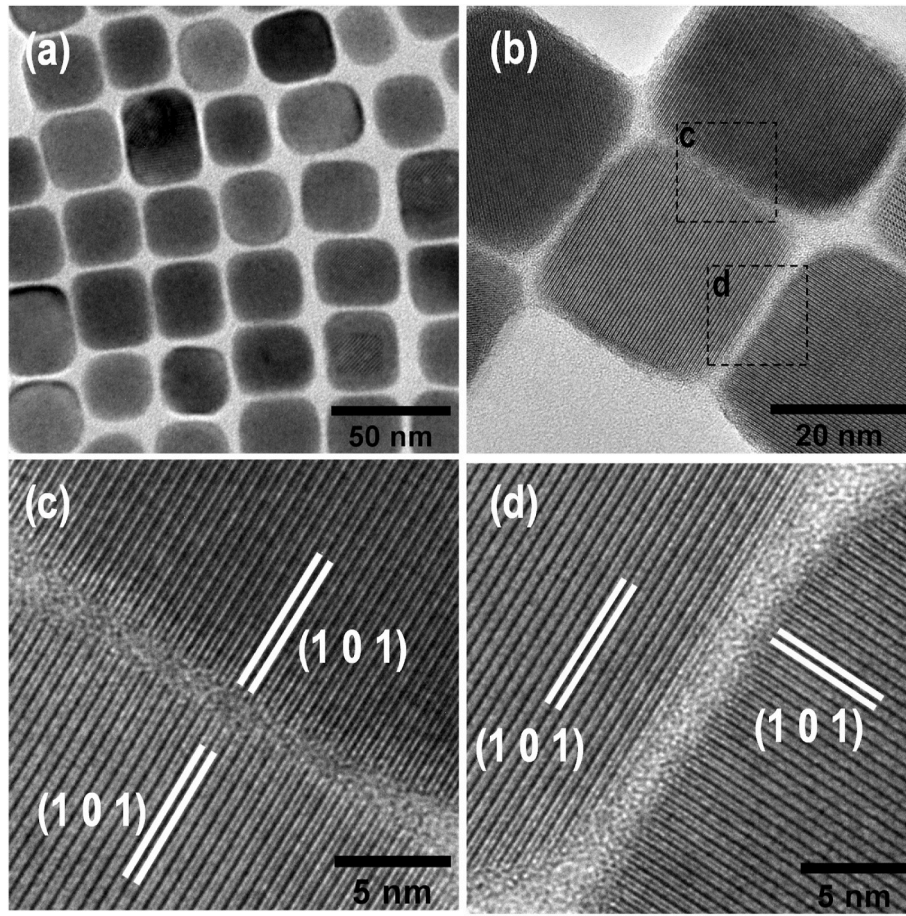
Fig. 2. TEM images of colloidal CsPbI$_3$ nanoparticles with different magnifications. a) spontaneous order of nanoparticles into an ordered array b) neighboring nanoparticles show a high level of alignment between their crystal planes. c) and d) interplanar distances correspond with (101) crystal planes.

[43,53,55–57].

$$\alpha(\mathrm{E}) \propto \mathrm{P_{cv}}\left[E_B \sum_{n=1}^{\infty} \frac{2\pi}{n^3} \bullet \delta\left(\hbar\omega - E_g + \frac{E_B}{n^2}\right) + \theta\left(\hbar\omega - E_g\right) \bullet \frac{\pi \exp x}{\sinh(\pi x)}\right] \quad (1)$$

In this expression $\hbar\omega$ is the photon energy, P_{cv} is a coefficient representing the allowed transition from the conduction to the valence band, E_g represents the bandgap energy, δ is a Dirac delta function (implemented with a Gaussian function), θ is a Heaviside function (implemented with a Sigmoidal function) and $x = \sqrt{\frac{E_B}{\hbar\omega - E_g}}$ with E_B representing the exciton binding energy i.e. the energy needed to dissociate the exciton intro a free electron and hole. The fitting, besides giving the relevant optical parameters, allows the deconvolution of absorption spectra into excitonic and interband contributions (dash and dash-dot traces respectively in Fig. 3 a and b). The excitonic absorption is obvious at 10 K and remains clearly distinguishable up to 220 K (Fig. S2). In the results obtained at room temperature the amplitude of the peak is not clearly visible but the Elliott fit shows that it is in fact present. Besides that, Elliott function analysis must be used instead of the usual Tauc plot, since the modeled α obtained from this last method clearly overestimates the absorption as shown in Fig. S3. This overestimation originates from the fact that the linear region to fit the Tauc plot is determined by the low energy shoulder of the Gaussian exciton absorption and not by interband transitions as it should [58,59]. Performing the Elliott analysis to all the measurements (considering only the first excitonic state) from 10 to 290 K the evolution of the parameters present in this function with temperature was obtained. These results show that E_g monotonically increases with temperature from 1.76 ±

0.01 eV to 1.84 ± 0.01 eV (blue circle in Fig. 4-a). This is the usual behavior for perovskites that is considered 'atypical', since is contrary to what is observed for covalent bonded semiconductors [42,55,60–63]. The origin of the atypical blueshift of E_g with increasing temperature is still a highly debated issue in the perovskite community. Theoretical results show that this dependence is produced by two competing phenomena (equation (2)): lattice thermal expansion (originated in the anharmonicity of crystal potential) and electron-phonon interaction [64–66].

$$\frac{dE_g}{dT} = \left[\frac{\partial E_g}{\partial T}\right]_{Expansion} + \left[\frac{\partial E_g}{\partial T}\right]_{e-ph} \quad (2)$$

Lattice contraction with decreasing temperature is related to the distortion in the electronic band structure when a hydrostatic pressure is applied. This relation is given by equation (3), [60,64,65] where α_V represents the volumetric expansion coefficient, B_0 the bulk modulus and $\left(\frac{dE_g}{dP}\right)$ the pressure coefficient of the bandgap.

$$\left[\frac{\partial E_g}{\partial T}\right]_{Expansion} = -\alpha_V B_0 \frac{dE_g}{dP} \quad (3)$$

Thermal expansion usually produces a reduction in the bandgap with increasing temperature caused by a positive hydrostatic pressure coefficient. This effect is less important than the electron-phonon term in conventional semiconductors [60,63,67]. Recently Francisco-López and collaborators [60] experimentally demonstrated that this parameter is negative for single crystals of methylammonium lead iodide (MAPbI$_3$). Besides, it is shown that thermal expansion cannot be neglected, and can even be considered the main cause of the atypical thermal behavior of
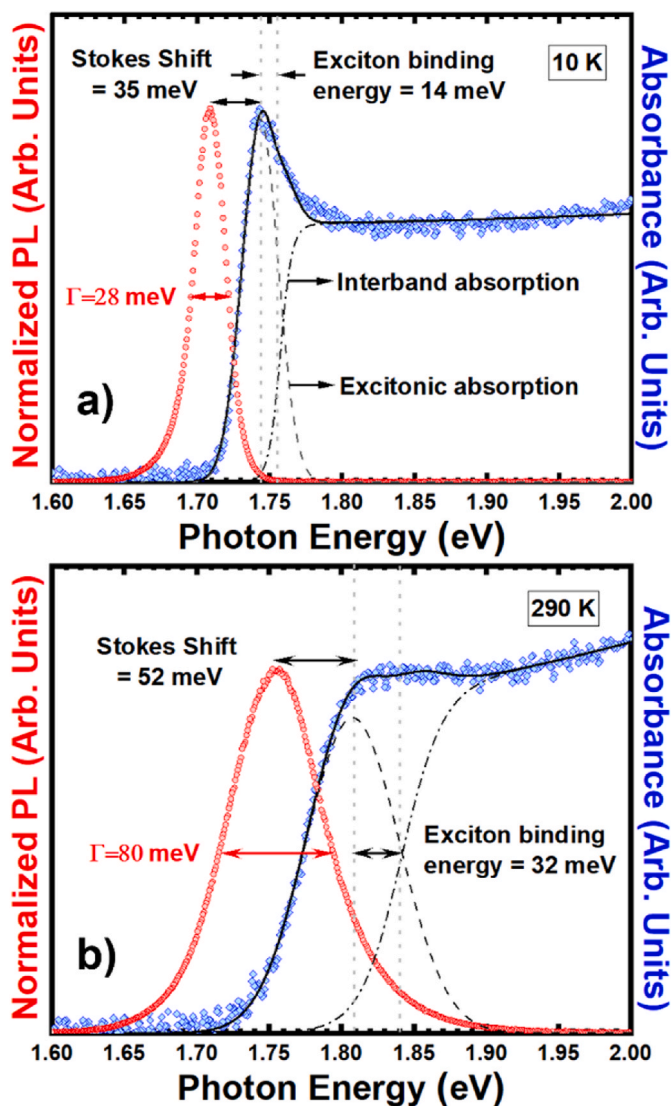
Fig. 3. Absorption (blue diamonds) and PL spectra (red circles) at 10 K (a) and 290 K (b). The Elliott function fit (solid-black) allows to perform a deconvolution of the Absorption spectra into Interband Absorption (black-dash-dot) and Excitonic absorption (black-dash).
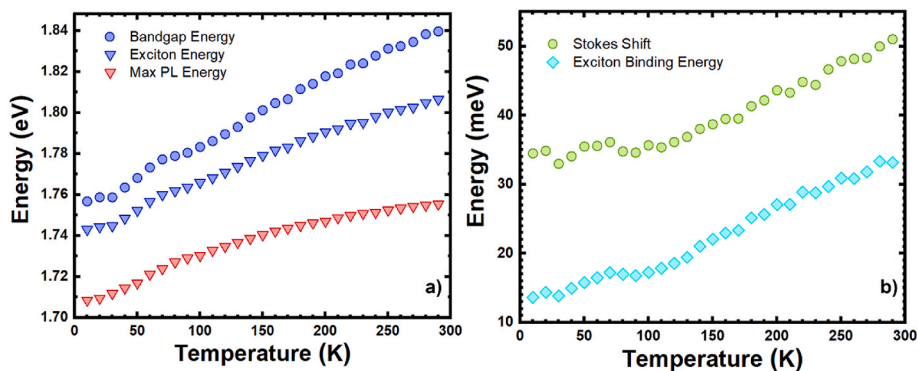
the bandgap in perovskites. It is also argued that this result can be extrapolated to all metal halide perovskites, so this can be considered the cause of the unusual bandgap shift observed. Unfortunately, given that the relevant parameters are not available for γ-CsPbI$_3$, we cannot perform the analysis for our samples to quantify the contribution of each term. However, an estimation of electron-phonon coupling can be given using a two Bose-Einstein oscillators model [63,66,68,69]. This analysis is presented in the supplementary information.

A correct determination of E_B is fundamental since this value determines the excitonic dissociation with temperature, and hence the nature of the photogenerated species which affects the working principle of devices. In our case E_B increases from 14 ± 1 meV at 10 K to 33 ± 1 meV at room temperature (cyan diamonds in Fig. 4 b). The value at room temperature is close to the one reported for α-CsPbI$_3$ (25 meV [70]) and smaller than the one reported for CsPbBr$_3$ (37–40 meV [52, 71]). For MAPbI$_3$ reported values differ wildly from 2 meV to 50 meV for thin films and bulk, and there is also evidence that E_B can increase considerably for nanoparticles [40]. Besides that, the temperature dependence of E_B in γ-CsPbI$_3$, produced by the change in the dielectric function with temperature originated in an increase of excitonic screening by optical polar phonons [72,73], is the opposite to what has been reported for hybrid MAPI perovskites [74–76]. This indicates that the fundamental processes responsible for the dielectric screening are different for both materials. An analysis of the mechanisms present in γ-CsPbI$_3$ is beyond the scope of this work. However, the increase of temperature would result in a dilatation of the material, which would reduce the dielectric constant, what would increase the exciton binding energy [59,77]. Moreover the increase of the bandgap energy with temperature would result in an increase of the effective masses of holes and electrons, which also tend to increase the exciton binding energy [59,77].

From Fig. 3 it can also be observed that at room temperature the amplitude of the excitonic absorption peak is smaller, and the full width at half maximum (FWHM or Γ) is much larger compared to the 10 K results. This trend is like the one followed by the PL spectra shown in Fig. 5 a. No discontinuities in the evolution of the PL energy are observed, so no crystalline phase transitions, common in hybrid LHPs [78–80], are present in the considered temperature range. Furthermore, from this image it can be observed that the maximum emission energy, as the bandgap energy, blueshifts with temperature. The dependence of Γ with temperature for the excitonic absorption obtained from the Elliott function and for the PL spectra obtained by fitting with a pseudo-Voight function (a lineal combination of a Gaussian G and a Lorentzian L function shearing the same full width at half maximum Γ and center of the emission peak) are presented in Fig. 5 b. This figure shows that the change in Γ with temperature is very similar in both cases, indicating that the mechanism responsible for the broadening for excitonic absorption and PL is the same. This can be considered as an indication of
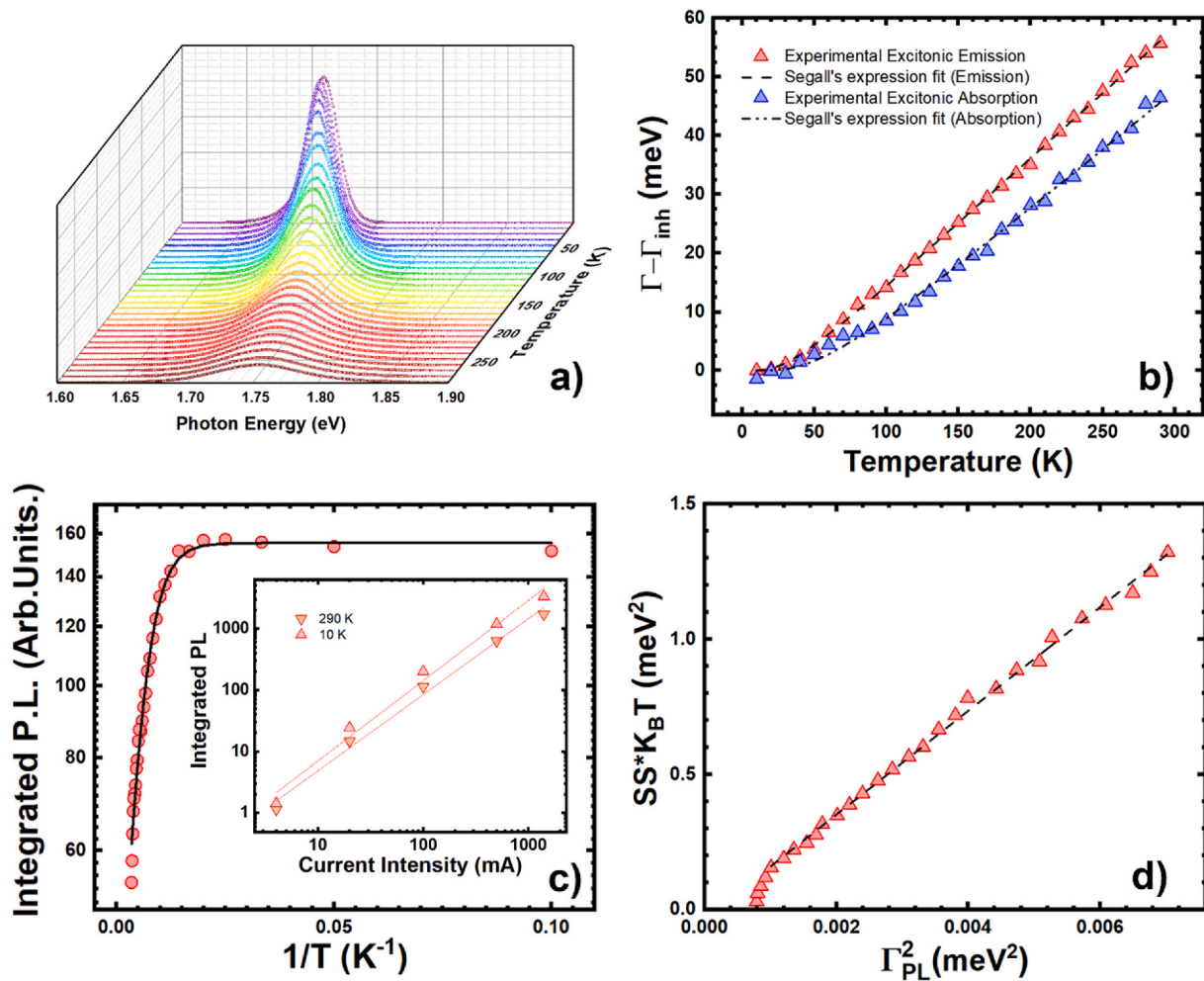

Fig. 4. Dependence with temperature of (a) Bandgap Energy (blue circles), Exciton Energy (blue down triangles) and Maximum PL Energy (red down triangles), (b) Stokes Shift (green circles) and Exciton Binding Energy (cyan diamonds). The origin of the temperature dependence of these parameters will be discussed in the following pages.

Fig. 5. a) Evolution of PL spectra with temperature between 10 K (red) and 290 K (blue). b) Temperature dependence of the photoluminescence (red up triangles) and absorption (blue up triangles) excitonic FWHM, and Segall's expression fit (dash and dash-dot) c) Arrhenius plot of Integrated PL vs 1/T (Inset: Integrated PL vs LED power) d) lineal relation between $SS*K_B T$ and Γ^2 predicted by Gurioli's equation.

the excitonic nature of the PL spectra. The temperature dependence of excitonic linewidths with temperature was theoretically analyzed by Segall and collaborators [81]. The authors show that exciton-phonon interactions can have three different origins [68,73,81–83]

i) **Piezoelectric effect:** In non-centrosymmetric crystals local strain can induce a local electrical polarization field thus affecting electrons.

ii) **Fröhlich interaction:** the presence of charge carriers in polar semiconductors locally distorts the lattice due to Coulombic interaction. These distortions can be transverse or longitudinal with the direction of propagation of the carrier. These distortions produce TO or LO phonons. The interaction produces an increase in the effective mass of carriers known as Fröhlich coupling.

iii) **Deformation potential:** phonons produce displacements of atoms form its lattice equilibrium sites which produces modifications in the band structure of the material, thus affecting carriers. For small deformations the change in energy is described by the deformation potentials.

Besides that, it is possible to quantify the influence of each of these processes by studding the FWHM (Γ)

with temperature using the Segall expression given by equation (4):

$$\Gamma(T) = \Gamma_{inh} + \Gamma_{Ac} + \Gamma_{LO} = \Gamma_{inh} + \varphi_{Ac} T + \frac{\varphi_{LO}}{e^{\frac{E_{LO}}{k_B T}} - 1} \qquad (4)$$

This expression has been used extensively to account for exciton-phonon interaction in perovskites [68,80,81,83]. Here, Γ_{inh} quantifies the inhomogeneous broadening present in the sample having its origin in crystal disorder. Second and third terms represents the couplings of electrons with acoustic and optical (LO) phonons respectively. Finally, φ_{Ac} and φ_{LO} are constants, and E_{LO} represent the energy associated with the optical phonons. Experimental results (Fig. 5 b) show, in both cases, a slope that tends to zero for low temperatures, indicating a low contribution of acoustic phonons. This is usually observed in experimental results on perovskites [80], and is also expected for polar inorganic semiconductors [84]. So, to fit the data we set $\varphi_{Ac} = 0$. The fittings show that for the excitonic absorption $\Gamma_{inh} = 30 \pm 1\ meV$, $E_{LO} = 12.5 \pm 2\ meV$ and a $\varphi_{LO} = 30 \pm 2\ meV$ and for PL $\Gamma_{inh} = 28 \pm 1\ meV$, $E_{LO} = 7 \pm 1\ meV$ and a $\varphi_{LO} = 18 \pm 2\ meV$. The results for E_{LO} are similar to the ones obtained for hybrid lead halide perovskites, where exciton-phonon interaction energies of 11.5 ± 1.2 meV and 11.5 meV for MAPbI$_3$ and formamidinium lead iodide (FAPbI$_3$) (T = 120 K–350 K), respectively, have been reported [80]. A deep knowledge of exciton-phonon coupling in perovskites is of the outmost importance since it has been proven that they have a deep impact in optoelectronic properties and hence in device performance [73]. In particular phonons produce scattering of excited carriers, thus setting a fundamental limit to charge carrier mobilities in a material with no scattering of impurities or interfaces [80,85]. The strong exciton-phonon interaction can also be responsible for the Gaussian line shape (see Fig. S3) of PL spectra at temperatures above

160 K [81].

The excitonic nature of the emitted radiation in γ-CsPbI$_3$ nanoparticles was further confirmed by several other results. First, the power dependence of the PL intensity can be used to determine the nature of the transitions originating the PL. These two magnitudes are related by a power law P^γ, with P representing the excitation power. When $1 < \gamma < 2$ PL has an excitonic origin whereas if $\gamma < 1$ PL is originated in free-to-bound carrier transitions or donor-acceptor pair transitions [86]. Experimental results at 290 and 10 K show that $\gamma = 1.3$ in both cases, as shown in the inset of Fig. 5 c, thus further confirming the excitonic nature of PL. Similar results have been obtained for CsPbBr$_3$ nanosheets and single crystals [87,88].

2.2. Photoluminescence

The dependence of the integrated photoluminescence I (area under the curve) with temperature T follows the typical behavior found in perovskites, shown in Fig. 5 c, contrary to what was reported by Tang and collaborators [47]. This can also be understood considering the excitonic nature of PL. To explain this, consider a model in which electrons can be free in the conduction band, with energy E_0, or forming an exciton. In this last case the electron has an energy $E_1(< E_0)$ with the difference between these two energies being the exciton binding energy E_B. The average number of electrons in the levels, N_0 and N_1 respectively, is governed by the Boltzmann law (equation (5)) and the total number remains constant, i.e:

$$N_0(T) + N_1(T) = N_G(T) \quad with \quad N_{0,1}(T) = \alpha_{0,1} \exp\left(-\frac{E_{0,1}}{k_B T}\right) \tag{5}$$

Thus, the dependence of the PL with temperature is determined by equation (6)

$$I(T) = \frac{I_0}{1 + a \exp(-E_B/K_B T)} \tag{6}$$

with $a = \frac{\alpha_0}{\alpha_1}$. In this scenario the activation energy calculated from the fitting of the Arrhenius diagram corresponds to the exciton binding energy E_B that in our case was $27 \pm 2\,meV$, which is close to the result obtained at room temperature using the Elliott equation (33 ± 1 meV). The difference can have its origin in the assumption that in the Arrhenius fit the only influence is excitonic dissociation, which is without a doubt an oversimplification [40]. In any case, both values are close to the room temperature thermal energy (26 meV), which is a very valuable feature for the use of this material in photovoltaic applications, since this implies that a large quantity of free carriers will be present after photoexcitation. This result shows that thermally activated dissociation of excitons is the most relevant channel for PL quenching as has been argued extensively in the literature for different MHPs [89–92]. A correct determination of this parameter is fundamental since it determines the equilibrium populations of excitons and free carriers [93]. From these results we can conclude that PL has its origin in excitonic recombination and I decreases with temperature because the excitons dissociate when temperature is increased.

Finally, the Stokes Shift (SS), defined as the difference between the energy of the excitonic absorption and the maximum of the PL emission, increases with temperature from 34 meV to 51 meV as seen in Fig. 4 b (green circles). More precisely, the SS presents a weak dependence with temperature up to 90 K, and then increases more rapidly. Similar trends have been obtained for MAPbI$_3$ and CsPbBr$_3$ single crystals [94]. The origin of the SS can be understood considering the analysis by Gurioli and collaborators [95]. In this, work the authors prove that if the Stokes Shift is originated in the thermalization of excitons in the inhomogeneously broadened excitonic band, a lineal relation between the product of the Stokes Shift and the thermal energy ($K_B T$) with the squared FWHM of the PL Γ^2 holds. This relation is explicitly given by equation (7)

$$SS \cong 0.180 \frac{\Gamma^2}{K_B T} \tag{7}$$

As shown in Fig. 5 d a lineal relation between these magnitudes, with a slope is 0.190, is present in our results which can be considered as another proof of the excitonic nature of the PL. This also explains the increase of the SS with temperature, that is produced by the increase in Γ of the PL. The temperature dependence of PL peak energy with temperature shown in red triangles in Fig. 4 is produced by the temperature dependence of the bandgap energy and the Stokes Shift.

2.3. Urbach tail and structural disorder

The low-energy edge of the absorption spectra in Fig. 3 shows an exponential increase as expected by the Urbach tail effect [96]. The mentioned edge has an energy dependence that can be modeled by an empirical expression given by equation (8) [67,97–99],

$$\alpha(E) = \alpha_0 \exp\left[\frac{(E - E_0)}{E_U}\right] \tag{8}$$

In this expression E_U is called Urbach Energy and is related to lattice disorder [97]. The total disorder has two components [67,100] one static (temperature independent) originated in intrinsic structural disorder in the lattice and another one dynamic (temperature dependent) produced by the excitation of phonon modes. On the other hand, E_0 is the Urbach Focus which is one of the characteristics of the Urbach like absorption. For regular semiconductors E_0 has a value that is above the bandgap energy but in lead halide perovskites, due to the atypical dependence of the bandgap with energy, this parameter takes values below the bandgap. Besides that, it has been argued that E_0 represent the minimum possible value for E_g in a defect free sample [67]. In our case this value is 1.71 ± 0.02 eV. According to equation (8) E_U can be calculated from a linear fit of the $\log \alpha$ vs. Energy plot, as shown in Fig. 6 a. Small values of E_0 are associated with low electronic disorder (i.e. high crystalline quality) and hence it also determines the electronic properties of the material. This parameter is also related with carrier mobility and determines the voltage deficiency (defined as the difference between bandgap voltage E_g/q and open circuit voltage) in solar cells [97,99].

E_U monotonically increases from 7 meV at 10 K to 21 meV at 290 K as shown in Fig. 6 b, which is a consequence of an increased carrier-phonon interaction [97] produced by a temperature induced increased phonon population. This behavior can be modeled using equation (9), [97,98]:

$$E_U(T) = E_U(0)\coth\left(\frac{E_{ph}}{2k_B T}\right) \tag{9}$$

where E_{ph} is a measurement of the energy of the involved phonons in the interactions, and $E_U(0)$ is a constant representing the static disorder contribution. The fitting of the model to the experimental data gives that $E_{ph} = 20 \pm 2\,meV$, which is within the same order of magnitude of the value calculated for LO phonons using the Segall's expression. On the other hand, $E_U(0) = 8 \pm 2meV$ which is very close to the results in thin films of different composition recently reported [67,97,99], although a bit higher as expected for nanoparticles. In the work by Zeiske and collaborators it is also argued that the very low values for $E_U(0)$ obtained in perovskites are produced by the excellent quality of the crystal structure and that the static contributions to Urbach energy are dominated by zero-point phonon energy.

3. Conclusions

Using the hot-injection method high crystallinity γ-CsPbI$_3$ cubic nanoparticles with excellent shape and size distribution were synthesized. TEM images revealed the presence of nanoparticles with a
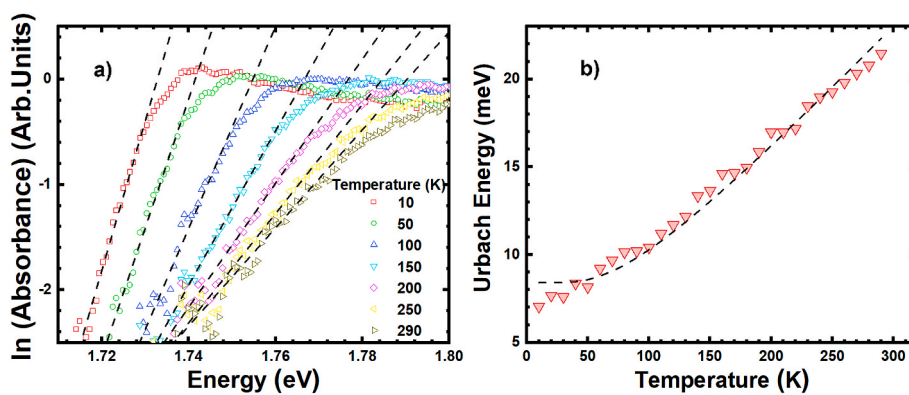
Fig. 6. a) Logarithm of low energy edge of absorbance (colored-scatter) and lineal fit (black-dashed) b) Temperature dependence of Urbach Energy calculated from lineal fit.

medium size of 32 nm and XRD measurements are consistent with an orthorhombic γ phase. Optical properties of the nanoparticles were measured using low temperature photoluminescence and transmittance spectroscopy. The results show that the onset of absorption spectra of γ-CsPbI$_3$ is strongly influenced by the presence of excitons, specially at low temperatures. An analysis using the Elliott equation shows that the bandgap energy follows the usual blueshift present in perovskites. At room temperature the bandgap reaches a value of 1.84 ± 0.01 eV, and the exciton binding energy is 33 ± 1 meV. The excitonic nature of PL was confirmed by analyzing the broadening of the spectra with temperature and the lineal relation of: i) the intensity (area under the curve) and the power of the incident radiation ii) the product of thermal energy and Stokes Shift ($k_B TSS$) and the square of the FWHM (Γ^2). So, considering the excitonic nature of PL is possible to explain all the changes with temperature experimentally observed in the spectra. Furthermore, fitting the broadening of the PL with temperature using the Segall equation reveals that the exciton-photon interaction is mostly produced by optical phonons with a characteristic energy of 7 ± 1 meV. This value is close to the one reported for organic perovskites commonly used in photovoltaic devices. Finally, an Urbach energy of 21 meV indicates an excellent crystal quality. The features reported in this research are very similar to the ones reported for other lead halide perovskites used in state-of-the-art devices. Besides that, the results show that γ-CsPbI$_3$ is a material which shows great promise to implement high-performance and high-stability optoelectronic devices that can compete with the currently developing perovskite devices. We hope the results presented in this paper can inspire researchers from all around the world to consider γ-CsPbI$_3$ for the implementation of perovskite based optoelectronic devices and solar cells.

4. Methods

CsPbI$_3$ nanoparticles were prepared using the hot injection method previously reported by Tang and collaborators [47]. Briefly, 0.4 mL of 0.06 M Cs-precursor was rapidly injected into a Pb-precursor at a higher temperature (180 °C). Cs-precursor was obtained by adding 0.407 g of cesium carbonate (Cs$_2$CO$_3$, Aldrich 99%) into 20 mL of octadecene (ODE, Aldrich 90%) and 1.25 mL of oleic acid (OA, Aldrich 90%) and heating at 120 °C in an inert atmosphere up to complete dissolution. Pb-precursor was obtained by adding 86.7 mg of lead iodide (PbI$_2$, Aldrich 99%) into 5 mL of ODE in an inert atmosphere. Then, 2 mL of OA followed by 2 mL of 3-aminopropyltriethoxysilane (APTES, Aldrich 99%) was added to the suspension. When PbI$_2$ was completely dissolved, Cs-precursor was injected, and the reaction was carried out for 10 s. After this, the mixture was cooled with Toluene at 4 °C in an ice bath. The black precipitate obtained was separated by centrifugation and washed several times with ethyl acetate. For subsequent optical and X-ray diffraction characterization the same sample, prepared by drop

casting the colloidal nanoparticles into a glass substrate, was used. The X-ray diffraction pattern of the samples was obtained with a Philips PW1729 diffractometer (with a Cu(K$_\alpha$) radiation, using a 0.02°/second speed and a Bragg–Brentano configuration). The low and high electron transmission microscope images were obtained with a JEOL 2100 microscope. The samples were prepared by drop casting the colloidal nanoparticles into a carbon coated copper grids. The images were analyzed using the Digital Micrograph 3 and Image J programs. Finally, the optical characterization was performed by continuous-wave photoluminescence (PL) spectroscopy and transmittance from 10 to 290 K. Sample was cooled in a CTI Cryogenics CRYODYNE cryostat. For PL measurements the excitation source was a Thorlabs M365FP1 LED (365 nm, 9.8 mW), filtered with a 400 nm low-pass filter, and the emitted light was collected with an Ocean Optics Flame S-UV-VIS-ES spectrometer. Then, changing the excitation source to a halogen lamp (Ocean-Optics HL 2000) and the spectrometer by an Ocean-Optics S2000, transmittance T was measured. From this we calculated the absorbance [58] $\alpha = -\ln T$.

Declaration of competing interest

The authors declare that they have no known competing financial interests or personal relationships that could have appeared to influence the work reported in this paper.

Data availability

Data will be made available on request.

Appendix A. Supplementary data

Supplementary data to this article can be found online at https://doi.org/10.1016/j.jlumin.2023.119765.

References

[1] A. Kojima, K. Teshima, Y. Shirai, T. Miyasaka, J. Am. Chem. Soc. 131 (2009) 6050.
[2] M. Kim, J. Jeong, H. Lu, T.K. Lee, F.T. Eickemeyer, Y. Liu, I.W. Choi, S.J. Choi, Y. Jo, H.B. Kim, S.I. Mo, Y.K. Kim, H. Lee, N.G. An, S. Cho, W.R. Tress, S.

M. Zakeeruddin, A. Hagfeldt, J.Y. Kim, M. Grätzel, D.S. Kim, Science (80) 375 (2022) 302.

[3] X. Zhao, T. Liu, Y.L. Loo, Adv. Mater. 34 (2022), 2105849.

[4] B. Conings, J. Drijkoningen, N. Gauquelin, A. Babayigit, J. D'Haen, L. D'Olieslaeger, A. Ethirajan, J. Verbeeck, J. Manca, E. Mosconi, F. De Angelis, H.G. Boyen, Adv. Energy Mater. 5 (2015), 1500477.

[5] T. Leijtens, E.T. Hoke, G. Grancini, D.J. Slotcavage, G.E. Eperon, J.M. Ball, M. De Bastiani, A.R. Bowring, N. Martino, K. Wojciechowski, M.D. McGehee, H. J. Snaith, A. Petrozza, Adv. Energy Mater. 5 (2015), 1500962.

[6] S. Bae, S.W. Lee, K.J. Cho, S. Park, S. Lee, Y. Kang, H.S. Lee, D. Kim, J. Phys. Chem. Lett. 7 (2016) 3091.

[7] J. Jiang, Q. Wang, Z. Jin, X. Zhang, J. Lei, H. Bin, Z.G. Zhang, Y. Li, S.F. Liu, Adv. Energy Mater. 8 (2018), 1701757.

[8] T. Wu, Y. Wang, Z. Dai, D. Cui, T. Wang, X. Meng, E. Bi, X. Yang, L. Han, Adv. Mater. 31 (2019), 1900605.

[9] G. Abdelmageed, L. Jewell, K. Hellier, L. Seymour, B. Luo, F. Bridges, J.Z. Zhang, S. Carter, Appl. Phys. Lett. 109 (2016), 233905.

[10] B. Chen, J. Song, X. Dai, Y. Liu, P.N. Rudd, X. Hong, J. Huang, Adv. Mater. 31 (2019), https://doi.org/10.1002/ADMA.201902413.

[11] A.F. Akbulatov, L.A. Frolova, M.P. Griffin, I.R. Gearba, A. Dolocan, D.A. Vanden Bout, S. Tsarev, E.A. Katz, A.F. Shestakov, K.J. Stevenson, P.A. Troshin, Adv. Energy Mater. 7 (2017), 1700476.

[12] H. Huang, H. Yuan, K.P.F. Janssen, G. Solís-Fernández, Y. Wang, C.Y.X. Tan, D. Jonckheere, E. Debroye, J. Long, J. Hendrix, J. Hofkens, J.A. Steele, M.B. J. Roeffaers, ACS Energy Lett. 3 (2018) 755.

[13] M.C. Brennan, S. Draguta, P.V. Kamat, M. Kuno, ACS Energy Lett. 3 (2018) 204.

[14] A.F. Akbulatov, L.A. Frolova, N.N. Dremova, I. Zhidkov, V.M. Martynenko, S. A. Tsarev, S.Y. Luchkin, E.Z. Kurmaev, S.M. Aldoshin, K.J. Stevenson, P. A. Troshin, J. Phys. Chem. Lett. 11 (2020) 333.

[15] A.F. Akbulatov, S.Y. Luchkin, L.A. Frolova, N.N. Dremova, K.L. Gerasimov, I. S. Zhidkov, D.V. Anokhin, E.Z. Kurmaev, K.J. Stevenson, P.A. Troshin, J. Phys. Chem. Lett. 8 (2017) 1211.

[16] E.J. Juarez-Perez, L.K. Ono, M. Maeda, Y. Jiang, Z. Hawash, Y. Qi, J. Mater. Chem. 6 (2018) 9604.

[17] M. Jung, T.J. Shin, J. Seo, G. Kim, S. Il Seok, Energy Environ. Sci. 11 (2018) 2188.

[18] T. Miyasaka, A. Kulkarni, G.M. Kim, S. Öz, A.K. Jena, Adv. Energy Mater. 10 (2020), 1902500.

[19] I. Spanopoulos, W. Ke, M.G. Kanatzidis, Helv. Chim. Acta 104 (2021), e2000173.

[20] W. Ahmad, J. Khan, G. Niu, J. Tang, Sol. RRL 1 (2017), 1700048.

[21] J. Shi, Y. Wang, Y. Zhao, J. Shi, Y. Wang, Y. Zhao, Energy Environ. Mater. 2 (2019) 73.

[22] R.J. Sutton, G.E. Eperon, L. Miranda, E.S. Parrott, B.A. Kamino, J.B. Patel, M. T. Hörantner, M.B. Johnston, A.A. Haghighirad, D.T. Moore, H.J. Snaith, Adv. Energy Mater. 6 (2016), 1502458.

[23] L. Protesescu, S. Yakunin, M.I. Bodnarchuk, F. Krieg, R. Caputo, C.H. Hendon, Nano Lett. 15 (2015) 3692.

[24] F. Liu, Y. Zhang, C. Ding, S. Kobayashi, T. Izuishi, N. Nakazawa, T. Toyoda, T. Ohta, S. Hayase, T. Minemoto, K. Yoshino, S. Dai, Q. Shen, ACS Nano 11 (2017), 10373.

[25] G.E. Eperon, G.M. Paternò, R.J. Sutton, A. Zampetti, A.A. Haghighirad, F. Cacialli, H.J. Snaith, J. Mater. Chem. 3 (2015), 19688.

[26] L.K. Gao, Y.L. Tang, ACS Omega 6 (2021), 11545.

[27] Q.A. Akkerman, G. Rainò, M.V. Kovalenko, L. Manna, Nat. Mater. 175 (17) (2018) 394, 2018.

[28] Y. Li, C. Zhang, X. Zhang, D. Huang, Q. Shen, Y. Cheng, W. Huang, Appl. Phys. Lett. 111 (2017), 162106.

[29] E.A. Gaulding, J. Hao, H.S. Kang, E.M. Miller, S.N. Habisreutinger, Q. Zhao, A. Hazarika, P.C. Sercel, J.M. Luther, J.L. Blackburn, Adv. Mater. 31 (2019), 1902250.

[30] A. Swarnkar, A.R. Marshall, E.M. Sanehira, B.D. Chernomordik, D.T. Moore, J. A. Christians, T. Chakrabarti, J.M. Luther, Science (80-.) 354 (2016) 92.

[31] E.M. Sanehira, A.R. Marshall, J.A. Christians, S.P. Harvey, P.N. Ciesielski, L. M. Wheeler, P. Schulz, L.Y. Lin, M.C. Beard, J.M. Luther, Sci. Adv. 3 (2017) 1.

[32] L.A. Frolova, D.V. Anokhin, A.A. Piryazev, S.Y. Luchkin, N.N. Dremova, K. J. Stevenson, P.A. Troshin, J. Phys. Chem. Lett. 8 (2017) 67.

[33] X. Ling, S. Zhou, J. Yuan, J. Shi, Y. Qian, B.W. Larson, Q. Zhao, C. Qin, F. Li, G. Shi, C. Stewart, J. Hu, X. Zhang, J.M. Luther, S. Duhm, W. Ma, Adv. Energy Mater. 9 (2019), 1900721.

[34] Q. Wang, Z. Jin, D. Chen, D. Bai, H. Bian, J. Sun, G. Zhu, G. Wang, S. (Frank) Liu, Adv. Energy Mater. 8 (2018), 1800007.

[35] P. Becker, J.A. Márquez, J. Just, A. Al-Ashouri, C. Hages, H. Hempel, M. Jošt, S. Albrecht, R. Frahm, T. Unold, Adv. Energy Mater. 9 (2019), 1900555.

[36] Y. Wang, T. Zhang, M. Kan, Y. Zhao, J. Am. Chem. Soc. 140 (2018), 12345.

[37] R.J. Sutton, M.R. Filip, A.A. Haghighirad, N. Sakai, B. Wenger, F. Giustino, H. J. Snaith, ACS Energy Lett. 3 (2018) 1787.

[38] X. Zhao, T. Liu, Q.C. Burlingame, T. Liu, R. HolleyIII, G. Cheng, N. Yao, F. Gao, Y.-L. Loo, Science (80) (2022), https://doi.org/10.1126/SCIENCE.ABN5679.

[39] Z. Zhang, R. Ji, M. Kroll, Y.J. Hofstetter, X. Jia, D. Becker-Koch, F. Paulus, M. Löffler, F. Nehm, K. Leo, Y. Vaynzof, Z. Zhang, R. Ji, M. Kroll, Y.J. Hofstetter, X. Jia, D. Becker-Koch, F. Nehm, K. Leo, Y. Vaynzof, F. Paulus, M. Löffler, Adv. Energy Mater. 11 (2021), 2100299.

[40] Y. Jiang, X. Wang, A. Pan, Adv. Mater. 31 (2019), 1806671.

[41] J.S. Manser, P.V. Kamat, Nat. Photonics 89 (8) (2014) 737, 2014.

[42] V. D'Innocenzo, G. Grancini, M.J.P. Alcocer, A.R.S. Kandada, S.D. Stranks, M. M. Lee, G. Lanzani, H.J. Snaith, A. Petrozza, Nat. Commun. 51 (5) (2014) 1, 2014.

[43] M. Saba, M. Cadelano, D. Marongiu, F. Chen, V. Sarritzu, N. Sestu, C. Figus, M. Aresti, R. Piras, A. Geddo Lehmann, C. Cannas, A. Musinu, F. Quochi, A. Mura, G. Bongiovanni, Nat. Commun. 5 (2014) 1.

[44] F. Deschler, M. Price, S. Pathak, L.E. Klintberg, D.D. Jarausch, R. Higler, S. Hüttner, T. Leijtens, S.D. Stranks, H.J. Snaith, M. Atatüre, R.T. Phillips, R. H. Friend, J. Phys. Chem. Lett. 5 (2014) 1421.

[45] N.-G. Park, H. Segawa, Multifunctional Organic–Inorganic Halide Perovskite: Applications in Solar Cells, Light-Emitting Diodes, and Resistive Memory, Jenny Stanford Publishing, Singapore, 2022.

[46] L. M. Herz, https://doi.org/10.1146/annurev-physchem-040215-112222 2016, 67, 65.

[47] B. Tang, L.J. Ruan, C. Qin, A. Shu, H. He, Y. Ma, Adv. Opt. Mater. 8 (2020), 2000498.

[48] Z. Long, H. Ren, J. Sun, J. Ouyang, N. Na, Chem. Commun. 53 (2017) 9914.

[49] G. Rainò, M.A. Becker, M.I. Bodnarchuk, R.F. Mahrt, M.V. Kovalenko, T. Stöferle, Nat 563 (2018) 671, 5637733 2018.

[50] M.V. Kovalenko, L. Protesescu, M.I. Bodnarchuk, Science (80) 358 (2017) 745.

[51] J. Liu, K. Song, Y. Shin, X. Liu, J. Chen, K.X. Yao, J. Pan, C. Yang, J. Yin, L.J. Xu, H. Yang, A.M. El-Zohry, B. Xin, S. Mitra, M.N. Hedhili, I.S. Roqan, O. F. Mohammed, Y. Han, O.M. Bakr, Chem. Mater. 31 (2019) 6642.

[52] D. Ramírez, G. Riveros, P. Díaz, J. Verdugo, G. Núñez, S. Lizama, P. Lazo, E. A. Dalchiele, D.L. Gau, R.E. Marotti, J.A. Anta, L. Contreras-Bernal, A. Riquelme, J. Idigoras, Chemelectrochem 7 (2020) 3961.

[53] X. Chen, H. Lu, Y. Yang, M.C. Beard, J. Phys. Chem. Lett. 9 (2018) 2595.

[54] F. Ruf, A. Magin, M. Schultes, E. Ahlswede, H. Kalt, M. Hetterich, Appl. Phys. Lett. 112 (2018), 83902.

[55] F. Ruf, M.F. Aygüler, N. Giesbrecht, B. Rendenbach, A. Magin, P. Docampo, H. Kalt, M. Hetterich, Apl. Mater. 7 (2019), 31113.

[56] R.J. Elliott, Phys. Rev. 108 (1957) 1384.

[57] F. Ruf, Excitonic Effects and Bandgap Instabilities in Perovskite Solar Cells, KIT Scientific Publishing, 2020.

[58] O. Stenzel, Phys. Thin Film Opt. Spectra an Introd, second ed., 2015, p. 1.

[59] M. Fox, Optical Properties of Solids, AAPT, 2002.

[60] A. Francisco-López, B. Charles, O.J. Weber, M.I. Alonso, M. Garriga, M. Campoy-Quiles, M.T. Weller, A.R. Goñi, J. Phys. Chem. Lett. 10 (2019) 2971.

[61] W. Shcherbakov-Wu, P.C. Sercel, F. Krieg, M.V. Kovalenko, W.A. Tisdale, J. Phys. Chem. Lett. 12 (2021) 8088.

[62] W. Wu, W. Liu, Q. Wang, Q. Han, Q. Yang, J. Alloys Compd. 787 (2019) 165.

[63] C. Yu, Z. Chen, J. Wang, W. Pfenninger, N. Vockic, J.T. Kenney, K. Shum, J. Appl. Phys. 110 (2011), 063526.

[64] P. Lautenschlager, P.B. Allen, M. Cardona, Phys. Rev. B 31 (1985) 2163.

[65] S. Gopalan, P. Lautenschlager, M. Cardona, Phys. Rev. B 35 (1987) 5577.

[66] M. Cardona, Solid State Commun. 133 (2005) 3.

[67] S. Singh, C. Li, F. Panzer, K.L. Narasimhan, A. Graeser, T.P. Gujar, A. Köhler, M. Thelakkat, S. Huettner, D. Kabra, J. Phys. Chem. Lett. 7 (2016) 3014.

[68] R. Saran, A. Heuer-Jungemann, A.G. Kanaras, R.J. Curry, Adv. Opt. Mater. 5 (2017), 1700231.

[69] R. Ahumada-Lazo, R. Saran, O. Woolland, Y. Jia, M.E. Kyriazi, A.G. Kanaras, D. Binks, R.J. Curry, J. Phys. Photonics 3 (2021), 021002.

[70] B.T. Diroll, H. Zhou, R.D. Schaller, Adv. Funct. Mater. 28 (2018), 1800945.

[71] D. Fröhlich, K. Heidrich, H. Künzel, G. Trendel, J. Treusch, J. Lumin. 18 (1979) 385.

[72] L. Pedesseau, D. Sapori, B. Traore, R. Robles, H.H. Fang, M.A. Loi, H. Tsai, W. Nie, J.C. Blancon, A. Neukirch, S. Tretiak, A.D. Mohite, C. Katan, J. Even, M. Kepenekian, ACS Nano 10 (2016) 9776.

[73] R.L.Z. Hoye, J. Hidalgo, R.A. Jagt, J.P. Correa-Baena, T. Fix, J.L. MacManus-Driscoll, Adv. Energy Mater. 12 (2022), 2100499.

[74] C.L. Davies, M.R. Filip, J.B. Patel, T.W. Crothers, C. Verdi, A.D. Wright, R.L. Milot, F. Giustino, M.B. Johnston, L.M. Herz, Nat. Commun. 91 (9) (2018) 1, 2018.

[75] N. Sestu, M. Cadelano, V. Sarritzu, F. Chen, D. Marongiu, R. Piras, M. Mainas, F. Quochi, M. Saba, A. Mura, G. Bongiovanni, J. Phys. Chem. Lett. 6 (2015) 4566.

[76] Y. Yamada, T. Nakamura, M. Endo, A. Wakamiya, Y. Kanemitsu, IEEE J. Photovoltaics 5 (2015) 401.

[77] F. Ruf, J. Phys. Chem. Lett. 9 (2018) 6853.

[78] M.I. Dar, G. Jacopin, S. Meloni, A. Mattoni, N. Arora, A. Boziki, S.M. Zakeeruddin, U. Rothlisberger, M. Grätzel, Sci. Adv. 2 (2016), https://doi.org/10.1126/SCIADV.1601156/SUPPL_FILE/1601156_SM.(PDF).

[79] A.D. Wright, R.L. Milot, G.E. Eperon, H.J. Snaith, M.B. Johnston, L.M. Herz, A. D. Wright, R.L. Milot, G.E. Eperon, H.J. Snaith, M.B. Johnston, L.M. Herz, Adv. Funct. Mater. 27 (2017), 1700860.

[80] A.D. Wright, C. Verdi, R.L. Milot, G.E. Eperon, M.A. Pérez-Osorio, H.J. Snaith, F. Giustino, M.B. Johnston, L.M. Herz, Nat. Commun. 7 (2016) 1.

[81] S. Rudin, T.L. Reinecke, B. Segall, Phys. Rev. B 42 (1990), 11218.

[82] X.B. Zhang, T. Taliercio, S. Kolliakos, P. Lefebvre, J. Phys. Condens. Matter 13 (2001) 7053.

[83] D.L. Gau, D. Ramírez, F. Iikawa, G. Riveros, P. Díaz, J. Verdugo, G. Núñez, S. Lizama, P. Lazo, E.A. Dalchiele, L. Contreras, J. Idigoras, J. Anta, R.E. Marotti, ChemPhysChem (2022), e202200286.

[84] X.B. Zhang, T. Taliercio, S. Kolliakos, P. Lefebvre, J. Phys. Condens. Matter 13 (2001) 7053.

[85] P.Y. Yu, M. Cardona, Fundamentals of Semiconductors, Springer Berlin, Heidelberg, Heidelberg, 2010.

[86] T. Schmidt, K. Lischka, W. Zulehner, Phys. Rev. B 45 (1992) 8989.

[87] X. Lao, Z. Yang, Z. Su, Z. Wang, H. Ye, M. Wang, X. Yao, S. Xu, Nanoscale 10 (2018) 9949.

94

[88] J.A. Peters, Z. Liu, O. Bulgin, Y. He, V.V. Klepov, M.C. De Siena, M.G. Kanatzidis, B.W. Wessels, J. Phys. Chem. Lett. 12 (2021) 9301.

[89] A. Dey, P. Rathod, D. Kabra, Adv. Opt. Mater. 6 (2018), 1800109.

[90] S. Sun, T. Salim, N. Mathews, M. Duchamp, C. Boothroyd, G. Xing, T.C. Sum, Y. M. Lam, Energy Environ. Sci. 7 (2013) 399.

[91] T.J. Savenije, C.S. Ponseca, L. Kunneman, M. Abdellah, K. Zheng, Y. Tian, Q. Zhu, S.E. Canton, I.G. Scheblykin, T. Pullerits, A. Yartsev, V. Sundström, J. Phys. Chem. Lett. 5 (2014) 2189.

[92] H.H. Fang, F. Wang, S. Adjokatse, N. Zhao, J. Even, M.A. Loi, Light Sci. Appl. 5 (2016), https://doi.org/10.1038/LSA.2016.56.

[93] D. Marongiu, M. Saba, F. Quochi, A. Mura, G. Bongiovanni, J. Mater. Chem. C 7 (2019), 12006.

[94] Y. Guo, O. Yaffe, T.D. Hull, J.S. Owen, D.R. Reichman, L.E. Brus, Nat. Commun. 101 (10) (2019) 1, 2019.

[95] M. Gurioli, A. Vinattieri, J. Martinez-Pastor, M. Colocci, Phys. Rev. B 50 (1994), 11817.

[96] F. Urbach, Phys. Rev. 92 (1953) 1324.

[97] S. Zeiske, O.J. Sandberg, N. Zarrabi, C.M. Wolff, M. Raoufi, F. Peña-Camargo, E. Gutierrez-Partida, P. Meredith, M. Stolterfoht, A. Armin, J. Phys. Chem. Lett. 13 (2022) 7280.

[98] T.H. Keil, Phys. Rev. 144 (1966) 582.

[99] M. Ledinsky, T. Schönfeldová, J. Holovský, E. Aydin, Z. Hájková, L. Landová, N. Neyková, A. Fejfar, S. De Wolf, J. Phys. Chem. Lett. 10 (2019), https://doi.org/10.1021/acs.jpclett.9b00138.

[100] G.D. Cody, T. Tiedje, B. Abeles, B. Brooks, Y. Goldstein, Phys. Rev. Lett. 47 (1981) 1480.

Origin of Photoluminescence and experimental determination of Exciton Binding Energy, Exciton-Phonon interaction, and Urbach Energy in γ-CsPbI$_3$ Nanoparticles.

Daniel L. Gau, Isabel Galain, Ivana Aguiar, Ricardo E. Marotti.
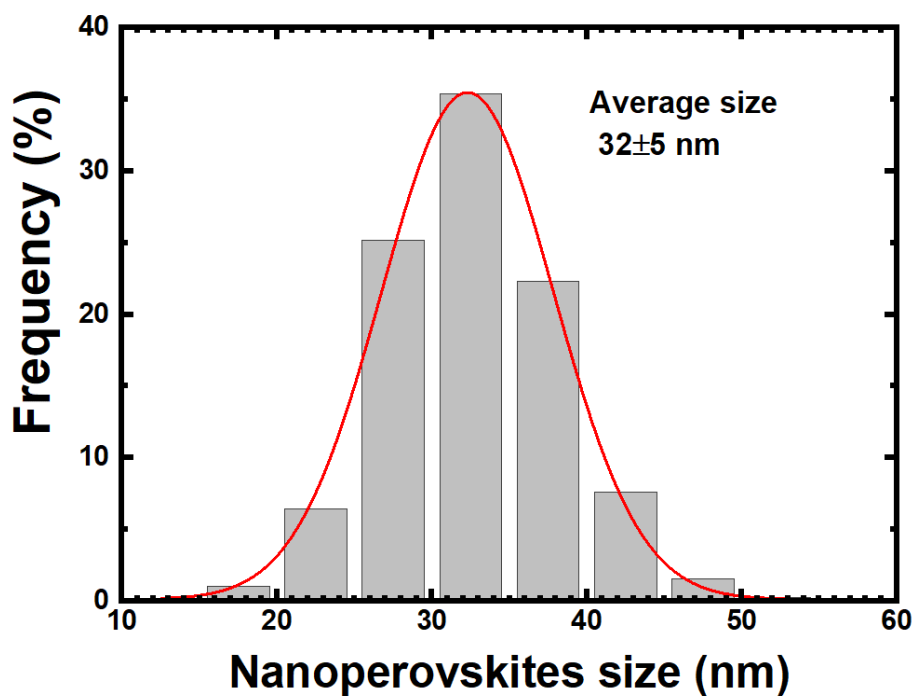
Figure S1: Size histogram of nanoparticles (bars) and Gaussian fit of the data (solid red).

Scherrer Equation:

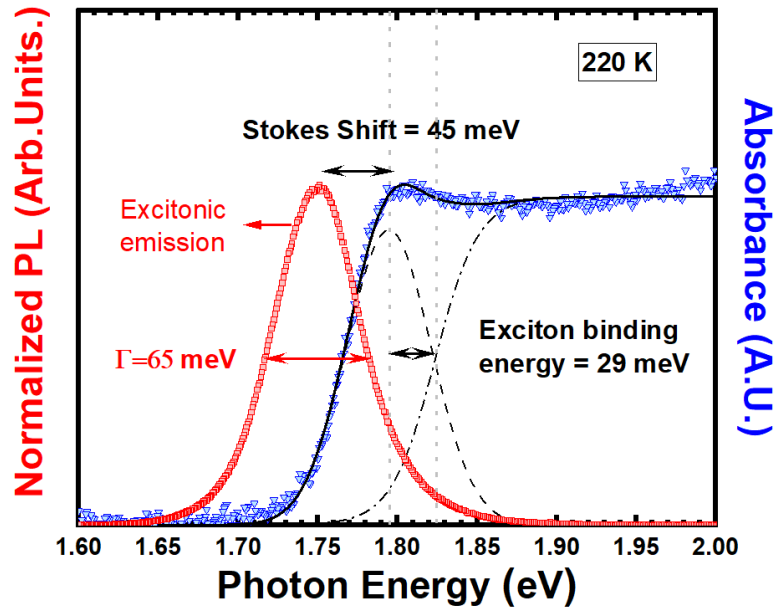$$D = \frac{K\lambda}{\beta \cos(\theta)} = \frac{0.89 * 1.5418\text{Å}}{0.36529 * \cos(14.31087)} \cong 30\ nm$$

Figure S2: PL spectra (red squares) and Absorption (blue triangles) at 220 K with Elliot function fit (solid-black), Interband Absorption (black-dash-dot) and Excitonic absorption (black-dash).
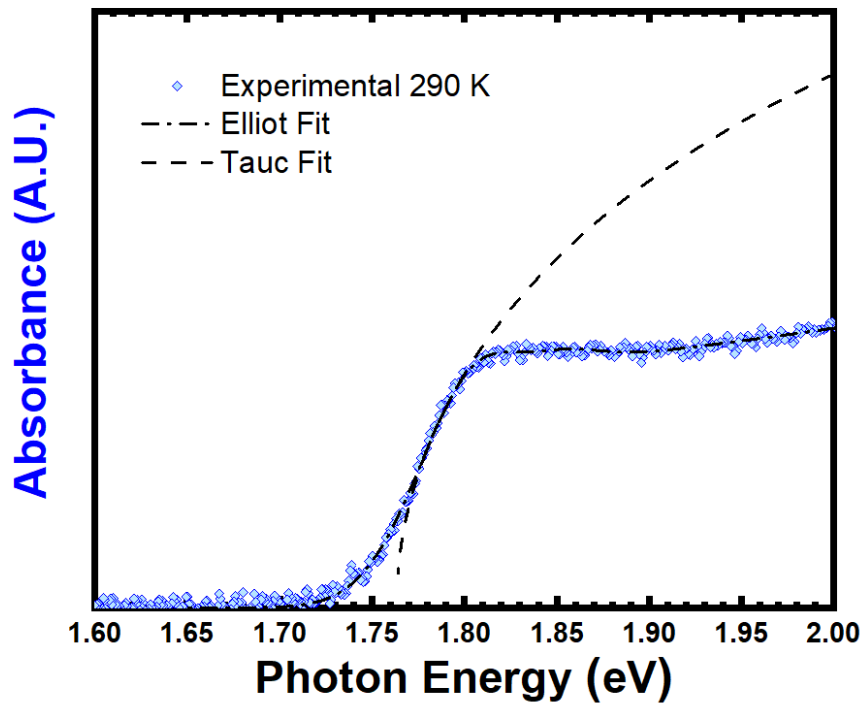
Figure S3: Comparison of Elliot function (dash-dot) and Tauc fit (dashed) of experimental results for absorbance at 290 K.

The PL spectra were fitted using a pseudo-Voigt function (S1). This function is a lineal combination of a Gaussian G and a Lorentzian L function and is generally used because it allows to quantify the homogeneous (Gaussian) and inhomogeneous (Lorentzian) broadenings in a peak. Besides that, it also allows a better determination of the center of the peak.

$$y(E) = fL(E) + (1-f)G(E) \tag{S1}$$

Figure S4 shows the temperature dependence of the Lorential Fraction of the Pseudo-Voight function PL lineshape with
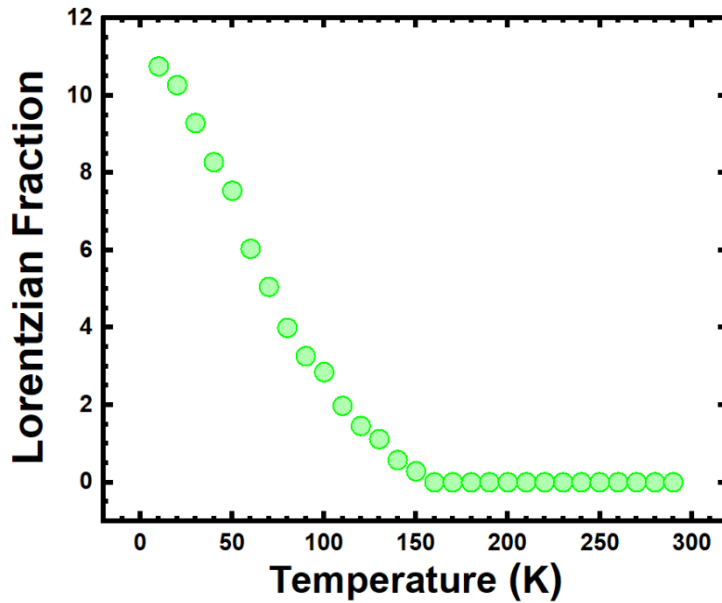
Figure S4: Lorentzian fraction of PL pseudo-Voight fit.

The line shape is Gaussian at high temperature and resembles a Lorentzian at low temperatures. This tendency is contrary to the observation that the broadening should be homogeneous at high temperature (due to a larger exciton-phonon coupling) and become inhomogeneous at low temperature (due to crystal disorder or particle size distribution)[1] However, it can be interpreted according to the strength of the exciton-phonon coupling. For weak exciton-phonon interaction it has a Lorentzian shape, while for large exciton-phonon interaction or sufficiently high temperature the exciton lineshape will be Gaussian[2].

Two-oscillators model:

Lattice expansion is produced by the product of the hydrostatic deformation potential $\frac{\partial V}{\partial T}$ and the expansion coefficient $\frac{\partial E_g}{\partial V}$. This last term can be either positive or negative and can be considered temperature independent[3]. On the other hand, electron-phonon interaction is determined by the product of phonon occupation number in the phonon branch j with wave vector $\vec{q}$, named $n_{j,\vec{q}}$, and $\left(\frac{\partial E_g}{\partial n_{j,\vec{q}}}\right)$. The total dependence of the bandgap with temperature can be therefore expressed as[4–6]:

$$\frac{\partial E_g}{\partial T} = \left(\frac{\partial E_g}{\partial V}\right)\left(\frac{\partial V}{\partial T}\right) + \frac{\partial}{\partial T}\sum_{j,\vec{q}}^{N}\left(\frac{\partial E_g}{\partial n_{j,\vec{q}}}\right)\left(n_{j,\vec{q}} + \frac{1}{2}\right)$$

The electron-phonon coupling calculated by this procedure must be considered as an upper bound. To analyze experimental data a simplified expression (S2) considering a two-oscillatior Bose-Einstein model, considering only effective energies of acoustic and optical modes, has been successfully used[5–9].

$$E_0(T, M) = E_0 + \frac{A_{ac}}{M_{ac}E_{ac}}\left(\frac{1}{\exp\frac{E_{ac}}{k_B T}-1} + \frac{1}{2}\right) + \frac{A_{op}}{M_{op}E_{op}}\left(\frac{1}{\exp\frac{E_{op}}{k_B T}-1} + \frac{1}{2}\right) \qquad (S2)$$

In this expression E_0 is an unrenormalized bandgap energy, A_{ac} and A_{op} are the relative weight of the acoustic/optical phonons in the coupling, E_{ac} and E_{op} are the effective energies of acoustic and optical phonons respectively, and M_{ac} and M_{op} represent the atomic masses of the oscillators. It has also been experimentally shown that the

contributions of acoustic and optical phonons have opposite influence in the bandgap energy[5,7]. Fitting the data with this model the obtained results were:

E_0= 1.75-1.9eV.

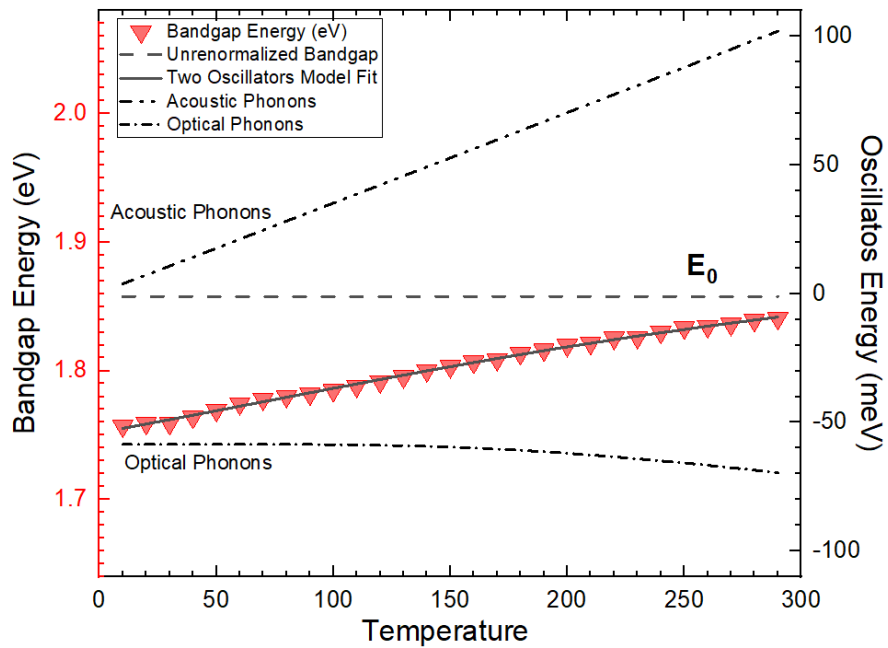E_{ac}=500µeV- 1000µeV.

E_{op}=60 meV-84 meV.

Figure 5: : Bandgap Energy dependence with temperature: red triangles are experimental points, full line is fitting according to equation S1, dashed line is unrenormalized bandgap energy, dash dotted line is optical phonon contribution, dash double dotted line is acoustic phonon contribution.

[1]   H. Pashaei Adl, S. Gorji, G. Muñoz-Matutano, R. I. Sánchez-Alarcón, R. Abargues, A. F. Gualdrón-Reyes, I. Mora-Seró, J. P. Martínez-Pastor, *J. Lumin.* **2021**, *240*, 118453.

[2]   S. Rudin, T. L. Reinecke, B. Segall, *Phys. Rev. B* **1990**, *42*, 11218.

[3]   A. Francisco-López, B. Charles, O. J. Weber, M. I. Alonso, M. Garriga, M. Campoy-Quiles, M. T. Weller, A. R. Goñi, *J. Phys. Chem. Lett.* **2019**, *10*, 2971.

[4]   D. L. Gau, D. Ramírez, F. Iikawa, G. Riveros, P. Díaz, J. Verdugo, G. Núñez, S. Lizama, P. Lazo, E. A. Dalchiele, L. Contreras, J. Idigoras, J. Anta, R. E. Marotti, *ChemPhysChem* **2022**, e202200286.

[5]   C. Yu, Z. Chen, J. Wang, W. Pfenninger, N. Vockic, J. T. Kenney, K. Shum, *J. Appl. Phys.* **2011**, *110*, 063526.

[6]   A. Göbel, T. Ruf, M. Cardona, C. Lin, J. Wrzesinski, M. Steube, K. Reimann, *Phys. Rev. B* **1998**, *57*, 15183.

[7]   R. Saran, A. Heuer-Jungemann, A. G. Kanaras, R. J. Curry, *Adv. Opt. Mater.* **2017**, *5*, 1700231.

[8]   R. Ahumada-Lazo, R. Saran, O. Woolland, Y. Jia, M. E. Kyriazi, A. G. Kanaras, D. Binks, R. J. Curry, *J. Phys. Photonics* **2021**, *3*, 021002.

[9]   M. Cardona, *Solid State Commun.* **2005**, *133*, 3.

Light-Induced Self-assembly and Effect of Amorphization in Photoluminescence Spectra of γ-CsPbI₃ Nanocrystals.

Daniel L. Gau[a], Isabel Galain[b], Ivana Aguiar[b], Ricardo E. Marotti[a].

E-mail: dgau@fing.edu.uy

[a]*Facultad de Ingeniería, Instituto de Física, Universidad de la República, Herrera y Reissig 565, C.C. 30, 11000 Montevideo, Uruguay.*

[b]*Grupo de Desarrollo de Materiales y Estudios Ambientales, Cátedra de Radioquímica, Facultad de Química, Universidad de la República, Av. General Flores 2124, Montevideo, Uruguay.*

This work was submitted to publication in the Journal of Luminescence and we are now performing the changes suggested by the reviewers to then accept a transfer proposed by the editor to the journal Optical Materials.

Abstract

Inorganic perovskites have gained significant interest in the scientific community due to their superior optoelectronic properties and enhanced stability compared to hybrid counterparts. Researchers are actively exploring new synthesis methods for creating advanced nanostructures. Besides that, understanding the fundamental properties of inorganic perovskites is crucial for optimizing their performance and unlocking their full potential in next-generation optoelectronic applications. In this study, we report for the first time the visible-light-induced self-assembly of cubic γ-CsPbI$_3$ nanoparticles into nanorods. Using temperature dependent continuous wave photoluminescence spectroscopy, the fundamental properties of nanoparticles such as exciton-phonon interaction and exciton binding energy is studied. The analysis reveals a blueshift in the photoluminescence spectra and an increase in the width of the spectra. This can be attributed to an amorphization of the crystal structure during the assembly process. Furthermore, we observe a decrease in exciton binding energy due to size effects. Our findings demonstrate that temperature-dependent CW-PL spectroscopy can be employed to characterize crystal quality and offers valuable insights into the fundamental properties of perovskite materials. This can contribute to the further development and optimization of perovskite-based devices in optoelectronic applications.

Introduction

In the last decade the flourishing field of colloidal nanocrystals has been deeply influenced by semiconducting lead halide perovskite nanocrystals (NPKs) [1,2]. This is rooted in the excellent optical properties among which we highlight: ease of bandgap tuning in the visible exploiting quantum confinement effects and composition[3,4], long charge carrier diffusion length[5,6], high absorption coefficient[7], high photoluminescence quantum yields[8–10] and high defect tolerance[2,11]. These properties are a fundamental part of the huge success that NPKs have had in the last decade as absorbing/emitting layer in optoelectronic devices as solar cells[12–14], light-emitting diodes[4,15,16], lasers[17], radiation scintillators[18] and single photon sources [19] between others. Remarkably the desired properties are obtained using low-temperature synthesis methods which allow the obtention of NPKs with high crystallinity, a very narrow size distribution and great uniformity[3,20]. It is also remarkable the short time that has taken to NPKs to jump to the center of attention for a large part of the scientific community.

Nowadays, the most used NPKs synthesis methods are Hot Injection (HI) and Ligand-Assisted Reprecipitation (LARP). With these methods varying ligands, reaction temperatures and precursors great control over shape, size and composition in high quality crystals can be obtained[2,3,21–23]. Besides, several post-synthetic treatments for surface treatment have also been developed. It has been proven that post-synthetic methods are a good way to improve the optical properties of NPKs[24]. The versatility with NPKs can be synthesized has been one of the main forces behind the great success leading the evolution of perovskite-based devices. In summary we can say that the work by the scientific community in the last decade has allowed the optimization of synthesis methods. Now it is possible to obtain monodisperse and stable samples with excellent optical properties using simple and low energy consuming methods. Recently alternative methods for preparation as inorganic NPKs have been explored. Light induced synthesis of perovskites has been explored, although these methods are still in their infancy. The most notable results have been reported for $CsPbBr_3$ where lamellar structures where synthesized by UV-light induced self-assembly of nanoplatelets and then the cubic nanocrystals into nanowires[25–27]. Then Liu et al, reported the assembly and posterior fusion of cubic $CsPbBr_3$ nanocrystals into defect free nanowires[25] after irradiation of the sample with visible light.

On the other hand, although great progress has been done in the comprehension of fundamental phenomena behind the outstanding properties, a long way is still ahead. Understanding these processes is important to understand the growth kinetics and the surface ligand properties of perovskites. These properties highly determine the properties of the crystals. The lack of techniques to translate the high performance of nanocrystals into solid films restricts the successful exploitation of such materials in optoelectronics applications[26].

In this work we report for the first-time evidence of the spontaneous assembly of γ-$CsPbI_3$ cubic nanoparticles into nanorods when irradiated with a Solar Simulator light. Performing temperature dependent CW-PL spectroscopy an in-depth analysis of the optoelectronic properties of both nanoparticles and nanorods was performed. We investigated the effect of exciton-phonon interaction, the influence in the exciton binding energy and structural disorder. Our results show that the as
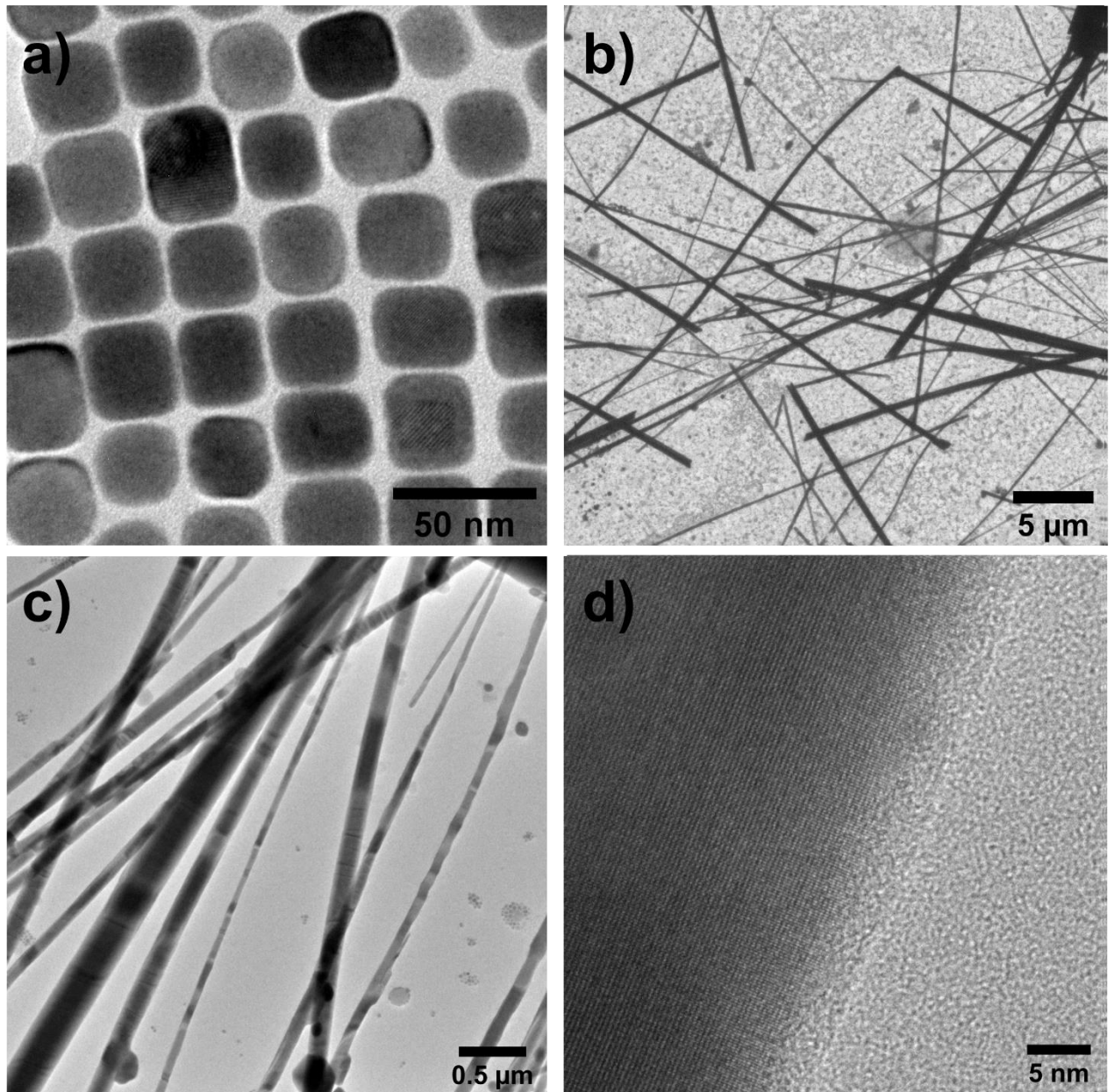
Figure 1: TEM images of γ-CsPbI₃ nanoparticles (a) and different magnifications of nanorods (b, c and d) obtained after irradiation of colloidal nanoparticles for 20 hours with a solar simulator.

mentioned characterization is an excellent tool to identify fundamental changes in the properties of crystals.

Results and discussion

TEM images (Figure 1-a) show that cubic nanoparticles with excellent crystallinity and an average size of 32±5 nm are present in the non-radiated sample as previously reported [20]. The irradiation of the samples with a Solar Simulator (see Experimental section for more details) effectively produced the assembly of the original nanoparticles into nanorods, with a length between 20 μm

and 35 µm and a width between 50 nm and 300 nm (Figure 1). Besides, the nanorods retained the crystalline structure in the original nanoparticles as shown in Figure 1 d. A similar behavior has been reported for CsPbBr₃ nanoparticles[25]. In this work, the self-assembly effect is attributed to the desorption of surface ligands (oleic acid/oleylamine), which reduces steric repulsion between adjacent nanocrystals. In our case, since the same ligands were used, the self-assembly process can be attributed to the same causes. It should be highlighted that no previous treatment or functionalization had to be performed to obtain the assembly.

Figure 2 a show the transmittance T spectra of γ-CsPbI₃ nanoparticles, where a clear absorption edge is observed around 700 nm (Figure 2). To determine the bandgap energy the experimental absorbance of the spectra was calculated as $\alpha_{exp} = -\ln(T)$. As shown in Figure 2 b an strong background, originated in reflectance at sample interface, below-gap absorption and light dispersion, generates uncertainty in the zero line position of α_{exp}. For a correct determination of the absorption edge this background signal was subtracted considering a residual absorption following an indirect Tauc relation (see inset in Figure 2). From this a background signal α_{BKG} is determined that when susbstracted to α_{exp} gives a corrected absorption α_{Corr} as shown in Figure 2. Performing this correction, the onset of the absorbance spectra the does not significantly vary from both samples and is located at 1.79±0.01 eV as seen in Figure 3.
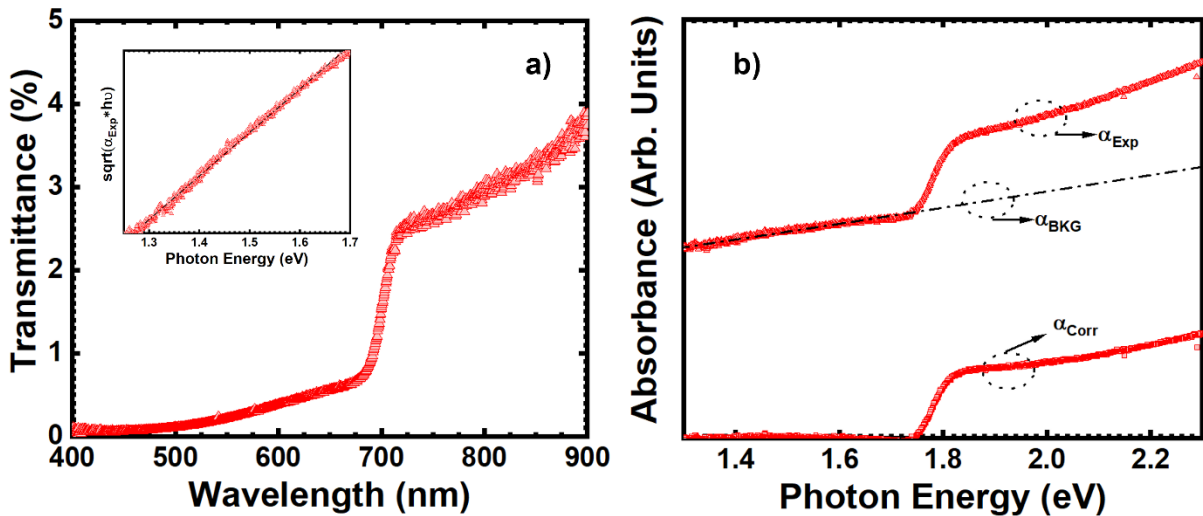

Figure 2: a) Transmittance of γ-CsPbI₃ nanoparticles b) corrected absorbance signal obtained by subtracting the background signal α_{BKG} calculated from an indirect Tauc plot as shown in the inset of a).
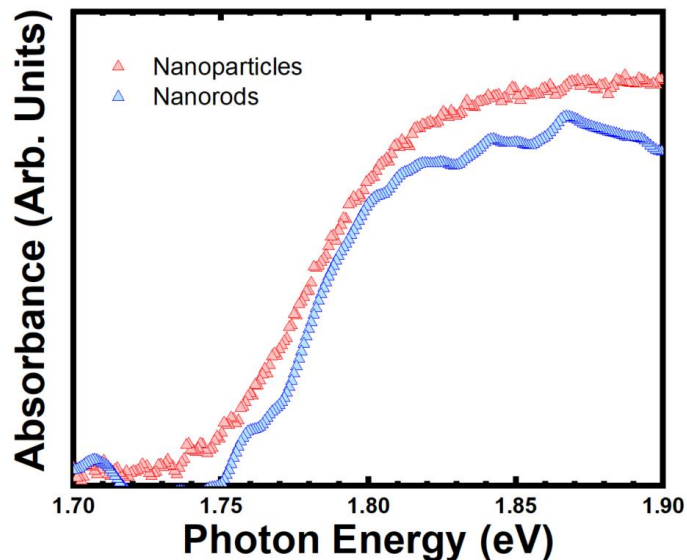
Figure 3: Absorbance edge of nanoparticles (red triangles) and nanorods (blue triangles).

In our previous work we showed that the photoluminescence (PL) in γ-CsPbI$_3$ is originated in excitonic recombination[20]. Therefore, when temperature is increased the full width at half maximum (FWHM or Γ) of PL spectra widens and its amplitude (I) decreases as shown in Figure 4 a and b for nanoparticles and nanorods respectively. The change in the shape of the mentioned spectra was quantified by fitting them with a pseudo-Voight function[28] (a lineal combination of a Gaussian and a Lorentzian function weighted by a mixing parameter determining the relative contribution of each peak). In both cases the maximum of PL spectra blueshifts when the temperature increases (as usually reported for perovskites) from 1.71±0.01 to 1.74±0.01 for nanoparticles and from 1.74±0.01 to 1.77±0.01 for nanorods (Figure 5 a). As proven in our previous work the blueshift is originated in the temperature dependence of bandgap energy and Stokes Shift[20]. Besides, the peak energy for the nanorods is in all cases ~30 meV larger than for the nanoparticles. Similar shifts in PL have been previously observed in pressure-induced experiments [29–31] and from focused ion beam milling[32]. In all cases the blueshift was attributed to an amorphization process producing AX$_6$ octahedral tilting and atomic orbital overlap suppression originated in the loss of long-range order in the perovskite structure[30,31]. In our case an amorphization process is also likely since the radiation from the solar simulator produces the desorption of the ligands, fundamental for the assembly effect, that is a known cause of destabilization of the crystal structure[33,34]. Besides, the solar simulator has a considerable UV component, which has been proven to produce a degradation of the crystal structure in perovskites[35,36]. This can be the cause of the rapid shift of the color of the sample from black to brown yellow after nanorods optical characterization.
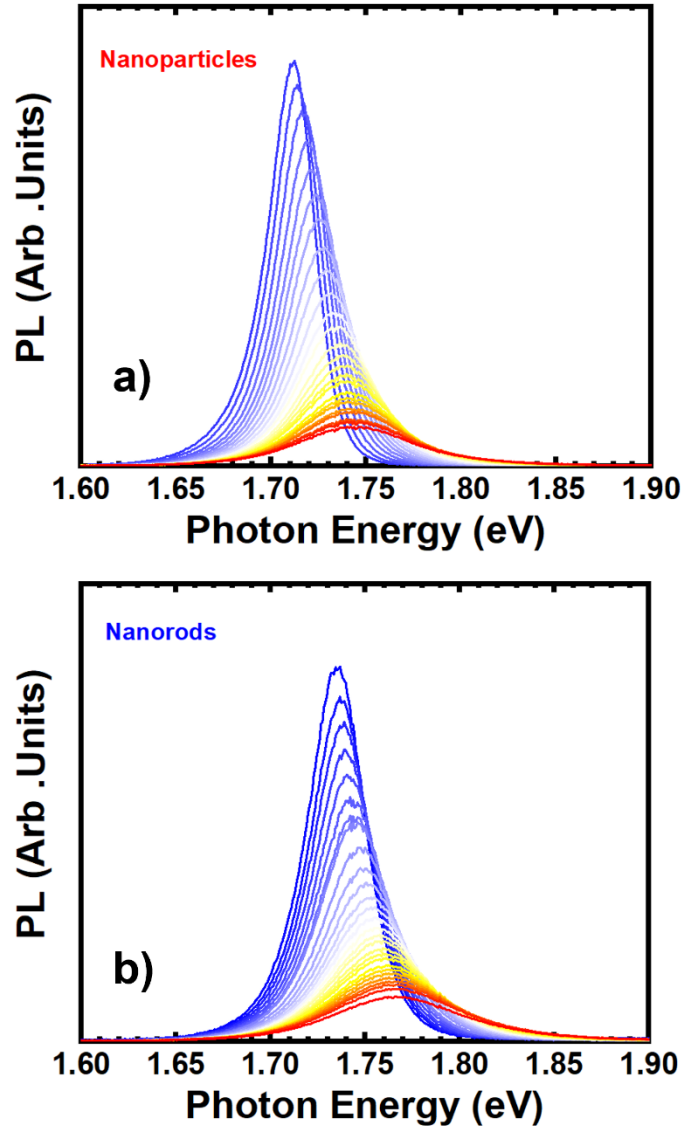
Figure 4: Temperature dependence of Photoluminescence spectra for nanoparticles (a) and nanorods (b) obtained between 50K (blue) and 290 K (red).

The increase in full width at half maximum Γ, depicted in Figure 5-b, is rooted in the interaction of excitons with LO phonons [20,37,38]. Therefore, the $\Gamma\ vs\ T$ dependence can be fitted with the Segall's model[39] ((1). This model considers the broadening as formed by three contributions: an inhomogeneous broadening Γ_{inh}, independent of T, originated in the intrinsic crystal disorder. On the other hand, the interactions of excitons with phonons (represented by Γ_{Ac} for acoustic and Γ_{LO} for longitudinal optical phonons) are determined by the population of phononic states i.e., by a Bose-Einstein distribution. In the case of acoustic phonons, given their low energy, the temperature dependence can be considered lineal.

$$\Gamma(T) = \Gamma_{inh} + \Gamma_{Ac} + \Gamma_{LO} = \Gamma_{inh} + \varphi_{Ac}T + \frac{\varphi_{LO}}{e^{\frac{E_{LO}}{k_B T}} - 1} \tag{1}$$

To perform the fitting of the data with this model the term accounting for the interaction with acoustical phonons is usually omitted, since perovskites are polar inorganic semiconductors[20,40]. With this consideration the inhomogeneous broadening increases from 29±1 meV in nanoparticles to 39±1 meV in nanorods. An increase in Γ_{inh} is also consistent with the amorphization of the crystal structure. On the other hand, E_{LO} is almost equal in both samples, 20±5 meV and 12±3 meV for nanoparticles and nanorods respectively. The small difference indicates that the process of amorphization is only partial, thus preserves the perovskite structure[32].
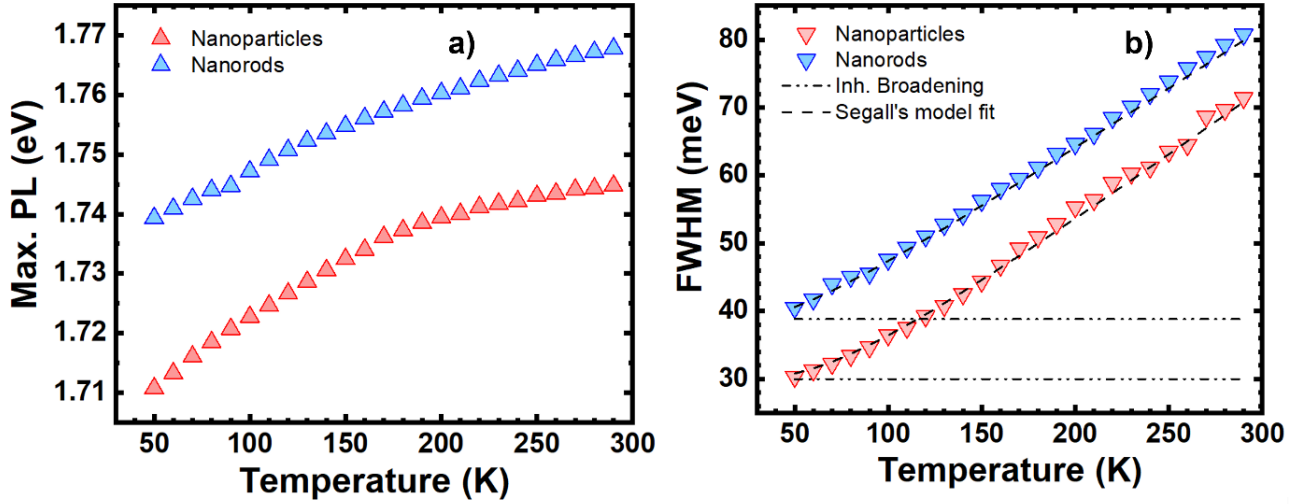

Figure 5: Evolution of maximum of PL (a) and FWHM (b) with temperature for nanoparticles (red) and nanorods (blue).

Another usual result reported for perovskites is the decrease in PL area I as temperature increases. As also proved in our previous work this is produced by an increase in the probability of dissociation of the exciton when the thermal energy is increased. The main cause of exciton dissociation is the thermal excitement of the carriers to the corresponding conduction (for electrons) and valence (for holes) band. So, the activation energy of this process should be the exciton binding energy. The binding energy of the exciton E_B is determined ((2) by the dielectric constant of the medium ϵ_r, m_0 the rest electron mass, μ the reduced mass of the electro-hole system and R_H the Rydberg energy of the hydrogen atom (13.6 eV). Besides, the principal quantum number n determines the relative level from the ionization energy[41,42].

$$E_B(n) = -\frac{\mu}{m_0 \epsilon_r^2} \frac{R_H}{n^2} \tag{2}$$

This energy can be calculated from the plot of PL area vs T^{-1} (Figure 6) fitting the data with an Arrhenius like expression given by (3 [20,37]. Obtained values in perovskites are comparable with the thermal energy at room temperature, which is desirable for applications in solar cells[43].

$$I(T) = \frac{I_0}{1 + a \exp(-E_B/K_B T)} \tag{3}$$

This fitting shows that E_B decreased from 35±2 meV in nanoparticles to 28±2 meV in nanorods. This effect is produced by a change in the characteristic size of the samples. There is extensive evidence, in both perovskites[43,44] and traditional semiconductors[45–47], proving that E_B decreases with increasing size.
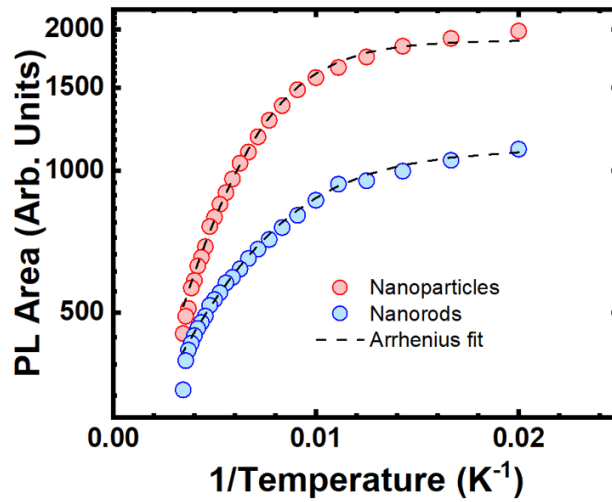

Figure 6: Arrhenius diagram of PL area (logarithmic) vs T^{-1} showing experimental results for nanoparticles (red) and nanorods (blue) and numerical fit with (3 (dashed black).

Conclusions

In this work we have demonstrated for the first time the capacity for γ-CsPbI$_3$ nanoparticles to self-assemble into nanorods when irradiated with visible light. Temperature dependent continuous wave photoluminescence characterization showed that the self-assembling process can negatively impact the crystalline structure of the nanorods. This amorphization process is manifested in a blueshift and an increase in the full width ah half maximum of nanorods PL spectra when compared with nanoparticles. The widening of the spectra increases the inhomogeneous broadening obtained by fitting experimental results with Segall's model for exciton-phonon interaction. This fitting also shows that the exciton phonon interaction is not considerably affected by the change in crystallinity. Finally, we also found that the exciton binding energy in nanorods is lower than in nanoparticles, what can be attributed to an increment in the size of the nanostructures. Our study shows also that temperature-dependent CW-PL spectroscopy can be employed to characterize crystal quality and to indirectly identify underlying processes such as amorphization. This method can provide valuable insights into the fundamental properties of perovskite materials and contribute to the further development of perovskite-based devices in optoelectronic applications.

Experimental

Cubic nanoparticles with an average size of 32 nm were synthetized using the hot injection method previously described in detail [20,48]. To trigger the assembly of the colloidal nanocrystals suspended in toluene the sample was radiated for 20 hours with a NEWPORT 9600 Solar Simulator. The intensity of the radiation was adjusted to one sun using a calibrated Silicon cell (Newport 99150V). Colloidal nanostructures before and after irradiation were drop casted on a glass substrate to perform the temperature dependent PL characterization. Continuous-wave photoluminescence (PL) spectroscopy from 10 to 290 K, cooling the sample with a CTI Cryogenics CRYODYNE cryostat, was performed on both samples. As excitation source for PL measurements a Thorlabs M365FP1 LED (365 nm, 9.8 mW), filtered with a 400 nm low-pass filter, was used. PL signal was collected with an Ocean Optics Flame S-UV-VIS-ES spectrometer.

Acknowledgments

References

[1]   M. V. Kovalenko, L. Protesescu, M. I. Bodnarchuk, *Science* **2017**, *358*, 745.

[2]   Q. A. Akkerman, G. Rainò, M. V. Kovalenko, L. Manna, *Nat. Mater.* **2018**, *17*, 394.

[3]   L. Protesescu, S. Yakunin, M. I. Bodnarchuk, F. Krieg, R. Caputo, C. H. Hendon, *Nano Lett* **2015**, *15*, 3692.

[4]   X. Li, Y. Wu, S. Zhang, B. Cai, Y. Gu, J. Song, H. Zeng, *Adv. Funct. Mater.* **2016**, *26*, 2435.

[5]   S. D. Stranks, G. E. Eperon, G. Grancini, C. Menelaou, M. J. P. Alcocer, T. Leijtens, L. M. Herz, A. Petrozza, H. J. Snaith, *Science* **2013**, *342*, 341.

[6]   P. Becker, J. A. Márquez, J. Just, A. Al-Ashouri, C. Hages, H. Hempel, M. Jošt, S. Albrecht, R. Frahm, T. Unold, *Adv. Energy Mater.* **2019**, *9*, 1900555.

[7]   N. A. N. Ouedraogo, Y. Chen, Y. Y. Xiao, Q. Meng, C. B. Han, H. Yan, Y. Zhang, *Nano Energy* **2020**, *67*, 104249.

[8]   F. Liu, Y. Zhang, C. Ding, S. Kobayashi, T. Izuishi, N. Nakazawa, T. Toyoda, T. Ohta, S. Hayase, T. Minemoto, K. Yoshino, S. Dai, Q. Shen, *ACS Nano* **2017**, *11*, 10373.

[9]   J. Zhang, C. Yin, F. Yang, Y. Yao, F. Yuan, H. Chen, R. Wang, S. Bai, G. Tu, L. Hou, *J. Phys. Chem. Lett.* **2021**, *12*, 2437.

[10]   A. Dutta, R. K. Behera, P. Pal, S. Baitalik, N. Pradhan, *Angew. Chemie Int. Ed.* **2019**, *58*, 5552.

[11]   H. Huang, M. I. Bodnarchuk, S. V. Kershaw, M. V. Kovalenko, A. L. Rogach, *ACS Energy Lett.* **2017**, *2*, 2071.

[12]   D. Ramírez, G. Riveros, P. Díaz, J. Verdugo, G. Núñez, S. Lizama, P. Lazo, E. A. Dalchiele, D. L. Gau, R. E. Marotti, J. A. Anta, L. Contreras-Bernal, A. Riquelme, J. Idigoras, *ChemElectroChem* **2020**, *7*, 3961.

[13]   X. Zhao, T. Liu, Q. C. Burlingame, T. Liu, R. HolleyIII, G. Cheng, N. Yao, F. Gao, Y.-L. Loo, *Science* **2022**, *377*, 307.

[14]   P. Roy, N. Kumar Sinha, S. Tiwari, A. Khare, *Sol. Energy* **2020**, *198*, 665.

[15]   X. Zhang, C. Sun, Y. Zhang, H. Wu, C. Ji, Y. Chuai, P. Wang, S. Wen, C. Zhang, W. W. Yu, *J. Phys. Chem. Lett.* **2016**, *7*, 4602.

[16]   H. Tsai, S. Shrestha, R. A. Vilá, W. Huang, C. Liu, C. H. Hou, H. H. Huang, X. Wen, M. Li, G. Wiederrecht, Y. Cui, M. Cotlet, X. Zhang, X. Ma, W. Nie, *Nat. Photonics* **2021**, *15*, 843.

[17]   S. Yakunin, L. Protesescu, F. Krieg, M. I. Bodnarchuk, G. Nedelcu, M. Humer, G. De Luca, M. Fiebig, W. Heiss, M. V. Kovalenko, *Nat. Commun.* **2015**, *6*, 1.

[18]   Q. Chen, J. Wu, X. Ou, B. Huang, J. Almutlaq, A. A. Zhumekenov, X. Guan, S. Han, L. Liang, Z. Yi, J. Li, X. Xie, Y. Wang, Y. Li, D. Fan, D. B. L. Teh, A. H. All, O. F. Mohammed, O. M. Bakr, T. Wu, M. Bettinelli, H. Yang, W. Huang, X. Liu, *Nature* **2018**, *561*, 88.

[19]   C. Zhu, M. Marczak, L. Feld, S. C. Boehme, C. Bernasconi, A. Moskalenko, I. Cherniukh, D. Dirin, M. I. Bodnarchuk, M. V. Kovalenko, G. Rainò, *Nano Lett.* **2022**, *22*, 39.

[20]   D. L. Gau, I. Galain, I. Aguiar, R. E. Marotti, *J. Lumin.* **2023**, *257*, 119765.

[21]   Y. Tong, B. J. Bohn, E. Bladt, K. Wang, P. Müller-Buschbaum, S. Bals, A. S. Urban, L. Polavarapu, J. Feldmann, *Angew. Chemie - Int. Ed.* **2017**, *56*, 13887.

[22]   H. Huang, L. Polavarapu, J. A. Sichert, A. S. Susha, A. S. Urban, A. L. Rogach, *NPG Asia Mater.* **2016**, *8*, e328.

[23]   M. C. Weidman, A. J. Goodman, W. A. Tisdale, *Chem. Mater.* **2017**, *29*, 5019.

[24]   J. Ye, M. M. Byranvand, C. O. Martínez, R. L. Z. Hoye, M. Saliba, L. Polavarapu, *Angew. Chemie* **2021**, *133*, 21804.

[25]   J. Liu, K. Song, Y. Shin, X. Liu, J. Chen, K. X. Yao, J. Pan, C. Yang, J. Yin, L. J. Xu, H. Yang, A. M. El-Zohry, B. Xin, S. Mitra, M. N. Hedhili, I. S. Roqan, O. F. Mohammed, Y. Han, O. M. Bakr, *Chem. Mater.* **2019**, *31*, 6642.

[26]   J. Shamsi, P. Rastogi, V. Caligiuri, A. L. Abdelhady, D. Spirito, L. Manna, R. Krahne, *ACS Nano* **2017**, *11*, 10206.

[27]   Y. Wang, X. Li, S. Sreejith, F. Cao, Z. Wang, M. C. Stuparu, H. Zeng, H. Sun, *Adv. Mater.* **2016**, *28*, 10637.

[28]   A. L. Stancik, E. B. Brauns, *Vib. Spectrosc.* **2008**, *47*, 66.

[29]   L. Zhang, Q. Zeng, K. Wang, *J. Phys. Chem. Lett.* **2017**, *8*, 3752.

[30]   Y. Wang, X. Lü, W. Yang, T. Wen, L. Yang, X. Ren, L. Wang, Z. Lin, Y. Zhao, *J. Am. Chem. Soc.* **2015**, *137*, 11144.

[31]   H. Zhu, T. Cai, M. Que, J. P. Song, B. M. Rubenstein, Z. Wang, O. Chen, *J. Phys. Chem. Lett.* **2018**, *9*, 4199.

[32]   F. U. Kosasih, G. Divitini, J. F. Orri, E. M. Tennyson, G. Kusch, R. A. Oliver, S. D. Stranks, C. Ducati, *Microsc. Res. Tech.* **2022**, *85*, 2351.

[33]   E. Moyen, A. Kanwat, S. Cho, H. Jun, R. Aad, J. Jang, *Nanoscale* **2018**, *10*, 8591.

[34]   Y. Liu, Y. Li, X. Hu, C. Wei, B. Xu, J. Leng, H. Miao, H. Zeng, X. Li, *Chem. Eng. J.* **2023**, *453*, 139904.

[35]   S.-W. Lee, S. Kim, S. Bae, K. Cho, T. Chung, L. E. Mundt, S. Lee, S. Park, H. Park, M. C. Schubert, S. W. Glunz, Y. Ko, Y. Jun, Y. Kang, H.-S. Lee, D. Kim, *Sci. Rep.* **2016**, *6*, 38150.

[36]   T. Leijtens, G. E. Eperon, S. Pathak, A. Abate, M. M. Lee, H. J. Snaith, *Nat. Commun.* **2013**, *4*, 2885.

[37]   D. L. Gau, D. Ramírez, F. Iikawa, G. Riveros, P. Díaz, J. Verdugo, G. Núñez, S. Lizama, P. Lazo, E. A. Dalchiele, L. Contreras, J. Idigoras, J. Anta, R. E. Marotti, *ChemPhysChem* **2022**, *23*, e202200286.

[38]   R. Saran, A. Heuer-Jungemann, A. G. Kanaras, R. J. Curry, *Adv. Opt. Mater.* **2017**, *5*, 1700231.

[39]   S. Rudin, T. L. Reinecke, B. Segall, *Phys. Rev. B* **1990**, *42*, 11218.

[40]   A. D. Wright, C. Verdi, R. L. Milot, G. E. Eperon, M. A. Pérez-Osorio, H. J. Snaith, F. Giustino, M. B. Johnston, L. M. Herz, *Nat. Commun.* **2016**, *7*, 1.

[41]   M. Fox, *Optical Properties of Solids*, AAPT, **2002**.

[42]   C. F. Klingshirn, **2012**, DOI 10.1007/978-3-642-28362-8.

[43]   R. L. Z. Hoye, J. Hidalgo, R. A. Jagt, J. P. Correa-Baena, T. Fix, J. L. MacManus-Driscoll, *Adv. Energy Mater.* **2022**, *12*, 2100499.

[44]   K. Zheng, Q. Zhu, M. Abdellah, M. E. Messing, W. Zhang, A. Generalov, Y. Niu, L. Ribaud, S. E.

Canton, T. Pullerits, *J. Phys. Chem. Lett.* **2015**, *6*, 2969.

[45]   J. M. Elward, A. Chakraborty, *J. Chem. Theory Comput.* **2013**, *9*, 4351.

[46]   P. Ramvall, S. Tanaka, S. Nomura, P. Riblet, Y. Aoyagi, *Appl. Phys. Lett.* **1998**, *73*, 1104.

[47]   S. I. Pokutnii, *Semiconductors* **2010**, *44*, 488.

[48]   B. Tang, L. J. Ruan, C. Qin, A. Shu, H. He, Y. Ma, *Adv. Opt. Mater.* **2020**, *8*, 2000498.

Work in Progress

"Concentrate all your thoughts upon the work in hand. The sun's rays do not burn until brought to a focus. " — Alexander Graham Bell

5.   Work in Progress

The published results so far constitute only a part of the total results obtained from a large number of measurements performed on samples with different compositions and morphologies. This chapter presents some interesting results that are currently being worked on and are expected to be included in a manuscript to be submitted for publication soon. In summary, the results comprise the observation of excitonic localization effects in γ-CsPbI$_3$ nanoparticles and the effect of different samples composition in stoichiometric and non-stoichiometric CsPbBr$_3$ thin films. In both cases the obtained results will be analyzed considering the model developed to explain the photophysical processes of absorption and emission[1] in nanoparticles. We believe this is the best to test the validity of this model and to find weak spots to modify it if necessary.

5. 1-Evidence of Excitonic Localization in γ-CsPbI₃ Nanoparticles Revealed by Photoluminescence Spectroscopy.

As previously stated, luminescence in γ-CsPbI₃ nanocrystals is produced by excitonic recombination. Excitons can move freely inside the lattice or be bound as a whole (bounded electron-hole system) or to point defects (donors or acceptors impurities). In the last case the excitonic recombination still produces a photoluminescence signal but with lower energy than the signal obtained from free excitons[2,3]. The impurity-exciton binding energy can be determined by the difference between the free exciton PL energy and the bound exciton PL energy (this should not be confused with the energy binding the electron-hole pair to form the exciton). It is also possible, when the carrier-phonon interaction is strong that the exciton becomes immobilized by its own lattice distortion, then becoming confined to a localized region of the crystal[4]. The formation of self-trapped states is particularly common in metal halides[4].

Excitonic localization has important consequences on the optical and electronic properties of semiconductor materials. For example, it can influence the efficiency of light emission in devices such as LEDs, as localized excitons can emit light less efficiently than non-localized excitons[5]. It can also influence the conduction of electric current through the material, as localized excitons can interfere with the movement of free electrons through the material. For this reason, understanding and controlling exciton localization is an important area of research in materials science and semiconductor physics.

The presence of localized excitons can be identified by the anomalous dependence on temperature of photoluminescence spectra. This was theoretically studied (for traditional semiconductors) by Q. Li et al. who showed that:

1. The maximum of PL spectra presents an S shaped dependence with temperature, where the maximum first redshift, then blueshifts and finally redshifts again.
2. There is a reduction in the width of the photoluminescence peaks Γ with increasing temperature, contrary to the monotonic increase that we observe in the case of free excitons.

These trends are originated in the thermal redistribution of localized carriers within the localized states. In the following lines we reproduce the most important results in the mentioned work and then compare the given predictions with experimental results obtained in γ-CsPbI₃ nanoparticles.

To prove this, consider that the localized electronic states are defined by a density of states (DOS) $\rho(E)$ and that the carrier population at energy E and temperature T is determined by the density function $N(E,T)$. In the weak excitation limit the rate of change in $N(E,T)$ is given by the rate equation:

$$\frac{dN(E,T)}{dt} = G(E) - \frac{N(E,T)}{\tau_{tr}} \exp\left(\frac{E - E_a}{k_B T}\right) - \frac{N(E,T)}{\tau_r} + \frac{\gamma_c N'}{\Lambda} \rho(E) \tag{4}$$

where k_B is the Boltzmann constant, $G(E)$ is the rate of carrier generation, and is proportional to $\rho(E)$ i.e. $G(E) = \kappa\,\rho(E)$ with κ constant; the second term represents the thermally activated scape rate, characterized by a $1/\tau_{tr}$ (attempt-to-scape ratio of localized carriers), of localized carriers to a delocalized state of energy E_a; the third term describes the depopulation rate of localized carriers due to radiative recombination characterized by $1/\tau_r$. Finally, the last term represents the number of carriers re-captured by the localized states per unit time, where γ_c represents the recapture coefficient, N' is the total number of thermally activated carriers away from the localized states and is determined by the expression

$$N' = \int\limits_{-\infty}^{+\infty} \frac{N(E',T)}{\tau_{tr}} \exp\left(\frac{E' - E_a}{k_B T}\right) dE'$$

and Λ represents the total number of localized states, hence it can be written as $\Lambda = \int_{-\infty}^{+\infty} \rho(E')dE'$. As an approximation τ_{tr} and τ_r are assumed to be constants. The solution of (4 in the steady-state condition $\frac{dN}{dt} = 0$ is

$$N(E,T) = A(T)\,n(E,T)$$

with

$$n(E,T) = \frac{\rho(E)}{\exp\left(\dfrac{E - E_a}{k_B T}\right) + \tau_{tr}/\tau_r}$$

and

$$A(T) = \frac{\kappa\tau_{tr}}{(1 - \gamma_e) + \left(\dfrac{\tau_{tr}}{\tau_r}\right)\gamma_e\,\xi_1(T)/\Lambda}$$

In this last expression $\xi_1(T) = \int_{-\infty}^{+\infty} n(E',T)dE'$. Besides that, $n(E,T)$ is representative of the luminescence spectra since is the only solution that depends on both energy and temperature.

Considering that $n(E,T) = f(E,T) \cdot \rho(E)$ an explicit expression for the distribution function, given by (5, is obtained.

$$f(E,T) = \frac{1}{\exp\left(\dfrac{E - E_a}{k_B T}\right) + \dfrac{\tau_{tr}}{\tau_r}} \tag{5}$$

In general, the DOS of the system can be described by a Gaussian function determined by an amplitude ρ_0, a peak position E_0 and a standard deviation σ, i.e.

$$\rho(E) = \rho_0 \exp\left(-\frac{(E - E_0)^2}{2\sigma^2}\right)$$

With the previous results it is now possible to predict the temperature dependence of the parameters defining the photoluminescence spectra. To obtain the maximum of PL it suffices to find the maximum of $n(E,T)$. By setting the condition $\frac{\partial n(E,T)}{\partial E} = 0$ it is found that the maximum of PL is determined by the expression

$$E = E_0 - x\, k_B T$$

where $x(T)$ is obtained numerically solving[6] (6

$$x \exp x = \left[\left(\frac{\sigma}{k_B T}\right)^2 - x\right]\left(\frac{\tau_r}{\tau_{tr}}\right) \exp\left(\frac{E_0 - E_a}{k_B T}\right) \tag{6}$$

This expression has a single solution for $0 < x < \left(\frac{\sigma}{k_B T}\right)^2$.

So, an expression for the temperature dependence of the PL maximum (approximating the temperature dependence of the bandgap with the Varshni equation[3,7]) is given by (7

$$E(T) = E_0 - \frac{\alpha T^2}{\Theta + T} - x\, k_B T \tag{7}$$

For traditional tetragonal semiconductors, in which the bandgap decreases with temperature, $E(T)$ has an S-shaped dependence as shown in Figure 7-a.
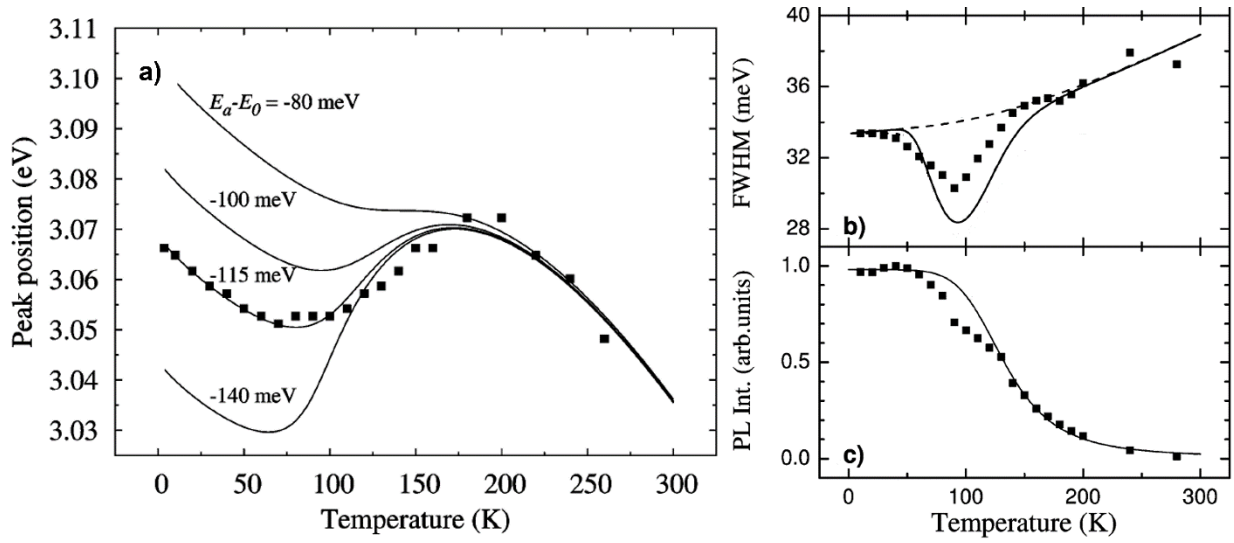

Figure 7: Experimental behavior for a) exciton peak energy b) FWHM and c) exciton PL as reported in InGaAs/GaAs and InGaN/GaN quantum dots by Q.Li et. al. (Figure adapted from reference [5])

From the expression of $n(E,T)$ it is also possible to derive the **Full width at half-maximum** of the PL spectra by numerically calculating $n(E,T) = n(E_{peak},T)/2$. It is possible to see that this magnitude can decrease with increasing temperature as shown in Figure 7-b. Finally, the variation of the integrated photoluminescence is proportional to the total number of localized carriers that can be calculated as

$$I(T) \propto \int_{-\infty}^{+\infty} N(E',T)\,dE' = A \int_{-\infty}^{+\infty} n(E',T)\,dE'$$

This expression can be approximately calculated obtaining the result[5,6]

$$I(T) \propto \left\{ 1 + (1 - \gamma_c) \exp\left[\frac{E_0 - E_a + k_B T \ln\left(\frac{\tau_r}{\tau_{tr}}\right)}{\sqrt{(k_B T)^2 + 2\left(\frac{\sigma}{2.41}\right)^2}} \right] \right\}^{-1} \tag{8}$$

This expression gives a monotonically decreasing variation of $I(T)$ with temperature as represented in Figure 7 c.

3. Experimental Results: Low temperature photoluminescence

The photoluminescence spectrum of the analyzed sample was measured between 12 K and 290 K using the experimental setup described in chapter 3. As observed in Figure 8-a PL spectra follows the usually observed trend of decreasing amplitude and increasing its width and maximum with temperature. However, in this case an asymmetry in the spectra appears for temperatures below 150 K. By performing a numerical fit with two Gaussian curves, it is possible to confirm that the asymmetry is produced by the appearance of a new peak in the low energy part of the spectra (Figure 8-b). On the contrary, for temperatures above 150 K, a good fit of the data is obtained by adjusting with a single Gaussian peak. The results obtained for the areas, peak energy positions, and widths of the Gaussian peaks show a great similarity with the predictions given by Q. LI's model, as we will discuss below. Therefore, we conclude that the appearance of the second peak is due to the localization of excitons produced by the absorption of high-energy photons.

Firstly, the variation of the total area of the PL with temperature follows an Arrhenius diagram as shown in Figure 9-a. Hence, the main quenching channel for photoluminescence is thermal dissociation of excitons[1]. In addition, by fitting an Arrhenius function with a single activation energy, we obtain that the
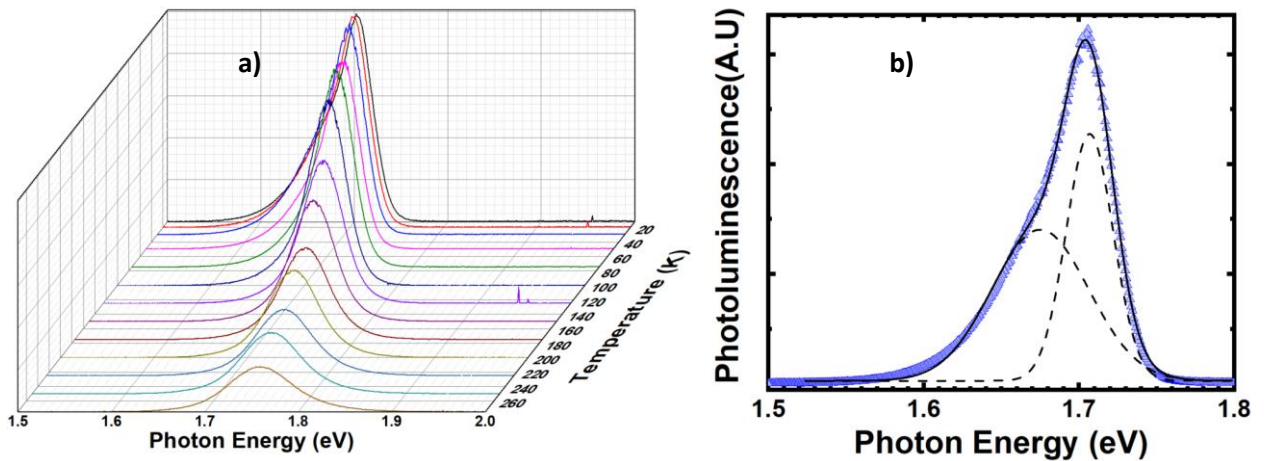
binding energy of excitons in this case is 6.0±2 meV. On the other hand, if we analyze the temperature dependence of the area of each peak separately (Figure 9-b), we see that the contribution of the low-energy peak decreases monotonically, as predicted by (8, until it becomes 0 at 150 K. In contrast, the high-energy peak increases up to 150 K and then decreases. This can be explained by considering that as thermal energy increases, the probability of excitons to delocalize increases and therefore recombine as free excitons (higher energy). This thermal transfer reduces the number of localized excitons and increases that of free excitons as temperature increases.

As can be seen in Figure 10 a, the temperature evolution of the energy of the two photoluminescence peaks is quite different. On one hand, the higher energy peak follows the typical trend of increasing with temperature as expected for free exciton recombination. On the other hand, the lower energy peak shows an increase up to around 100 K, reaching a local maximum, and then decreases until it disappears. This behavior does not follow the S shaped predicted by Q. Li's model for the maximum of PL in localized excitons. The discrepancy may be due to the fact that the aforementioned model is derived for conventional semiconductors (such as GaAs and I don't know what else) in which the bandgap decreases with temperature (see (7). Therefore, the anomalous behavior of perovskites, increasing bandgap with temperature, compensates for the initial decrease, causing the energy to tend towards an approximately constant value. Similar results have been reported in $CsPbBr_3$ nanosheets[8].
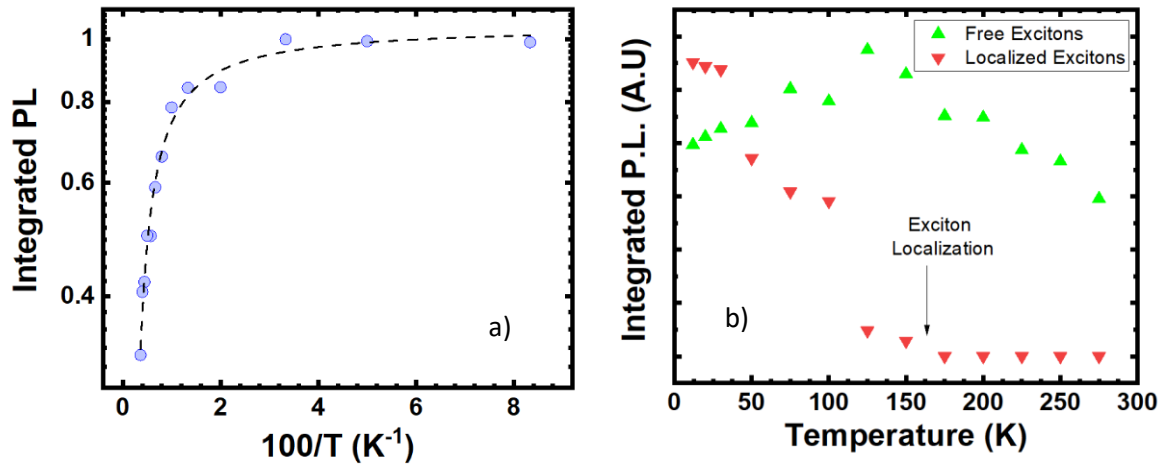

Figure 9: The total area of PL peaks follows an Arrhenius-like behavior indicating that thermal dissociation is the most relevant mechanism for PL quenching b) PL area of free (green triangles) and localized (red triangles) excitons.

Finally, the evolution of the peak widths Γ with temperature is shown in Figure 10 b. For the high-energy peak a monotonic increase with temperature, as the one predicted by Segall's model, was obtained. On the other hand, the low-energy peak maintains its width practically constant until 100 K, and then this parameter decreases rapidly. This reduction is also consistent with the

prediction of the Q. Li's model although the valley predicted is not fully viewed as the amplitude of localized excitons falls to cero before increasing again.
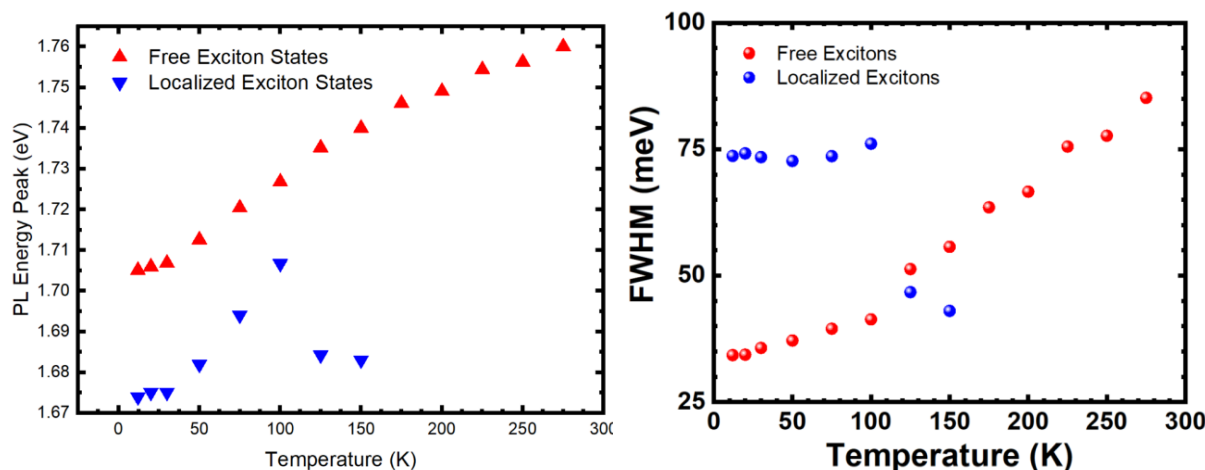

Figure 10: a) Evolution of excitonic emission energy corresponding with free (red triangles) and localized excitons (blue triangles) b) Evolution of the Full Width at Half Maximum of photoluminescnece peaks asociated with free (red circles) and localized excitons (blue circles).

Conclusions:

The excitonic behavior of a sample of γ-CsPbI$_3$ nanoparticles was studied using temperature-dependent photoluminescence spectroscopy. The results show that in this case the usual behavior observed in perovskites is generally obtained, i.e. a decrease in the spectral area, as well as broadening and blue shift as the temperature increases. However, a detailed analysis reveals the appearance of a second low energy peak in the photoluminescence spectrum that appears for temperatures below 150 K. By fitting the results with one or two Gaussian curves, depending on the case, the dependency of each peak with temperature were obtained. The high-energy peak follows the already-known behavior of free excitons. On the other hand, the low-energy peak shows a non-monotonic dependence of its maximum and a reduction in its half-width at half-maximum as the temperature increases. This behavior, very similar to that described by Q. Li's model of exciton localization, being a strong indication that this peak is originated by the radiative recombination of localized exciton. This thesis is further supported by the fact that the number of localized excitons decreases with temperature until disappearing, while the number of free excitons increases. This behavior suggests that thermal energy is responsible for providing energy that allows localized excitons to be released and thus recombine as free excitons. Determining the causes of exciton localization is, indeed, a significant challenge. Although empirical observations and comparisons with existing models, such as the one proposed by Q. Li, can provide strong indications of the presence of localized excitons, the task of identifying the specific factors causing this localization is more complex. To draw more definitive conclusions about the causes of exciton localization, it would be necessary to carry out additional, more detailed investigations. These could

include a deeper study of the structure and properties of perovskites, as well as the use of more sophisticated characterization techniques or the exploration of different theoretical models.

5. 2 – Excitonic behavior in stoichiometric and non-stoichiometric CsPbBr₃ thin films.

In the manuscript entitled "Photophysical and Photoelectrochemical Properties of CsPbBr₃ Films Grown by Electrochemically Assisted Deposition", only some of the data obtained from photoluminescence and transmittance measurements as a function of temperature were published. The published data were obtained for the sample with optimized stoichiometry and allowed us to report several relevant parameters such as the characteristic energies of exciton-phonon interaction and the Stokes Shift, among others, as well as their dependence on temperature. While the aforementioned work constituted an interesting and valuable contribution, it was when we extended the studies to CsPbI₃ nanostructures[1] that we acquired a deeper and more mature understanding of the subject. This allowed us to be much more critical of the abundant results published in the literature for CsPbBr₃ and their interpretations. As mentioned earlier, it was through this work that we were able to distill a model based on excitonic behavior that explains the majority of the photophysical absorption and emission processes in inorganic perovskites. Additionally, given the similarities reported in the literature for the behavior of CsPbI₃ with other perovskites, both inorganic and hybrid, we believe that this model can be extended to other materials with the perovskite structure. We are currently working intensively to formalize this extension, exploring two paths:

1 -Analysis of stoichiometric CsPbBr₃ sample

Thanks to the previously mentioned model, we have been able to take a fresh look at the results obtained for CsPbBr₃ films. For example, we now understand that the activation energies mentioned in "Photophysical and Photoelectrochemical Properties of CsPbBr₃ Films Grown by Electrochemically Assisted Deposition" correspond to two channels of photoluminescence quenching. We can say that one of them, with a characteristic energy of 39 meV, is associated with the thermal dissociation of excitons, whose recombination produces photoluminescence. This interpretation is supported by the fact that this value is very close to the exciton binding energy reported in our first work obtained by fitting with the Elliott function[9]. The other energy obtained from the Arrhenius plot allows us to identify the presence of a second channel with an energy of 13 meV. Unfortunately, with the information we currently have, we cannot identify its nature.

By analyzing the absorbance spectra with the Elliot function (Figure 11-a), we extended the initial analysis to study the dependence of the bandgap energy, excitonic absorption maximum energy, and Stokes Shift on temperature. First, by analyzing the dependence of the bandgap energy on temperature, we can see a monotonically increase of this value with temperature, and not the nonmonotonically dependence observed for photoluminescence spectra peak position[10]. This non monotonically dependence is due to both, the dependence of bandgap energy with temperature and the strong dependence with temperature of the Stokes shift. Moreover, we can see that by fitting with the two-phonon model (see supplementary information in[1]) as previously described,

the contribution of optical phonons to the variation of the bandgap occurs through interaction with a phononic channel of 32 meV (Figure 11-b).
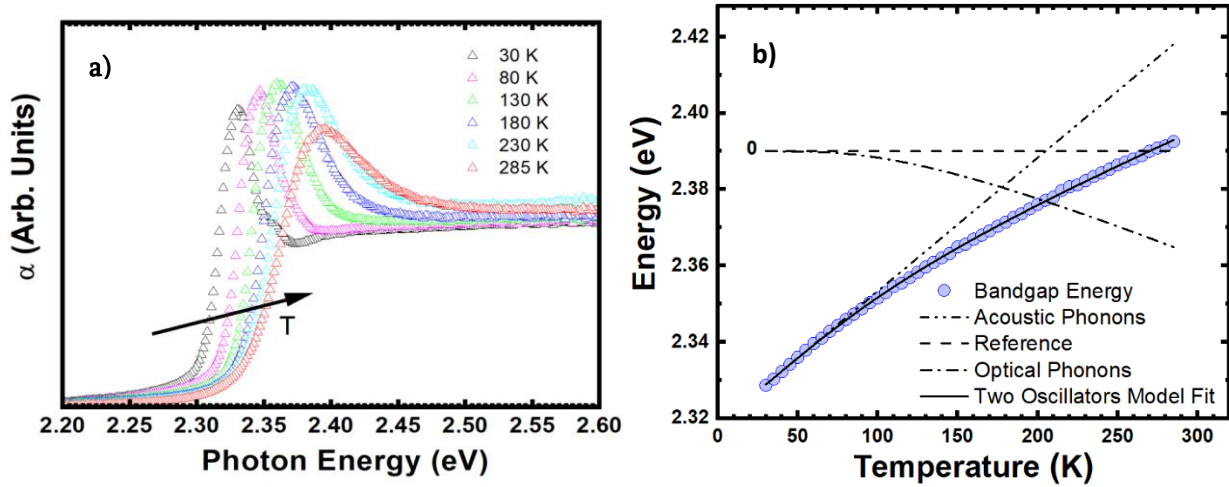

Figure 11: a) Temperature dependence of absorbance in stoichiometric CsPbBr₃ films. B) Bandgap energy dependence with temperature and contributions of acoustic and optical phonons obtained from the two oscillators model.

We consider this result very important since this value is very similar to the exciton-phonon interaction energy (30±4 meV) obtained by fitting the temperature dependence of the photoluminescence linewidth Γ with the Segall function[10].
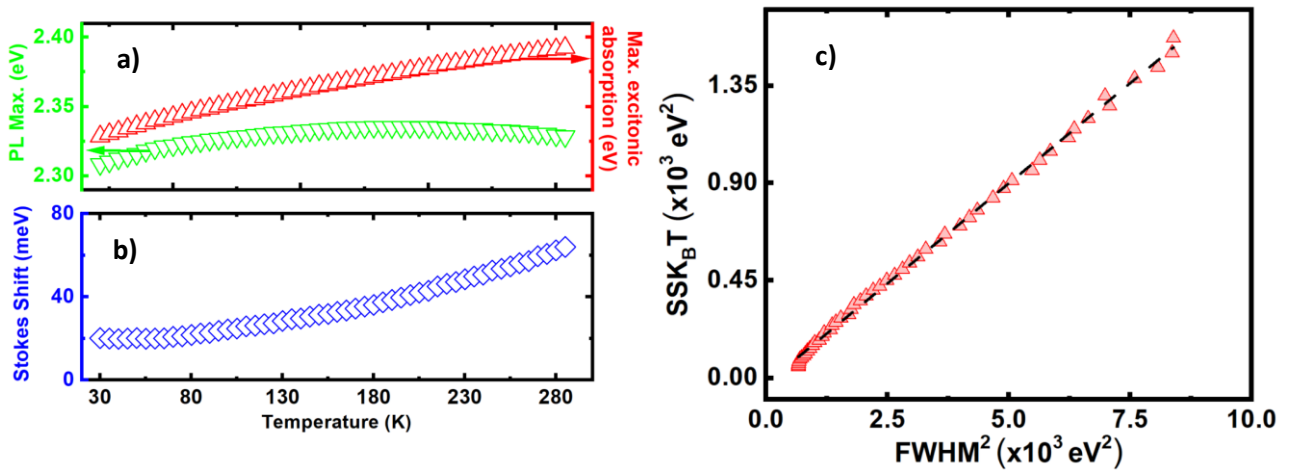

Figure 12: a) Maximum of excitonic absorption (red triangles), excitonic emission (green triangles) b) Stokes Shift (blue squares) as a function of temperature. C) Gurioli's model fit indicating thermalization of excitons as the cause of Stokes Shift.

From the Elliot function fitting, it is also possible to obtain the maximum corresponding to excitonic absorption. The difference between this value and the maximum of the photoluminescence (red and green triangles respectively in Figure 12-a) determines the Stokes Shift, which, as seen in Figure 12-c, increases monotonically with temperature, as in the case of CsPbI₃ nanoparticles[1].

Besides, when the product of the Stokes Shift and k_B T is plotted against Γ^2, a straight line with a slope of 0.185±0.02 is obtained, as shown in Figure 12-c. We can then conclude that the photoluminescence originates from excitonic recombination in CsPbBr₃, and that the Stokes Shift is produced by the thermalization of these pseudoparticles, as predicted by Gurioli's model[11].

Exciton Binding Energy:

From the fit with the Elliot function, it is also possible to determine the exciton binding energy as previously explained. Performing this analysis on the CsPbBr₃ measurements results in a non-monotonic variation as shown in Figure 13. Specifically, this parameter decreases slightly from 21.0 meV at 30 K to 19.7 meV at 100 K. From this temperature on there is a monotonous increase up to 35 meV at room temperature. This last value is in good agreement with the calculated value of 40 meV calculated using equation 5 from chapter 2, using average effective masses for electron and holes of 0.15 and 0.14 in free electron mass units and a dielectric constant of 4.96 as reported by Protesescu et. al.[12]. As mentioned earlier, variations in E_B are mainly determined by variations in the material's dielectric function ϵ. The results obtained indicate that this variation is more complex for CsPbBr₃ than for CsPbI₃, with some process that is activated around 100 K. This dependence is the result of the processes of increasing effective mass with temperature (due to the increase of the bandgap energy) and the reduction of permittivity due to thermal expansion, which tend to increase the binding energy of the exciton. On the other hand, screening due to phonons (which tends to decrease the Coulomb interaction) is used as an argument in the literature when this energy decreases with temperature.
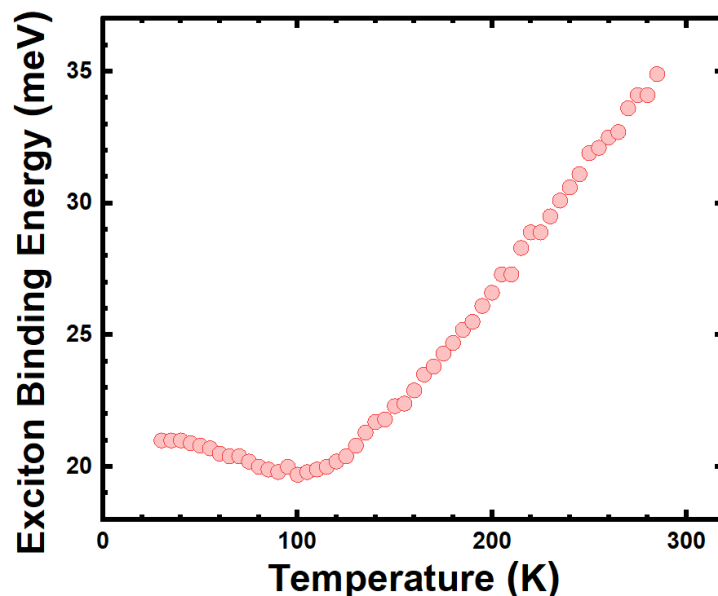

Figure 13: Temperature dependence of Exciton Binding Energy in stecheometric CsPbBr₃ film.

Urbach Energy

As in the case of CsPbI3, the low-energy end of the absorption presents a rapid increase that can be modeled with an exponential from which it is possible to obtain the Urbach Energy of the system. As previously mentioned, this is a measure of the disorder present in the crystal structure. By calculating the dependence of the Urbach Energy on temperature and fitting it with the model mentioned in our previous work[1], it is possible to obtain the energy $E_U(0)$, which represents 10 ± 1 meV, and the effective phononic mode energy that produces the increase in disorder of thermal origin. In this particular case, the latter value was 27 ± 2 meV, which is very close to the phononic mode energy that produces the exciton-phonon interaction and the increase in the bandgap energy with temperature.
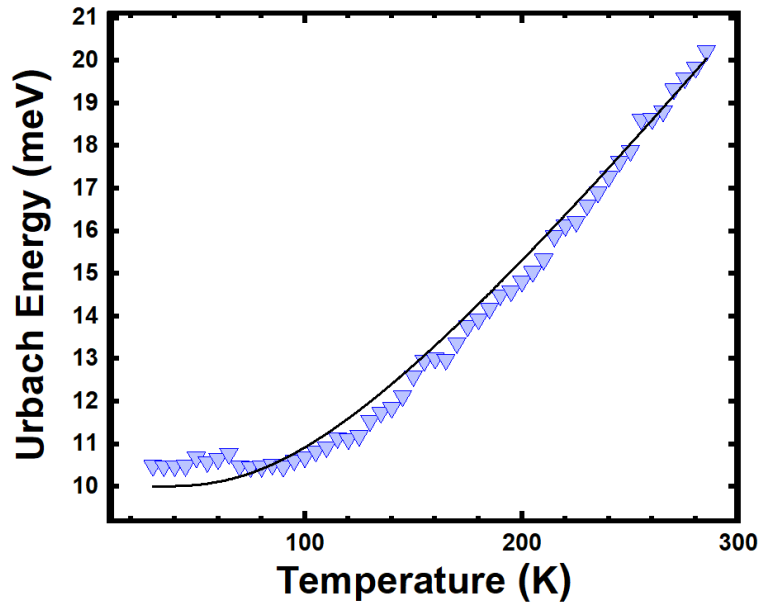

Figure 14: Temperature dependence of Urbach energy.

Having understood the excitonic nature of photoluminescence, it is also possible to interpret other results obtained with time-resolved photoluminescence spectroscopy performed at UNICAMP during 2020. This findings, partially published in reference [10], stem from the use of a streak camera, which generates a two-dimensional matrix of data points (as illustrated in Figure 15-a. Each point in this matrix represents a count from the light detector, contingent on both the wavelength and the time. By integrating this matrix over wavelength, we can produce time-resolved spectra. This process enables us to determine the time decay of photoluminescence from the acquired data. Equivalently, integrating over time provides us with the dependence on wavelength. Integrating the data in the first nanosecond from measurements taken at temperatures ranging from 6 K to 60 K, we yield the spectra depicted in Figure 15-b. These results show the same anomalous blueshift in PL when temperature is decreased than the previously described. Besides that, the shape of the peak tends to become more asymmetric widening towards the low-energy edge. This change is

produced by the appearance of a second peak with lower energy than the associated with the recombination of free excitons that increases its amplitude as the temperature is lowered. These changes are similar to the ones mentioned in the previous section. So, the second peak may be produced by the recombination of localized excitons. This localization, whose existence and origin are widely debated in the literature[8], causes the excitonic recombination to produce a photon with slightly lower energy than that corresponding to the recombination of the free exciton.
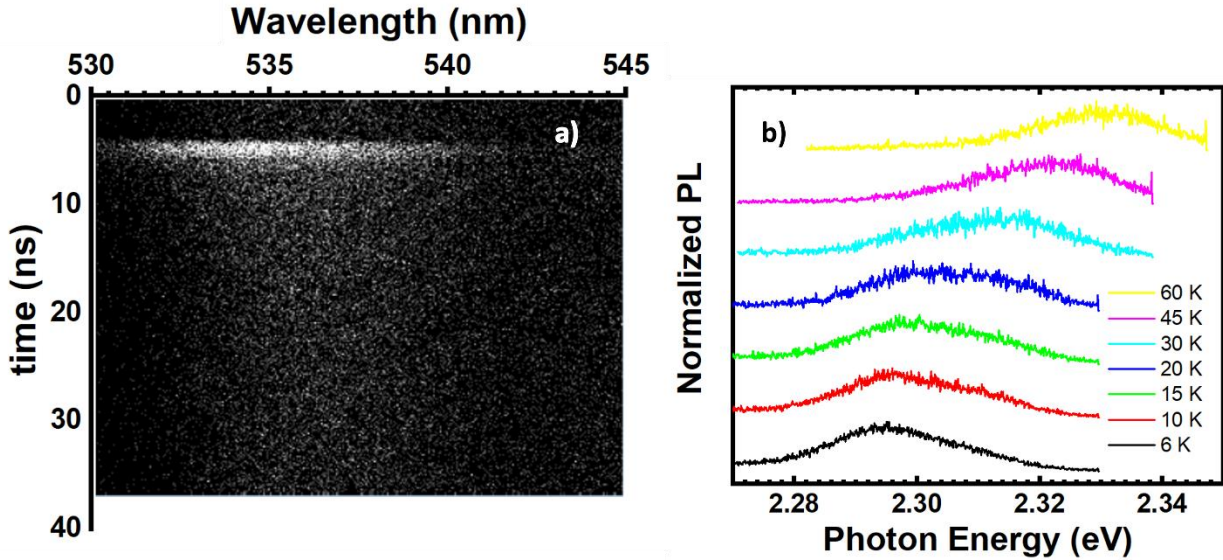

Figure 15: Dependence of the normalized PL spectra with the temperature (obtained from t = 0 s time resolved PL results). As the temperature increases a blue shift of both emission bands associated with free (higher energy) and localized excitons (lower energy) is observed.

2 – Analysis of non-stoichiometric samples: effect of composition in PL spectra

With this more complete view, we now focus on studying the possible variations that may exist in the properties of non-stoichiometric samples obtained with 4 and 13 spin-coating cycles during preparation, as described in reference [9]. As demonstrated in that work with the variation of spin-coating cycles besides the expected $CsPbBr_3$ phase, other minority phases of $CsPb_2Br_5$ and Cs_4PbBr_6 are obtained. The optical properties obtained from the variations in the photoluminescence spectrum with temperature are initially studied. Results obtained from the Arrhenius plot (Figure 16-a) show that E_B increases with variations in the stoichiometry of the samples while the energy associated with the second (low energy) dissociation channel remains almost constant as detailed in Table 1.

Table 1: Optical parameters obtained for samples synthesized with different spin-coating cycles.

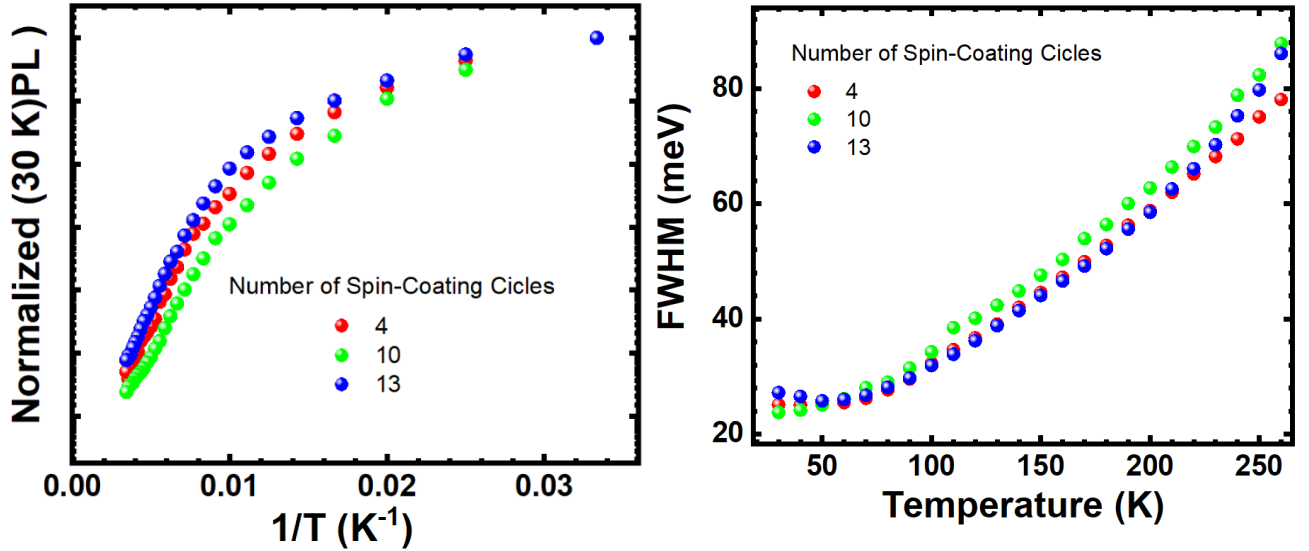| Spin-coating cycles	$E_B(meV)$	$E_{Act}(meV)$	$\Gamma\_inh(meV)$	$E_{LO}(meV)$
4	53 ± 3	14 ± 1	25 ± 1	22 ± 1
10	39 ± 5	13 ± 2	23 ± 2	30 ± 4
14	65 ± 10	15 ± 1	27 ± 1	35 ± 1

Figure 16: a) Arrhenius plot with PL area normalized to 30 K for better comparison and b) FWHM vs temperature for samples electrochemically synthesized using 4 (red), 10 (green) and 13 (blue) spin-coating cycles.

Fitting the dependence of the FWHM with temperature using Segall's expression the effect of composition in exciton phonon interaction was studied. Results show that inhomogeneous broadening is not significantly affected by the secondary phases. On the other hand, characteristic energy of LO phonons is considerably lower (22 ± 1 meV) for the 4 cycles sample when compared to the other two samples. It is possible that this is produced by the reduced grain size for this sample as previously reported[9].

Finally, we observed (as shown in Figure 17-a) that PL spectra became notably asymmetric specially for the non-stoichiometric samples. Asymmetry introduces uncertainty in the determination of maximum energy and FWHM. To avoid this uncertainty and to quantify the asymmetry the data was fitted with an asymmetric pseudo-Voigt function. The pseudo-Voigt function is is a mathematical function used to model the shape of peaks in spectroscopy and is the sum of a Gaussian ($G(E)$) and a Lorentzian function ($L(E)$) sharing its width and center and whose amplitudes are determined by a mixing parameter f ($0 \leq f \leq 1$), i.e.

$$y(E) = fL(E) + (1 - f)G(E)$$

The mixing parameter, f, determines the relative contribution of the Lorentzian and Gaussian functions to the pseudo-Voigt function. The sum of this kind of peak remains symmetric. To

introduce asymmetry[13] the width of the distributions is allowed to vary according to a sigmoidal function $\gamma(E)$. It must be noted that a new asymmetry parameter a is introduced in this procedure, and that the lower the parameter the more asymmetric the spectra.

$$\gamma(E) = \frac{2\gamma_0}{1 + \exp[a(E - E_0)]}$$

Fitting the experimental data with an asymmetric function shows that in all cases the asymmetry parameter increases with temperature as shown in Figure 17.
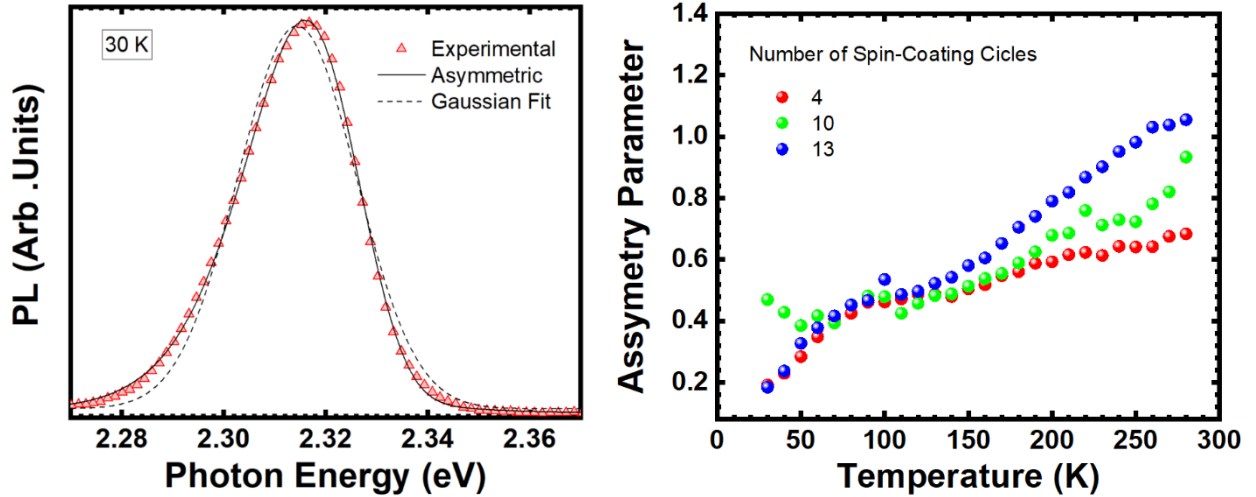

Figure 17: Temperatrue dependence of asymmetry parameter for samples with different stoichiometry.

The origin of the previously mentioned asymmetry is still unclear. However in a recent study by Boziki et al[14] suggest that the asymmetry may be produced by the preferential localization of Cs^+ in either of two off-centre positions of the inter-octahedral empty space between the $PbBr^6$ octahedra. This produces a local dipole moment, and consequently a Stark effect that affects the electronic energy levels, and then the emission spectra.

Conclusions:

The previously presented results can be interpreted clearly using the model presented in our manuscript on $CsPbI_3$. In particular, it is now clear the origin that the dependence of bandgap energy with temperature is mainly produced by exciton phonon interaction and that the Stokes Shift is originated in excitonic thermalization. We believe that this greatly strengthens our model, as it allows us to correctly interpret results obtained from a sample with different composition and morphology. Recently, we have been working on extending these results for the bandgap energy, Stokes Shift, Urbach energy and exciton binding energy to non-stoichiometric samples, which we expect to exhibit variations in these properties due to differences in phonon spectra, among other factors. We believe that the analysis we can achieve will be of great importance, as it has been shown that the composition of perovskite films strongly influences device performance, and the reasons for this have only begun to be understood. For this reason, we believe that the results we

can obtain with our model can make a significant contribution to understanding this important topic.

References

[1]   D. L. Gau, I. Galain, I. Aguiar, R. E. Marotti, *J. Lumin.* **2023**, *257*, 119765.

[2]   S. Shionoya, *Lumin. Solids* **1998**, 95.

[3]   C. F. Klingshirn, **2012**, DOI 10.1007/978-3-642-28362-8.

[4]   R. T. Williams, K. S. Song, *J. Phys. Chem. Solids* **1990**, *51*, 679.

[5]   Q. Li, S. J. Xu, M. H. Xie, S. Y. Tong, *Europhys. Lett.* **2005**, *71*, 994.

[6]   Q. Li, S. J. Xu, W. C. Cheng, M. H. Xie, S. Y. Tong, C. M. Che, H. Yang, *Appl. Phys. Lett.* **2001**, *79*, 1810.

[7]   Y. P. Varshni, *Physica* **1967**, *34*, 149.

[8]   X. Lao, Z. Yang, Z. Su, Z. Wang, H. Ye, M. Wang, X. Yao, S. Xu, *Nanoscale* **2018**, *10*, 9949.

[9]   D. Ramírez, G. Riveros, P. Díaz, J. Verdugo, G. Núñez, S. Lizama, P. Lazo, E. A. Dalchiele, D. L. Gau, R. E. Marotti, J. A. Anta, L. Contreras-Bernal, A. Riquelme, J. Idigoras, *ChemElectroChem* **2020**, *7*, 3961.

[10]   D. L. Gau, D. Ramírez, F. Iikawa, G. Riveros, P. Díaz, J. Verdugo, G. Núñez, S. Lizama, P. Lazo, E. A. Dalchiele, L. Contreras, J. Idigoras, J. Anta, R. E. Marotti, *ChemPhysChem* **2022**, *23*, e202200286.

[11]   M. Gurioli, A. Vinattieri, J. Martinez-Pastor, M. Colocci, *Phys. Rev. B* **1994**, *50*, 11817.

[12]   L. Protesescu, S. Yakunin, M. I. Bodnarchuk, F. Krieg, R. Caputo, C. H. Hendon, *Nano Lett* **2015**, *15*, 3692.

[13]   A. L. Stancik, E. B. Brauns, *Vib. Spectrosc.* **2008**, *47*, 66.

[14]   A. Boziki, M. I. Dar, G. Jacopin, M. Grätzel, U. Rothlisberger, *J. Phys. Chem. Lett.* **2021**, *12*, 2699.

Discussion

beginning is the end is the beginning and the beginning and the

gingerlouis
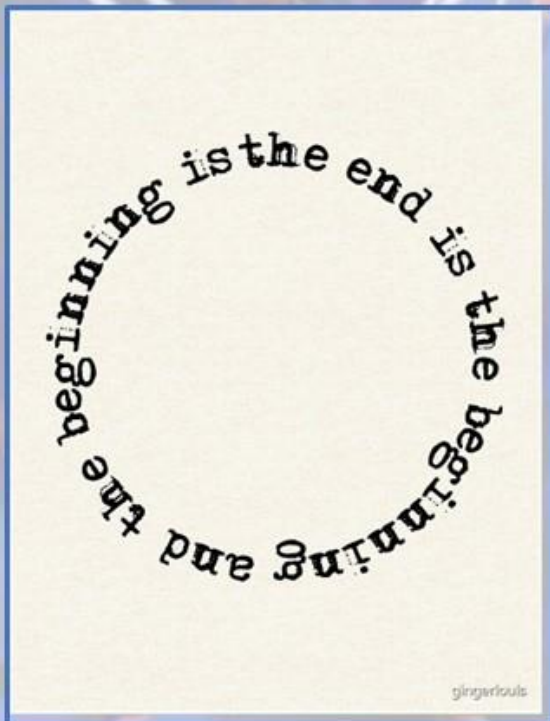
"We lose the precious sense that an end is only a beginning in disguise."
-Craig D. Lounsbrough

6. Work Summary

Optoelectronic fundamental properties of inorganic lead halide perovskites with different compositions and morphologies were studied. The work started with the investigation of $CsPbBr_3$ thin films electrochemically prepared on FTO substrates. Following this, γ-$CsPbI_3$ nanoparticles synthesized using the Hot-Injection method were characterized after being drop-casted onto a glass substrate. Nanorods of the same material were produced from these nanoparticles through illumination in their colloidal form with a solar simulator, exploiting the light-induced self-assembly property exhibited by perovskites. Obtained results constitute the first report of this effect in the literature for γ-$CsPbI_3$ nanoparticles.

The mentioned systems were examined using low-temperature (10K – 290K) photoluminescence and transmission spectroscopy techniques, which enable the determination of fundamental quantum processes of absorption and emission near the bandgap. The findings reveal that inorganic perovskites display prominent excitonic behavior, especially in low-temperature absorbance spectra. Furthermore, by analyzing variations in the photoluminescence spectrum shape with temperature and excitation power it was possible to prove that in both materials that photoluminescence is originated in excitonic recombination. Besides that, it was also possible to prove that in both cases, the interaction of excitons with phonons occurs mainly through LO phonons, especially at high temperatures. Exciton-phonon interaction is produced by a phononic mode with an effective energy that can be calculated using Segall's model of exciton-phonon interaction. Results show that this characteristic energy is 30 meV in $CsPbBr_3$ and 15 meV in γ-$CsPbI_3$ nanoparticles. In addition, the Arrhenius diagram obtained from the dependence of the photoluminescence area on temperature makes it possible to obtain the energies associated with the mechanisms that produce photoluminescence quenching. One of these channels corresponds to the thermal dissociation channel of excitons. Moreover, as in the case of $CsPbBr_3$, a second quenching channel may be present and can be identified by the aforementioned analysis. However, this analysis does not provide information about the origin of this activation energy.

The Elliot formula, which is a fundamental analysis tool, was used for the analysis of absorbance spectra. Using Elliot's model several important fundamental parameters were obtained, such as the excitonic absorption energy and its spectral width, as well as the bandgap energy, which can be used to determine the exciton binding energy. Analyzing the temperature dependence of these parameters, several fundamental mechanisms were identified. First, the broadening of the excitonic peak in absorption follows a very similar broadening than the photoluminescence. When the broadening is analyzed using Segall's model a very similar interaction energy is obtained, thus implying that phonons are also responsible for this broadening. Analyzing the temperature dependence of the bandgap with a two oscillator Einstein model some evidence that the same phononic mode is also involved in this process. However, results are not conclusive given that other processes, as lattice expansion, are also involved. Exciton binding energy at room temperature was 40 meV for $CsPbBr_3$ and 33 meV for $CsPbI_3$. In both cases these values are close to thermal energy what ensures that most excitons will dissociate at room temperature producing free charge carriers.

The results also demonstrate the exceptional crystal structure achievable in inorganic perovskites, as evidenced by the remarkably low Urbach energy values obtained in both samples. Previously, such crystallinity was attainable only through costly deposition techniques like Molecular Beam Epitaxy and Metal-Organic Chemical Vapor Deposition. However, it can now be accomplished using simple, locally available solution-based deposition methods. This outstanding crystallinity enabled the clear observation of previously mentioned fundamental processes. Moreover, analyzing the increase of Urbach energy with temperature it was possible to show that the same phononic mode involved in the broadening of photoluminescence and in increasing bandgap is also responsible for increasing the thermal disorder in the lattice.

From the obtained results it was possible to formulate a fully consistent model that allows for the interpretation of all the results obtained in temperature dependent photoluminescence and transmittance spectroscopy obtained in inorganic perovskites. It is expected that this model can also be applied in hybrid perovskites since very similar results are usually reported in the literature. For this reason, I believe the developed model can be an important contribution that can be of high value to the scientific community. Besides that, a MATLAB algorithm for the analysis of the data that extracts many valuable parameters automatically from measurements was implemented.

The developed theoretical model, along with the MATLAB code, played a critical role in explaining several other results. First, it allowed us to identify the phenomena of exciton localization, which is manifested in the photoluminescence spectra as an additional peak with lower energy than the peak produced by free exciton recombination. The change in energy, full width at half maximum and area of the low energy peak is very different to the one observed in free excitons and can be explained by Li's model. Localization of carriers is a ubiquitous phenomenon in semiconductors and can have profound effects in charge carriers' mobility and hence in device performance. So, its identification is of great importance for device optimization. Next, the optical properties characterization also allowed the identification of an amorphization process in the light induced self-assembly of nanoparticles into nanorods. Amorphization is manifested in an increase of the photoluminescence energy and in Urbach energy. This process also increases the inhomogeneous contribution in Segall's model for exciton-phonon interaction and decreases the exciton binding energy due to the change in the characteristic size of the samples.

It is expected that the application of this algorithm in measurements performed in samples synthesized in different conditions will enable the extraction of valuable information for a better understanding of fundamental processes in absorption and emission. By identifying and understanding the relationships between the optical, morphological, and compositional properties of these materials, we can optimize their performance and deposition conditions in optoelectronic devices. This can be an important asset for future work done in our group in the field of perovskites.

Looking forward, there are several promising possibilities for future work on perovskite materials. Firstly, addressing the toxicity concerns associated with lead-based perovskites is of outmost importance. Research efforts should focus on substituting lead with non-toxic elements, for example tin and bismuth, while maintaining or even improving the desirable properties of perovskites. Successful replacement of lead will allow us to develop more environmentally friendly materials that could then be used to produce a new generation of optoelectronic devices. It is also fundamental to gain a deeper understanding of the origin of self-assembly in perovskites.

Investigating the underlying mechanisms driving this phenomenon can provide valuable insights into the formation of perovskite nanostructures with controlled morphologies and properties. Gaining a thorough comprehension of self-assembly processes can enable the development of a wider variety of nano and microstructures simply processed from nanoparticles. In turn access to a wider variety of structures will advance perovskite-based devices, enhancing their performance and broadening their applicability across a range of applications. Besides that, given that self-assembly is heavily influenced by perovskites surface properties, understanding this process can be an excellent tool to better understand the origin and properties of superficial states. It has been proven that superficial states have a direct impact in optoelectronic properties, device performance and crystal stability in perovskite nanocrystals.

Even though during our work the stability of colloidal γ-CsPbI$_3$ perovskites nanoparticles for several weeks was empirically corroborated a systematic study of stability is still needed. Γ-CsPbI$_3$ is a particularly interesting material due to the as proved excellent optoelectronic properties, but its inherent instability, especially in thin films, has limited its widespread adoption in practical applications. Therefore, gaining a deeper understanding of the factors affecting its stability is essential for broader consideration by the scientific community. Future work should also involve a comprehensive investigation of the intrinsic and extrinsic factors that contribute to the degradation of γ-CsPbI$_3$. In particular, the role of environmental factors, such as temperature, humidity, and exposure to light should carefully be investigated to better understand how these external conditions contribute to the degradation processes. Besides, an exploration of the influence of various synthesis methods, processing conditions, and material compositions on the material's stability could be of high value.

In addition to the research directions previously discussed, there is also potential to further improve the Matlab algorithm used for data analysis. The current algorithm has proven to be valuable for extracting important parameters from optical measurements. However, it can be enhanced by implementing additional analysis techniques to extend its capabilities and provide more comprehensive insights into the materials' properties. One such extension could involve implementing the f-sum rule algorithm. This method allows a more precise determination of exciton binding energy. Additionally, future work could involve developing advanced algorithms to incorporate machine learning techniques to identify patterns in the data once a large database of parameters has been built.

The research conducted on perovskite materials is anticipated to provide valuable insights into their fundamental properties and contributions for the development of perovskite-based devices. These devices, including solar cells, LEDs, and other optoelectronic systems, hold great promise for enhancing efficiency and reducing production costs. The wider adoption of perovskite-based technologies has the potential to positively impact society by providing more accessible, sustainable, and efficient energy solutions. Besides that, the study of perovskite materials presents a significant opportunity for making tangible contributions to the development of perovskite-based technologies using the capabilities of local laboratories in Uruguay. By advancing our understanding of the fundamental properties of perovskites and optimizing their deposition methods to obtain desired properties, we can potentially establish Uruguay as a key player in this burgeoning field. The research conducted in our local laboratories can pave the way for the synthesis and production of perovskite devices in Uruguay in the near future. This could ultimately contribute to the

development of eco-friendly technology that can be an important player in the transformation of the energy production matrix. So, the potential impact of this work extends beyond the realm of academia. As we continue to explore the rich possibilities presented by perovskite materials, we are committed to fostering innovation and positive change for the benefit of the environment and the world at large.